UNIVERSITY OF SOUTHAMPTON

FACULTY OF PHYSICAL SCIENCES AND ENGINEERING

SPACE CHARGE DYNAMICS IN POLYETHYLENE UNDER PERIODICAL HIGH VOLTAGE ELECTRIC FIELDS

By

CHURUI ZHOU

A thesis submitted for the degree of Doctor of Philosophy

Electronics and Computer Science
Faculty of Physical and Applied Science
University of Southampton

United Kingdom

June 2017

UNIVERSITY OF SOUTHAMPTON

ABSTRACT

FACULTY OF PHYSICAL SCIENCES AND ENGINEERING

ELECTRONICS AND COMPUTER SCIENCE

Doctor of Philosophy

SPACE CHARGE DYNAMICS IN POLYETHYLENE UNDER PERIODICAL HIGH VOLTAGE ELECTRIC FIELDS

By Churui Zhou

During the last two decades, space charge has been recognised to be a major factor influencing the electrical performance of cable insulation. A significant amount of work has been carried out to investigate space charge dynamics within polymeric insulation under high voltage direct current (HVDC) fields. Modern charge mapping techniques are adopted to obtain the necessary information about space charge within the insulation. However, the underlying physics of charge transport and the charge trapping characteristics of space charge are not well understood. Employing theoretical modelling based on numerical simulation to analyse the space charge features can provide an insight view into the charge distribution in dielectrics under realistic conditions. This thesis focuses on the analysis of space charge phenomenon within polyethylene insulation under common operating electric fields through both experimental and numerical investigations.

An improved pulsed electro-acoustic system along with a data processing procedure has been developed to investigate space charge in polyethylene under AC and superposed AC and DC voltages. Raman spectra and Attenuated Total Reflectance Fourier-transform Infrared (ATR-FTIR) spectra are collected to confirm the influences of the magnitudes and frequency of AC fields on the physical characteristics of polyethylene. Evaluation of pure AC and DC voltage tests as specified in the international standard, BS EN 61378-2:2001, has also been done by comparing the space charge profiles under the real superposed AC and DC voltage and the deduced testing voltages.

A numerical simulation model based on bipolar charge transport theory has been developed to analyse space charge phenomenon in polyethylene under periodical complex electric fields. The build-up of space charge in polyethylene under DC electric fields has been modelled, and the simulation setting has been optimised based on the measured results. The model is also introduced to simulate the charge dynamics under AC and superposed AC and DC fields. The simulation results exhibited good agreement with the measured profiles.

Besides, the effects of applied field characteristics (frequency, field magnitude, and field composition) on the charge formation and transportation have also been investigated and using both the experimental and numerical approaches. Furthermore, the numerical model has been further applied to analyse the relationship between space charge phenomenon and electrical breakdown in insulation. It has been found that the different region where breakdown happens caused by different charge dynamics is a significant reason leading the various breakdown strengths of the same material different, under AC and DC voltages.

The outcome of this dissertation can aid the fundamental understanding of charge dynamics in the insulating materials under general operating high voltage electric fields.

Table of Contents

List of Tables

List of Figures

Publications

Journal and Articles

"***Space charge and AC electrical breakdown strength in polyethylene***"
Churui Zhou and George Chen
IEEE Transactions on Dielectrics and Electrical Insulation (TDEI). 24. 1(2017):pp. 559-566

"***Model to estimate the trapping parameters of cross-linked polyethylene cable peelings of different service years and their relationships with DC breakdown strengths***"
Liu, Ning, Churui Zhou, George Chen, Yang Xu, Junzheng Cao, and Haitian Wang.
High Voltage 1, no. 2 (2016): pp. 95-105.

"***Space charge behaviours in polyethylene under combined AC and DC electric fields***"
Churui Zhou and George Chen
High Voltage Engineering 41.4 (2015): pp. 1167-1177.

"***Determination of threshold electric field for charge injection in polymeric materials***"
Ning Liu, Churui Zhou, George Chen, and Lisheng Zhong,
Applied Physics Letters 106.19 (2015): pp. 192901.

Conference Papers and Presentations

ORAL PRESENTATIONS:

"**D*ynamics of space charge within low density polyethylene under different magnitudes of HVAC electric field***"
Churui Zhou and George Chen, International Conference on High Voltage Engineering and Application (ICHVE), 2016 IEEE Conference, IEEE. **(Students best paper award)**

"***Space charge and its role in electric breakdown of solid insulation***"
George Chen, Churui Zhou, Shengtao Li and Lisheng Zhong, Power Modulator and High Voltage Conference (IPMHVC), 2016 IEEE Conference, IEEE.

POSTER PRESENTATIONS:

"***The influence of DC component of combined AC and DC voltage on charge dynamics in polyethylene***"
Churui Zhou and George Chen, International Conference on Electrical Materials and Power Equipment (ICEMPE), 2017 IEEE Conference, IEEE.

"***Influences of frequency on space charge formation in polyethylene under high voltage AC electric fields***"
Churui Zhou and George Chen, Electrical Insulation and Dielectric Phenomena (CEIDP), 2016 IEEE Conference, IEEE.

"***Space charge and AC electric breakdown strength in polyethylene***"
Churui Zhou and George Chen, Electrical Insulation and Dielectric Phenomena (CEIDP), 2015 IEEE Conference, IEEE.

"***Space charge behaviours in polyethylene under combined AC and DC electric fields***"
Churui Zhou and George Chen, Electrical Insulation and Dielectric Phenomena (CEIDP), 2014 IEEE Conference, IEEE.

"***The influence of frequency of ac component on space charge behaviours in polyethylene under combined AC and DC electric fields***"
Churui Zhou and George Chen, Electrical Insulation and Dielectric Phenomena (CEIDP), 2014 IEEE Conference, IEEE.

DECLARATION OF AUTHORSHIP

I, ……

declare that this thesis and the work presented in it are my own and has been generated by me as the result of my own original research.

SPACE CHARGE DYNAMICS IN POLYETHYLENE UNDER PERIODICAL HIGH VOLTAGE ELECTRIC FIELDS …………………………………………………………………………………………………

I confirm that:

1. This work was done wholly or mainly while in candidature for a research degree at this University;
2. Where any part of this thesis has previously been submitted for a degree or any other qualification at this University or any other institution, this has been clearly stated;
3. Where I have consulted the published work of others, this is always clearly attributed;
4. Where I have quoted from the work of others, the source is always given. With the exception of such quotations, this thesis is entirely my own work;
5. I have acknowledged all main sources of help;
6. Where the thesis is based on work done by myself jointly with others, I have made clear exactly what was done by others and what I have contributed myself;
7. None of this work has been published before submission

Signed: ……

Date: ……

Acknowledgements

I would like to present my sincere appreciation to my supervisor and inter-examiner, Prof George Chen and Dr Mihai Rotaru. George gives me patient guidance and essential suggestions all the work presented in this thesis. He also provides valuable comments and solutions to my confusion and problems occurring during the research. Mihai provides me more chances to communicate with the others especially on the numerical modelling algorithm and gives valuable support on academic writing. I must thank them gratefully for their essential supervision and help.

Thanks are also given to Dr Zhiqiang Xu and Dr Miao Hao, who gave me training on the experiment, especially the detection of space charge under AC electric fields. Thanks to Mrs. Allison Shaw who provides the measurement data of ATR-FTIR by which I could use to investigate the structure of aged samples along with Raman spectra results. I would also like to give my sincere thanks to the technicians in the Tony Davies High Voltage Laboratory for their support on experimental work.

Finally, thank all my friends for their companies in Southampton, and I especially appreciate my family for their keen support from China.

Definitions and Abbreviations

Symbols

A	Richardson constant, $A = 1.2 \times 10^{6}$ Am^{-1} K^{-2}
d	Sample thickness, m
D_T	Breakdown testing sample thickness,m
E	Electric field, Vm^{-1}
E_C	Lowest energy level of the conduction band of insulator
E_F	Fermi level of the insulator
$E_{F'}$	Fermi level of the contact between the metal and an insulator
E_{Fm}	Fermi level of the metal
E_G	Band gap of the insulator voltage
e_p	Magnitude of the pulse,V
E_V	Highest energy level of the valence band of insulator
f	Frequency,Hz
f_m	The maximum local electric field, kV/mm
Δf	The maximum field distortion, %
J, j	Current density, Amm^{-2}
k_B	Boltzmann constant, $k=1.38 \times 10^{-23}$ $m^{2}kgs^{-2}K^{-1}$
n	Density of mobile species, Cm^{-3}
min/m	Mfinutes
q	Electronic charge, C
R	Ramping voltage ratio, Vs^{-1}
s	Source term for each species, $Cm^{-3}s^{-1}$
S	Apparent breakdown strength, kV/mm
S_0, S_1, S_2, S_3	Recombination coefficients
T	Temperature, K
T_0	Time to breakdown, s^{-1}
TC	Total charge amount, C
v	Attempt-to-escape frequency, s^{-1}
V	Voltage potential, V
v_{sa}	Sound velocity through the material
β_{sch}	Potential barrier for the Poole-Frenkel, eV
ε	Permittivity of dielectric, Fm^{-1}
μ, μ_H, μ_h, μ_E, μ_e	Mobility of charge carrier, $m^{2}V^{-1}s^{-1}$
ρ	Net Charge density, Cm^{-3}
σ	Conductivity, Sm^{-1}
σ_1, σ_2	Density of surface charge, Cm^{-2}
ϕ	Working function of the insulator
φ_0	Phase anger
ϕ_B	Potential barrier height at the interface
ϕ_m	Working function of the metal
χ	Electron affinity of the insulator
ω	Angular velocity, s^{-1}

Abbreviations

AC, ac	Alternating current
ATR-FTIR	Attenuated Total Reflectance Fourier-Transform Infrared
CFL	Courant-Friedrich-Levy
CCD	Charged coupled device
DC, dc	Direct current
EL	Electroluminescence
FFT	Fast fourier transform
FTIR	Fourier-Transform Infrared
HDPE	High density polyethylene
HVAC	High voltage alternating current
HVDC	High voltage direct current
Hz	Hertz
IFFT	Inverse Fast Fourier transform
kV	Kilo volts
LDPE	Low density polyethylene
LIMM	Laser intensity modulation method
LIPP	Laser induced pressure pulse method
LLDPE	Linear low density polyethylene
LTI	Linear time-invariant
PDE	Partial differential equation
PE	Polyethylene
PEA	Pulsed electro-acoustic method
PVDF	Polyvinylidene fluoride
SCLC	Space charge limited current
SSC	Single site catalysts
TRR	Total recombination rate
XLPE	Cross-linked polyethylene

Chapter 1: Introduction

Over the years, space charge phenomenon has been regarded as an important factor causing the ageing and electrical failures of insulation designed for high voltage apparatus. Localised charges produced either by electronic injection or material ionisation can slowly (comparing with charge transport in metal) transport within the insulation due to the applied fields and distort the internal electric field in return. The interactive effects of mechanical and thermal stress caused by either the applied electric field or the local environment could further exacerbate this distortion. In long-term time, the enlarged distortion will accelerate the emission of light electroluminescence (EL) and partial discharge (PD) processes, which are the primary incentive of cable ageing [1]. During the last three decades, a few non-destructive charge-mapping methods have been established to investigate the space charge dynamics within polymer materials [2-5]. Considerable efforts have also been made to interpret space charge characteristics based on numerical modelling [6-9]. In this Chapter, the general solid insulating material, polyethylene, the charge dynamics, and the space charge detection methods are discussed and illustrated respectively from 1.1 to 1.3. 1.4 summaries the motivation and objective of the dissertation, and 1.5 highlights the contribution of the research. An outline of the structure of the thesis is presented in 1.6.

1.1 Polyethylene

1.1.1 Structure of polyethylene and its electrical properties

Polyethylene is a common solid polymer, composed of long chain molecules within branching of methylene groups. The long chain molecule contains numerous repeated monomers (Methylene bridge) connected by covalent bonds. The number of monomers in the chain can be tens of thousands, which results in a molecular weight of millions of atomic units. The structures of ethylene (C_2H_4) and polyethylene are shown in Figure 1-1. The parameter n represents the scale of polymerisation of the material, which can range from 100 to 25000 or more [10]. The polymerised structure gives polyethylene some unique characteristics compared with simple ethylene. Ethylene, a hydrocarbon with carbon-carbon double bonds, is a gas at room temperature. After polymerisation under high pressure and temperature, the molecules are tightly bonded together, producing a solid. Polyethylene is a semi-crystalline polymer. Some molecular chains are arranged in an ordered fashion, forming a crystalline region, whilst others retain a disordered irregularly and entangled structure. During melting, they create an amorphous region within the polymer.

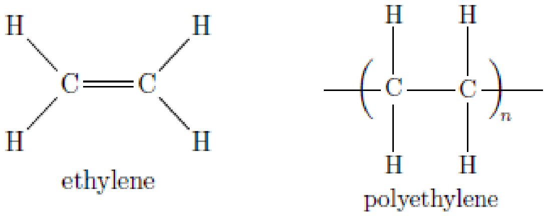

Figure 1-1 Structure of ethylene and polyethylene [10]

Aiming to analyse and understand the crystalline and amorphous regions within polyethylene, Hermans proposed a fringed-micelle model in early 1930 [11]. This model suggests that long fibrillar polymer chains grow parallel with or perpendicular to each other through some portion of a volume. This process continues until the chains stretch into amorphous regions, as shown in Figure 1-2. Due to the long-chain macromolecules, polyethylene seldom forms straight chains. Herman's model is partly inaccurate as it is not in agreement with the electron diffraction results of polyethylene. Later in 1938, Storks [11] proposed another model suggesting that polymer (polyethylene) chains can align and strack on the top of one and another, piling up together into so-called 'lamella'. Consequently, the molecules form a crystalline region, as illustrated in Figure 1-3. In some cases, the chain of polyethylene can depart the lamella areas and drift into an amorphous region. These chains can enter an amorphous region for a space or re-enter at an adjacent site as shown in Figure 1-4 (the 'switchboard' model) [11] . Besides this behaviour, lamella fibrils can extend from a nucleus in radial directions, forming a spherulite. This behaviour occurs when they are crystallised from molten polymers (polyethylene), as illustrated in Figure 1-5 [11]. The amorphous areas between layers always contain weak chain ties, which easily break under high temperature or pressures. Spherulites can be observed under microscopes. Time and length of crystallisation influence the size of spherulites. As Figure 1-6 shows, spherulites normally terminate their growth upon encounting anthor spherulte. If such termination doesnot occur, they are idealy spherical [12].

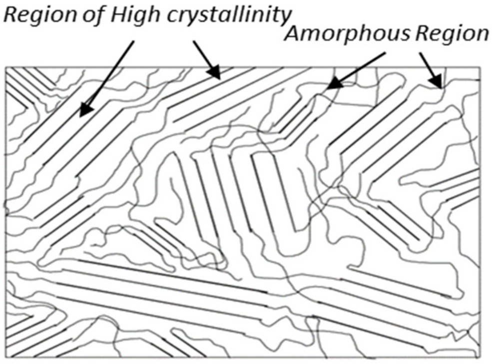

Figure 1-2 Fringed micelle model of polymer [12]

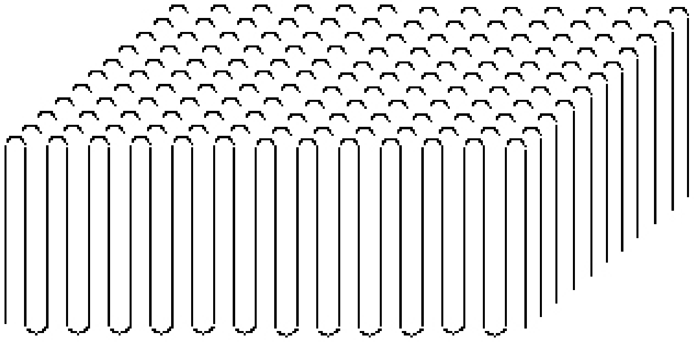

Figure 1-3 Lamella configuration: stacked chains [12]

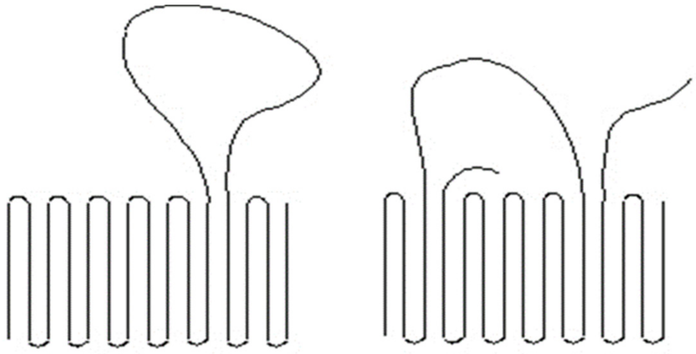

Figure 1-4 The switchboard model of lamella [12]

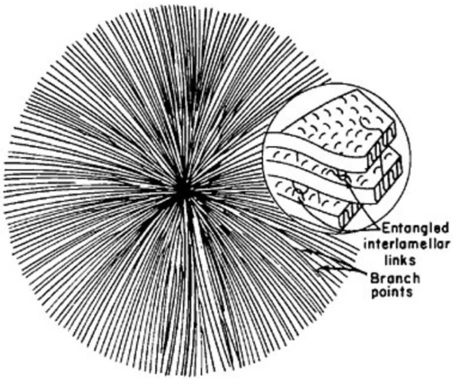

Figure 1-5 Schematic diagram of a polymer spherulite with chain-folded lamella [11]

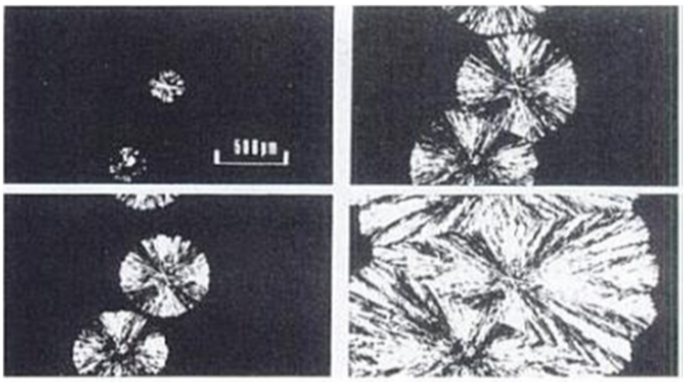

Figure 1-6 Growth of partitioned spherulites of polyethylene from melt over one minute [12]

Polyethylene as a non-polar thermoplastic material has relatively low permittivity and high breakdown strength comparing with conventional paper insulation. Polyethylene is hence becoming a more competitive insulating material for high voltage apparatus, especially for power transmission cables. Compared with paper/oil insulation, polyethylene insulation systems have low manufacturing, installation and maintenance costs. Table 1-1 lists the common electrical properties of polyethylene [13-17].

Since the introduction of polyethylene as cable insulation in the 1950's, the methods of designing, manufacturing and maintaining solid insulated high voltage cables have advanced rapidly. In 1969, a 225 kV low-density polyethylene (LDPE) insulated cable was firstly installed in France. The application of 400 kV cables has been performed since 1985. Further investigation of 500 kV cable has been made since the 1990s [18, 19]. Due to the relatively low melting temperature and large thermal expansion coefficient, LDPE is not suitable for insulating underground cables, whose average operating temperature can reach 90˚C [20]. The sustained current rating, overload and short-circuit temperature of LDPE cables are also limited. This problem was solved by introducing the cross-linking technology to the manufacture of polyethylene in 1980s [21]. The resulting cross-linked polyethylene (XLPE) can still maintain adequate strength under temperatures in the range of 120–150 ˚C. The mechanical properties at relatively high temperature and the susceptibility to water treeing of the material have also been improved. Based on all of the above, the XLPE insulated cable has gradually replaced the paper/oil variety in newly constructed transmission or distribution power systems. The economical manufacture, installation and maintenance of XLPE cable enable it suitable for underground transmission among highly populated cities and urban areas. The first extruded 145 kV XLPE submarine cable was installed in 1973 by ABB. Since then high voltage XLPE cables varying from 110 kV to 500 kV have come into service with the help of improved methods for producing clean polyethylene, advanced cable manufacturing technology and a new generation of extrusion systems [21, 22]. In the past decade, the research and installation of high voltage direct current (HVDC) cables with polymeric insulation has been emerging globally, with the development of HVDC power transmission techniques. [23].

Table 1-1 Electrical properties of polyethylene [13-17]

Parameters	**LDPE**	**HDPE**	**XLPE**
Permittivity (@1 MHz)	2.25-2.35	2.3-2.35	2.4
Tanδ (@1MHz)	$<5*10^{-4}$	10^{-3}	10^{-3}
Breakdown strength (kV/mm)	20-160	20-160	50
Volume resistivity (Ω·cm)	$>10^{16}$	$>10^{16}$	$\sim10^{16}$
Arc resistance (sec)	135-160	200-250	-

1.1.2 Classification of polyethylene

Classification of polyethylene is mainly dependent on its density and branching, as the mechanical properties of polymers are significantly influenced by the crystal structure, the extent, and types of branching. In consideration of solid materials, Low-Density Polyethylene (LDPE), High-Density Polyethylene (HDPE), Cross-linked Polyethylene (XLPE) and Linear Low-Density Polyethylene (LLDPE) are the most commonly used polyethylenes. A brief introduction of the four materials is presented below.

- ***Low Density Polyethylene***

Low-Density Polyethylene (LDPE) is regarding the polyethylene having a density range from 0.910 to 0.940 g.cm^{-3} [10].Typical LDPE has a significant amount of short and long chain branching, and these chains are not combining the crystal structure under certain cases. Consequently, there is less force between the molecules, due to the reduced instantaneous-dipole and the induced-dipole attraction. All these above, cause the tensile strength of the LDPE is relatively low, while its ductility is excellent. Besides, the great extent of long chains branching gives molten LDPE the unique flow properties. LDPE can be manufactured by free radical polymerization [17]. It is a primeval polyethylene insulator and mainly used as rigid containers and plastic film.

- ***High Density Polyethylene***

High-density polyethylene (HDPE) is defining polyethylene with a density equal or greater to 0.941 g/cm^3 [10]. Unlike LDPE, HDPE has a relatively small extent of branching. Thus, the intermolecular forces of HDPE are reduced. HDPE is produced by polymerisation of ethylene using Ziegler-Natta or supported chromium catalysts [17]. In some cases, HDPE is copolymerized with a tiny amount of 1-alkenes, aiming to introduce some short-chain branching, and reducing the crystallinity of HDPE. In this way, the toughness and crack resistance of HDPE can be enhanced. HDPE is mainly used in production and packaging industry. Containers like milk jugs, detergent bottles, butter tubs, and water pipes are generally produced using HDPE. Moreover, HDPE owns an outstanding advantage in recyclability. Degraded HDPE does not diffuse hazardous emissions containing toxic chemicals, leaving less harm to the environment.

- ***Cross-linked Polyethylene***

The volume mass density of cross-linked polyethylene (XLPE) is smaller than that of high-density polyethylene. Due to plenty of cross-link bonds inside the material, XLPE is changing into thermoset rather than thermoplastic. Both the chemical and physical stabilities of XLPE under high temperature are improved, and its corresponding chemical resistance of it is enhanced. Peroxide cross-linking method (developed by Engel in 1960s), Silane-based method (proposed by Monosil in 1974), and vinylsilane method (1986) are extensively used to produce XLPE in high voltage cables manufacture [20, 21].

• *Linear Low Density Polyethylene*

Linear Low-Density Polyethylene (LLDPE) is defining polyethylene with a density range of 0.915–0.925 g/cm^3. LLDPE can be treated as a compromised product between LDPE and HDPE in consideration of structure and property. LLDPE is named accounting its linear polyethylene backbone components, which are usually randomly attached with short alkyl groups [10]. In comparison with LDPE, LLDPE is improved on tensile strength, impact, puncture resistance, and cracking resistance. Meanwhile, LLDPE remains LDPE's high toughness and flexibility under stress. However, the manufacture of LLDPE is relatively complex compared with LDPE, and LLDPE is not as transparent as LDPE, caused by its lower content of amorphous regions. Moreover, similar to HDPE, LLDPE is usually copolymerized with 1-alkene. Widely used methods to produce HDPE are Ziegler-Natta catalyst, metallocene catalysts, and supported chromium or SSC (Single Site Catalysts) [17].

1.1.3 Degradation of polyethylene

When a When a polyethylene-insulated cable is in operation, the insulating material will experience a combined action of electric fields, thermal stresses, and mechanical forces. The degradation of insulation could be initiated where high or divergent electrical pressure occurs due to the influence of impurities, defects and microvoids inside the insulation or at the interfaces between insulation and conductive metal. The degradation in polyethylene can develop into different behaviours such as electroluminescence, partial discharge, treeing and eventual breakdown, at various ageing stages. The treeing in polyethylene regarding as a prebreakdown phenomenon can be classified into three types: electrical tree, water tree and electrochemical tree [24]. The electrical tree is one of the essential reasons for long-term degradation of polymeric insulation in high voltage ac (HVAC) system. Extensive research has been focused on electrical trees in polyethylene [25]. Electrical trees grow within the regions under high stress, like metallic asperities, conducting contaminants or structure irregularities. It is ineluctable that microvoids exist in polyethylene. These voids have relatively low permittivity and electrical strength. Thus, the local electrical field within voids could be higher than outside, and it may cause breakdown of gas in voids, triggering partial discharge within the insulating material. Partial discharge can accelerate the degradation of void surface, which can further facilitate the electrical treeing phenomenon [11]. At the initial stage of electrical trees, the formation of degradation region and electroluminescence (EL) are generally observed [26]. The relationship between EL and the degradation of XLPE has been analysed and presented by Fan et al. in 2001 [27]. The results suggest that the electron impact theory can explain the EL and electrical degradation rather than photo-degradation mechanism. Until now, the degradation of polyethylene is still not fully understood due to the complex dynamic nature and various factors (electrical, thermal and mechanical stresses) affecting the process. Nevertheless, all kinds of electrical degradation are regarded to be related to charges within materials or at the interfaces, especially at the initial stages. Charges inside the insulation are generated from either electrode injection or dissociation from ionization of impurities and particles within dielectric materials. Polyethylene’s low conductivity and charge trapping sites will further contribute to local accumulation of charges (space charge phenomenon). The localised charges will distort the electric field distribution within polyethylene. Partial discharges, electrical trees, electroluminescence and other degradation processes are more natural to initiate within insulation under the enlarged electric field [11, 25, 26]. Therefore, remarkable space charge accumulation and intensive charge dynamics can accelerate general degradation or ageing process based on their significant contribution to local field distortion within polyethylene.

1.2 Space charge phenomenon in polyethylene

Space charge describes localised charges accumulated in the bulk of dielectrics and insulators or at the interface between different materials, which are commonly carried by electrons, ions or charged particles. Some of these charge carriers are sourced from electrode injection, and others are from polarisation, dissociation or ionisation of the contamination inside the material. Besides, these charges can be either mobile or trapped in the dielectric materials. Charge carriers with opposite polarities can be recombined and neutralised. This process often results in photonic emission effects.

Generally, space charge can be classified into two types: homocharge and heterocharge. Charge with the same polarity as the adjacent electrode is called homocharge and that with opposite polarity is named heterocharge. Homocharge generally comes from the electrode injection while heterocharge is mainly caused by ionisation within the insulating materials. As shown in Figure 1-7, the Homecharge usually results in the field enhancement in the middle of the insulation, while heterocharge often cause field enhancement in the surface region of insulation.

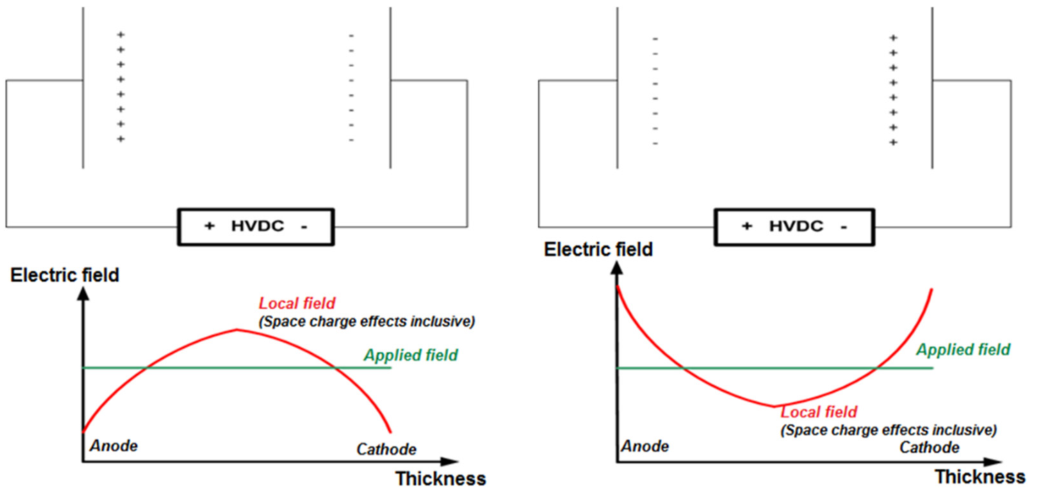

Homo-charge where charges close to the electrode have the same polarity as the charges on the electrode.

Hetero-charge where charges close to the electrode have the opposite polarity to the charges on the electrode.

Figure 1-7 Schematic illustration of Homo-charge and Hetero-charge

The parameter conductivity is generally defined to demonstrate the material’s ability of charge transportation, in the description of charge transport within the dielectrics. The conductivity σ is described as follows:

$$\sigma = \mu n q \tag{1-1}$$

Where q is the elementary charge; μ is the drift mobility of charge carriers; and n is the concentration of free charge carriers [28].

As for polyethylene, the typical value for conductivity, σ, is around 10^{-15} Sm^{-1}, while the mobility μ is about $10^{-14}\mathrm{m}^2\mathrm{V}^{-1}\mathrm{s}^{-1}$, and q is equal to 1.60×10^{-19} C [29]. In this way, the corresponding amount of charge carriers within polyethylene is of $10^{18}\mathrm{m}^{-3}$, and the intrinsic concentration of charges within insulator is usually less than 10^{15} m^{-3} [11]. The larger difference between the two values indicates the existence of non-intrinsic sources of charge carriers in dielectrics. These sources are primarily affecting the electrical performance of insulators when subject to electric fields as they contribute the major charges within the materials. Their generation and transportation process are mainly discussed here.

1.2.1 Charge generation

There are two major sources of charge generation in an insulator: ionic process and electronic injection. Ionic process is the process by which an atom or a molecule capture a negative or positive charge by gaining or losing electrons to form ions in insulation. This process is mainly caused by chemical impurities or dissociation of additives. Electronic injection describes a phenomenon that electrons or holes immigrate from the electrodes (conductors) into the bulk of the insulators (polyethylene) when the applied electric field exceeds a certain value. The ionic process within the insulating polymers has been greatly reduced along with the significant improvement of material production, leading to the electronic process dominating the charge sources within the polyethylene. Therefore in this work the charge caused by ionic process is neglected and in this part, the procedure of electronic charge injection is mainly discussed.

When the electrodes (metal) are in contact with the insulators, free carriers will flow from the electrodes to the insulator or reversely from the insulator towards the electrodes until the Fermi levels of both are equal, which indicates that an equilibrium condition is established. The direction of the flow is determined by contact states and work functions of both materials [30]. Under HVDC conditions, as shown in Figure 1.8, the work function of the anode, φ_{m1}, is higher than that of insulator (φ), while the work function of the cathode, φ_{m2} , is lower than φ initially due to the polarity of the applied field. Therefore initially electrons within the system flow from the cathode to the insulator and transport towards the anode. Because of these, positive charges are left in the insulation near the positive electrode, while negative charges accumulate at the interface and bulk of the insulator adjacent to the negative electrons.

In Figure 1-8, E_{Fm} is the original Fermi level of the electrode (metal); E_F is the initial Fermi level of the insulator, χ is the electron affinity of the insulator; E_C is the lowest energy level of the conduction band of insulator; E_V is the highest energy level of the valence band of insulator; E_G is the band gap of the insulator; $E_{F'}$ is the Fermi level of the contact system and φ_B is the potential barrier height at the interface of connection.

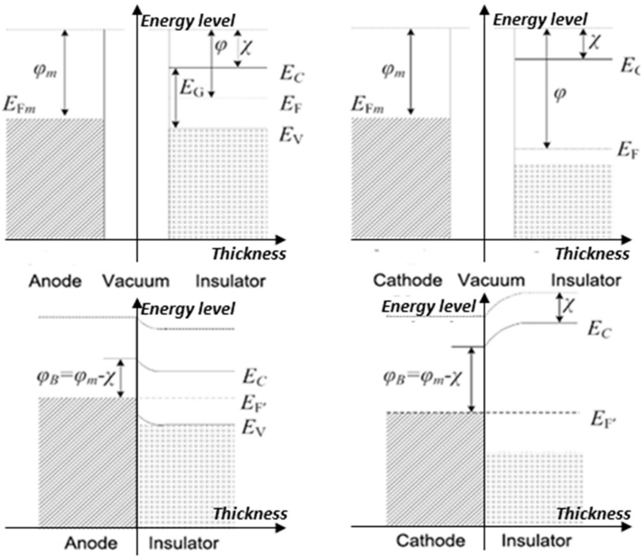

Figure 1-8 Energy diagrams of the electrical contacts between electrodes and insulator [30]

According to Figure 1-8, it is the potential barrier at the interface of electrodes and insulator that blocks the charge injection, which can be reduced by the image force (Effects of charges built up in the electrodes as charges inside dielectrics approach the metal-dielectrics interface) of the applied electric field. Consequently, the external field can enhance the injection of charge carriers at the interface between electrodes and insulator. A Richardson-Schottky injection theory has often been applied to analyse this phenomenon.

Richardson-Schottky injection

The lowering of the potential barrier under a uniform field to the neutral contact (metal and insulator sharing the same Fermi level before their contact) between a metal and an insulator is illustrated in Figure 1-9.

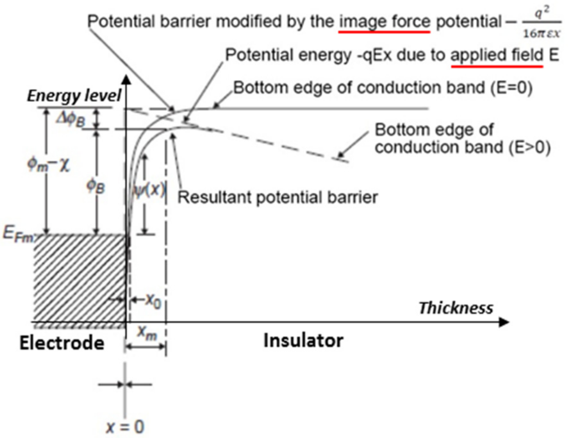

Figure 1-9 Schottky injections at the interface of electrodes under electric field [30]

As shown before in Figure 1-8, the original potential barrier φ_B is equal to (φ_m - χ). Once a field *E* is applied, a new barrier will be generated in consideration of the field and image force, and the new potential barrier, $\psi(x)$, can be obtained using the following equation according to Richardson-Schottky theory.

$$\Psi(x) = \varphi_m - \chi - \frac{q^2}{16\pi\varepsilon x} - qEx \qquad \textbf{1-2}$$

χ indicates the electron affinity force. From the equation, it is clear that the image force (third term in the equation) tends to attract electrons back to the metal, while the force of the applied field (fourth term in the equation) drives electrons away from the metal. Resulting from this conflict trend, an optimal point exists, where the overall lowering effect becomes maximal. Using the differential of equation 1-2, the value of distance where the lowest potential barrier, x_m, can be calculated, with respect to *x*.

When $x = x_m$, $\frac{d\Psi(x)}{dx} = 0$. So

$$x_m = \sqrt{\frac{q}{16\pi\varepsilon E}} \qquad \textbf{1-3}$$

Then the lowering potential barrier height $\Delta\varphi_B$ is

$$\Delta\varphi_B = \left(\frac{q^2}{16\pi\varepsilon x}\right) + qEx = \sqrt{\frac{q^3E}{4\pi\varepsilon}} \text{ when } x = x_m \qquad \textbf{1-4}$$

In this way, the lowered potential barrier height becomes

$$\Psi = \varphi_B - \Delta\varphi_B = \varphi_m - \chi - \sqrt{\frac{q^3E}{4\pi\varepsilon}} \qquad \textbf{1-5}$$

The lowered potential barrier of the contact interface will result in the thermionic emission of electrons from the electrodes (metal). According to the Richardson-Dushman equation, the rate of thermionic emission of electrons from a unit area is

$$J = A \cdot T^2 \exp\left(-\frac{\Psi}{k_BT}\right) \qquad \textbf{1-6}$$

Where *A* is a constant equal to $1.2*10^6$ $Am^{-2}K^{-2}$, ψ is the potential barrier height and k_B is the Boltzmann constant.

Combined equations 1-5 and 1-6, the injected current density from the electrodes (metal) into an insulator caused by the lowered potential barriers height at the interface can be obtained, known as a Richardson-Schottky injection (equation 1-7).

$$J = A \cdot T^2 exp\left(-\frac{\varphi_B}{k_BT}\right) exp\left(\frac{1}{k_BT}\sqrt{\frac{q^3E}{4\pi\varepsilon}}\right) \qquad \textbf{1-7}$$

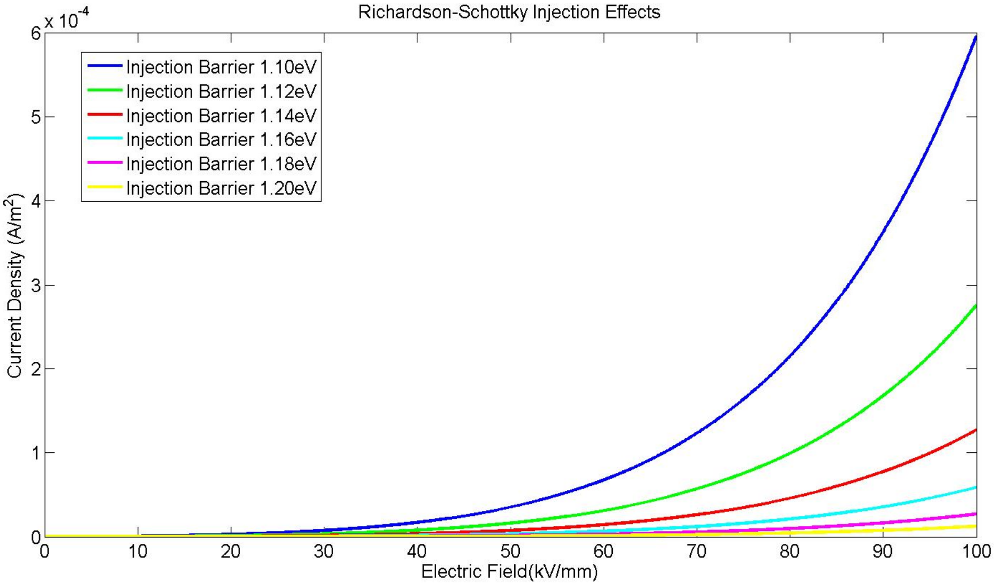

Figure 1-10 Current density caused by Schottky injection

The current density resulting from various injection barriers based on Schottky injection theory is illustrated in Figure 1-10. The graph clearly demonstrates the injected current density increases exponentially with the reduction of Schottky injection barrier.

1.2.2 Charge transportation processes

The conduction within the insulator is a complex process and demonstrates a field dependent feature when the external electric stress is applied. The defects and impurities within the insulator are believed to cause a bulk limited conduction effect, whilst the charges injected from the electrodes can similarly bring an effect called electrode limited conduction. These two effects share almost the same influences in consideration of the charge transportation within the insulator. Besides, the distribution of space charge caused by the above conduction processes will in return distort the electric field within the material and consequently affect the behaviour of charge carriers, which complicates the situation furthermore.

In general, there are three theories proposed to analyse the charge transportation within insulators: hopping mechanism, Poole-Frenkel effect, and space charge limited current (SCLC).

A wide band gap, between the conduction and valence bands, is believed to be possessed by polyethylene (The experimental measured result is from 7.6eV to 9eV [11]). In reality, a few localised energy states exist within the wide band gap. Electrons can easily move between them, although they are rarely travel through the full gap. These localised states are caused by polyethylene's mixed structure of crystalline and amorphous regions, for example, the wave tails of electrons within the amorphous regions, which can extend themselves into the band gap and create the localised energy states. Other chemical defects like additives and impurities can also generate the localised energy states within the gap. A graph (Figure 1-11) shows the nature of the forbidden energy band of polyethylene.

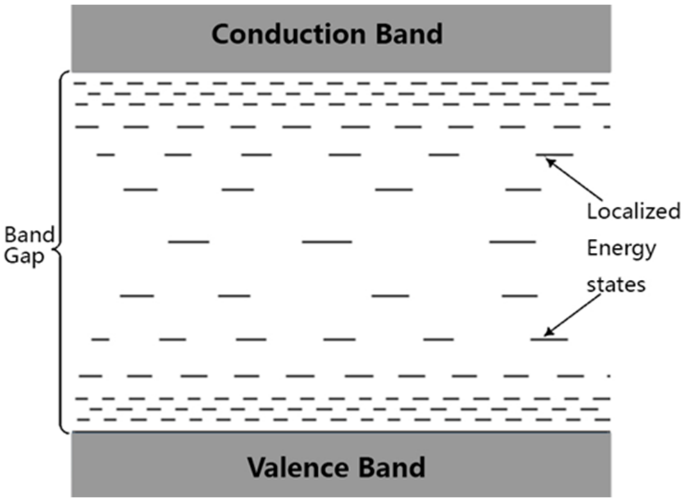

Figure 1-11 Schematic graph of energy band in polyethylene [31]

Hopping mechanism

The hopping mechanism assumes that a series of single-level trap sites with an energy of φ are localised in the band gap of polymers. Electrons, which are trapped in these sites, can jump between traps with a separation distance a, after thermal excited. The probability of electrons hopping over during a unit time can be described as [32].

$$\boldsymbol{P = v\mathbf{exp}(-\frac{\varphi}{k_B T})} \quad \mathbf{1\text{-}8}$$

where v is the attempt-to-escape frequency, and normally is around 10^{12} to $10^{14}\mathrm{s}^{-1}$; φ is the single level trap site's energy; k_B is the Boltzmann constant, $1.38\times 10^{-23}\mathrm{m}^2\mathrm{kgs}^{-2}\mathrm{K}^{-1}$, and T is the temperature. Based on 1-8 the mobility of electrons hopping over can be obtained:

$$\boldsymbol{\mu_H = \frac{qva^2}{k_B T}\mathbf{exp}(-\frac{\varphi}{k_B T})} \quad \mathbf{1\text{-}9}$$

When an electric field E is applied, the potential barrier will tilt in the direction of electric field, and the potential barrier height will be lowered. Consequently, the potential barrier will be modified into $(\varphi - \frac{1}{2}qaE)$.Then the current density contributed by the hopping over process can be described as:

$$\boldsymbol{J = 2qnvaexp(-\frac{\varphi}{k_B T})sinh(\frac{qEa}{2k_B T})} \quad \mathbf{1\text{-}10}$$

where q is the electronic charge, $1.60\times10^{-19}\mathrm{C}$; n is the concentration of charge carriers.

Poole-Frenkel effects

An internal Schottky injection-like effect can be assumed to happen in the bulk of insulator between the localised energy states. Just the Columb force in the Poole-Frenkel effect, which causes the reduced potential barrier, is due to a fixed positive charge, while the Schottky effect causes the image force to lower the barrier induced by the mobile charge. Therefore, the general theories for these two effects are similar, and the only difference is the lowering extent.

The lowering effect of the potential barrier for the Poole-Frenkel mechanism is twice as large as that of Schottky injection [33, 34]. The corresponding conductivity contributed by Poole-Frenkel effect is deduced as below:

$$\boldsymbol{\Delta\varphi_{sch} = \beta_{sch}\sqrt{E} = \sqrt{\frac{q^3 E}{4\pi\varepsilon}}} \quad \mathbf{1\text{-}11}$$

$$\boldsymbol{\Delta\varphi_{PF} = \beta_{PF}\sqrt{E} = 2\beta_{sch}\sqrt{E} = \sqrt{\frac{q^3 E}{\pi\varepsilon}}} \quad \mathbf{1\text{-}12}$$

$$\sigma = \sigma_0 \, exp\left(\frac{\beta_{PF}\sqrt{E}}{2k_BT}\right) = \sigma_0 \, exp\left(\frac{q}{2k_BT}\sqrt{\frac{qE}{\pi\varepsilon}}\right) \qquad \textbf{1-13}$$

where σ_0 is the low-filed conductivity of the insulator.

Space charge limited current (SCLC)

This theory proposes an analysis of current density caused by the accumulated space charge neglecting the effects of traps in the bulk of insulation. This approach is based on the following three assumptions [35]:

(a) Only one type of carrier (holes or electrons) is injected at the contact from a metal into an insulator;

(b) The mobility of free charge carriers is independent of electric field;

(c) The diffusion of charge carriers is not considered.

If only hole injection is considered, the contributed current density can be expressed as:

$$J = q\mu_h n_h(x)E(x) \qquad \textbf{1-14}$$

where q is the electronic charge; μ_h is the mobility of free holes; $n_h(x)$ is the concentration of holes within the material; $E(x)$ is the local electric field in the material and x is the coordination axis in the direction of the material thickness.

The corresponding electric field can be obtained using Gauss's Law below:

$$\frac{\partial E(x)}{\partial x} = \frac{qn_h(x)}{\varepsilon} \qquad \textbf{1-15}$$

ε is the permittivity of the materials.

After that, integrate equation 1-15 using the boundary conditions of:

$$E(0) = 0 \; and \int_0^d E(x)dx = V \qquad \textbf{1-16}$$

where d is the material thickness, and V is the applied voltage. The electric field E at the electrode is assumed to be zero due to the large amounts of charges injected adjacent to the electrode. The electric field caused by these injected charges neutralise the applied field at the boundary.

Therefore, the current density can be expressed as following (Square law):

$$J = \frac{9}{8}\varepsilon\mu_h\frac{V^2}{d^3} \qquad \textbf{1-17}$$

While under low electric stress (≤10kV/mm for LDPE) [30], the ohmic conduction is dominant in the current density composition and its induced current density can be expressed below:

$$\boldsymbol{J_{\Omega} = q n_0 \mu_h \frac{V}{d}} \qquad \textbf{1-18}$$

In this way, the whole picture of conduction current density through a theoretical insulator over the voltage range can be obtained, as shown in Figure 1-12.

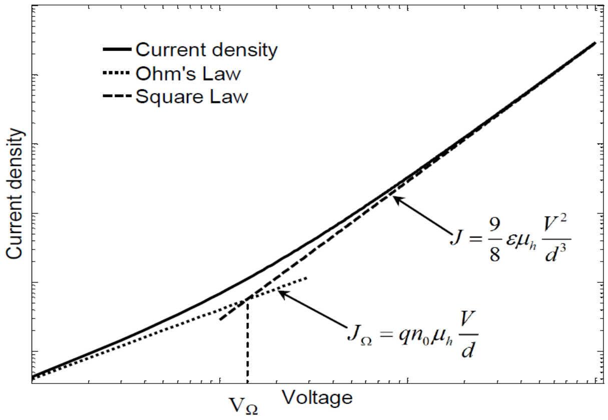

Figure 1-12 Log scaled current density for holes injection in a trap free insulator [30]

1.3 Space charge measurement methods

1.3.1 Charge detection techniques

Space charge detection techniques for insulating materials are classified into two kinds: destructive and non-destructive ones. The early approaches were destructive, e.g., dust figure method [36] and probe method [37]. The general principle of these techniques is cutting samples into pieces and then detecting the charge distribution characteristic on the surface of slices [38]. However, sample preparation procedures including the cutting can significantly affect the detected results [39]. A non-destructive method for measuring charge dynamics in solids was first proposed by Collins in the middle of 1970s [40], and it has been developed into multi-branch of techniques. The fundamental principle for non-destructive methods is externally applying series of waves (thermal or acoustic/pressure) to the sample and allowing them propagating through the whole sample to create a temporary and non-destructive displacement of space. This displacement will add amounts of time-dependent changes to total induced space charge, which can be detected from the electrodes. Non-destructive methods can be divided into three categories as presented below, according to the applied waves' type:

•Methods using thermal propagation: thermal pulsed methods (TPM) [41], laser intensity modulation method (LIMM) [42], thermal step method (TSM) [43].

•Methods using elastic wave propagation: laser induced pressure pulse method (LIPP) [44, 45], piezo-electrically induced pressure pulse (PIPP) [46, 47], non-structured acoustic pulse method (NSAPM) and pulsed electro-acoustic method (PEA) [48, 49].

•Methods under electric stresses: field probe methods used for surface charge and surface potential measurements [50-52].

A brief introduction of generally used non-destructive charge detection methods is presented below in Table 1-2.

Table 1-2 Summary and comparisons of space charge detection methods [52]

	Method	**Disturbance**	**Scan mechanism**	**Detection process**	**Resolution**	**Sample Thickness**	**Comments**
1	Thermal pulse method	Absorption of short–light pulse in front electrode	Diffusion according to heat conduction equations	Voltage change across sample	2 µm	25 µm	High resolution, Requires deconvolution
2	Laser intensity modulation method	Absorption of modulated light in front electrode	Frequency-dependent steady–state heat profile	Current between sample electrodes	2 µm	25 µm	Numerical deconvolution required
3	Laser induced pressure pulse method	Absorption of short laser light pulse in front electrode	Propagation with longitudinal sound velocity	Current between sample electrodes	1 µm	100-1000 µm	No deconvolution required
4	Thermoelectrically generated laser induced pressure pulse	Absorption of short laser light pulse in thin buried layer	Propagation with longitudinal sound velocity	Current/voltage between sample electrodes	1 µm	50-70 µm	Deconvolution required
5	Piezo-electrically Induced pressure Pulse	Absorption of piezo-electrically generated short pulse in metal target	Propagation with longitudinal sound velocity	Current/voltage between sample electrodes	10 µm	5-200 µm	Resolution improved with deconvolution. Uses for surface charge measurements.
6	Non–structured acoustic pulse method	HV spark between conductor and metal diaphragm	Propagation with longitudinal sound velocity	Voltage between sample electrodes	1000 µm	10000 µm	Used for solid and liquid dielectrics. Higher resolution with deconvolution.
7	Laser generated acoustic pulse method	Absorption of laser light in thin paper target	Propagation with longitudinal sound velocity	Voltage between sample electrodes	50 µm	3000 µm	Deconvolution is required. Target and sample immersed in dielectric liquid.
8	Acoustic probe method	Absorption of laser light pulse in front electrode	Propagation with longitudinal sound velocity	Voltage between sample electrodes	200 µm	2000-6000 µm	
9	Piezo-electrically generated pressure step method	Electrical excitation of piezoelectric plate	Propagation with longitudinal sound velocity	Current between sample electrodes	1 µm	25 µm	Deconvolution is required
10	Thermal step method	Applying two isothermal	Thermal expansion of the sample	Current between sample electrodes	150 µm	2000–20000 µm	Deconvolution is required

		sources across sample					
11	Electro–acoustic stress pulse method	Force or modulated electric field on charges in sample	Propagation with longitudinal sound velocity	Piezoelectric transducer at sample electrode	100 μm	10000 μm	Deconvolution is required. Also used for surface charge measurements.
12	Photoconductivity method	Absorption of narrow light beam in sample	External movement of light beam	Current between sample electrodes	1.5 μm	-	Non-destructive for short illumination time.
13	Space charge mapping	Interaction of polarized light with field	Parallel illumination of sample volume or movement of the light beam or sample	Photographic record	200 μm	-	Mostly used on transparent dielectric liquids.
14	Spectroscopy	Absorption of exciting radiation in sample	External movement of radiation source or sample	Relative change in the observed spectrum	50 μm	-	Few applications
15	Field probe	None	Capacitive coupling to the field	Current	200 μm	-	Non-destructive, surface charge tests

1.3.2 Pulsed electro-acoustic method (PEA) technique and schematic of equipment

In consideration of measuring range, resolution and construction costs, Pulsed electro-acoustic (PEA) technique is adopted in this work to detect charge dynamics in insulation. The primary principles and structures of the space charge measurements are presented below.

PEA is mainly using the Coulomb force induced by a pulsed electric field to cause the exchanges of momentum and consequently generating acoustic waves. The generated waves propagate in the specimen and at the end are detected by a piezoelectric sensor changing into electrical signals. The piezoelectric sensor is assembled at the ground electrode. The amplitude of the detected signal will be proportional to the charge amount, while the distribution of the accumulated charges can be deduced from the coordinate position of the detected signal. The acoustic waves will be converted into electrical signal by the piezoelectric sensor.

Figure 1-13 [38] shows a sketch of a PEA system for the general purpose used for the measurements under DC fields. In the system, a DC source applies the high voltage to the sample through a protecting resistor to prevent the fault current which may damage the voltage source. A coupling capacitor is connected between the pulse source and the electrodes to allow the high-frequency pulse signal going through while filtering the DC noise associated with the pulse signal. The sample will be firmly pressed between the top and ground electrodes. The thickness of the ground electrode is typically designed to create a suitable time delay, for filtering the disturbances from the pulse and avoiding the overlap between original waves and reflected ones [38]. Beneath the ground electrode, a polyvinylideneuoride (PVDF) is used as the piezoelectric transducer, converting the acoustic signals into electrical ones. The magnitude of the converted signal is positively proportional to the thickness of the PVDF. The converted electrical signal is then amplified by the connected amplifiers. The PEA system used for DC space charge measurements in this work has a typical spatial resolution of 10µm and a sensitivity of 0.1 Cm^{-3} [53].

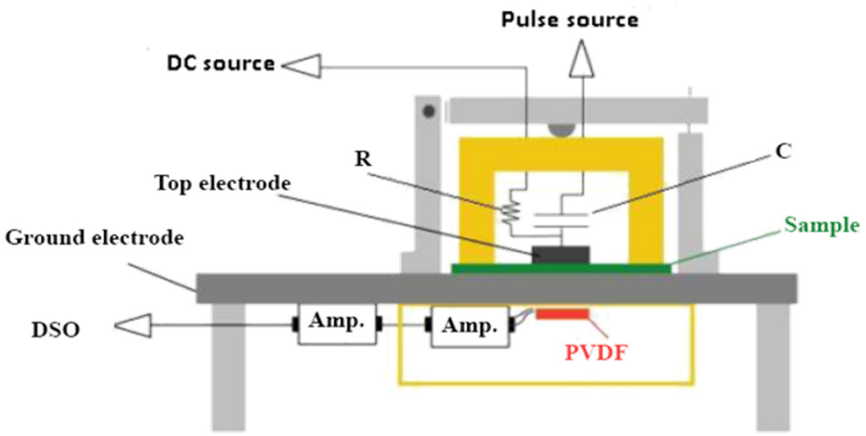

Figure 1-13 Structure of PEA system used in HVDC measurements [38]

All the space charge measurements in this work were conducted on the low-density polyethylene (LDPE) films. The experiments were implemented using the same batch of LDPE products to ensure the consistency of the quality of the tested materials. (Additive free for virgin samples, and aged samples are prepared using the same batch products as the virgin ones.) The LDPE films are stored in a dark and dry condition at the room temperature.

The DC experimental work (including DC polarity reversal tests) described in this thesis was obtained using a PEA measurement system associated with a user-defined data acquisition processing LabVIEW program. The testing DC voltage range of the system is 1 to 30 kV. The pulse voltage used in the measurement system has a voltage amplitude of 1 kV and a width of 5 ns. The frequency of the pulse voltage is 1 kHz. The amplified output electric signal is acquired and averaged by a digital oscilloscope with a sampling frequency of 2 GSs^{-1}. Besides, a thin layer of silicone oil is filled at the interfaces of the testing sample and electrodes for supplying a good contact to minimise the reflection and attenuation of acoustic waves during the acoustic signal propagation. Furthermore, an absorber is assembled to firmly contact with the sensor to delay and suppress the acoustic reflections.

Unlike DC measurements, the PEA system needs to be further improved for measuring space charge under complex fields, e.g., AC, superposed AC and DC fields. The space charge dynamics are frequently altered, following the alliteration of applied fields. Two essential components are enhanced: a higher frequency and high voltage pulse generator to shorten the averageing time required and ensure enough measuring points for situations under the field with high frequency, and a high-speed digital signal computing unit, for data acquisition, average, and storage. Generally, the oscilloscope cannot store or transmit a large amount of data continuously, and results under certain phases of applied fields are always randomly lost under high frequency cases. Therefore, to measure the space charge dynamics under the periodical complex electric field, a high voltage pulse with 2kHz frequency and a signal averager, Eclipse, is used in my experiment. Eclipse uses binary numbers to store and transmit data to computers, which is super quick and qualified to proceed measured data under relatively high frequency fields. A schematic diagram of the measuring system under periodical complex electric fields is shown in Figure 1-14.

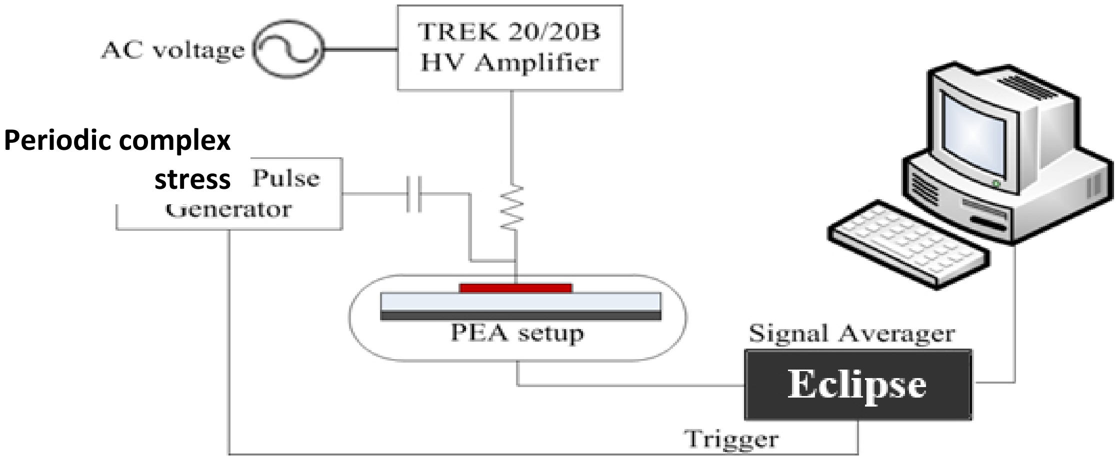

Figure 1-14 Schematic diagram of space charge measurement under periodic complex fields [53]

The space charge under periodic voltage signals within a frequency range of 0 to 100Hz can be successfully measured by using a 2kHz high voltage pulse [31]. The large memory computing component, Eclipse, can capture the details of the space charge dynamics. As Figure 1-14 shows, the field is applied across the polymer sample using a high voltage amplifier. The output of the high voltage amplifier is controlled by a function generator to apply designed periodical fields to the testing sample. The high voltage pulse voltage is applied to sample to excite the localised charges within the sample, generating acoustic signals, and simultaneously, to trigger the Eclipse for data acquisition. The raw data of the PEA system is acquired by Eclipse and stored in its memory, and then transferred to a PC for subsequent data processing and analysis. To distinguish the phase-resolved PEA signals and resultant space charge profiles, a purpose-designed data processing program is developed and applied in this project. Its detail is presented in Section 3-1

1.4 Motivation and objectives of research

During the last few decades, extensive efforts have been made to understand the correlation between space charge and electrical performances of insulating materials. A bipolar charge transport model has been proposed to analyse the space charge dynamics in polyethylene under DC voltage. Based on this model, the dynamics of charge transport, trapping/detrapping, and recombination under DC conditions have been studied. However, the applied electric field plays a vital role on the space charge behaviours, which has rarely been investigated, either experimentally or numerically, for example, under alternative or more complex high voltage. Therefore, the general objective of this research work is to obtain a better understanding of space charge dynamics characteristics in polyethylene under various complex electric fields. The current lack of research is mainly due to the following two reasons:

1) Space charge phenomenon is relatively hard to be detected under power frequency AC and superposed fields. This difficulty results from three main reasons. Firstly, to acquire sufficient information under AC and superposed fields, high frequency data acquisition, transmission, and storage are essential, especially for electric fields under power frequency, the three processes should be finished within 0.001 seconds considering 20 results per cycle. Besides, high resolution of the measurement system, as well as precise phase determination process are required to accurately present the charge profiles within insulation under AC and superposed fields. The procedures are virtual because significant amounts of charges may accumulate adjacent the electrodes due to the continuous reversal of applied field polarity and the applied field phase of AC and superposed fields can remarkable affect the charge dynamics inside the insulation. Furthermore, breakdown and surface flashover happen under relatively low strength under AC fields. Particular attention should be focused on the electrical pressure relief of the PEA system designed for AC and superposed AC and DC fields.
2) In primeval, researchers believed space charge phenomenon is insignificant under HVAC fields due to consistent polarity reversals. This idea based on the assumption that the characteristics of electrons' and holes' generation and transportation within the insulation are entirely the same, whereas different features of electrons and holes are widely observed under high voltage stresses. Moreover, severer electrical ageing and degradation of insulation are observed under HVAC comparing with under HVDC, and all electrical ageing and degradation within insulation are affected or related to the space charge phenomenon.

The features of applied fields (magnitude, composition, and frequency) can also in return affect the space charge phenomenon inside the insulation. Therefore, in the present research, another objective is to investigate the influence of the applied fields' features on the charge dynamics based on the measured and simulated results.

Moreover, the presence of space charge in solid dielectric materials can lead to electric field distortion and affect the electrical performance. Local electric field enhancement in the solid dielectric materials may significantly contribute to the early ageing and even electrical breakdown. The above effects have been highlighted in many research papers under HVDC conditions and space charge has been considered as the key to the understanding of many observed phenomena under high electric fields. Therefore, in this thesis, the effect of space charge on the electrical breakdown of polymeric material is also aimed to be investigated based on the proposed charge transport numerical model.

1.5 Contribution of the research

This thesis aims to aid the understanding of space charge characteristics in polymeric insulation through both theoretical modelling and experimental investigations. The dynamics of space charge in polyethylene under various categories of periodical electric fields are investigated using both PEA measurements and numerical simulations. The influences of applied field features on the space charge phenomenon within insulation are researched based on obtained experimental and numerical results. Space charge's role in the electrical breakdown has also been evaluated in this dissertation. In this research, the main contributions are summarised as follows:

1) An improved PEA system and data analysing procedure have been proposed in this thesis. This improvement enables the accurate recovery of the applied field phases under high frequency stresses. The system and process combined with the subtraction method can precisely demonstrate the localised charge profiles inside insulation under high frequency complex electric fields. Besides, Raman and Attenuated Total Reflectance Fourier Transform Infrared (ATR- FTIR) Spectra have been used to investigate the ageing effects on the structure of LDPE caused by the frequency and the magnitude of electric fields.

2) An evaluation of British converter transformers standard dielectric testing has been applied based on measured charge results. Two significant signs, charge amounts and local field distortion, indicating space charge effects inside insulation have been analysed and compared between results under practical operating fields and reduced standard testing fields. Advice on the improvement of the standard has been proposed.

3) The existing DC bipolar charge simulation model has been revised and modified in this work. The revised model is capable of analysing charge dynamics under more general applied fields (AC, superposed fields and even under ramping voltage up to breakdown). A procedure to enable the simulated results directly comparable to the measured data has also been proposed.

4) Adopting the proposed experimental and numerical method, the effects of applied field magnitude, frequency, as well as the composition of applied fields on the charge dynamics and

local field distribution have been studied in this research. The numerical model has also been used to investigate the underlying relationship between space charge phenomenon and electrical breakdown of insulation. Elaborated analysis and discussion have been made to interpret the empirical principles (Relationships between breakdown strength and testing sample thickness, Relationships between breakdown strength and testing voltage ramping rates) and experimental observations (Significant differences between the measured AC and DC breakdown strengths of same materials).

1.6 Outline of thesis

The thesis contains seven chapters in total.

Chapter 1 Introduction: This part gives an overview of the background of the project. The structure and characteristics of the experimental material, low-density polyethylene is included. Additionally, a brief introduction of space charge detection techniques is provided. Furthermore, the objective and outcomes of the project are presented.

Chapter 2 Space charge mechanism and measurement: This part reviews the literature using the bipolar charge transport theory to analyse the charge dynamic in insulation. The development of pulsed electro-acoustic (PEA) has also been illustrated. In addition, a discussion has been made on the relationship between space charge and electrical breakdown.

Chapter 3 Measurements of space charge under high voltage electric fields: This part presents and analyses the results of space charge measurements under various kinds of electric fields. Specific procedures for data collection, calibration, and analysis are illustrated. The characteristics of charge dynamics under different types of applied fields are discussed. The corresponding local field distortion and ageing effects on the tested samples have also been evaluated.

Chapter 4 Modelling of space charge under high voltage electric fields: This chapter illustrates a method to simulate charge dynamics in polyethylene under various categories of electric fields, based on bipolar charge transport theory. Simulated charge motion and physics behind are analysed and discussed. A procedure to proceed the simulated results capable of direct comparison with the experimental data has also been presented.

Chapter 5 Space charge dynamics under complex stresses: This chapter investigates the relationship of influences of three features (magnitudes, frequency, and percentage of the AC and DC voltage) of the applied electric fields on the charge dynamics within the polyethylene.

Chapter 6 Space charge and its role in the electrical breakdown of solid insulation: In chapter 6, the proposed numerical model is used to explain the impact of space charge during the electrical breakdown process. Features of applied fields, the thickness of samples', as well as testing voltage ramping rate's influence on the breakdown strengths are analysed and discussed using the numerical model.

Chapter 7 Conclusions and Future work: This section summarizes the findings from above chapters, discusses the limitations of my work and outlines the possible work for future.

Chapter 2: Space charge mechanism and measurement

The space charge formation within insulation is widely applied as a sign for evaluating the degradation of the dielectric material [2]. This application is considering the degradation phenomena are generally affected or related to electric charges within insulation or at interfaces. The low conductivity and trapping sites in the insulation will lead to the accumulation of space charge, which could result from either the charge injection from electrodes or the ionisation of impurities or particles within the insulation. The localised charges in bulk or at the interfaces of insulator/electrode can distort the electric field distribution, and enhance the local electric field. This distortion could in certain circumstances enlarge the local field strength several times larger than the applied field, which may eventually accelerate the damage of dielectrics. This damage can be early degradation, electric treeing or even complete insulation failures. Thus, numerous researchers, both numerically and experimentally, have been carried out on investigating the space charge accumulation, transportation, and recombination in polymeric materials [5][54].

In this Chapter the related literature of PEA charge detect techniques, bipolar charge transport theory, and relationship of space charge, and electrical breakdown are reviewed and discussed.

2.1 The evolution of pulsed electro-acoustic method

Pulsed Electro-acoustic (PEA) technique is a widely used method in both research and industry studying the profiles of space charge dynamics in insulation [64]. Since it was proposed in 1983 [48], PEA method has been continuously improved and modified fulfilling different specific requirements. A conception of the pulsed electroacoustic method produced by Takada is illustrated in Figure 2-1. In this work, the PEA technique is adopted to detect charge dynamics in polyethylene under various electric fields conditions.

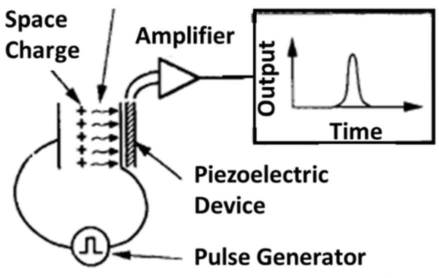

Figure 2-1 A conception of the pulsed electroacoustic method produced by Takada [48]

In 1987, Takada initiatively presented a result of space charge measurements using the PEA technique [65]. In the paper, Takada demonstrated in theory that this method could be used to determine the space charge profiles. Unfortunately, the obtained signals are not directly indicating the charge profiles within the sample, because the used ceramic piezoelectric transducer (PZT) had only a limited frequency band. When a narrow single acoustic pulse propagates through the ceramic transducer, part of the high frequency components of this pulse is lost. Therefore, the detected charge profiles were not triggered by a single pulse signal and contained some oscillations which have no relation with the charge dynamics inside the insulation.

To obtain accurate space charge profiles, a deconvolution technique was developed in 1988 [66]. The measurement results of the PZT was also improved after using this method to avoid the loss of high frequency component. With this data processing technique, the accurate charge profiles can be obtained.

A new polarized homo-polymer family of piezo and pyroelectric transducers based on highly polar polyvinylidene fluoride (PVDF) film has become a commercial reality in the 1990s [67]. The ceramic transducer initially leads zirconium titanate (PZT), or lithium niobate ($LiNbO_3$) was replaced by the PVDF transducer. PVDF's high levels of piezo activity, an vast frequency range, broad dynamic response, and low acoustic impedance, make it possible to overcome the disadvantage of the ceramic transducer in frequency characteristics and to simplify the deconvolution technique. It also assists the application of the PEA methods to very thin samples. The polymeric transducer is a flexible, compliant, and optically clear plastic film, which can be readily cut, shaped and adhered, to form transducers for the complex application. It was also used as adhering electrode in coaxial cable systems [67-69]. A comparison of the piezo-ceramic and piezo-polymer is presented and discussed in Table 2-1.

Along with the development of signal transducer, efforts on the improvement of the PEA measurement system have been made over the decades. Initially, Hozumi et al. in 1992 [68] adjusted the system enabling the measurements of charge profiles under high electric fields. Liu et al. in 1996 [70] introduced a three-electrode system to ensure the uniform electric field distribution that applies to the sample. Later in 1999, Vazquez et al. [49] proposed a signal processing technique to recover the actual charge distributions from dispersive samples, by taking consideration of acoustic attenuation and dispersion factors of the insulating material. In 2003, Fu and Chen et al. [5] made a further improvement on the application of a flat outer electrode in the PEA system to enable space charge measurements in extruded polymeric cables with different geometries. Subsequently, in 2006, a novel calibration technique for PEA measured data was developed by Chen et al. [72] to solve the problem of the induced charge on electrodes and to reduce the impacts of the pulse voltage on space charge.

Table 2-1 Comparison of piezo-ceramic and piezo-polymer transducers

	Piezo-ceramic transducers		**Piezo-polymer transducers**
Typical sensor material	Lead zirconate titanate	Lithium niobate	Polyvinylidene fluoride
Chemical formula	$Pb[Zr_xTi_{1-x}]O_3$ $(0 \le x \le 1)$.	$LiNbO_3$	$-(C_2H_2F_2)_n-$
Centre frequencies	≤10MHz		Precision acoustics even for frequency higher than 35MHz
Acoustic impedance	Integral complex electrical impedance to ensure acoustic impedance closer to 50 Ohms		Impedance could be matched over a limited frequency range, and simple inductive matching are effectively used
Testing sample range	Up to millimetre stages sample		Up to micrometre stages sample

Waveforms obtained from PEA measurements may be distorted due to the acoustic signal attenuation and dispersion, especially when using the loss or dispersive media of thicker samples. In most cases, the magnitude will be reduced by attenuation while the waveform will be broadened by dispersion. Effects of these two will lead to the more deteriorated second peak of the sensed signal. In 1994, Li [31] developed an approach to recover the distorted waveform, and this is applied to recover the measured waveform of the solid insulation samples.

Since then a relatively mature PEA space charge detecting system has been established. Numerous experimental works under DC voltage have been done using PEA system along with the development of the detecting system [73-77]. In 2000, Montanari et al. [78] proposed a method based on HVDC charge measurement to detect space charge under HVAC stresses using a time-resolved PEA system. The work proposed a method to improve the detection quality to capture the quantitative information from the PEA system of small and fast-depleted trapped charges under HVAC fields. However, this method requires a complicated mathematical analysis process, and it is not able to present the phase differences of charge profiles within the cycles of the applied fields. Subsequently, in 2004, Chong et al. [79] proposed a phase-resolved based PEA system. This method avoided the massive calculations in the data recovery of a time-resolved system and enabled detecting and averageing data according to the phase. Therefore, cycle differences of charge profiles can be distinguished and illustrated using this modified system. In 2008, Thomas et al. performed some measurement work of space charge under AC electric fields and proposed a new method of detecting charge dynamics under arbitrary periodic stress using PEA techniques [80, 81]. Their results have confirmed that the PEA technique is also suitable for measuring space charge under complex electric fields.

In 2014, Zhao et al. [82] presented some initial charge profiles measured by a similar PEA system under combined ac and dc fields. His results demonstrate that DC component within the applied fields can significantly affect the charge dynamics within the insulation. However, peak values (at the entry electrode) of the PEA signals were used in Zhao’s results as the basis for determining the applied field phase of the obtained profiles. This approach is inappropriate as significant amounts of charges can accumulate in the region close to the surface of the insulation even under power frequency periodical fields, which will make the charge peaks at the electrodes not proportional to the applied voltage.

In 2015, a subtraction process was proposed by Ning [84] which assists better illustration of space charge inside the insulation. The method can remove the effects of capacitive charges at PEA electrodes while not losing any localised charges inside the insulation. This process is more suitable for space charge analysis under AC and more complex applied fields than traditionally used volt off method (Short time voltage off measurements), as a remarkable percentage of accumulated charges under the fields is shallow trapped which can be significantly lost during the volt off measurements.

2.2 The development of bipolar charge transport theory

The first version of bipolar charge transport model in dielectrics was proposed by Alison and Hill in 1994. This model was introduced to simulate the behaviours of space charge in degassed XLPE. [7] They proposed injections and extractions of charge carriers from the both electrodes. A schematic representation of their bipolar charge generation, trapping, and recombination model is shown in Figure 2-2 [7].Their simulated results demonstrated charge could be localised due to the traps inside the insulation and supported the qualitative interpretation of space charge dynamics in XLPE. However, in this primary model, they neglected the existence of potential barriers, assuming that charges can freely immigrate in both injection and extraction processes. Other mechanisms, such as charge trapping and recombination, are only briefly proposed by simplifying the mobility of charge carriers is constant in solid. Therefore, their numerical results were not well matched with the experimental data.

In the same year, Fukuma et al. introduced Schottky injection mechanism into Alison's model to further describe the potential barriers of injection and extraction at the electrodes. Hopping conduction mechanism was also applied to analyse the charge transport process with a field dependent velocity. [59] These efforts enormously refined the bipolar model, and the obtained results can fit the measured ones better.

In 1999 Kaneko et al. proposed a similar revised model but considering the extraction of charge at the boundaries without a barrier. [60] This revised model can generate packet-like charge distribution curves, which are more suitable for analysis of charge dynamics under relatively high HVDC electric fields (> 50kV/mm).

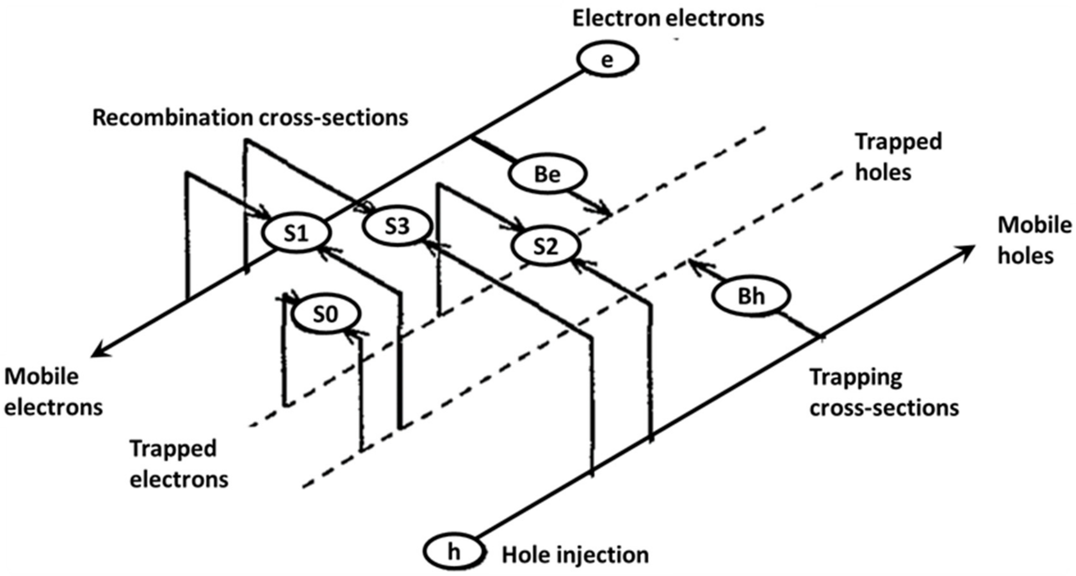

Figure 2-2 Schematic representation of bipolar charge trapping dynamics within insulation [7]

All these above bipolar models can simulate reasonable charge profiles in dielectrics, and they together present an evolution of the bipolar charge transport theory. Their works characterised the charge dynamics within in dielectrics and established the basic framework of the bipolar charge transport theory. Numerous researchers have further improved the charge transport model to extend the model on the space charge behaviour under various conditions and explore the understanding of the charge dynamics in insulation. [6, 8, 9, 61] However, the majority of these works were limited to the study of charge dynamics under HVDC with the extension of the charge transport mechanisms from the semiconductors to the insulators. Limited research was focused on the application of the bipolar theory on charge dynamics under complex electric stresses such as AC and superposed AC and DC fields or the illustration of the relationships between space charge characteristics and dielectric properties, such as conductivity or breakdown strengths.

In 2010, Zhao et al. [62] demonstrated that the bipolar model is reasonable for analysing the space within polyethylene under HVAC. His results also showed the bipolar charge transport theory's potential on studying space charge under complex conditions, e.g., dynamics under superimposed electric fields or under temperature gradient environments. A bipolar charge transport model similar to the simulations under HVDC has been used, and a power's law was involved computing the mobility of charge carriers. The obtained results presented reasonable matching in net charge amounts and current density along with the measured results. Nevertheless, no specific charge distribution comparison was presented in the work, and Zhao has stated the model required further improvements to give proper fittings of charge positions and amounts, comparing with the experimental results. In 2012, Chen et al. [63] offered an approach to use measured charge velocity versus the electric field curve to analyse the charge transportation process, giving a more factual analysis for the proposed numerical model. The principal features of these bipolar charge models are reported in Table 2-2.

Table 2-2 Features of the principal bipolar transport models

Reference	**Alison and hill [7]**	**Fukuma et al. [59]**	**Kaneko et al. [60]**	**Zhao et al [62]**
Issuing conditions	DC fields, XLPE			AC fields, LDPE
Generation	Constant source	Schottky injection		
Extraction	Non-blocking electrodes	Extraction barriers	Extraction according to mobility, and non-blocking electrodes issued	Extraction according to mobility, and non-blocking electrodes issued
Transport	Constant effective mobility	Hopping conduction		Power's law controlled mobility
Trapping	One deep trapping level, no detrapping			
Recombination	For mobile and trapped charges carriers	Only for mobile charges carriers		For mobile and trapped charges carriers
Other		Joule effects accounted for initial bulk charges		

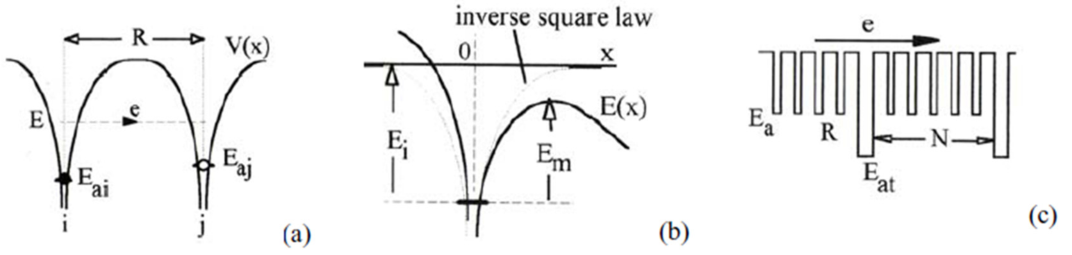

(a) Resonant tunnelling between two states. An electron in site *i* is thermally excited to an energy *E* at which it proceeds by resonance tunnelling through the intermolecular energy barrier *V(x)* to a state *j*. In this example, *i* and *j* are acceptor states.

(b) Poole-Frenkel mechanism. The potential energy E_i of the site is assumed to be of Columbic form. In the presence of a field, the energy of the site is modified (Lowering of the barrier in the drift direction).

(c) Trap controlled mobility. The migration of an electron occurs through trapping in successive states. Mobility is deduced from the average time charges stay in traps.

Figure 2-3 Three basic principles for charge transportation [83].

Coulomb shape of barriers exist in cases (a), and (b) (sites in interactions) and the square shape is generally used in case (c). The diagrams (a) and (c) are represented in zero field conditions.

The main theoretical difference between models designed for AC and DC simulation is the procedure of deducing charge transport mobility. For DC conditions due to the limited change of electrical fields within insulation, trap controlled mobility, mobility deduced from the average time charges stay in traps, can be used to analyse charge transport for the sake of calculation simplification. However when concerning charge transport under AC applied fields, the mobility field dependent effect become quite significant, and therefore more complex mobility deducing procedures are generally involved in illustrating the charge transport process better. Figure 2-3 illustrates some basic principles of charge transport theories.

2.3 The role of space charge in electrical breakdown of solid insulation

Electrical breakdown tests are often performed to assess the electric performance of insulation systems. Several mechanisms, including electronic, avalanche, electromechanical, thermal theory, and partial discharges have been proposed to explain the processes [85]. In mechanical breakdown theory, it is believed that the internal electric fields induce the mechanical force, which breaks the whole material when it is sufficiently high [85]. For thermal breakdown theory, the increased temperature, which is caused by adding electrical conductivity, results in a thermal runaway of the material [85]. Besides, in the electrical breakdown theory, it is assumed that breakdown process happens when the internal field reaches a critical value, “intrinsic” dielectric breakdown strength. [85] Figure 2-4 illustrates the variation of breakdown strength of solids with the time of applied field stressing. From the graph, it is clear that the intrinsic breakdown is accomplished in the time order of 10^{-8} s and therefore, has been postulated to be electronic and regarded as a property of the material and temperature only. For low-density polyethylene (LDPE), the “intrinsic” dielectric breakdown is estimated to be 500kV/mm [86].

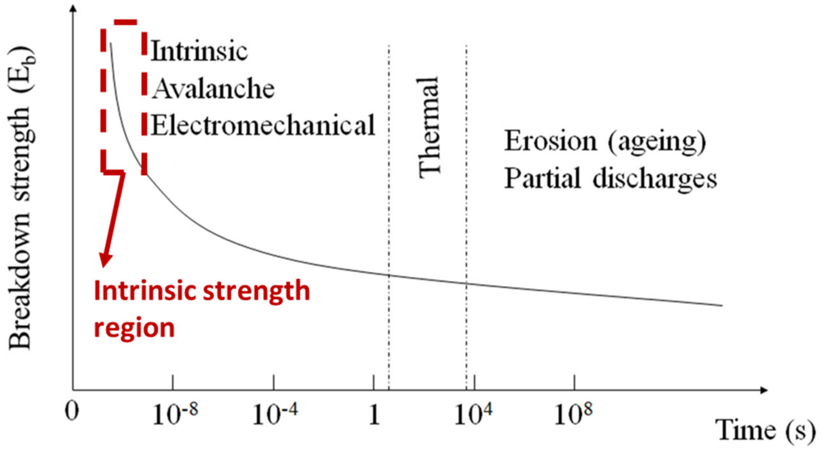

Figure 2-4 Variation of breakdown strength in solids with time of stressing [11]

According to the three types of breakdown theories mentioned above, only the electrical breakdown mechanism has considered the breakdown position within the testing sample. In the mechanical breakdown theory, the internal field is usually regarded as the applied field, regardless of the distorted local fields induced by the trapped charges. Therefore, the breakdown process can randomly happen anywhere within the testing sample in the mechanical theory. Similarly, in the thermal breakdown theory, it assumes that dielectrics are under homogeneous electric fields, as only the average electrical conductivity and the electric field strength are considered. This assumption is not appropriate, which has been demonstrated in Matsui's work as shown in Figure 2-5, [86]. The localised electric fields just before breakdown can be twice larger than the applied fields in the case of LDPE. Based on the mechanical and thermal breakdown theories, the probability of breakdown occurs at this electric field enhanced region is much higher than the other areas. This distorted field region will also accelerate the charge dynamics within the insulation, which could shorten the time to reach breakdown.

The relationship between the space charge accumulation and breakdown phenomenon in dielectric materials is still poorly understood, although many efforts have been made on investigating various materials under different conditions [87-89]. The significant impacts of space charge on breakdown phenomenon have been widely realised after Bradwell's report in 1971 [87]. However, few direct evidence has been obtained during the following three decades due to the complex nature of breakdown process and the difficulty of establishing measurement equipment. In 2003, Matsui et al. developed a PEA system capable of detecting charge dynamics under a very high electric field until electrical breakdown occurs [90]. Using that measurement system, Matsui later in 2005 published a space charge observation in LDPE at prebreakdown [86]. His results demonstrated the experimental evidence of the impacts of space charge phenomenon on the electrical breakdown. The results also confirmed the electrical breakdown theory and obtained an estimated intrinsic breakdown strength of LDPE. Using that estimated breakdown strength, Chen et al. in 2012 applied a bipolar charge transport model to simulate LDPE's electrical breakdown strength under DC conditions [63]. Their results indicated the breakdown strength of LDPE is strongly related to the thickness of the testing sample and the ramping rate of the testing voltage. An inversed power's law, which was used for describing the breakdown strength versus testing sample thickness, was obtained and well agreed with the trend introduced in [87], although they are using different analysing theories. Their results also demonstrated and emphasised the influence of the external voltage ramping rate on the DC breakdown strength. In more details, their charge distribution results obtained by the model presented the trends of holes dominating the overall charge transportation process, and the amount of trapped positive charges was apparently larger than negative charges. Under this circumstance, severe electric field distortion occurs when plenty of positive charges and negative charges encounter, as shown in Figure 2-6 (Maximum field distortion happens where positive and negative charges meet.). These trends are consistent with experimental results under HVDC conditions, which, however, are not matching with experimental results under HVAC fields. Much fewer charges are trapped within LDPE under HVAC than those under HVDC. Moreover, there is no evidence showing that the positive charges l dominate the overall charge dynamics under HVAC.

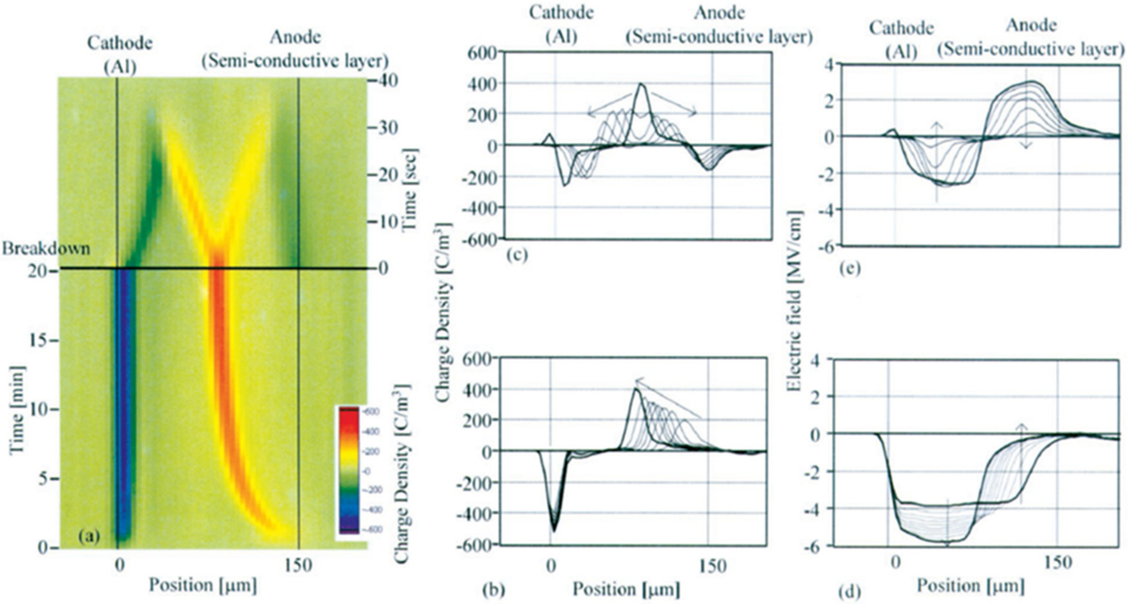

Figure 2-5 Matsui's measured space charge profiles before and right after breakdown. Space charge and electric field profiles in 150 μm LDPE under 50 kV. (a) Time dependence space charge profiles; Space charge distributions before breakdown (b) and after breakdown (c); Electric field distributions before breakdown(d) and after breakdown (e).

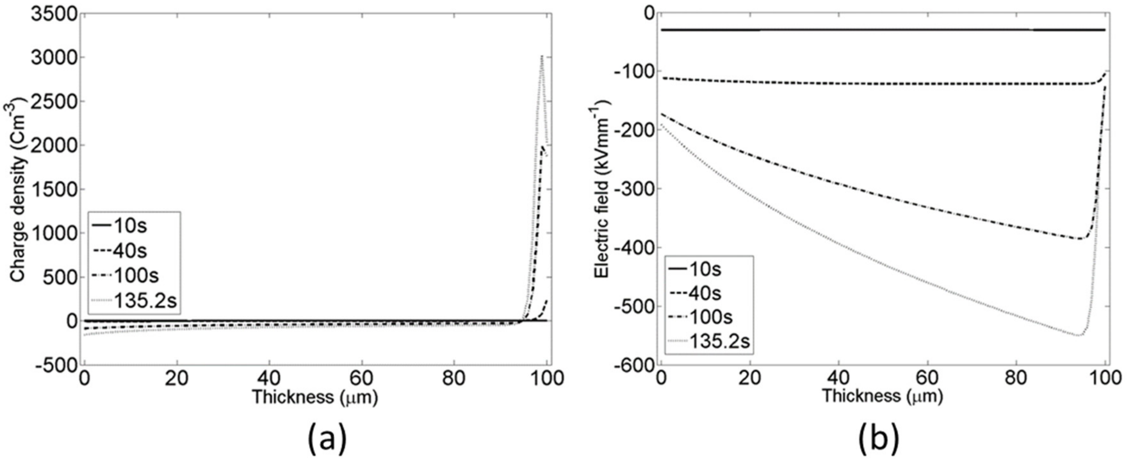

Figure 2-6 Simulated space charge dynamics (a), and electric field distribution (b) under ramping voltage till breakdown by Chen et al [63]

2.4 Summary

Based on above review, it is clear that concerted efforts have been made worldwide to investigate space charge within dielectrics both experimentally and numerically. Before this research, relatively sophisticated PEA techniques capable to accurately detect charge profiles under HVDC fields are available. Based on that numerical model which offers a reasonable physical explanation of charge dynamics and are capable of qualitative prediction under HVDC fields are proposed. However little method has been introduced in literature either to measure or to simulate charge profiles under AC and more complex high voltage fields. For space charge under AC fields, significant amounts of researchers regarded its effects on the electrical performances of dielectrics were limited based on their initial hypothesis and rough detected results. As for superposed AC and DC fields, the majority of researchers agree space charge should have significant influences on the dielectric performance. However, no specific methods have been proposed to evaluate or predict the effects. When it comes to dielectric breakdown, the situation becomes even worse. No comprehensive and convincing theory has been proposed to explain the process, and the relationship between space charge and dielectric breakdown is ambiguous.

This research aims to improve the current experimental approaches to enable more precise detection and analysis of charge profiles under AC and superposed AC and DC fields. Based on that, more reasonable and accurate evaluation of space charge’s effects within dielectrics under AC and superposed AC and DC fields can be obtained. Further improvement of current testing standards can also be made based on the analysis and evaluation. Besides, the numerical model in literature are also aimed to be revised. The new model is capable of analysing charge dynamics under general operating and testing electric fields (AC, superposed AC and DC fields and ramping breakdown testing fields). The underlying physics behind the observation in measurements are explained and discussed based on the improved model. Space charge's contribution to dielectrics' electrical performances are also aim to be better assessed.

Chapter 3: Measurements of space charge under periodic high voltage electric fields

Space charge dynamics under HVDC HVAC and superposed AC and DC fields are experimentally investigated and discussed using the PEA system in this chapter. The details of the improved measurement system and the revised data processing technique are exhaustively interpreted in this Chapter. Moreover, to further investigate the influences of AC field's magnitudes and frequency on the physical and chemical characteristics of polyethylene, results of Raman spectra and Attenuated Total Reflectance Fourier Transform Infrared spectra (ATR-FTIR) have been presented and discussed in 3.3.1. The different impacts caused by the pure AC, pure DC and superimposed AC and DC stress on space charge dynamics are investigated based on measured results in 3.3.2.

3.1 Experimental setup and data processing

When a pulsed field is applied across a specimen with internal charges, these charges will be excited by the high voltage pulse stress, generating acoustic waves. Those acoustic signals will propagate through the sample and be detected and converted into electrical signals by the piezoelectric transducer, which is attached to the ground electrode. In this way, the obtained electrical signals contain the spatial position and magnitude information of charges. These charges include both the accumulated and induced charges, and the accumulated ones are the charges that are mainly concerned in this work. A sketch of the above process is illustrated in Figure 3-1. It is assumed that acoustic propagation is primarily focused on the vertical dimension of the sample with a constant acoustic velocity in a uniform material is kept the same. The effects of attenuation and dispersion of the acoustic wave are generally ignored in thin polyethylene films. The linear superposition principle is applicable when two or more acoustic waves interact. Based on all above, the obtained electric signal can be represented as [31]

$$\boldsymbol{V_s(t) = K\left[\sigma_1 + \sigma_2 + v_{sa}\Delta T \rho_{(x=v_{sa}t)}\right]e_p} \qquad \textbf{3-1}$$

where *K* is the constant associated with the electro-mechanical coupling property of the transducer, σ_1 and σ_2 are the surface charges at electrodes, v_{sa} is the sound velocity through the material, ΔT is the width of the pulse, ρ is the bulk charge and e_p is the magnitude of the pulse. For a planar sample with no bulk charge inside, the third term in equation 3-1 is zero.

Therefore, the output signal at the electrodes can be written as

$$V_s = K\sigma_s e_p \tag{3-2}$$

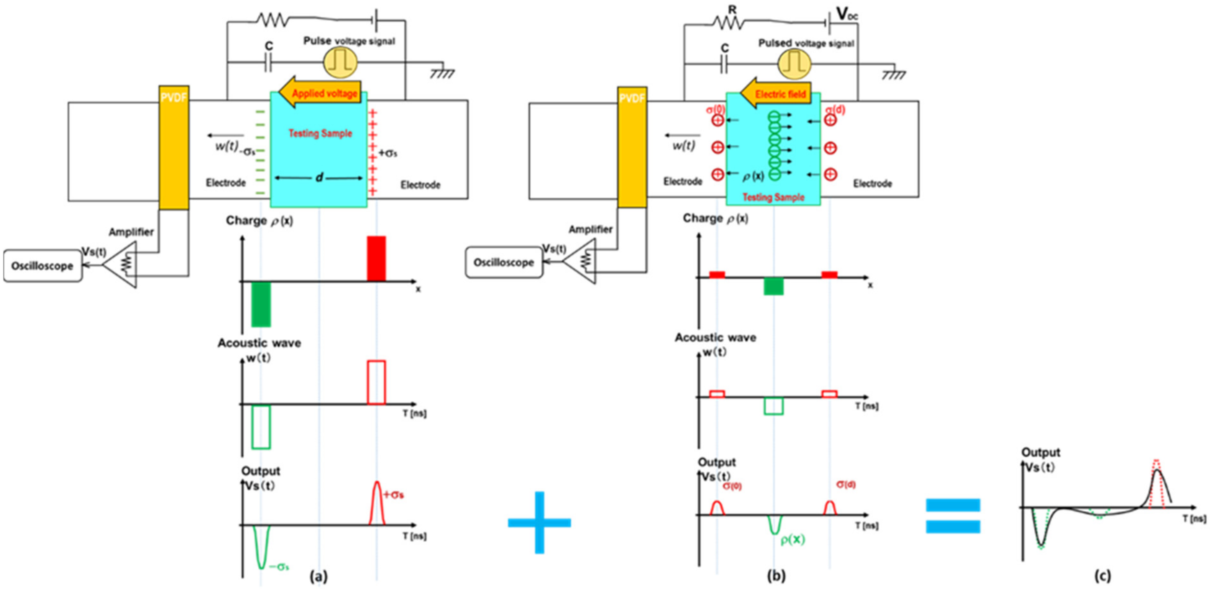

Figure 3-1 The principle of pulsed electro-acoustic (PEA) system [53]

(a): The signal only caused by the external electric field; (b): The dynamics only caused by the internal charges, and the induced charges on the electrodes. (c): The final PEA output signal containing both the influences of applied fields and internal charges.

3.1.1 Calibration and deconvolution process

The PEA output signal contains the information of spatial position and quantity of trap charges within the insulation. A deconvolution process can be used to remove the overall system response of the PEA system, and to obtain the original charge profiles. This is because that in most cases, the PEA system can be regarded as a linear time-invariant (LTI) system [65]. Besides, an amplifier with the broadband width is typically attached to the PEA system. The amplifier is another LTI system.

If the unit pulse response *h(t)* of an LTI system is known, the respond of the system can be obtained based on the input signal, *x(t)*. The standard system yields an output *y(t),* which is the convolution of the input *x(t)* with the impulse response *h(t)*. Therefore, to obtain *x(t)* by a known output *y(t)* and *h(t)*, a deconvolution process can be applied. The deconvolution process is illustrated in Figure 3-2. In summary, assuming the transfer function of the system is *G(j)*, encompassing the influence of transducer *H(j)*, the amplifier *A(j)*, and the resisters and capacitors circuit *W(j)*. Therefore, if *G(j)* can be found, the actual space charge distribution can be efficiently computed using Fast Fourier transform (FFT), division, software filtering and inverse Fast Fourier transform (IFFT).

Figure 3-2 (c) demonstrates a typical oscilloscope output of signals from a solid insulation which contains almost no internal charge. (For virgin LDPE it is generally believed all charges are from electrodes injection [53]. When the applied field’s strength is below the injection threshold, it is generally regarded, as no charge will be injected from the electrodes [29, 92]). The obtained curves commonly contain overshoot peaks immediately after the electrode peaks (Figure 3-2(a)), due to the limitation of the frequency response of a piezoelectric transducer and the amplifier. However, the peak is not representing the real charge density and needs to be removed from the raw signal. The calibration process is presenting in Figure 3-2 (d).

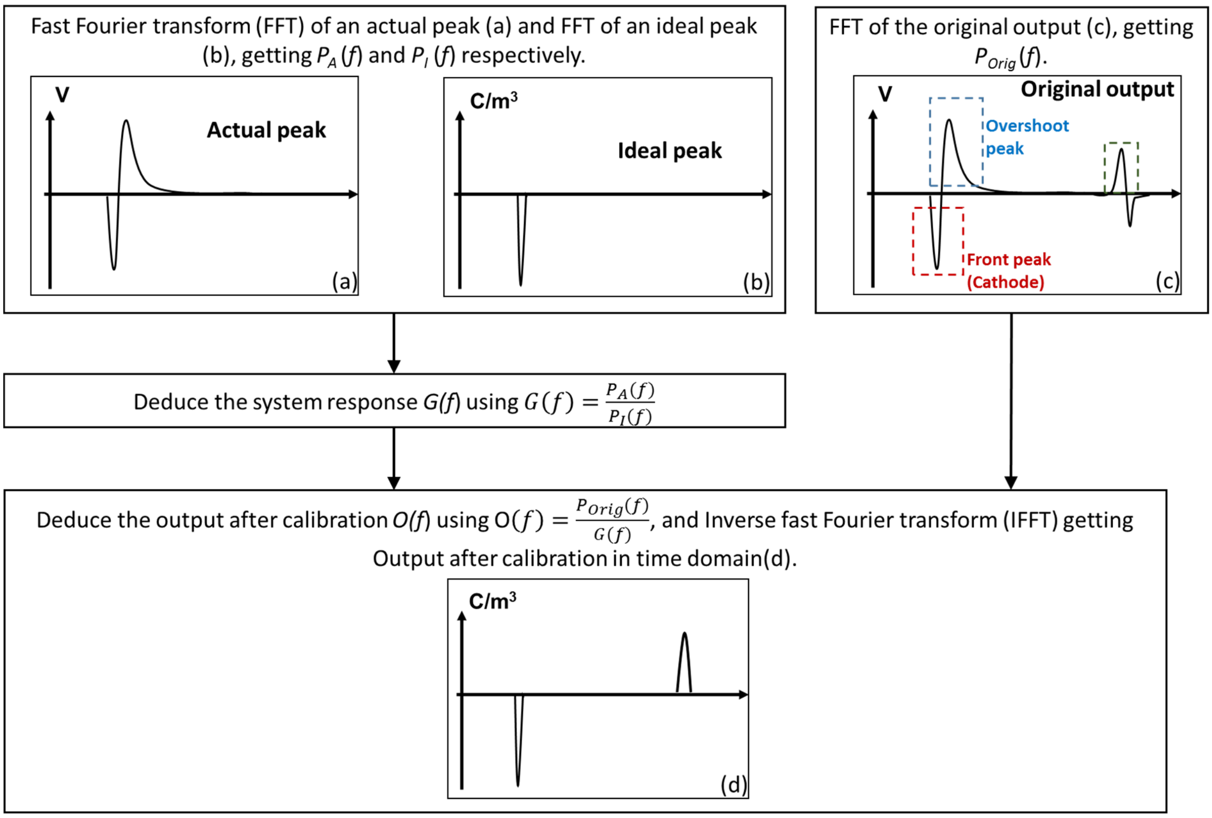

Figure 3-2 Calculation flow of calibration process [38]

(a): The measured peak at the top electrode; (b): The ideal peak at top electrode; (c): The original output of oscilloscope; (d) The results after calibration

3.1.2 Analysis techniques to remove capacitive charges

Although the system response and noises are removed by the calibration process, it still contains the capacitive charges caused by the applied fields on the electrodes. The amount of capacitive charges usually are much larger than that of the accumulated charge, which could cause difficulties on the observation of the accumulated charges. Moreover, the numerical model only simulates the dynamics of the accumulated charges. Therefore, to achieve the comparability of the measured data and the simulated data, two methods can be further utilised: removing the effects of the non-ideal pulse and the capacitive charges within the measured data, or adding in these effects to the simulated data. As for the elimination of the effects of capacitive charges, two methods: Volt off measurements and Subtraction methods are commonly adopted.

Volts off measurements are defined based on the volts on measurements, and the specific descriptions of these two methods are presented as following:

Volts-on measurements:

Space charge within the sample is measured during the application of external voltage. Results contain charge dynamics of insulation in bulk and at the electrodes. The charges at electrodes comprise both the induced charges and the capacitive charges. This is a most commonly applied space charge measurements.

Volts-off measurements:

Space charge is measured while the DC voltage is absent and while the test object is short-circuited. The space charge present in the bulk of the insulation is detected. Besides, charges, which are induced by the space charge, are also detected at both electrodes. This method loses certain amounts of charges, and the amounts are relatively negligible compared with the overall accumulated amounts under HVDC as significant amounts of charges are generally deep trapped under relatively HVDC fields. [3,5,29,38,53] However, for HVAC or other complex field conditions while large amounts of shallow trapped charges accumulated adjacent to the electrodes, Volts-off measurements are inaccurate and subtraction method is introduced as a replacement for this work. Details of performing time of Volts-on & Volts-off measurements is illustrated in Figure 3-3.

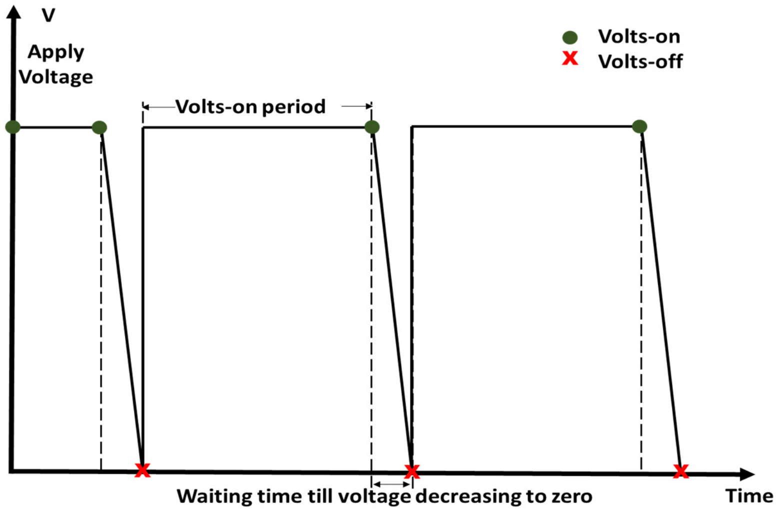

Figure 3-3 Schematic diagram illustrates volts-on and volts-off measurement time

Subtraction process is a method proposed by Ning et al. [84] to directly illustrate dynamics of accumulated charges' movements without losing any of them. The subtraction method is using the measured space charge data under applied high electric fields (higher than charge injection thresholds) subtract the amplified reference data under low electric fields (lower than the thresholds). The amplified reference data can be regarded as the charge density data at applied voltage without the accumulation of space charges in bulk. (It is assumed that there is no charge injection under field lower than the injection threshold.) The amplified ratio is equal to the magnitude proportion of applied fields verse the reference fields by reasonably assuming that the induced charges on electrodes are linear to the applied voltage. An example of the subtraction process is presented in Figure 3-4.

For the case, the space charge measurements were taken from a 180µm LDPE sample under 3.6kV, and the reference was data recorded under 1kV. The subtraction process is carried out as follows: Figure 3-4 (a) is the measured results under 3.6kV after calibration at fields stressing time 60min, Figure 3-4(b) is the corresponding reference, and Figure 3-4(d) is the final result.

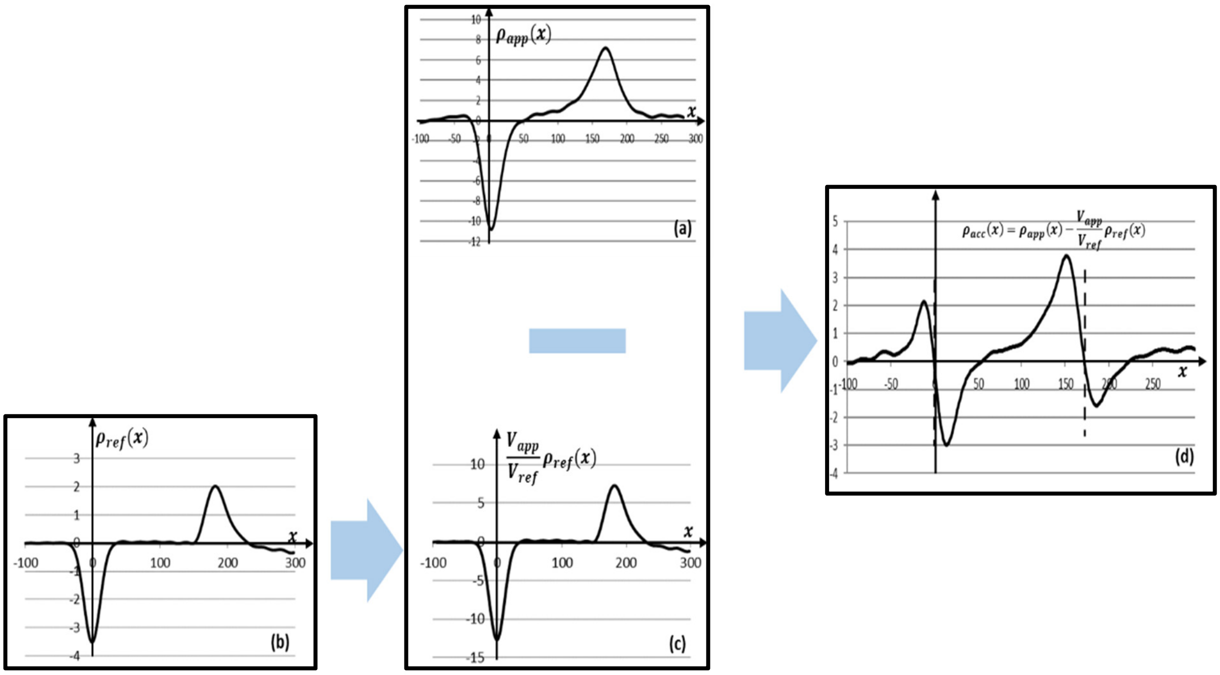

Figure 3-4 An example of subtraction process:

(a) Charge density at applied fields, $\rho_{app}(x)$; (b) Charge density at reference voltage, $\rho_{ref}(x)$; (c) enlarged reference data where V_{ref} and Vapp denote reference and applied voltages; (d) Charge density after subtraction, $\rho_{acc}(x)$.

The obtained results after subtraction are aiming to illustrate only the trapped charges within the insulation, eliminating the other, such as the pulse responses and the capacitive charges on the electrodes. It is clear from Figure 3.4 (d) that significant amounts of positive and negative charges can be observed in the vicinities of the cathode and anode respectively. The corresponding induced charges at the electrodes can also be observed.

Subtraction is a perceived way to demonstrate the trend of space charge dynamics within the insulation. The accuracy of the results is sufficient for qualitative analysis. However, unexpected errors may occur as the amplified noise in the reference data (the noise has also been amplified by the ratio). Therefore, a further improved method, which can minimise the adjustments of the measured data, will be described in Section 4.3.

3.1.3 Phase determination for periodical electric fields

The PEA system for periodical electric fields measurements comprises a 2 kHz, 5ns fast HV pulse which is used to excite charges to generate acoustic waves and to trigger the signal average device (Eclipse) simultaneously. The PEA signals were detected by a 9 µm thick piezoelectric transducer to achieve a spatial resolution of 10µm. In experiments, 20 PEA signals were detected within each applied voltage cycle. For example for the power frequency, 50Hz, the cycle time is 20ms, and the time for acquisition and processing is less than 1ms. Eclipse is used accounting for its superfast data acquisition and data storage rate (stable performances within 0.5ms). An example of PEA system sampling process for data under 50Hz AC stresses is presented in Figure 3-5.

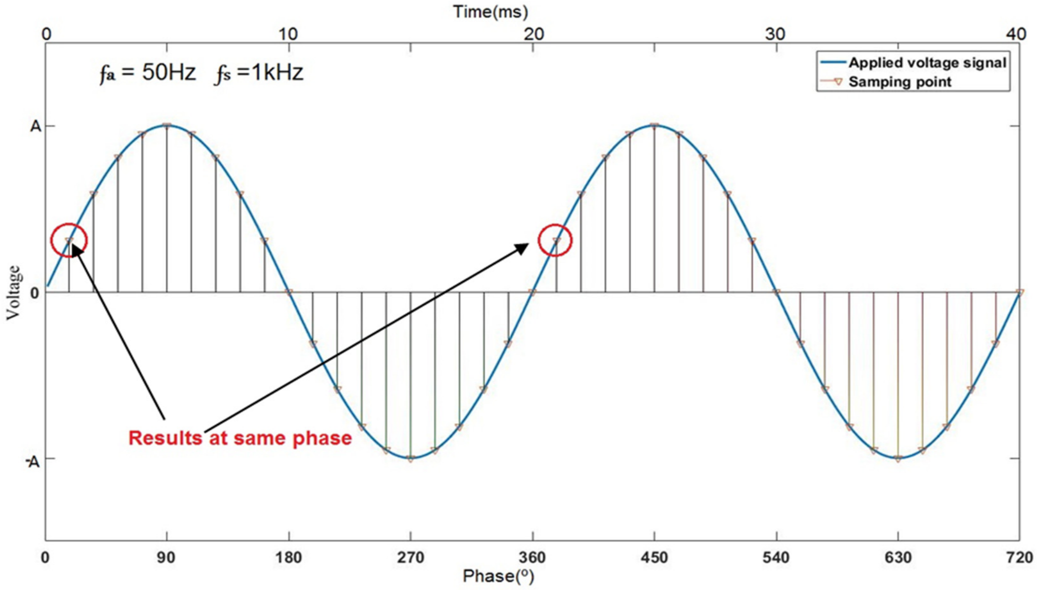

Figure 3-5 PEA system sampling process for 50Hz AC stresses

The phase angles of the obtained signals are randomly distributed with an interval of 18° within the applied voltage's cycle, as the start of data acquisition was not synchronised with a specific phase of AC voltage supply. The benefit is that the space charge dynamics in any phase angle has the probability to be measured, although an additional phase angle determination technique is required. The phase angles of specific charge profiles are determined according to a comparison of their deducing voltage (obtained by integrated electric fields distribution) and applied voltage, rather than peak values at the entry electrode of PEA signals using in Zhao's work 2014 [82]. This is in consideration of significant amounts of charges present in the region close to the surface of the insulation under power frequency HVAC fields [93], which makes the charge peaks at the electrodes not proportional to the applied voltage strengths. The specific processes of determining phase angle are stated following: Firstly, a charge profile under relatively low (<threshold) HVDC fields of the testing sample was initially measured (before applying AC voltage) as the reference to calibrate charge profiles measured under AC voltage. A calibration process as presented in section 3.1.1 is applied to transform the PEA signals from voltage values into charge density values and to obtain the distributions of electric fields in the bulk of testing sample films. The electric field results of the 20 signals (tested within an applied voltage cycle) are individually integrated to get 20 estimated real-time applied voltages. These 20 results are combined into an array, *Y*, which is then curve-fitted with a sinusoid function as shown in equation 3-3 to obtain the initial phase shift, φ, of the start of data acquisition. The precise applied voltage at each sampling point can be obtained using the curve fitted equation 3-3. An example of the phase angles determining procedure is illustrated in Figure 3-6.

$$\boldsymbol{Y = V \cdot \mathbf{Sin}(\omega t + \varphi)} \tag{3-3}$$

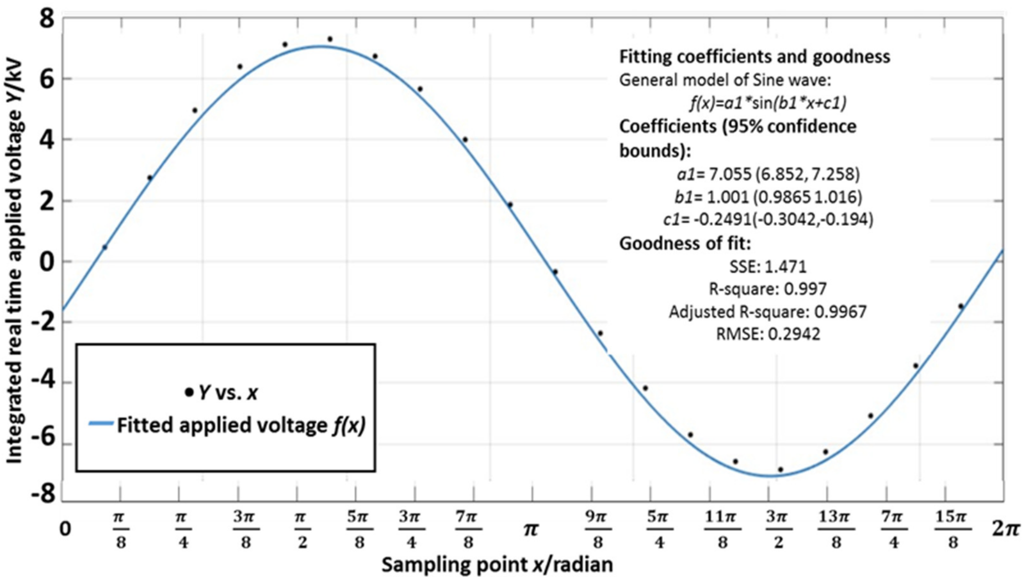

Figure 3-6 An example of phase angles determination process

Y is the estimated real-time applied voltages in kV. *x*b1* is equal to *ω*t*, where *x* is an array of radian[π/10: π/10: 2*π]. Consequently, *a1* is equal to *V* (The apply voltage magnitude), while *c1* is equal to φ. For this specific case, the testing applied voltage is 5kV (rms) 50Hz HVAC and 20 results are even sampled with an interval of 18°. Therefore, the ideal values for *a1* and *b1* should be 7.071 and 1, which are close to the fitted results (<0.5% differences). The final deduced phase angles for this group of 20 signals are [3.75° 21.76° 39.78° 57.80° 75.82° 93.84° 111.85° 129.87° 147.89° 165.91° 183.93° 201.94° 219.96° 237.98° 256.00° 274.02° 292.03° 310.05° 328.07° 346.09°]. The curved fitted signal function for real-time applied voltage is 7.055sin(1.001*18°*t- 0.2491/ π *180°).

3.2 Space charge phenomenon under DC voltage

Under HVDC fields, charge dynamics within polyethylene generally demonstrate three stages depends on the magnitude of applied fields. At the first stage when the applied field strength is lower than the injection threshold of materials, charges accumulate at the electrode and insulation interface, while almost none of them are capable of transferring through the materials. Plenty of researchers has focused on the injection threshold of insulations, and the threshold level of LDPE is generally believed to be 10kV/mm [29, 92]. When the applied field is more intensive than the threshold level, noticeable charges can be injected into the insulation, which can further transport or trapped, generating localised charges within the material. The second stage indicates the applied field strength is higher than the threshold level while not intensive enough to cause charge packet phenomenon. The third defines the field strength, which will generally cause the charge packet phenomenon. Charge packet phenomenon indicates the charge accumulated like a packet, and the shape is maintained as they travel across the insulation due to the high density of localised charge amounts. Charge packet stated here is slow charge packets, which have a low mobility in the order of 10^{-16} to 10^{-14} $m^2V^{-1}s^{-1}$, and strongly related to homocharge injection. For LDPE the charge packet phenomenon generally happens when the applied strength is higher than 50kV/mm, and generally, only positive charge packet can be observed [86, 94, 95]. As little localised charge exists under stage one, charge dynamics under stage two and three are generally used to investigate the space charge phenomenon under HVDC. Figures 3-7 to 3-12 present the space charge dynamics evolving with the increase in applied field. Figures 3-13 and 3-14 record the integrated charge amounts (Obtained using equation 3-4) and field distortions (Obtained using equation 3-5) respectively to further analyse the trend. Based on the results, the characteristics of bipolar injection and transport under various extents HVDC are clearly demonstrated and compared.

3.2.1 Charge and field distribution under DC voltage

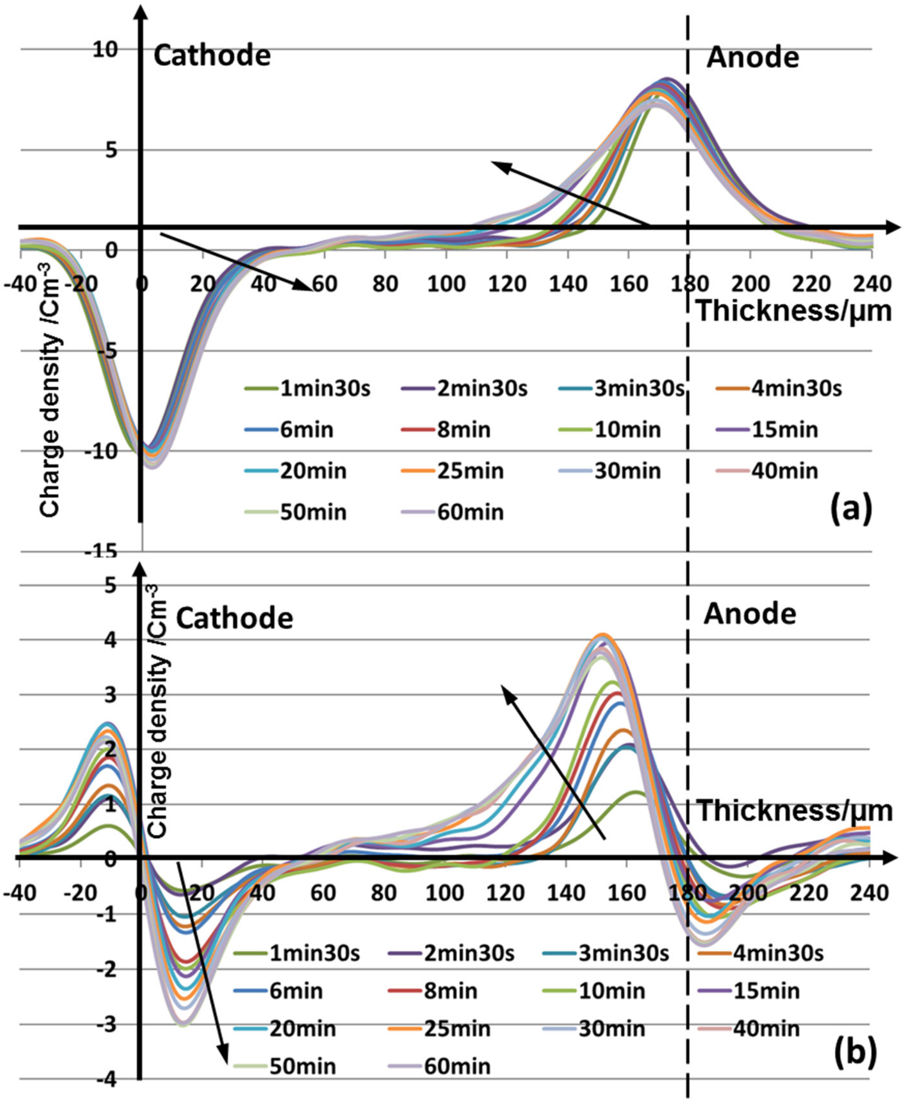

Figure 3-7 Charge profile of LDPE under 20kV/mm HVDC, (a):Charge profiles after calibration, (b):Subtracted results of (a)

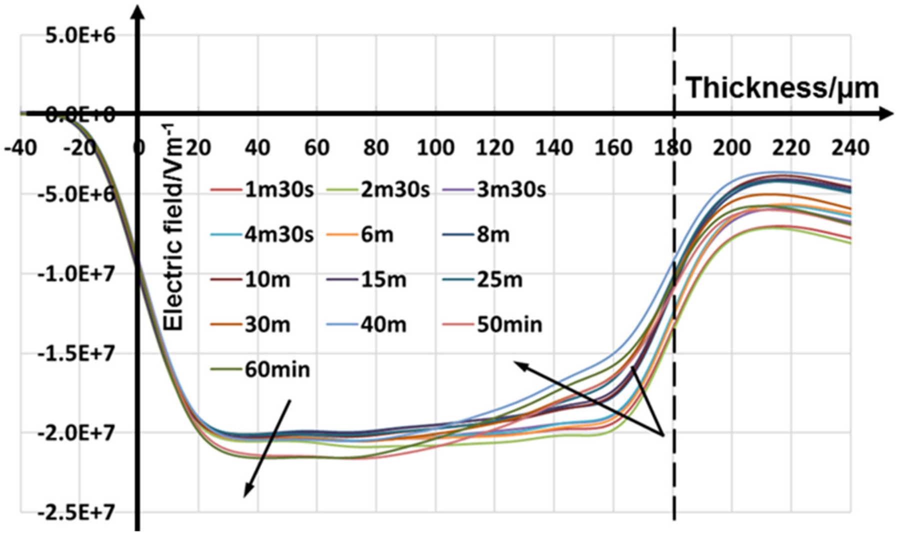

Figure 3-8 Electric field within LDPE under 20kV/mm HVDC

Figure 3-7 presents the charge dynamics under 20kV/mm electric field, and Figure 3-8 illustrates the local field evolution. From the results, it is clear that homocharge accumulation can be observed, and the charge amounts of electrons and holes are similar under 20kV/mm fields. The maximal field distortion happens where the electrons and holes encounter each other. The electron has higher mobility under this field strength, as the position is initially adjacent to the anode and later move back in the central area of the material. After around 40 minutes of field stressing, the charge transport reach a dynamic equilibrium, therefore the accumulated charge amounts and maximum field distortion remain almost no charge.

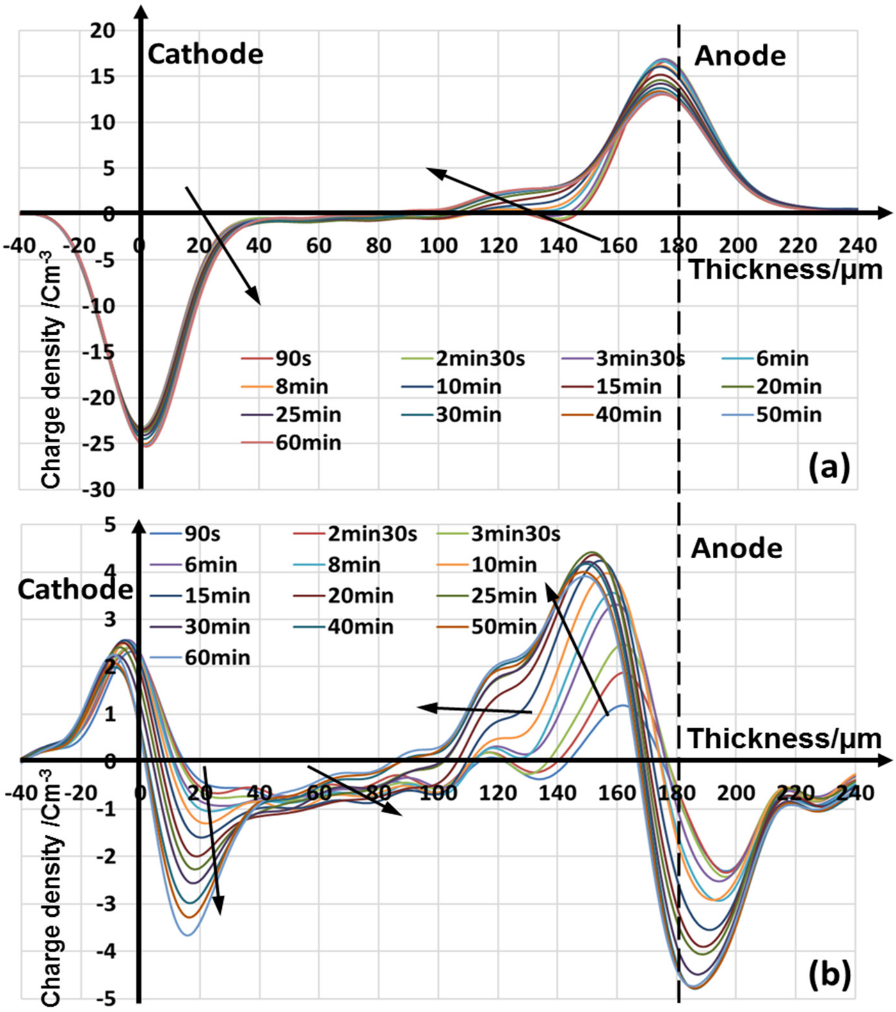

Figure 3-9 Charge profile of LDPE under 40kV/mm HVDC, (a):Charge profiles after calibration, (b):Subtracted results of (a)

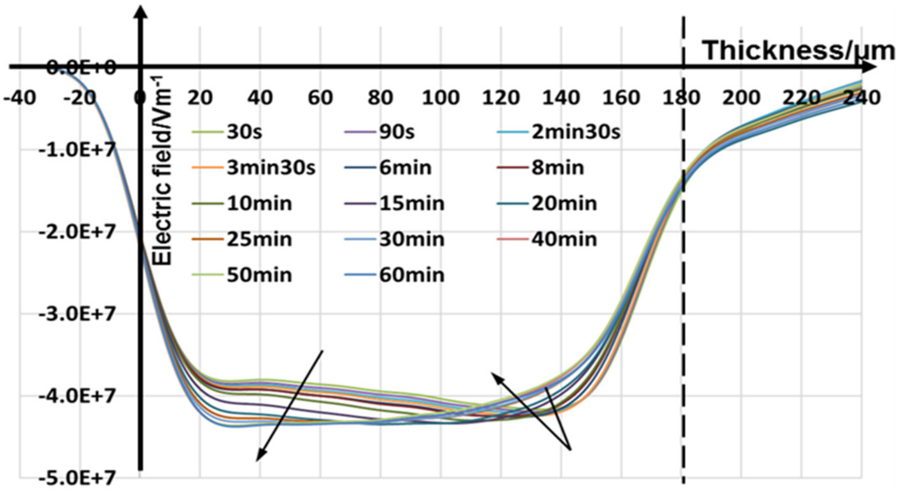

Figure 3-10 Electric field within LDPE under 40kV/mm HVDC

Larger amount of accumulated charges can be observed at both electrodes when the applied electric field is 40kV/mm. It is also noticeable that dynamic equilibrium can be reached in a shorter time (30minutes), due to the quicker charge movement. The local field distribution presents a similar dynamic trend as under 20kV/mm, but the maximum field distortion is significantly enhanced.

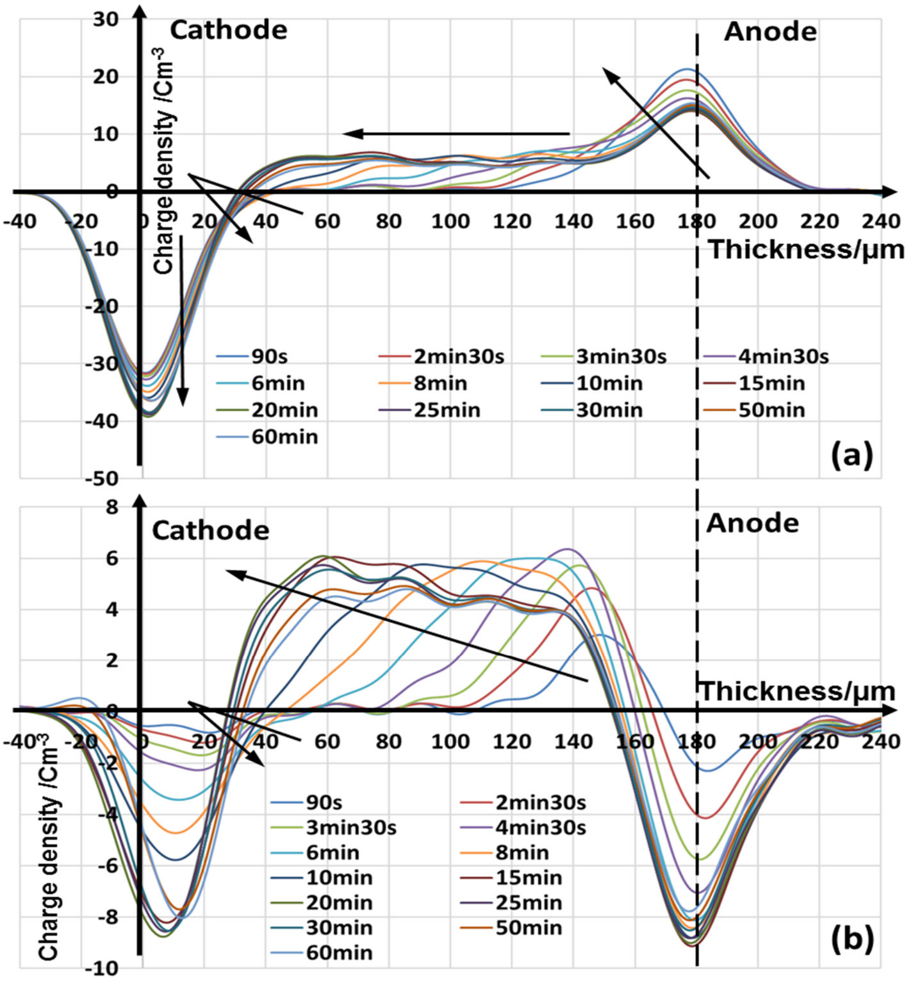

Figure 3-11 Charge profile of LDPE under 60kV/mm HVDC, (a):Charge profiles after calibration, (b):Subtracted results of (a)

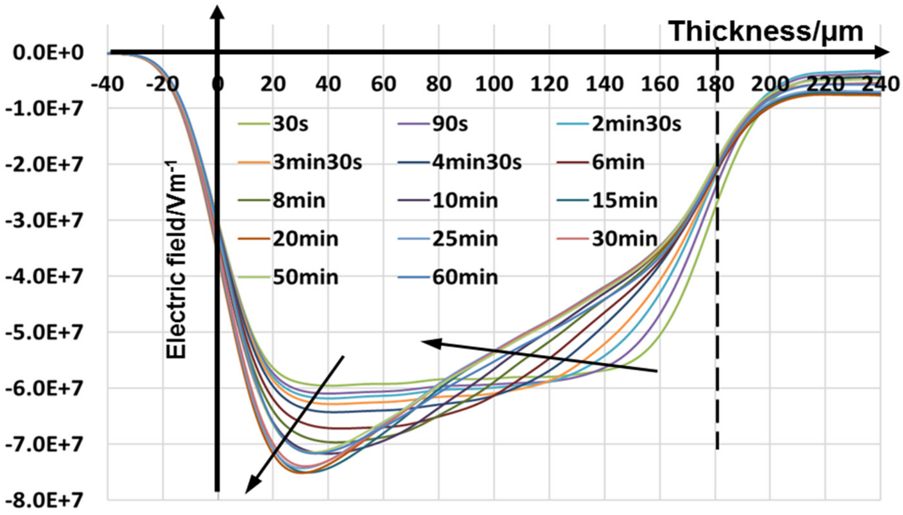

Figure 3-12 Electric field within LDPE under 60kV/mm HVDC

The above two cases relate to charge dynamics under relatively low amplitude of HVDC fields, where the charge packet phenomenon is not significant. For LDPE when the applied field strength is higher than 50kV/mm, positive charge packet phenomenon can be clearly observed.(Figures 3-11 and 3-12) The positive charges packet phenomenon indicates positive charge present a pocket-like motion transporting towards the opposite electrodes, and the motion is repeated along with the stressing time. Under 50kV/mm, the positive charge movements will dominate the overall charge profiles after a short period of field stressing as presented in Figure 3-11. The amount of the accumulated positive charges is much larger than that of negative charges. For the charge dynamics, the front edge of negative charge peak is moving away from the anode due to the effects of positive charge pocket transport. The field distortion is further enlarged under this strength, and the region where it occurs is moving towards the cathode due to the transportation of the positive charge pocket. Saturation happens around 20minutes of field stressing, while the overall accumulated charge amount and maximum field distortion decreases a little after reaching the dynamic equilibrium.

3.2.2 Discussion of total charge amount and maximum field distortion

In order to evaluate the contribution of the accumulated charge on the overall characteristics of the material, the maximum electric field distortion is recorded. Moreover, the charge distribution over spatial coordinate is integrated to obtain the total charge amount, which can be used as a useful evaluation tool to analyse and discuss the simulation results. The integration of charge used is shown in equation 3-4, and the maximum local electric field has been compared with the applied field, deducing the maximum field distortion (Equation 3-5).

$$\boldsymbol{TC(t) = \int_0^d \rho(x,t)dx} \qquad \textbf{3-4}$$

Where *TC* is the total charge amount as a function of time, *d* is the sample thickness and ρ is the charge density, a function of time and spatial coordinate.

$$\Delta f = \frac{f_m - V/d}{V/d} \times 100\% \qquad \textbf{3-5}$$

where Δf is the maximum field distortion, f_m is the maximum local electric field and V is the applied voltage.

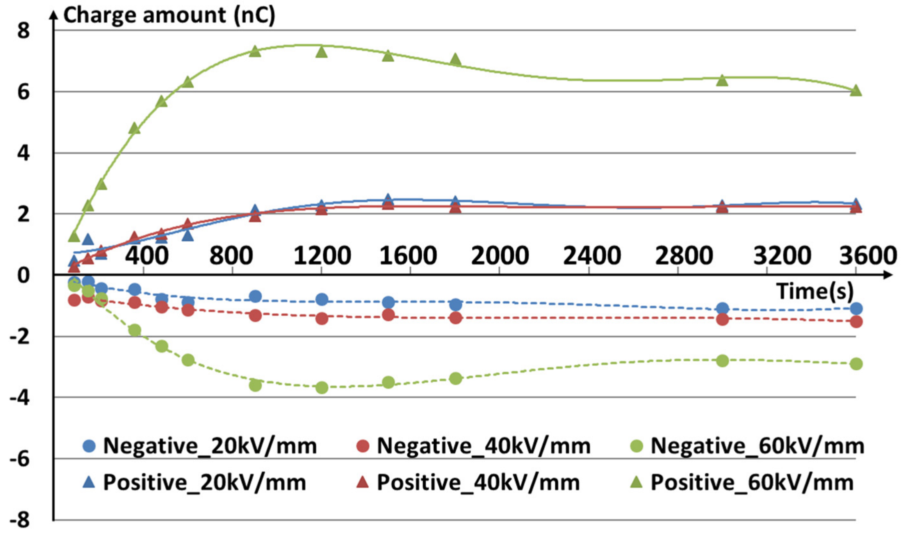

Figure 3-13 Positive and negative charge amounts comparison under various strengths of HVDC stresses

Figure 3-13 presents the calculated charge amounts within the LDPE under various magnitudes of HVDC electric fields. Positive and negative charges are considered separately. It is clear that the amounts of the both positive and negative charges will reach to a stable value eventually during one hour of HVDC field stressing. The time for reaching the steady state decreases with the increase of the applied field. Besides, negative charges amount increase gradually with the magnitude of external fields. On the other hand, the positive charge amounts demonstrate significant changing when the fields are enhanced from 40kV/mm. This indicates the holes' packet-like motion can significantly enhance the amounts of positive charge. Therefore, positive charges dominate the overall charge dynamics. Furthermore, the amounts of positive charges accumulated are always about one time larger than those of negative charges. This indicates the electrical injection and transportation processes are more severe for holes rather than electrons under high strength HVDC in LDPE.

Local field distortion can be affected by both the amounts and the position of the accumulated charge charges, illustrating an integral effect of space charge phenomenon, which is strongly related to dielectric strength, ageing, and degradation of the materials. [84, 86, 87] A comparison of the maximum field distortion evolving with time under various amplitudes of HVDC fields is presented in Figure 3-14. For 20kV/mm, the maximum field distortion is still increasing after the accumulated charge amounts reach steady values. This indicates the charges inside insulation are still in intensive motion after the homocharge injection are suppressed by the internal field distribution caused by the space charge. When the applied field is high, the trend of field distortion (More rapidly to reach the steady state) is similar to the accumulated charge amount, due to the higher charge carriers' mobility accelerating the charge dynamics.

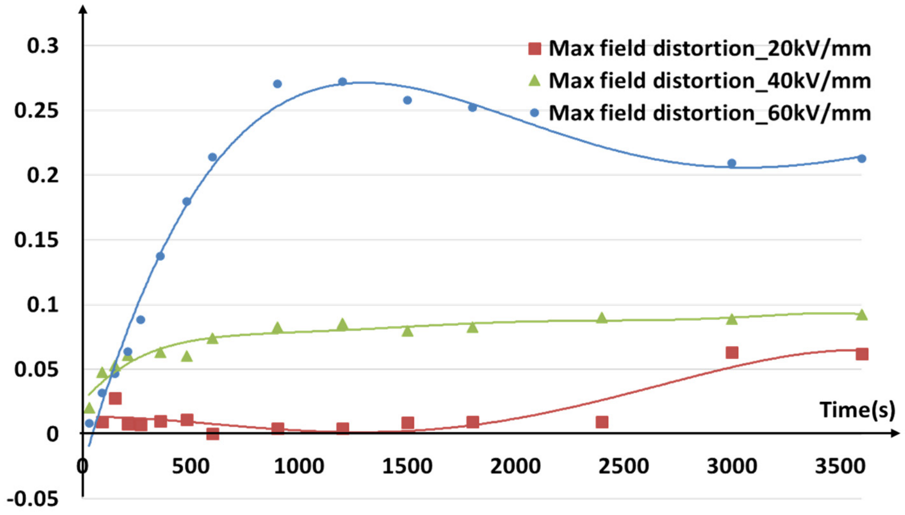

Figure 3-14 Comparison of maximum field distortion under various strengths of HVDC stresses

3.2.3 Conclusions

Based on above, it is clear that space charge phenomenon is noticeable within dielectrics under HVDC. Homo charge injection and bipolar charge transport can be observed in LDPE. Charge dynamics under all issued cases reach a dynamic balance within one hour of field stressing. This duration to reach equilibrium is relatively short compared with the operating lifetime of insulation, which generally can up to decades. Various charge accumulation characteristics can be observed when the magnitude of applied field changes. This different feature indicates the transport and injection of charges are strongly related to the magnitude of fields. Under HVDC fields, especially when the magnitude is high, the positive charge packet phenomenon is significant, which can remarkably increase the accumulated positive charge amounts. Besides, the noticeable local field distortion caused by space charge phenomenon can be observed. This distortion indicates charge dynamics in return can further modify the local fields. The maximum field distortion occurs in bulk of insulation where the positive and negative charges encounter under all the measured HVDC fields. The maximum field distortion also increases along with increasing applied field magnitude, and the percentage can approach 25% when the applied field magnitude is larger than 40 kV/mm.

When the applied field magnitude reaches this stage, the positive charge packet phenomenon is remarkable in the insulation.

3.3 Space charge phenomenon under AC and superimposed AC and DC voltage

Space charge measurements are of great difficulties under periodic electric stresses due to the altering polarities. This is because the amount of accumulated charges is generally small under the field with alternating polarities, which results in a small signal to noise ratio. Based on the introduction of the schematic structure of space charge measurements under complex periodic fields, as mentioned in section 1.3.2, the experimental results will be analysed and discussed in this section.

Firstly, to describe the percentage of DC component within the combined electric stress, a DC offset ratio is defined as equation 3-7:

$$\mathbf{DCoffset's\ ratio} = \frac{V_{DC}}{V_{AC_{RMS}}+V_{DC}} \qquad \textbf{3-4}$$

Eclipse is used to measure space charge under periodic complex fields, and the charge profiles can be classified and averaged according to their phase angles. The results in this section are mainly focused on the electric field with a power frequency, 50 Hz, in order to investigate the space charge characteristics closed to reality. Besides, the overall RMS values of all the applied voltages are 5kV, for the LDPE samples with a thickness of 100µm. This RMS value is chosen to clearly demonstrate the charge accumulated under AC and superposed AC and DC high voltage electric fields without damageing the system. (LDPE under AC electric fields is easy to breakdown, normally around 100kV/mm.) Furthermore, the maximum testing duration for AC and superposed AC and DC cases in this work is 7 hours. Choosing this period is because surface flashover and discharge are occasionally happen under AC fields testing, which requires monitoring during the testing and the maximum working hour within our laboratory is 8 hours. The influence of applied field magnitude, frequency and composition on the charge dynamics within insulation is analysed and discussed in detail in Chapter 5.

3.3.1 Charge dynamics under AC voltage

From the results under HVDC fields, it is clear that the electrons and holes present a different relationship with the electric field regarding charge injection and charge transport phenomena. Electrons generally have a much higher mobility than holes, depending on the electric field. On the other hand, the relationship of holes' mobility and the applied field is more complicated. Numerous researches indicated that the mobility initially increases with the electric field, while start decreasing after the field reaching certain levels. [91, 96, 97] The observation of positive charge packet is the direct consequence of the combination of electrons and holes mobility characteristics. Under AC fields, electrons and holes are injected during the first half cycle, and then neutralised a significant amount by the injected opposite charge carriers during the next half cycle with the opposite polarities. However, due to holes and electrons' various characteristics, a few charges can be left within the material after a cycle of field stressing, and the amounts of residual charges could be increased with the application of electric fields. A schematic hypothesis of the charge dynamics is shown in Figure 3-15, to demonstrate the space charge phenomenon under ac conditions.

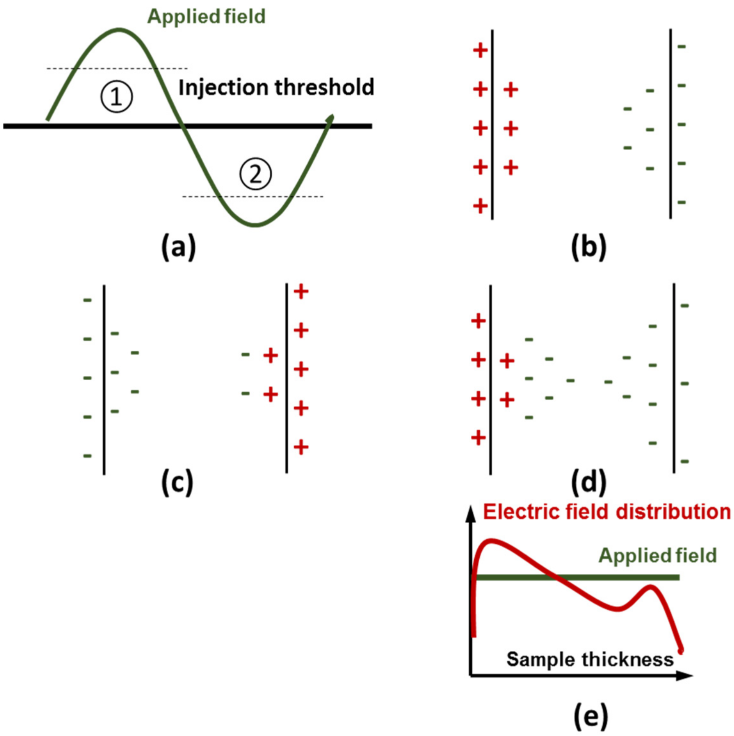

Figure 3-15 Schematic model for ac space charge formation

Figure 3-15(a) shows a typical AC voltage waveform. The two dot lines represent the threshold voltages for charge injection. In the first half cycle, when the applied electric field exceeds the charge injection threshold field, both electrons and holes can be injected into the material, and charge distribution will be represented in Figure 3-15(b). When the polarity changes in the next half cycle, all the injected holes will recombine with part of the accumulated electrons due to larger injected amounts of electrons comparing with holes. More importantly, as the holes travel much slower than electrons under the majority of applied field phases, only electrons trapped adjacent the electrode are neutralized, while those electrons away from the electrode are less affected. These electrons can move towards the opposite electrode due to the applied field. Similar trend happens at the opposite electrode. The picture of a possible charge distribution after a complete cycle is illustrated in Figure 3-15(c). The electrons can move further in bulk in subsequent cycles. The above processes will be repeated many times along with cycles proceeding, the final charge distribution will look like Figure 3-15(d), and the corresponding local field distribution is illustrated in Figure 3-15 (e). The assumption predicts the charge accumulation under HVAC stresses will mainly accumulate adjacent to the electrodes, and the localised charges generally cause field distortion near the electrodes, which may gradually age the surface region of the insulation.

Figure 3-16 and Figure 3-17 illustrate the volts on results of charge dynamics within an AC field cycle initially and after 7 hours of AC field stressing. The results before and after subtraction are all illustrated as comparison. Figure 3-18 demonstrates the time dependant charge dynamics when applied field phase angle is around 90°. The corresponding local field distribution is presented in Figure 3-19. Besides, typical charge decay result of the testing samples after 7 hour field application is shown in Figure 3-20.

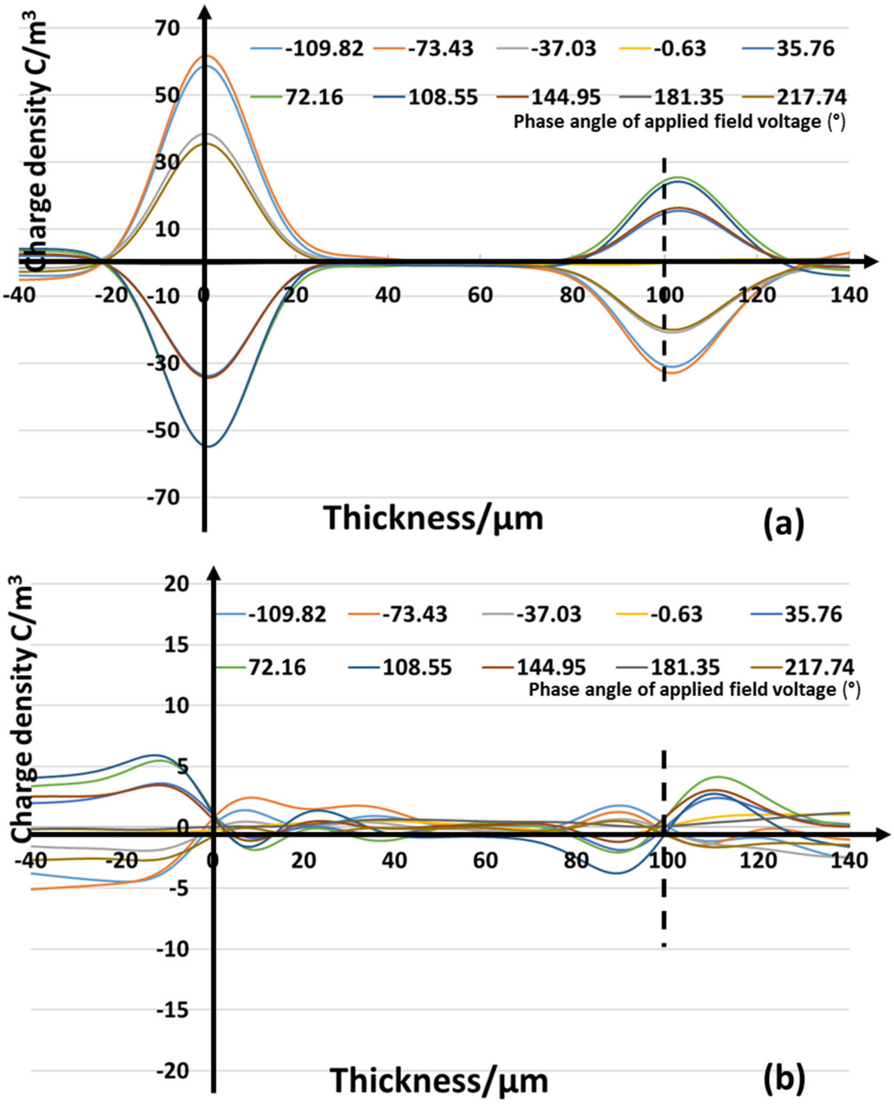

Figure 3-16 Charge profiles (a) and subtracted results(b) within the cycle instantly after apply fields (50kV/mm, 50Hz)

The charge dynamics caused by the different field phases are clearly illustrated in Figure 3-16 (initial) and Figure 3-17(7 hours). Comparing Figure 3-16 with Figure 3-17, it can be noticed that charge dynamics within an applied field cycle present significant differences after 7 hours of field application. The differences of the accumulated charges dynamics are relatively hard to directly distinguish from the original charge distribution profiles, due to the remarkable amount of capacitive charges at electrodes. Therefore, the subtraction method is applied to remove the influences of capacitive charges within the profiles, and the corresponding results are shown in Figure 3-16(b) and Figure 3-17(b).

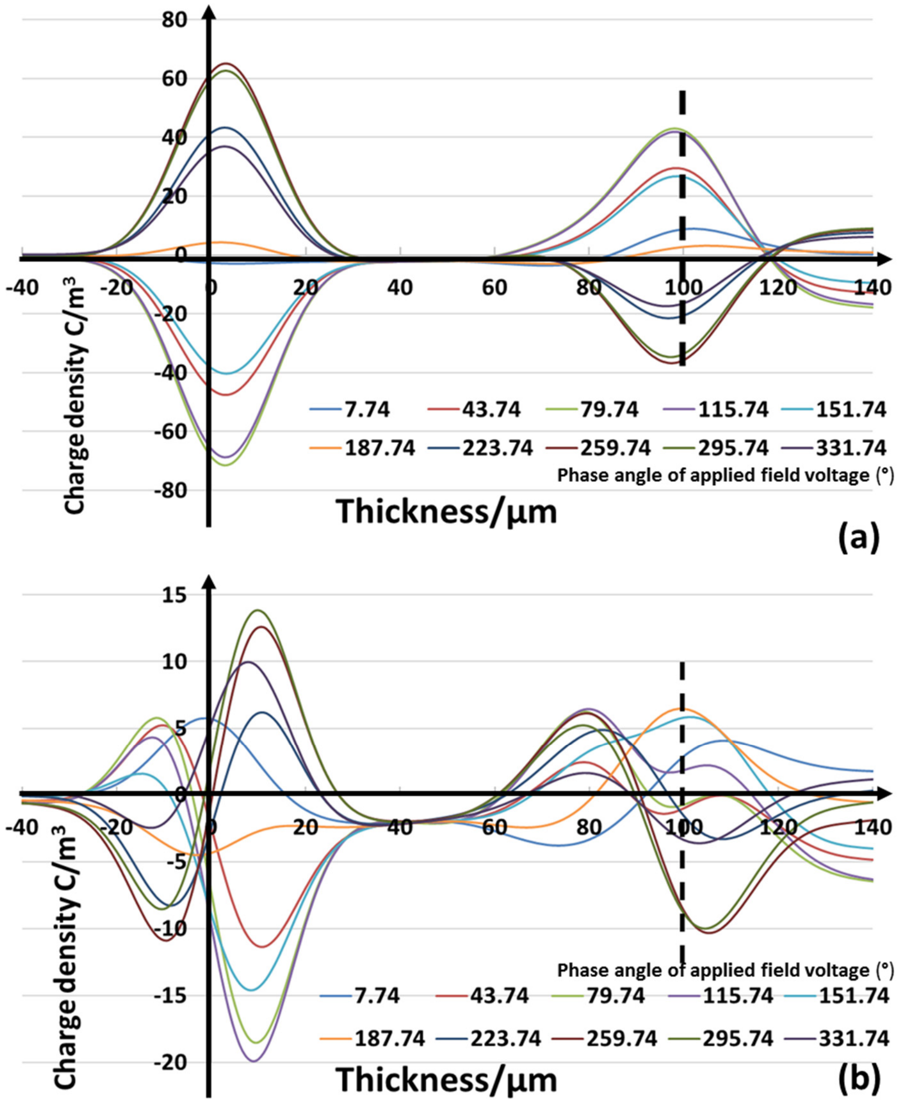

Figure 3-17 Charge profiles (a) and subtracted results(b) within cycle after 7 hours apply fields ageing (50kV/mm, 50Hz)

As shown in Figure 3-16 (b), very few charges can be observed shortly after the voltage application. On the other hand, in Figure 3-17 (b), severe charge accumulation can be observed in the regions adjacent to the electrodes. This indicates the characteristics of the surface region of the insulation material may have been aged following a certain time of HVAC fields application. To further verify the change of surface region characteristics, Raman and ATR-FTIR spectroscopy tests have been done, which will be discussed in Figure 3-20 to Figure 3-22. When the amount and mobility of injected charges are increased, the charges can further intensify the electric field distortion adjacent to the electrodes. Besides, the accumulated charges are very close to the electrode, which can be overlapped with the capacitive charge peaks at the electrodes in the original charge distribution curves, as shown in Figure 3-17. Due to the limited resolution of the PEA system, it is hard to distinguish them in the overall charge distribution profiles (Figure 3-16(a), Figure 3-17(a)).

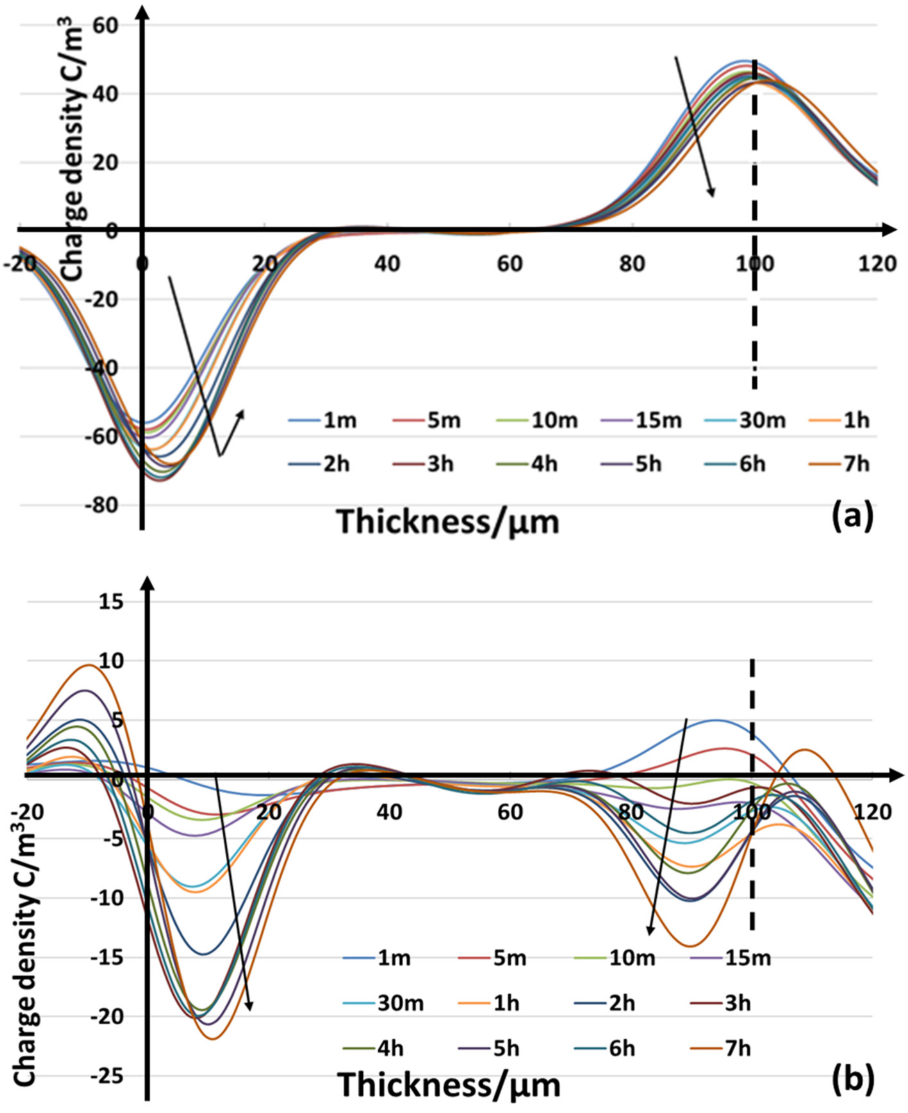

Figure 3-18 Charge evolution around applied fields phase 90°(a), and after removing the capacitive charge (b) within 7 hours of ac field stressing (50kV/mm, 50Hz)

Figure 3-18 demonstrates the charge evolution within the sample with stressing time. Charge profiles under the applied voltage at the phase angle of 90° with different ageing times are discussed to reduce the influence of different phases of the applied voltage on the charge distribution. From Figure 3-18(b), it can be observed that the amount of the accumulated charges adjacent to the electrodes increases with the ageing time. This trend can also be observed in 3-18(a) significantly. Another interesting observation is the dominant of negative charges within the charge profiles, especially for a long duration of the voltage application. Similar features have been reported previously in [98]. This may be related to the different charge injection rates and mobility for positive and negative charge carriers, as discussed in Figure 3-15.

Figure 3-19 presents the decay results after 7 hours of 50Hz 50kV/mm HVAC ageing. Comparing with Figure 3-17, it is apparently that the amount of charges within the sample are much smaller than that when the voltage applied, indicating the majority of charge shown in Figure 3-17 are mobile charges. These mobile charges generally have a high mobility so that they can escape from the insulation quickly after the removal of the applied voltage. Besides, due to their high velocities, those charges were hardly observed in previous decay or Volts_off measurements [98, 99].

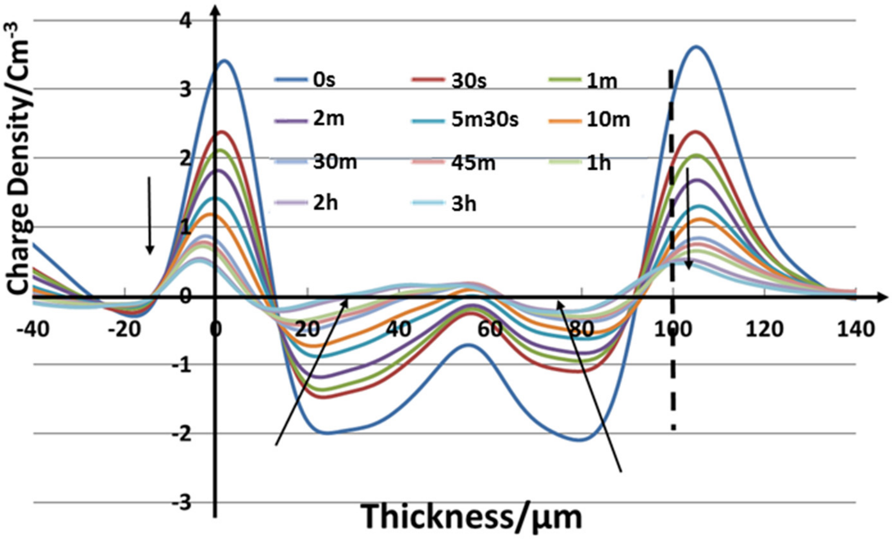

Figure 3-19 Decay results of trapped charge after 7 hours apply fields ageing (50kV/mm)

In summary, a significant amount of charges (Maximum charge density after 7 hours is around 20 C/m^3.) within LDPE can be observed under 50Hz HVAC stresses based on the improved AC PEA system and the proposed data analysis method. It also indicates that the little space charge amounts of measurement under relatively high frequency (>0.1Hz) HVAC in the literature [81, 82, 99, 100] may not be accurate, due to the following three reasons. Firstly, a significant amount of fast velocity charges was ignored in some of their results [99, 100], and only deeply trapped charges (like charges measured in the decay results) were observed. This is because these mobile charges can evolve within the applied sinusoidal field cycle and escape from the insulation quickly after removing the applied field. Therefore, those fast charges are hard to observe, if the measurement systems are unable to distinguish profiles under different applied fields' phase or simply use Volts_ off measurement to detect the charge inside the insulation. Secondly, the majority of these measured charge dynamics are under relatively low applied field (<40kV/mm) [81, 100]. The overall trapped charge amounts, both deep and shallow, are small when the strength of applied fields is lower than 40kV/mm. A detailed discussion of the influences of applied field magnitudes is presented in section 5.1. Finally, a high resolution for the measuring system is essential to distinguish the accumulated charges adjacent to the electrodes, and a method to remove the effect of capacitive charges without losing any charges inside samples is also necessary. Otherwise, they will be overlapped with the capacitive charges at the electrodes and hard to be observed [81, 82].

Based on results in this section, it is clear that the observed significant charges mainly accumulate close to the electrodes. They can respond to the voltage change with power frequency. The range of their evolution is enhanced with the duration of its application. This will further deteriorate the internal field distortion within the insulation. Overall, when the insulation is stressed under high fields (>40kV/mm) for several hours, the internal electric fields within the material will be severely distorted in the region close to the electrodes, which may cause ageing to the surface region of testing material and even trigger a breakdown of the entire material. In fact, several breakdown occurred during charge measurements when 60kV/mm was applied to the samples. Figure 3-20 presents the charge profiles under 60kV/mm, 50Hz AC fields within 4 hours of field stressing. For this case, the testing sample breakdown happened around 5 hours of field stressing.

Comparing this with Figure 3-18, it is clear that under 60kV/mm, after only 4 hours of stressing the accumulated charges amounts are similar to the cases after 7 hours of 50kV/mm field stressing. This further confirms the accumulated charge amounts in the surface region of samples increase along with applied field strengths and can accelerate the breakdown of materials by severely distorting local electric fields.

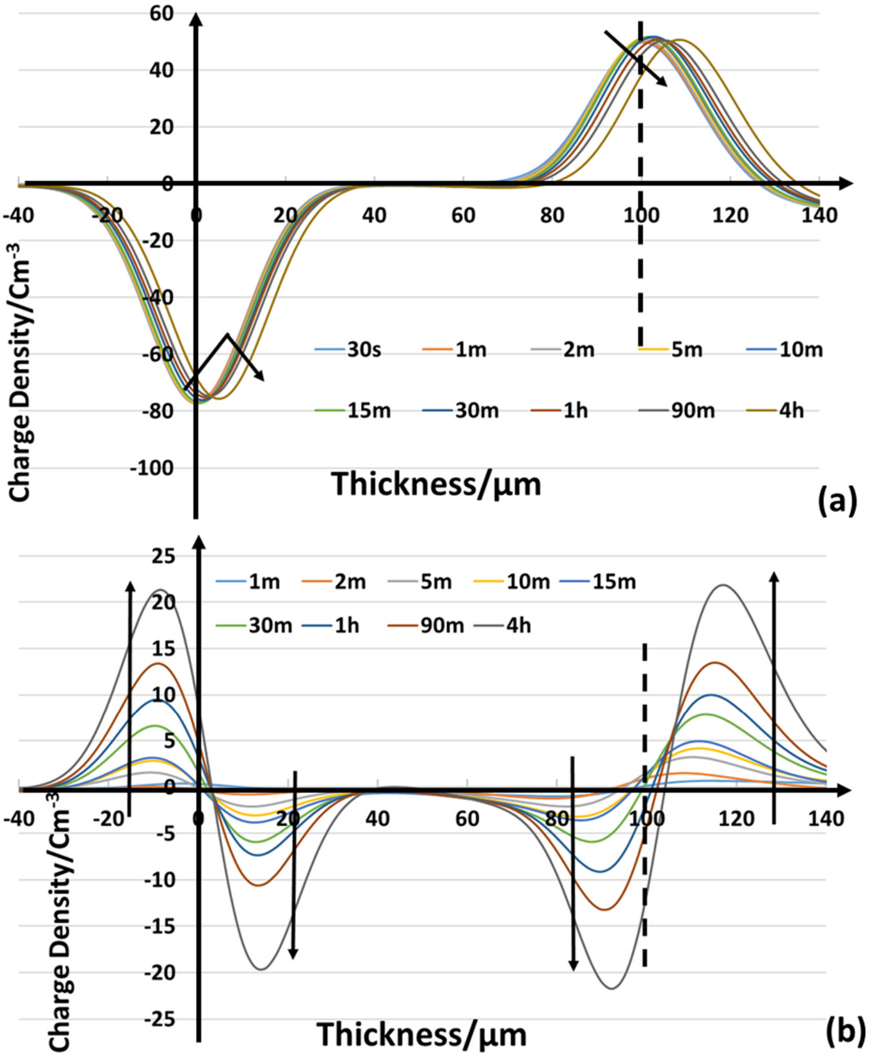

Figure 3-20 Charge evolution around applied fields phase 90°(a), and after removing the capacitive charge (b) within 4 hours of ac field stressing (60kV/mm, 50Hz)

3.3.2 The chemical and physical structure characteristics of AC stressed samples

In order to further investigate and validate the effect of space charge phenomenon on ageing within the surface region of testing samples under HVAC fields, the structure characteristics of virgin LDPE samples and samples after 7 hour of various AC field stressing were measured by the means of Raman spectra and Attenuated Total Reflectance Fourier Transform Infrared (ATR-FTIR) spectra. Raman tests can provide information about functional groups or chemical bonds of a particular layer within testing samples through the testing sample thickness, while ATR-FTIR techniques are applied to a thin layer of the testing sample and measure the functional groups' formation within the surface region of the materials. Combined the results of these two, the structural differences of surface region and bulking area of testing samples after 7 hours of AC fields stressing can be clearly classified.

The Raman experiment was conducted using Leica microscope and Renishaw Raman RM1000 system with a 785 nm CW diode laser of 25 mW. The system uses Peltier cooled charged coupled device (CCD) detector. There is a holographic grating of 1800 grooves mm^{-1}, to disperse the scattered radiation by wavelength. A holographic (notch) filter is also attached that prevents back-scattered radiation from entering the detector. The device was set up in confocal mode, with a slit width of 15 μm and a CCD area of 4 pixels (image height) x 574 pixels (spectrometer range) which, together with the mechanical slit, acts as a virtual confocal pinhole. These settings are consistent with Renishaw's recommendations for the confocal mode. For a start, the lens was focused on the top of the sample. Then the focal point was adjusted to go 10 μm deeper and further until it reached the bottom (around 100μm) of testing sample.

Table 3-1 Band assignments of Raman bands of polyethylene [101]

Bands(cm^{-1})	**Assignments**	**Features**
1465	C-H rocking	Crystalline; Anisotropic
1454, 1439	C-H bending	Anisotropic
1445, 1417	C-H bending	Crystalline
1370	C-H wagging	Amorphous
1308	C-H twisting	Amorphous
1299	C-H twisting	Crystalline; Anisotropic
1169	C-H rocking	Crystalline
1128, 1062	C-C stretching	Crystalline; Anisotropic
1084	C-C stretching	Amorphous

Table 3-1 presents all of the key peaks in the results of Raman spectra for identifying the structure of polyethylene, and their band assignments [101]. Among them, 1439 1417 C-H bending, 1370 C-H wagging, 1169 C-H rocking, and 1128 1062 C-C stretching peaks are selected for the characteristics analysis. The trends to describe the groups changing v.s. the position within samples under different stressing conditions are illustrated in Figure 3-20. The original Raman spectra and details of data processing are illustrated in the Appendix B. A similar trend of the intensity changing along with virgin sample thickness like blue lines in Figure 3-21, has been observed by Macdonald et al [102] in 2003. It is noticeable that the different groups of the surface region of the testing samples have been modified after 7 hours of AC fields stressing with different trends, comparing with the virgin ones. However, the general trend for the position-dependent group characteristics is challenging to be concluded due to the altering of spectra focus. Therefore, ATR-FTIR tests have been down to identify the relationship further.

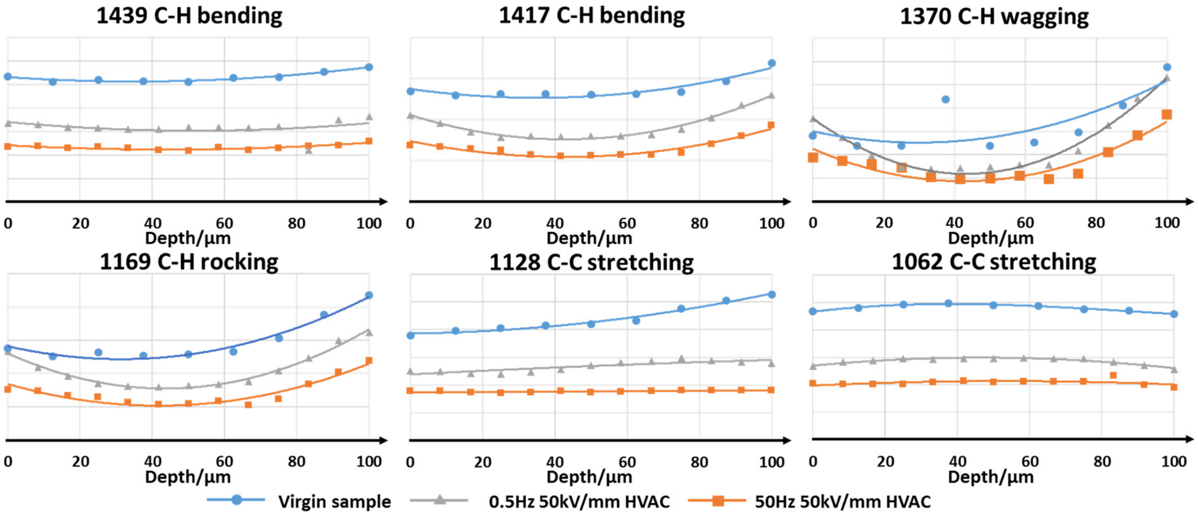

Figure 3-21 Comparison of polyethylene characteristic band peaks in Raman spectra. The points in curves indicate the actual measured results and the lines are the fitted trends, using polynomial functions.

ATR-FTIR is a very sensitive technique and is especially suitable for surface analysis. A sketch illustrating the ATR technique is presented in Figure 3-22 [103]. The incoming light is focused through the crystal onto the sample/crystal interface. Some light is absorbed by the sample while the left unabsorbed light is reflected out of the ATR crystal to the detector. A Thermo Scientific iD7 ATR device is used as the accessory to produce ATR-FTIR tests. Critical band peak, 750–650 cm^{-1}, indicating the C-H rocking of the crystalline structure of Polyethylene is chosen as an example for comparison of the relationship between the characteristics of testing samples and the trends of intensity. The results are illustrated in Figure 3-23. The whole comparison of the ATR-FTIR results and the data analysing process are shown in Appendix B.

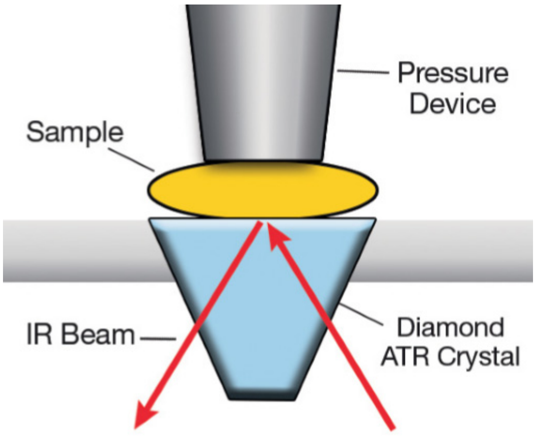

Figure 3-22 A sketch of ATR technique [103]

Based on the charge dynamics under HVAC stresses, it demonstrates that 1): under the higher strength of applied fields, more charges can be accumulated within the insulation, 2): under the higher frequency of applied fields, charges will be accumulated more closely to the electrodes. Consequently, the surface region of samples under 50Hz 50kV/mm fields stressing should be the most severely aged one comparing with samples under 0.5Hz 50kV/mm fields and 50Hz 30kV/mm fields. Figure 3-23 clearly illustrates the trend, and it demonstrates that the applied frequency (versus applied field strength) having more significant effects on surface ageing of materials.

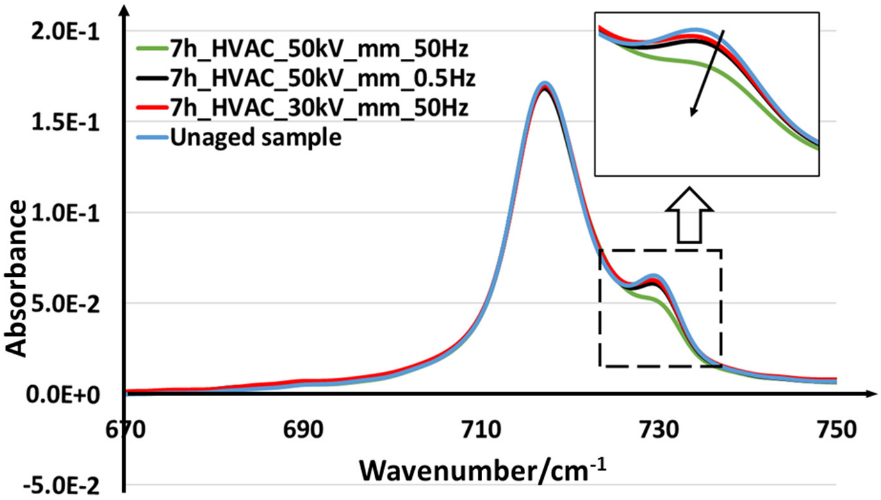

Figure 3-23 Reflectance Fourier transform infrared (ATR-FTIR) spectroscopy of LDPE sample after 7 hour of various AC field stressing

Based on the Raman and ATR-FTIR results, it is clear that the high frequency HVAC field can influence the structural characteristics of the surface region of polyethylene. (Maybe physical or chemical, and current results are not sufficient to qualify the characteristics.) These results also verify the existences of adjacent electrodes charge peaks accumulated under HVAC stresses. This is because the severe charge dynamics can accelerate the material ageing at the surface area or break some weak bond between branches within crystalline or amorphous regions by severely distorting the local electric fields and the movement of the energised charges. The damaged regions could further enhance the injection and transportation of charges, causing more significant field distortion within materials.

3.3.3 Charge dynamics under superimposed AC and DC voltage

Under relatively high frequency, AC electric field, a significant amount of negative charges can be observed within LDPE after several hours field stressing, as discussed in the previous section. This is due to the difference in charge transport and injection characteristic between electrons and holes under intensive electric fields. The charge dynamics will become more complicated when a DC offset is superposed. The offset, itself could also cause stable charge formation and transportation, which may promote or neutralise the influence caused by the AC fields

Figure 3-24 presents the measured decay results of charge profiles after 7 hours of the applied field with DC offset ratios are 0.2(a) and 0.5(b). It is evident that under field with a smaller DC component, the distribution of the residual charges is similar to those under pure AC fields. Negative charges still dominate the overall charge accumulation. The additional dc offset only cause the uneven distribution and increase the total deep trapped charge amounts from -2.3 nC to -9.9 nC. When the DC offset ration increases to 0.5, the residual charges distributions after 7 hours are more similar to the charge distributions under pure DC, i.e., the influences of polarity reversal towards the charge dynamics can hardly be observed.

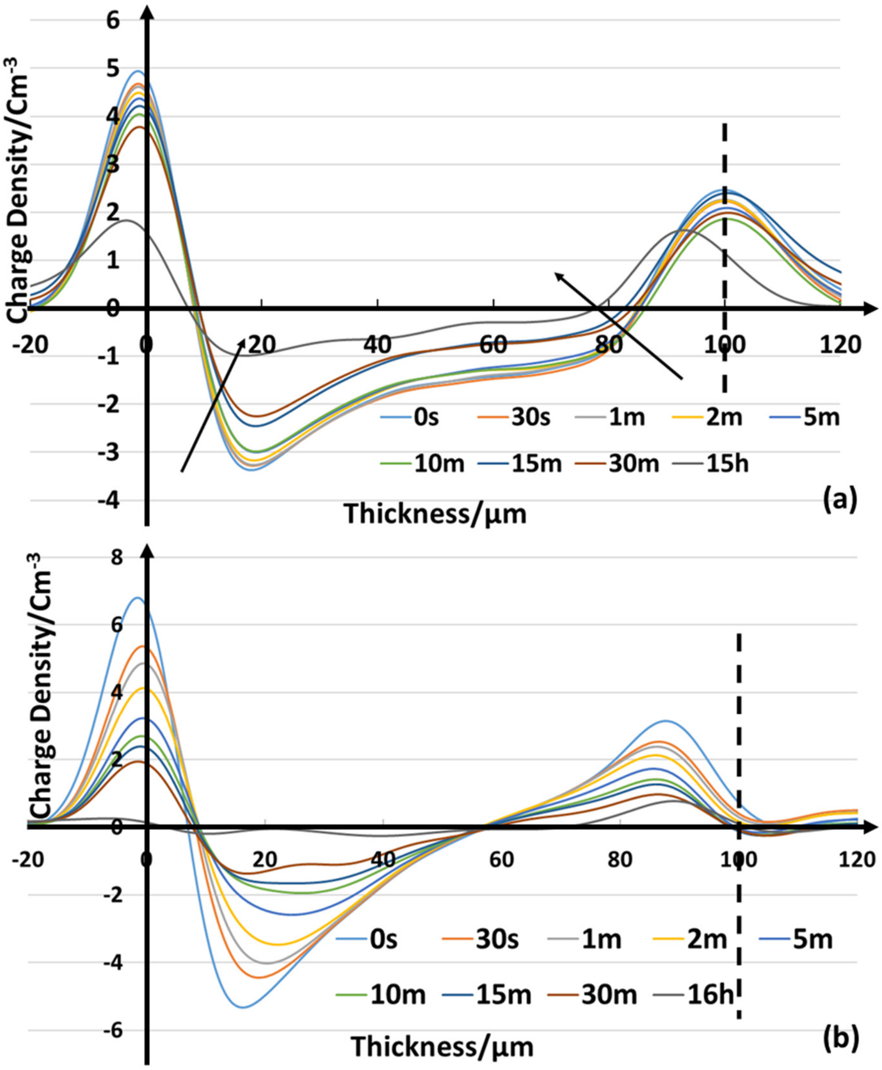

Figure 3-24 Decay results of charge profiles within LDPE after 7 hours of 50Hz combined stresses with DC offset ratio 0.2(a) and offset ratio 0.5(b) with overall strength 50kV/mm (RMS)

Measured space charge distribution under combined fields with various DC offset ratios are presented below in Figure 3-25. The displayed results are the injected charge profiles with the applied voltage on, after the subtraction process (method discussed in section 3.1.2). It is also validated that under fields with lower offset ratio, as shown in Figure 3-25 (a), the field's polarity reversal still contributes significantly to the charge dynamics. Negative charges still dominate the charge dynamics in the bulk area due to their high mobility and more considerable accumulated amount, like under pure AC stresses. The additional DC offset only causes an unbalanced charge distribution, and generally increase the amount of accumulated charges, which cannot entirely overcome the impact caused by the AC component. When a large DC ratio is applied (Figure 3-25 (c)), the effects of polarity reversal can only be distinguished at very initial stage (<2 minutes). After a short period, the charge dynamics present almost no difference comparing with trends under pure DC stresses.

The corresponding local electric field distributions (Figure 3-26) also support the above explanation. Similar to the situation under AC fields (Figure 3-18), and the maximum field distortion happens adjacent to the electrodes in Figure 3-26(a). In contrast, field trends under higher DC offset ratio (Figure 3-26(c)) are identical to those under pure DC (Figure 3-8, Figure 3-9), and the maximum field distortion happens in the middle of the sample.

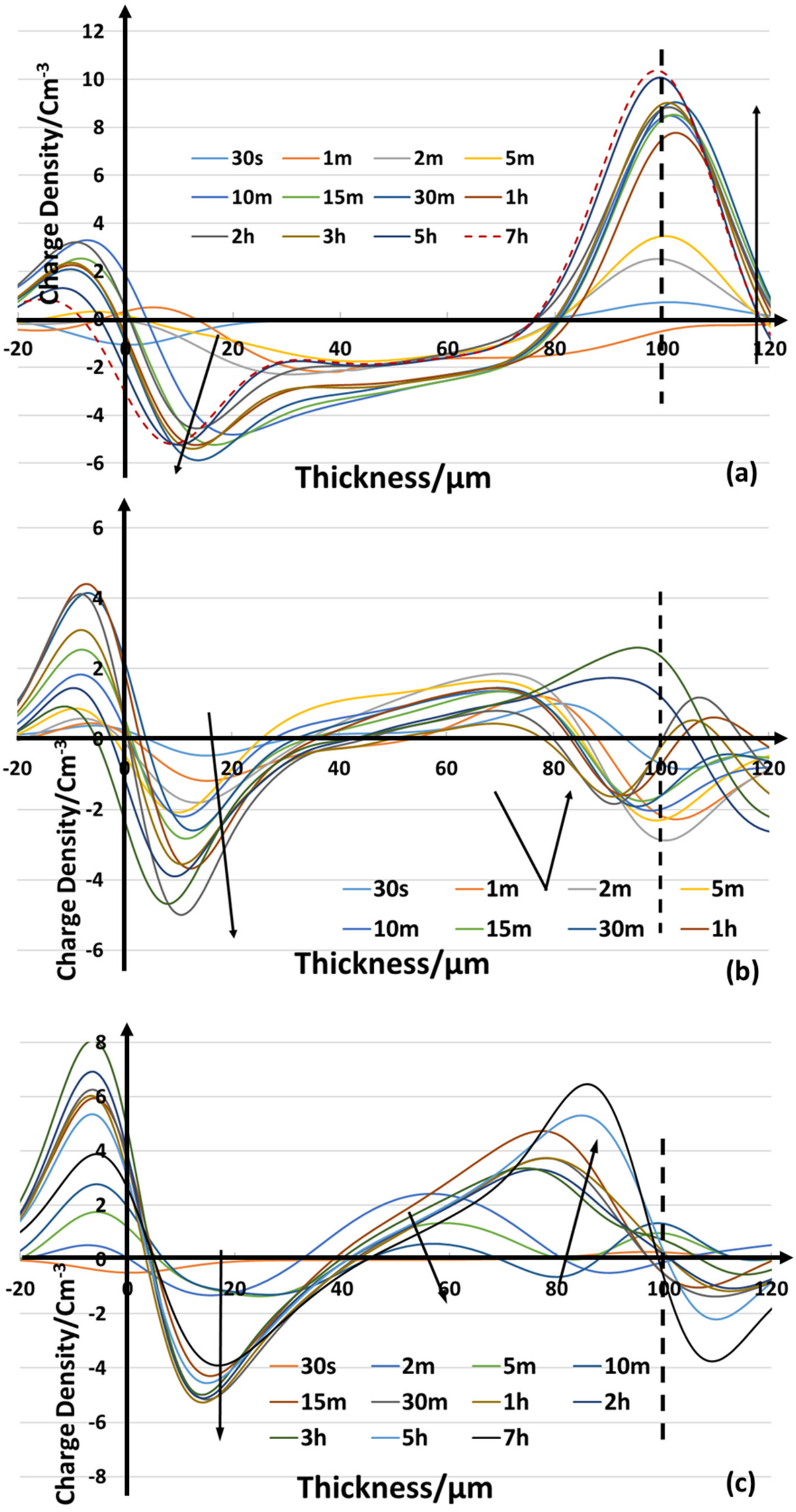

Figure 3-25 Subtracted volt_on results of charge evolution under combined stresses (50Hz 50kV/mm) with DC offset ratio 0.2(a) ratio 0.4(b) and ratio 0.5(c) Phase 90°)

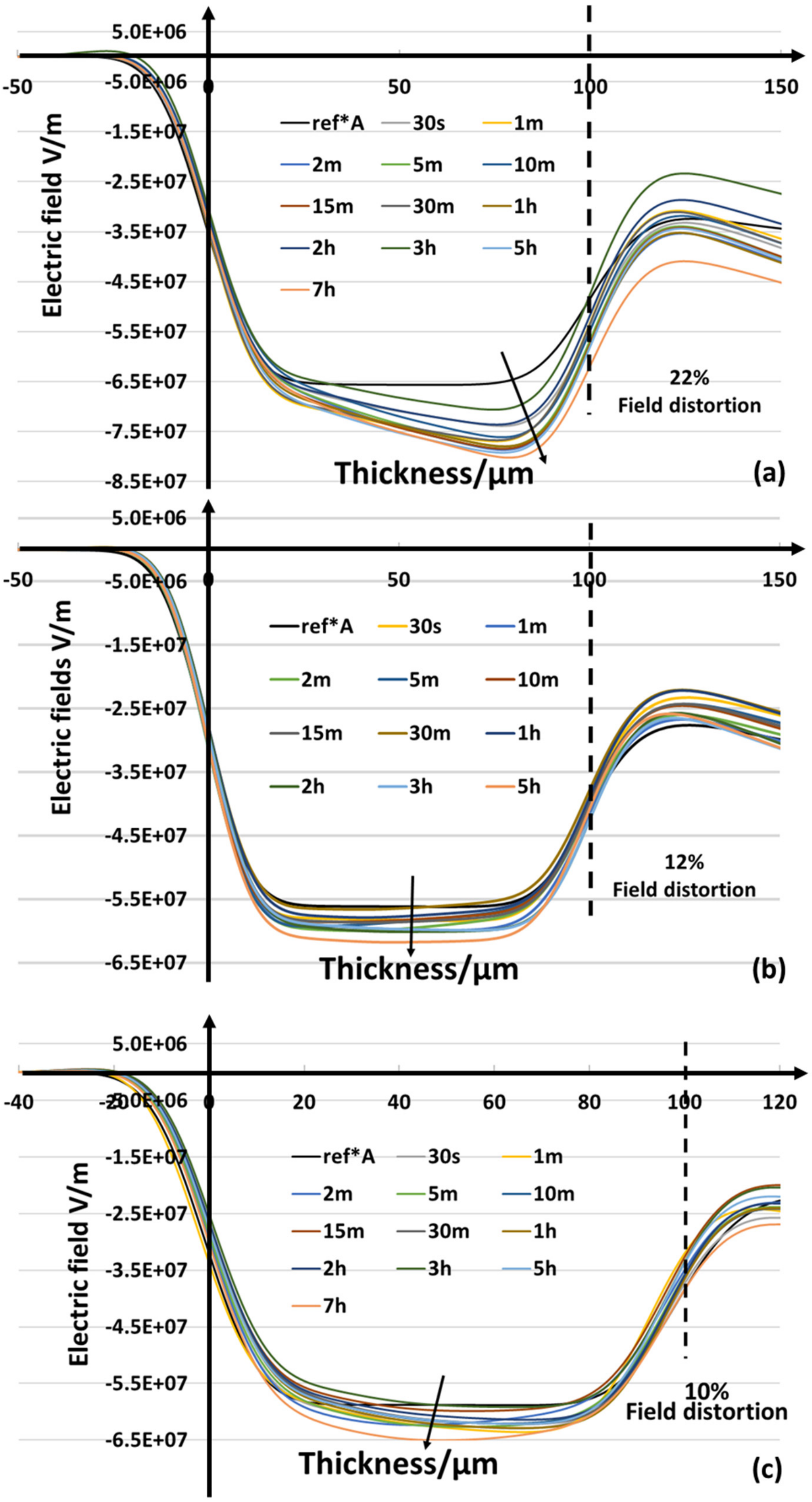

Figure 3-26 Field distribution within LDPE within 7hours of combined field stressing with DC offset ratio 0.2(a) ratio 0.4(b) and ratio 0.5(c) (Phase 90° ref*A is the normal line used to estimate field distortion deduced from fields with no space charge influences)

3.3.4 Conclusions

In summary, charge dynamics are obviously different under AC and DC electric fields. When the polarity of the applied field is frequently reversing, significant unbalanced charge distribution can be observed due to the different characteristics of electrons and holes. This uneven charge distribution can cause outstanding field distortion, which may eventually result in the various dielectrics ageing features under AC and DC fields. When a DC offset is superposed to the AC stresses, the situation becomes more complicated, as both the offset magnitude and the frequency of the applied field can remarkably affect the charge dynamics. In general, the additional DC offset can significantly enhance the trapped charge amount within dielectrics. On the other hand, the frequency of polarity reversal caused by the AC elements can induce the significant charge accumulation adjacent the electrodes, which can cause the corresponding local field distribution severely distorted. The effects of DC offset and AC component within combined AC and DC fields on the charge dynamics within insulating dielectrics are exhaustively investigated in Chapter 5.

Chapter 4: Modelling of space charge based on bipolar charge transport theory

This chapter presents the fundamental principles of the bipolar transport model and the procedures for establishing the numerical model to analyse charge dynamics under general periodical high voltage fields (HVDC, HVAC and superposed AC and DC fields). The methodology of the bipolar transport theory is stated in Section 4.1. Next, the specific numerical model descriptions for various cases and typical simulated results are illustrated in Section 4.2. Finally, a methodology of fitting simulated results with the measured ones is demonstrated in Section 4.3.

4.1 Bipolar charge transport theory

The bipolar charge transport theory assumes that there are two kinds of charge carriers transporting within the insulation under high electric fields. This affects the whole charge dynamics process: charge generation, transportation, trapping, and recombination.

The theory assumes charges can be injected from both electrodes through the interface of metal and insulator (Electrons from the cathode and holes from the anode). Schottky injection mechanism is used to describe the process. The injection threshold phenomenon [29, 92] is ignored, due to the applied field strength is significantly larger than the testing materials' threshold. After injection, electrons and holes can drift into the bulk of the insulator towards the opposite electrodes following the distribution of the applied electric stress, forming the conduction current. This current is normally very small, because of insulator's large band gap. However, the localised energy levels will block or assist this conducting process by forming trap centres. It is generally believed that shallow traps, originated by the physical defects, will help the charge carriers to transport within the insulator's wide band gap. This is because both electrons and holes are able to easily detrap from the shallow traps. But for deep traps, which are usually caused by chemical defects, charges trapped are generally considered to be unable to detrap. Therefore, they can prevent the carriers to move further [7,60-62]. The transportation of charge carriers is described using the Ohmic conduction theory. The diffusion process is neglected, to simplify the mathematical treatment. When charges with opposite polarities encounter each other, they will recombine and give out the energy in the form of light (Electroluminescence).

To describe the space charge dynamics in the polyethylene, three essential equations: Gauss's Law, Ohmic's Law, and Continuity equation are adopted. In all these equations, charge carrier's behaviour is described in a function of time and position, which significantly complicates the computing process. The three equations are illustrated below:

Gauss's Law:

$$\frac{\partial E(x,t)}{\partial x} = \frac{\rho(x,t)}{\varepsilon} \qquad \textbf{4-1}$$

Where *E* is the local electric field, Vm^{-1}; ρ is the net charge density, Cm^{-3}; ε is the dielectric permittivity of solids, Fm^{-1}; *x* is distance of the spatial coordinate, m; and *t* is the time, s [104].

Ohmic's Law:

$$J(x,t) = \mu n(x,t)E(x,t) \qquad \textbf{4-2}$$

Where *J* is the conduction current density, Amm^{-2}; μ is the mobility of carriers, m^{2}V^{-1}s^{-1} and *n* is the density of mobile species, Cm^{-3} [104].

Continuity equation:

$$\frac{\partial n(x,t)}{\partial t} + \frac{\partial J(x,t)}{\partial x} = s \qquad \textbf{4-3}$$

And *s* is the source term.

We can solve equation 4-3 by dividing it into two parts :

$$\frac{\partial n(x,t)}{\partial t} + \frac{\partial J(x,t)}{\partial x} = 0 \qquad \textbf{4-4}$$

and

$$\frac{\partial n(x,t)}{\partial t} = s \qquad \textbf{4-5}$$

The equation 4-5 can be solved using the solution of 4-4 [104].

The source term is designed to present the effects of charge recombination and trapping, in consideration of each species (mobile/trapped electrons/holes), and therefore the equation 4-5 should be presented in the following four terms.

$$s_1 = \frac{\partial n_{e\mu}}{\partial t} = -S_1 n_{ht} n_{e\mu} - S_3 n_{hu} n_{e\mu} - B_e n_{e\mu}(1 - \frac{n_{et}}{n_{0et}})$$

$$s_2 = \frac{\partial n_{h\mu}}{\partial t} = -S_2 n_{et} n_{h\mu} - S_3 n_{hu} n_{e\mu} - B_h n_{h\mu}(1 - \frac{n_{ht}}{n_{0ht}})$$

$$s_3 = \frac{\partial n_{et}}{\partial t} = -S_2 n_{h\mu} n_{et} - S_0 n_{ht} n_{et} + B_e n_{e\mu}(1 - \frac{n_{et}}{n_{0et}})$$

$$s_4 = \frac{\partial n_{ht}}{\partial t} = -S_1 n_{ht} n_{e\mu} - S_0 n_{ht} n_{et} + B_h n_{h\mu}\left(1 - \frac{n_{ht}}{n_{0ht}}\right) \qquad \textbf{4-6}$$

where s_1, s_2, s_3, s_4 are the source term for each species; S_0, S_1, S_2, S_3 are the recombination coefficients; B_e, B_h are the trapping coefficients for electrons/holes; $n_{e\mu}$, n_{et}, $n_{h\mu}$, n_{ht} respectively indicate the densities of each species: mobile electrons, trapped electrons, mobile holes and trapped holes; n_{0et} and n_{0ht} are the trap densities for electrons and holes. The relationship of these parameters is illustrated below in Figure 4-1 [104].

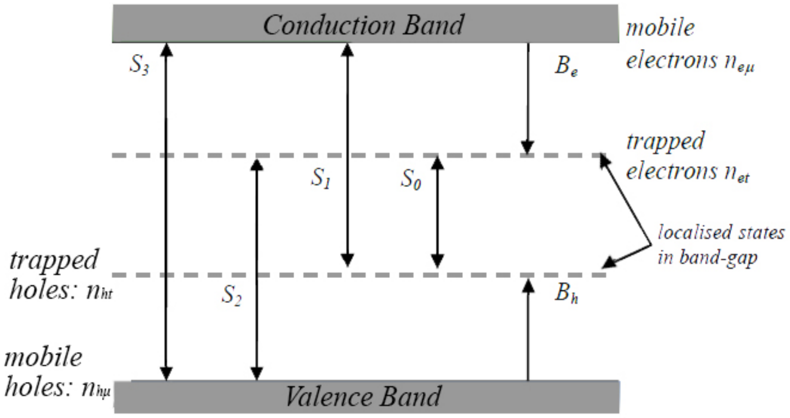

Figure 4-1 Trapping and recombination of bipolar charge carriers [104]

It is assumed that the charge generation mainly results from Schottky injection of the electrodes, the boundary conditions of the current density can be defined as:

$$j_e(0,t) = AT^2 \exp\left(\frac{-ew_{ei}}{k_B T}\right) \exp\left(\frac{e}{k_B T}\sqrt{\frac{eE(0,t)}{4\pi\varepsilon}}\right)$$

$$j_h(d,t) = AT^2 \exp\left(\frac{-ew_{hi}}{k_B T}\right) \exp\left(\frac{e}{k_B T}\sqrt{\frac{eE(d,t)}{4\pi\varepsilon}}\right) \qquad \textbf{4-7}$$

Where $j_e\ (0, t)$ is the current density flux of electrons at the cathode while $j_h\ (d, t)$ is the flux of holes at the anode; T is the temperature; A is the Richardson constant, 1.2×10^6 $\mathrm{Am^{-1}\ K^{-2}}$; and w_{ei}, w_{hi} are the injection barriers for electrons and holes.

The extraction of charge carriers at the electrodes can be obtained using Ohmic's Law. Furthermore, as the diffusion effects are not considered in this work, the extraction fluxes can be expressed as:

$$j_e(d,t) = \mu_e n_{e\mu}(d,t) E(d,t)$$

$$j_h(0,t) = \mu_h n_{h\mu}(0,t) E(0,t) \qquad \textbf{4-8}$$

The total current density $J\ (x, t)$ is obtained from the Maxwell equation as follow:

$$J(x,t) = j(x,t) + \varepsilon \frac{\partial E(x,t)}{\partial t} \qquad \textbf{4-9}$$

where the first item is the conduction current density and the second is the displacement current density.

The total recombination rate can be expressed as:

$$\boldsymbol{TRR = S_0 n_{ht} n_{et} + S_1 n_{ht} n_{e\mu} + S_2 n_{et} n_{h\mu} + S_3 n_{h\mu} n_{e\mu}} \qquad \textbf{4-10}$$

4.2 Numeric modelling of the charge behaviour within polyethylene under various electric fields

Bipolar charge transport theory has been used to analyse space charge within insulation for more than thirty years. The majority of the work contributes to the modelling under HVDC. The accuracy of the model is improved based on the comparison of computed and experimental results. Besides, as for parameters setting for mobility, numerous works used constant mobility for charge carriers to simulate space charge dynamics under HVDC fields [8, 9, 61], which illustrated reasonable results and qualitatively explained the dynamics within insulators under relatively low electric fields (≤30kV/mm). However, when constant mobility is used for simulating space charge dynamics under higher fields (≥30kV/mm), the value of the mobility needs alteration to fit with experimental results well. The errors increase further when the applied HVDC field is too high to form packet-like positive charge movements [91, 97]. Thus, the consideration of the field dependent charge carriers' mobility effects is essential to establish a universal charge transport model under various strengths of electric fields. The solution for this problem becomes more important when building a model to analyse cases under HVAC and other periodical high voltage fields. This is because the magnitude of these fields is continuously changing, which will cause significant error in computing charge dynamics if the constant mobility setting is applied. To overcome this problem, a field dependent mobility is used in the numerical model in this work. The mobility for holes is calculated using the measured velocity results, whilst power's law relationship [53] is used for analysing the mobility of electrons (Specific analysis for building the mobility field dependent model is illustrated in section 4.3.3).

The finite element method is applied for the numerical simulation. The first step is to divide the specimen into certain elements (*m*) according to computing sample thickness (*d*) and decide calculation time step (Δt). Generally, a Courant-Friedrich-Levy (CFL) relation [106] should be satisfied when choosing m and Δt values for specific cases. The CFL relation indicates the charge displacement within Δt should be less than the calculation slice size ($\Delta d = \frac{d}{m}$) [107]. Equal divisions are used for HVDC simulation in this work while the unbalanced divisions (more precisely divided slices near the electrodes) are used in computing HVAC and complex periodical fields' conditions.

This is because the majority of the charges under HVAC and complex periodical fields are accumulated near the electrodes, according to the results in Chapter 3.

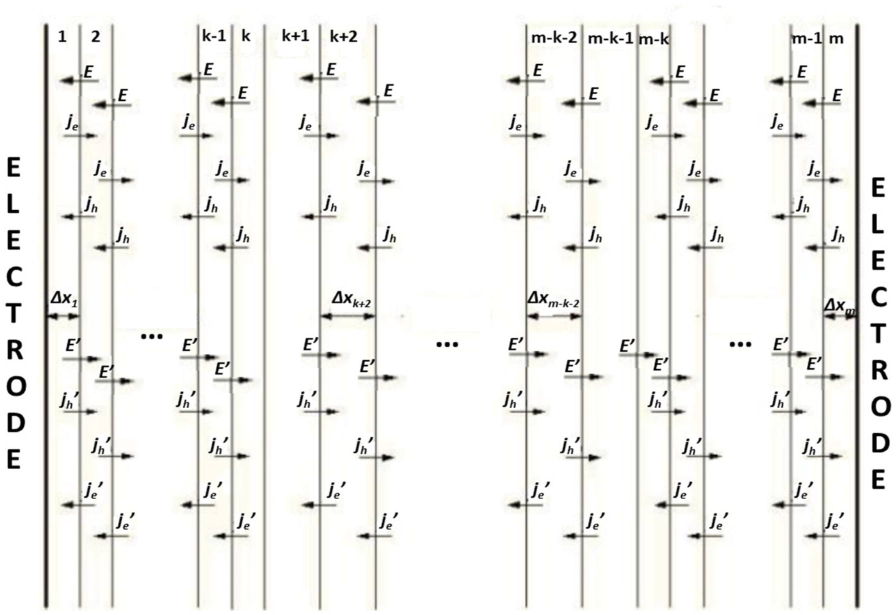

Figure 4-2 Discretion of the specimen under high voltage electric stress

In Figure 4-2, *E* is the local electric field of each element; j_e is the flow of mobile electrons from the k^{th} division into the $k+1^{th}$ division, and j_h is the flow of mobile holes. $E^{'}$, $j_e^{'}$ and $j_h^{'}$ are the field, flow of electrons and flow of holes respectively, when the polarity of the applied field reversed. E, $E^{'}$, j_e, $j_e^{'}$, j_h and $j_h^{'}$ of each element are computed progressively from the 1^{st} division to the m^{th} division at each time step Δt (Δt =0.1s for HVDC while $(100 \cdot f)^{-1}$s for periodical applied fields with a frequency of *f*).

The simulation procedure flow is presented in Figure 4-3. The simulation is implemented using MATLAB coding and PDE (Partial Differential Equation) solvers.

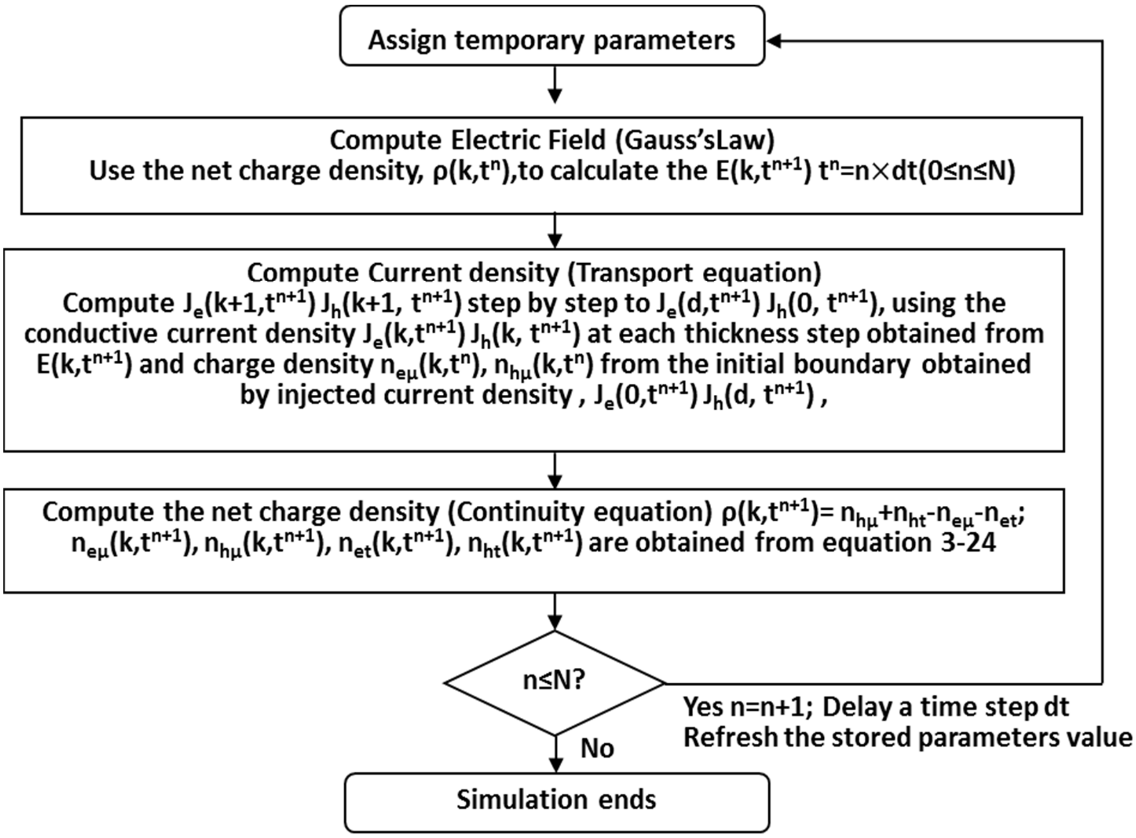

Figure 4-3 Flow chart of space charge simulation, $N = \frac{Simulation\ duration}{Simulation\ time\ step}$.

4.2.1 Numerical modelling under DC electric fields

In section 1.2 and 4.1, the charge transport is specifically described using the conduction process characterised with the mobility of the charge carriers. The mobility of the electrons and holes are computed differently in consideration of their different field dependent characteristics. The mobility of electrons is analysed using the power's law, while for holes, the mobility is obtained from the experimental results of [91] by utilising a curve-fitting procedure as shown in Figure 4-4(a). The specific process is illustrated below:

It is believed that the charge mobility can be obtained from drift velocity using: [91]

$$\mu = v/E \tag{4-11}$$

Then the velocity of electrons using Power-law can be expressed as:

$$v_e = \mu_0 E^{m_1} \tag{4-12}$$

where μ_0 is the low field mobility in LDPE, [108] and m_1 is the power index. The velocity of holes can use curve-fitting results of Figure 4-4(a), getting:

$$\begin{cases} v_h = a_1E + a_2E^2 + a_3E^3(0 < E \le E_c) \\ v_h = bE^{-m_2}(E > E_c) \end{cases} \tag{4-13}$$

Where m_1 is the power index, and E_c is a critical field distinguishing the low and high electric field phenomena for positive charge carriers. In Figure 4-4(a). Its value is 100kV/mm [91, 97].

The velocity of both electrons and holes of this model is presented below in Figure 4-4(b).

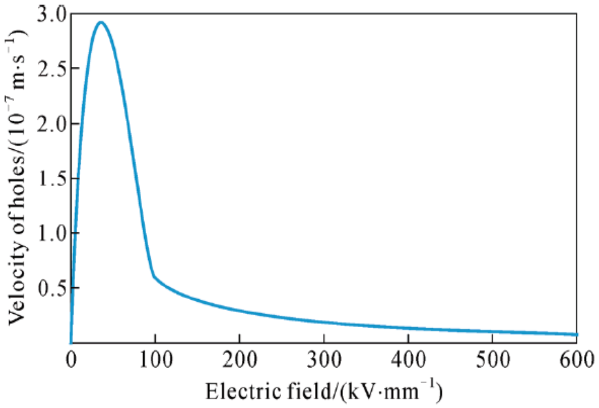

(a) Measured results of Chen

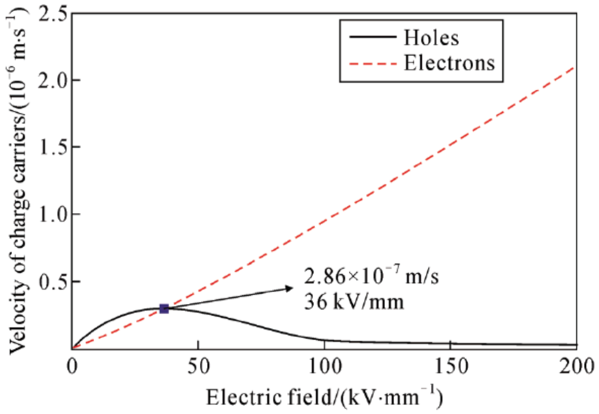

(b) Used velocities of holes and electrons in the simulation

Figure 4-4 Measured holes' velocity versus fields and used velocities versus fields

The final parameters used for charge dynamics simulation under HVDC is presented in Table 4-1. The parameters are selected based on previous simulation work [8, 63, 91], and the specific values of injection barriers, mobility constant and trap coefficients are further determined according to the fitting results with the experimental data The details of obtaining these values are discussed in section 4.4.

Table 4-1 Parameters for charge dynamics under DC electric fields

Parameter	Value	Unit
Barrier height for injection		
W_{ei} (electrons)	1.26	eV
W_{hi} (holes)	1.18	eV
Power-law Mobility (n=1.165**)**		
μ_0 (electrons)	1.095×10^{-14}	$m^2V^{-1}s^{-1}$
Trap density		
N_{0et} (electrons)	100	Cm^{-3}
N_{0ht} (holes)	10	Cm^{-3}
Trapping coefficients		
B_e (electrons)	0.1	s^{-1}
B_h (holes)	0.2	s^{-1}
Recombination coefficients		
S_0 trapped electron-trapped hole	4×10^{-3}	$m^3C^{-1}s^{-1}$
S_1 mobile electron-trapped hole	4×10^{-3}	$m^3C^{-1}s^{-1}$
S_2 trapped electron-mobile hole	4×10^{-3}	$m^3C^{-1}s^{-1}$
S_3 mobile electron-mobile hole	0	$m^3C^{-1}s^{-1}$
Temperature T	300	K

The simulated results using parameters in Table 4-1 for 180mm LDPE under various extents of HVDC fields are presented from Figure 4-5 to Figure 4-7.

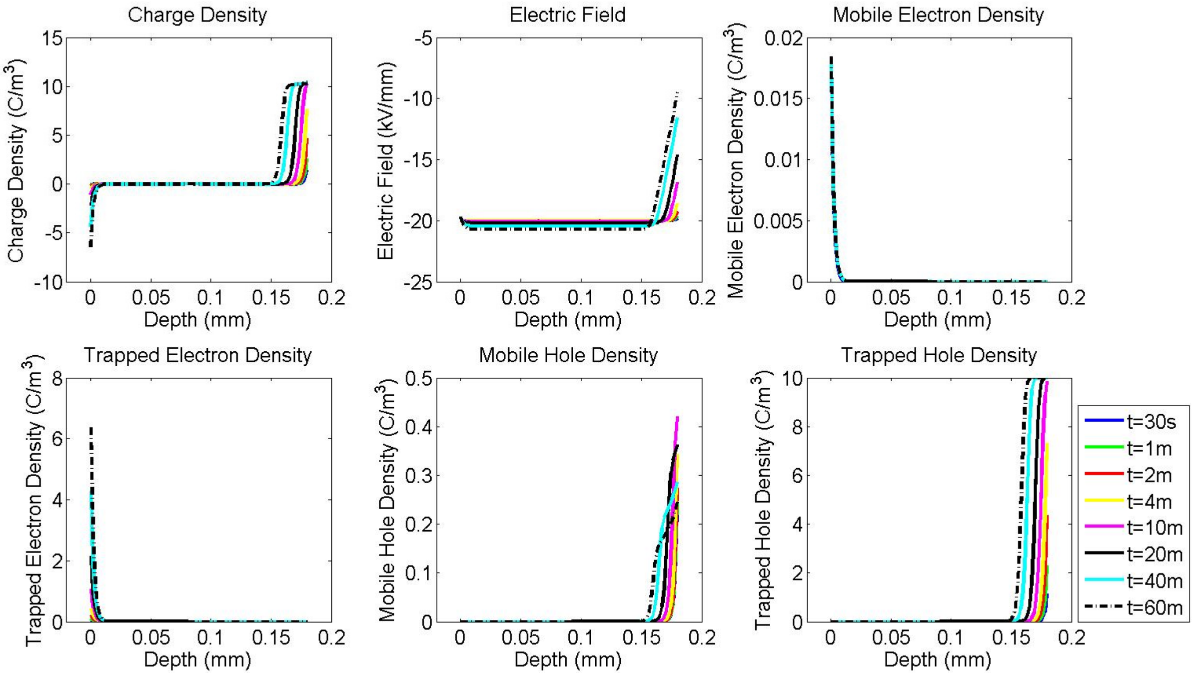

Figure 4-5 Simulated charge and local field distributions of 180mm LDPE under 20kV/mm HVDC fields

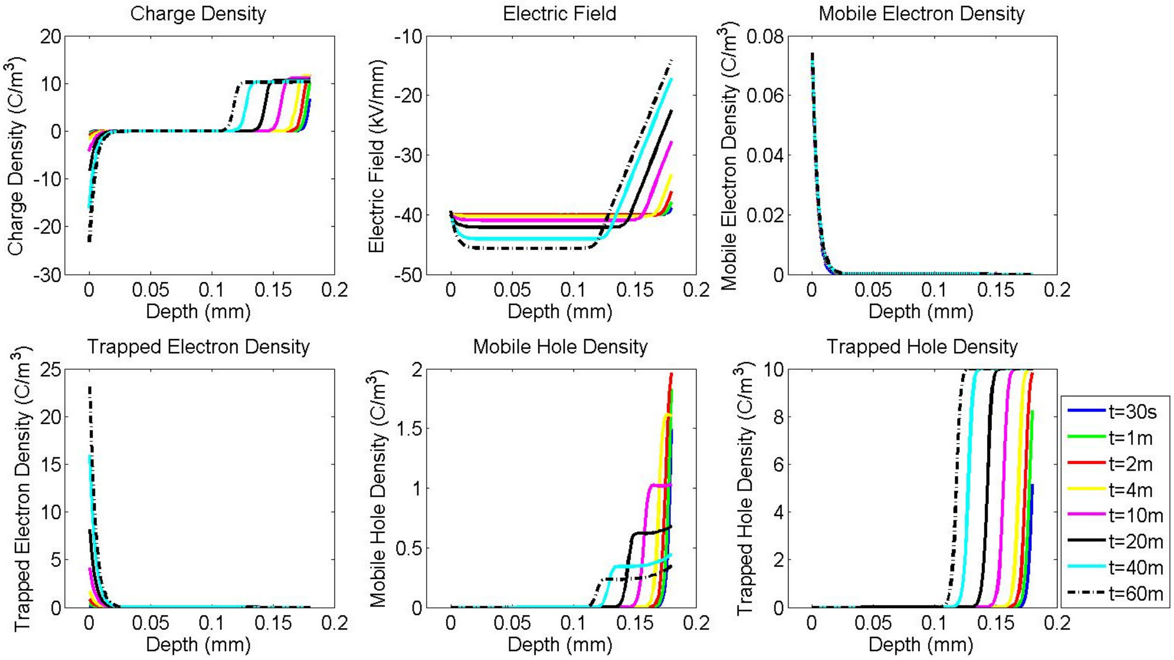

Figure 4-6 Simulated charge and local field distributions of 180mm LDPE under 40kV/mm HVDC field

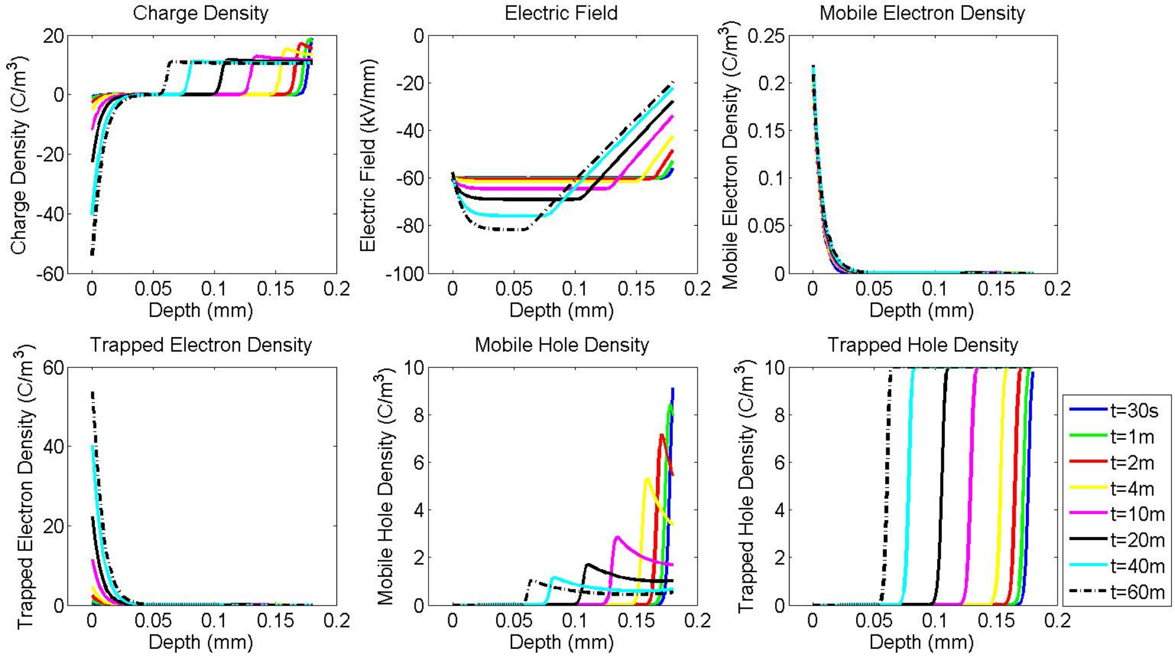

Figure 4-7 Simulated charge and local field distributions of 180mm LDPE under 60kV/mm HVDC field

The simulated results do not contain the capacitive charges caused by the applied stresses. Therefore, the obtained charge density values cannot be compared directly with the measured results. However, both the charge distribution and charge amounts are consistent with the experimental data. Besides, the maximum field distortion deduced from the computed local field distribution in the simulation is also compatible with what observed in experiments (Figure 3-8, Figure 3-10 and Figure 3-12). The specific comparison of the simulated and measured results under the three fields is demonstrated in section 4.3, where a procedure of fitting simulated results with measured ones is presented.

Furthermore, the simulation results can offer additional information explaining the observation in measurements. In measurements, it is observed that under HVDC, the maximum charge density of positive charge keeps almost the same with the increasing of the applied field strengths. That is the main reason causing the positive charge moving like “a packet” under high applied HVDC fields (Figure 3-7, Figure 3-9 and Figure 3-11). From the simulated results under various fields, it is clear that for both positive and negative charges, the percentages of mobile charge amounts are relatively small, which indicates the shape of accumulated charges is mainly contributed by the trapped charges. The simulated “packet-like” positive charge profiles indicate the less amount of positive charges traps and negative differential mobility are the main reason for the limited maximum density for the positive charges and their “packet-like” movements when the applied DC field is enhanced.

4.2.2 Numerical modelling under AC and other periodical complex electric fields

In 2010, Zhao et al. published a paper on the space charge simulation under AC electric fields using the bipolar charge transport theory [109]. In this work, a similar numerical model is applied to simulate the conditions under the HVAC and periodical superimposed AC and DC fields. The core computing mechanism is identical to the case under HVDC fields. The mobility for electrons is using power’s law to fit, while the mobility for holes is using a curve-fitted function of the measured velocity results (Specifics process is demonstrated in section 4.2.1 and Figure 4-4). However, the strategy of element division for AC and DC electric stresses are different in consideration of charge dynamics nature caused by various applied voltage types. For AC conditions, the charges are primarily accumulated close to the surface due to constant alteration of the polarity of the electric fields, which requires higher precision to ensure accuracy.

The parameters used in under the periodical fields are presented in Table 4-2. The parameters are chosen consulting the previous work of numerical modelling (Zhao et al. [109] and Murakami et al. [110]) and the measured charge profiles presented in Chapter 3. The application of asymmetrical parameters demonstrates the different characteristics of electrons and holes. Similar to the DC optimised parameter values, the holes are assumed to be more easily injected into the materials, compared to electrons. For example, the lower injection barrier heights are applied, in considering observations in the literature [109] that applied combined AC and DC electric stresses can lower electrical injection barriers of insulating materials. Trap density and trapping coefficients are defined in a different order of magnitude to illustrate the holes' pocket moving effects [91].

Table 4-2 Parameters for charge dynamics under AC and combined AC and DC fields [109, 110]

Parameter	Value	Unit
Barrier height for injection		
W_{ei} (electrons)	1.18	eV
W_{hi} (holes)	1.16	eV
Low field Mobility: μ_0	4.5×10^{-16}	$m^2V^{-1}s^{-1}$
Power law's index of mobility: n	1.165	$m^2V^{-1}s^{-1}$
Trap density		
N_{0et} (electrons)	100	Cm^{-3}
N_{0ht} (holes)	10	Cm^{-3}
Trapping coefficients		
B_e (electrons)	7×10^{-3}	s^{-1}
B_h (holes)	7×10^{-5}	s^{-1}
Recombination coefficients		
S_0 trapped electron-trapped hole	4×10^{-3}	$m^3C^{-1}s^{-1}$
S_1 mobile electron-trapped hole	4×10^{-3}	$m^3C^{-1}s^{-1}$
S_2 trapped electron-mobile hole	4×10^{-3}	$m^3C^{-1}s^{-1}$
S_3 mobile electron-mobile hole	0	$m^3C^{-1}s^{-1}$
Temperature T	300	K

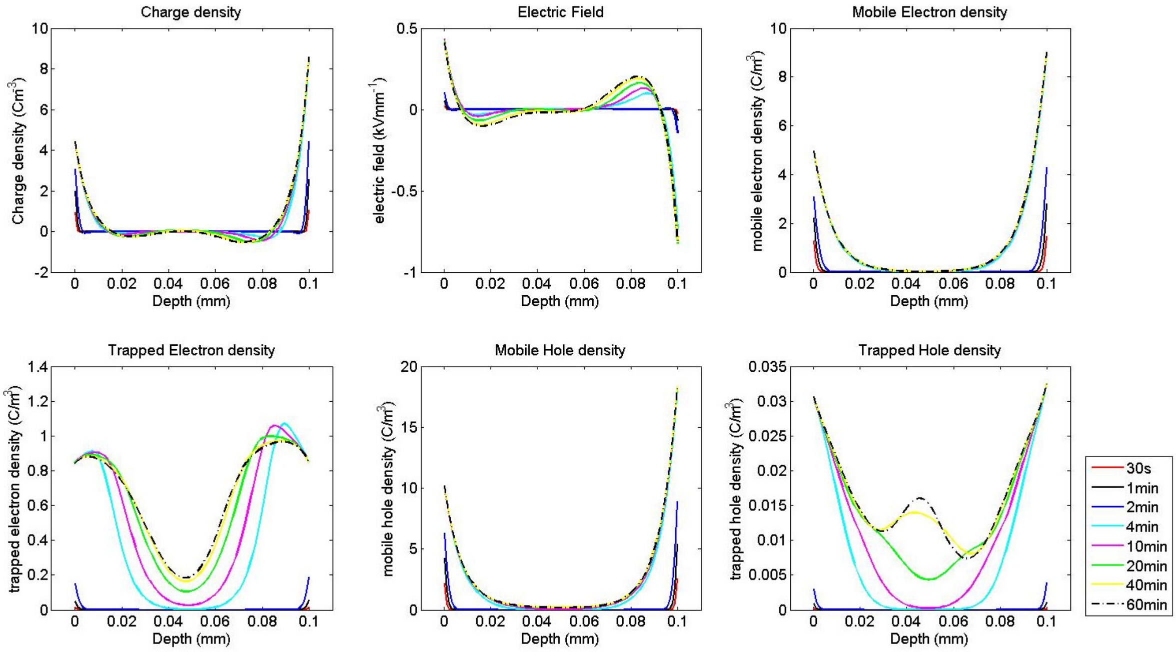

Figure 4-8 Simulated dynamics within LDPE under 50Hz, 50kV/mm HVAC (phase 0)

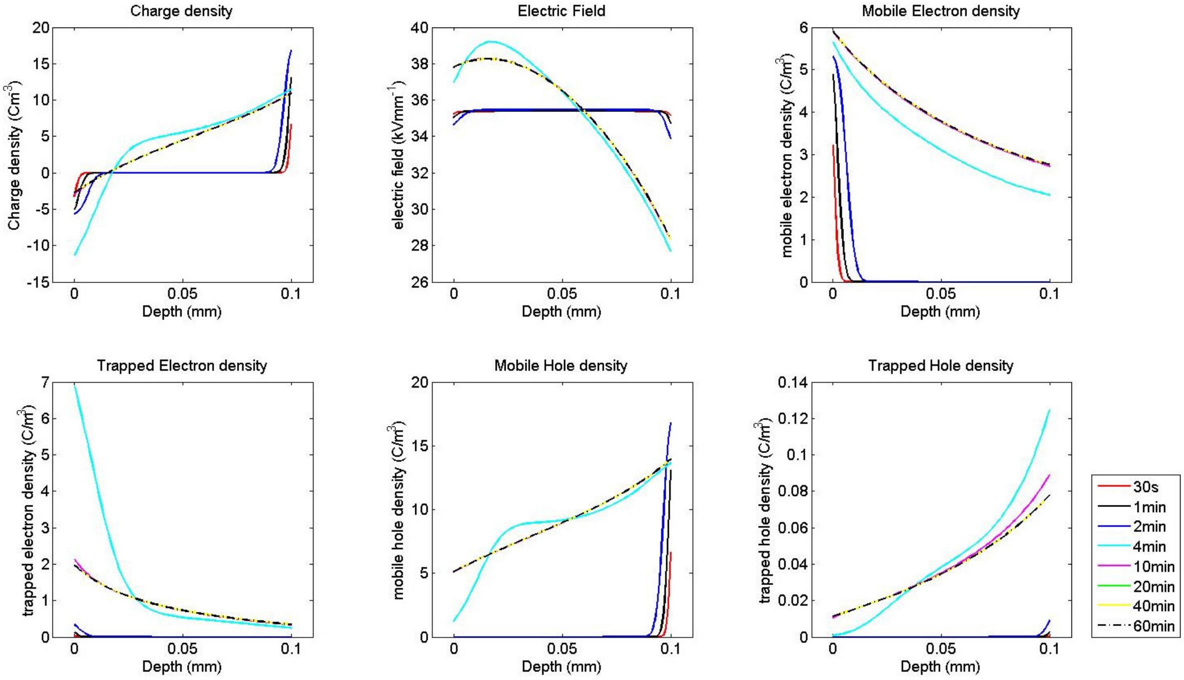

Figure 4-9 Simulated charge dynamics within LDPE under 50Hz, 50kV/mm superposed HVAC and HVDC field with DC offset ratio 0.5 (phase 0)

For simulation of charge dynamics under HVAC and combined electric fields, numerical factors caused by the characteristics of the applied fields can influence the charge dynamics within the insulation. For applied HVAC electric fields, both the frequency and fields' magnitudes can affect the charge dynamics within LDPE. As for the combined conditions, the composition of the superposed fields can act as a third factor influencing charge dynamics. All these factors complicate the analysis of the simulation results under the periodical complex electric fields. However, in this chapter, the main concern is illustrating the numerical model used in the work. Thus, two typical simulated results (HVAC in Figure 4-8, superimposed fields in Figure 4-9) are presented and discussed. The specific analysis of the influences of factors within periodical electric fields on charge dynamics within LDPE is illustrated and discussed in Chapter 5.

Comparing the simulated results (Figure 4-8) with measured data (Figure3-16 to Figure 3-18), it is clear that the simulated charge dynamics under HVAC can correctly demonstrate the different dynamics of holes and electrons. The majority of the accumulated charges is mobile rather than trapped. Furthermore, the significant field distortion caused by the accumulated charge adjacent to electrodes can be observed in both measurements and simulations. As for the superimposed condition, the influences of the DC offsets are clearly demonstrated in the simulation. Stable charge formation and transportation caused by the additional DC offsets can be clearly observed. The impacts of AC component within the applied field towards the charge dynamics can hardly be observed under large DC offset ratio (0.5) case. However, the mobile charges still occupy a significant percentage in the overall accumulated charges like cases under pure HVAC fields. Also, from both the simulated and measured results, it is clear that the additional DC offsets can significantly increase the accumulated charge amounts and accelerate the charge transportation.

According to the discussion, the present model is reasonable in qualitatively analysing charge dynamics under HVAC and superimposed conditions, although the specific values of the computed profiles still present some differences when comparing with the measured ones. Those differences may because the simulation has not considered the injection thresholds phenomenon [29, 92] and charges are therefore consistently injected from the interface between the electrodes and insulation. Besides, the mobility calculation model in the simulation may involve some errors for the cases when the applied electric field is lower than the injection thresholds, which can further enlarge the differences. Therefore, the numerical model proposed here for periodical complex electric fields can be considered as an initial qualitative analysis model and requires further adjustments with the development of space charge detect techniques.

4.3 Fitting simulated results with experimental data

One of the essential factors evaluating the performance of simulation models is to compare the simulated results with measured ones. In Chapter 3, a subtraction method is proposed to obtain the trapped charges within LDPE, aiming to be compared with simulated results. However, the subtracted results are the convolution results of trapped charge density distributions with a Gaussian filter due to the non-ideal reality of the measuring pulse in the PEA system. Besides, the subtracted results can sometimes contain certain unexpected errors, as the references are linear magnified and used as subtrahend, which at the same time, causing the noise levels within the results are magnified. Due to all these above reasons, it is clear that the subtraction method is not suitable for high accuracy quantitative comparison of the simulated and measured results. Therefore, in this section, another method is proposed to fit the simulated results comparable to the measured ones and to evaluate the simulated results quantitatively. Eventually, an optimised simulation parameter setting for computing charge dynamics within LDPE under HVDC fields is obtained.

4.3.1 Methodology of the fitting procedure

Space charge profiles obtained by the PEA method are influenced by the system responses, e.g., the effects of the excitation pulse, the bandwidth of the piezoelectric sensor, the amplifier, and the oscilloscope. Therefore, capacitive charges measured within a perfect insulator under applied field appear as Gaussian peak curves.

On the other hand, the simulation is only computing internal localised charges. The results do not include the capacitive charges at the electrodes caused by the applied field and induced charge on the electrodes caused by the space charge in bulk. In this way, it is essential to figure out the surface charge densities to construct overall charge profiles comparable to the measured results. The surface charge at the electrodes can be calculated using [33]:

$$\boldsymbol{\rho_{cath}} = -\frac{\mathbf{1}}{\boldsymbol{dx}}\int_{\mathbf{0}}^{\boldsymbol{d}} \frac{\boldsymbol{d-x}}{\boldsymbol{d}}\boldsymbol{\rho(x,t)\partial x} - \frac{\boldsymbol{\varepsilon_0 \varepsilon_r V}}{\boldsymbol{dx \cdot d}}$$

$$\boldsymbol{\rho_{anod}} = -\frac{\mathbf{1}}{\boldsymbol{dx}}\int_{\mathbf{0}}^{\boldsymbol{d}} \frac{\boldsymbol{x}}{\boldsymbol{d}}\boldsymbol{\rho(x,t)\partial x} + \frac{\boldsymbol{\varepsilon_0 \varepsilon_r V}}{\boldsymbol{dx \cdot d}} \tag{4-14}$$

where the first term on the right is the induced charge density on the electrode. The second is the capacitive charge density. *dx* is the discrete element size; *d* is the thickness of polyethylene film; *ρ(x,t)* is the charge density in the bulk of polyethylene; ε_0 is the permittivity of free space; ε_r is the relative permittivity of polyethylene; *V* is the applied voltage.

As it is not practical to correct the position of charges in experimental data, a numerical filter is applied to the simulated data aiming to lose parts of the resolution. This was achieved by convoluting the simulated data with a Gaussian filter. The numerical filter is applied to both electrodes and internal charges and then combining them to generate a charge profile comprising both simulated space charge and induced surface charge.

Furthermore, electrons and holes have different properties in charge injection and transportation. Consequently, asymmetric parameters for electrons and holes are employed in the simulation to improve the fitting of the measured space charge dynamics in polyethylene under dc electric fields. For a particular applied field, constant mobilities are applied to holes and electrons respectively. Those two constant mobilities, which will not vary with the local electric field, represent the “apparent” mobilities under the certain magnitude of the applied field. Different “apparent” mobilities will be obtained under different applied field magnitudes, by the optimised fittings with experimental data. By doing this, the trend of the “apparent” mobility against the applied field magnitudes can be acquired. An example of the procedure of the optimised fitting by the comparisons of computed results with experimental data is presented in Figure 4-10, and Figure 4-11. The parameters adjusted are injection barriers for holes and electrons. In Figure 4-10 and Figure 4-11, ‘*E*’ represents the injection barrier for electrons, while ‘*H*’ indicates the injection barrier for holes and the units for these two barriers are eV.

In Figure 4-10, the 20kV/mm DC experiment data is compared within a group of simulated results with various injection barriers of charge carriers. The differences among all the results are limited (Errors around 10%). This is because the duration of the applied stress is very short, which causes very few charge accumulation within the insulation. Therefore, the adjustments of the parameters in the simulation should be determined based on the comparison of simulated results and experimental results with longer applied field's duration.

From Figure 4-11, it is clear that when the field stressing time comes to 60 minutes, the differences among various injection barriers' results are noticeable. It is clear the symmetric parameters (used in numerical simulation work [7-9]) for injection barriers (1.2eV for both electrons and holes) results in a lower amount of holes injection and a higher amount of electrons compared with experimental results. Therefore, the injection barrier for electrons is raised, and for holes, it is lowered for optimising simulation parameters. The optimised injection barriers for simulation are 1.255 for electrons and 1.18 for holes based on the comparison of simulated results with measured ones (Figure 4-11).

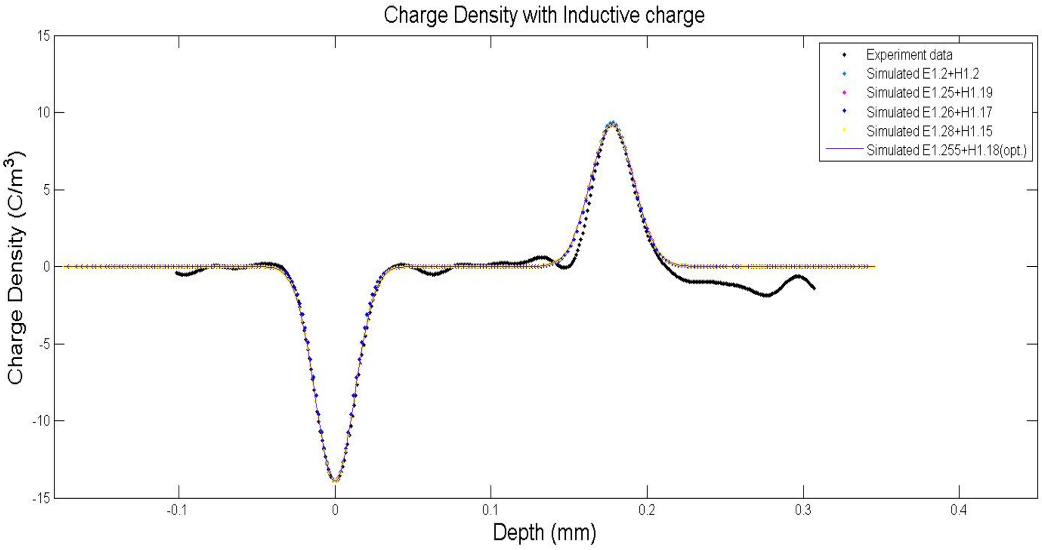

Figure 4-10 Curve matching results at 30s for LDPE under 20kV/mm DC fields

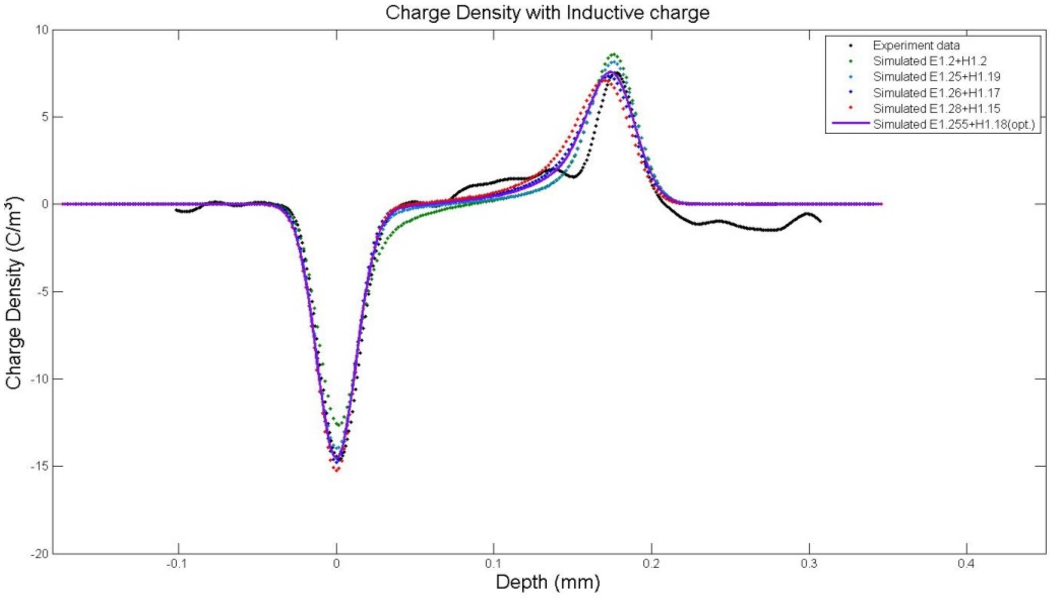

Figure 4-11 Curve matching results at 60min for LDPE under 20kV/mm DC fields

Moreover, when the number of variable parameters is more than 2, the optimisation of the fitting process becomes much more complicated. A multiple parameters optimisation program is developed to solve the problem. This program can find the optimised parameters to achieve the minimal differences between the simulation and experimental results by continuously enumerating the parameters in their variable ranges (proposed by Alison [7]) and saving those results within 10% difference compared with the experimental data. The final fitted simulation results are subtracted from the measured results to demonstrate the differences between them, as Figure 4-12 "Errors" line indicates.

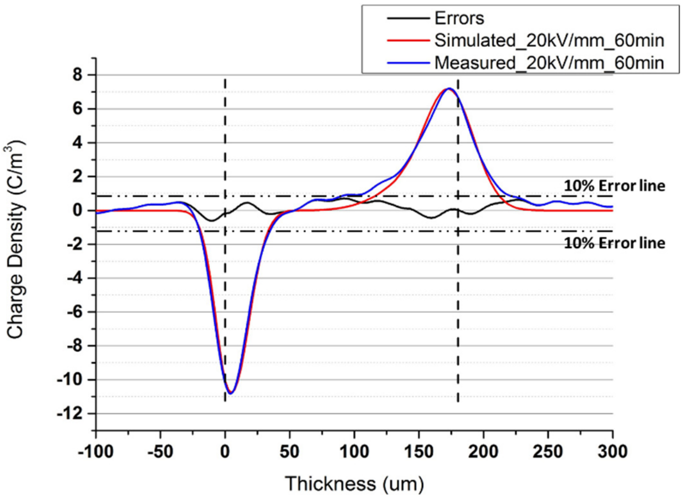

Figure 4-12 Differences of the simulated and measured results after 60mins 20kV/mm DC fields

4.3.2 Optimised fitting results under various magnitudes of HVDC fields

The final optimised parameter values for charge dynamics under various magnitudes of HVDC fields are demonstrated in Table 4-3. The differences between the simulated and measured results under different applied fields are demonstrated in Figure 4-13, to evaluate the optimisation under various circumstances.

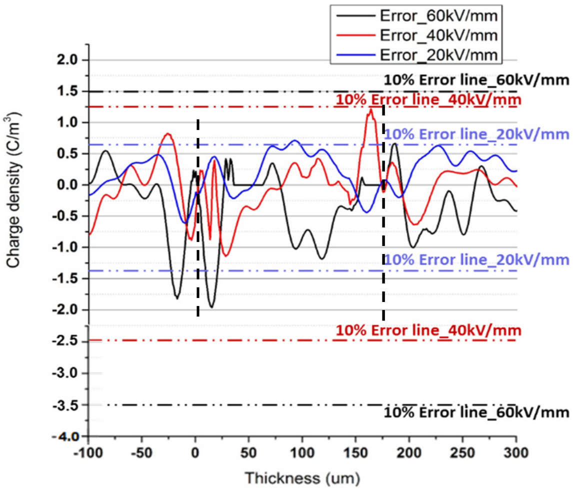

Figure 4-13 Differences between the simulated and measured results under various extends of external fields

Table 4-3 Fitted parameters for dc space charge simulation with a constant mobility

DC electric stress **Parameter**	**20kV/mm**	**40kV/mm**	**50kV/mm**	**60kV/mm**	**80kV/mm**
Barrier height for injection					
w_{ei} (electrons) /eV			1.26		
w_{hi} (holes) /eV			1.18		
Mobility					
μ_e (electrons)/ $m^2V^{-1}s^{-1}$	6.5×10^{-15}	7.8×10^{-15}	8.3×10^{-15}	8.6×10^{-15}	9.1×10^{-15}
μ_h (holes)/ $m^2V^{-1}s^{-1}$	1.2×10^{-14}	7.5×10^{-15}	5.3×10^{-15}	3.7×10^{-15}	1.7×10^{-15}
Trap density					
N_{0et} (electrons) / Cm^{-3}			100		
N_{0ht} (holes) / Cm^{-3}			100		
Trapping coefficients					
B_e (electrons)	0.025		0.05	0.1	
B_h (holes)	0.05		0.1	0.2	
Recombination coefficients					
S_0 trapped electron-trapped hole			4×10^{-3} $m^3C^{-1}s^{-1}$		
S_1 mobile electron-trapped hole			4×10^{-3} $m^3C^{-1}s^{-1}$		
S_2 trapped electron-mobile hole			4×10^{-3} $m^3C^{-1}s^{-1}$		
S_3 mobile electron-mobile hole			0		
Temperature T/K			300		

In Figure 4-13, it is clear that the severe difference between the simulated results and the measured ones occurs near the electrodes. The overall differences are within 10% of the maximum measured charge density under cases (as marked in Figure 4-13). Moreover, the differences increase slightly with the increased applied field magnitudes, due to the larger accumulated charge amounts under higher electric fields. The specific fitting results of charge dynamics under 40kV/mm and 60kV/mm fields are attached in Appendix C.

4.3.3 Effect of field dependent mobility and an embellished simulation model for space charge under HVDC field

From the fitting results in 4.3.2, it can be found that the constant mobility used in the previous work [6-9] of modelling is not accurate for describing charge transport under relatively high HVDC fields. In Table 4-3, the optimised charge carriers' average mobility for the three electric stresses is distinct, showing a strong field-dependence effect of the mobility. Therefore, in this part, three types of field-dependent carrier mobility, Hopping, Power-law, and Poole-Frenkel, have been used to analyse and an improved field-dependent mobility model for space charge simulation under HVDC fields has been proposed.

Hopping mobility

Hopping mobility model describes the transport of electrons or holes within the insulations, which can hop between the trap sites localised in the band gap, and even into the conduction or valence band of polymers. The mobility of the carriers caused by the hopping effect can be expressed as [11]:

$$\mu = \frac{2va}{E} exp(-\frac{w}{k_B T}) sinh(\frac{qEa}{2k_B T}) \qquad \textbf{4-15}$$

where *v* is the attempt-to-escape frequency; *a* is the separation distance between trap sites; *w* is the energy level of trap depth; *E* is the local electric field; *q* is the electronic charge; k_B is the Boltzmann constant and *T* is the temperature.

Power-law mobility

Power-law mobility model is a mathematical analysis method, which describes the mobility of carriers as a power function of the electric field, [11]

$$\mu = \mu_0 E^{n-1} \qquad 4\text{-}16$$

where μ_0 is the mobility at low electric field [108]; *n* is the power index, and *E* is the local electric field.

Poole-Frenkel mobility

In the Poole-Frenkel mobility model, the mobility can be computed as [11]:

$$\mu = \mu_0 exp(\sqrt{\frac{q^3 E}{4\pi k_B^2 T^2 \varepsilon_0 \varepsilon_r}}) \qquad \textbf{4-17}$$

where μ_0 is the zero-field mobility [111]; *e* is the electronic charge; ε_0 is the permittivity of free space; ε_r is the relative permittivity of dielectrics; k_B is the Boltzmann constant and *T* is the temperature.

The overall mobility field dependent effects of the three models are illustrated in Figure 4-14. The processes of mobility vary with the electric field, described in the above three models and the experimental fitting results of mobility are presented below in Figure 4-15.

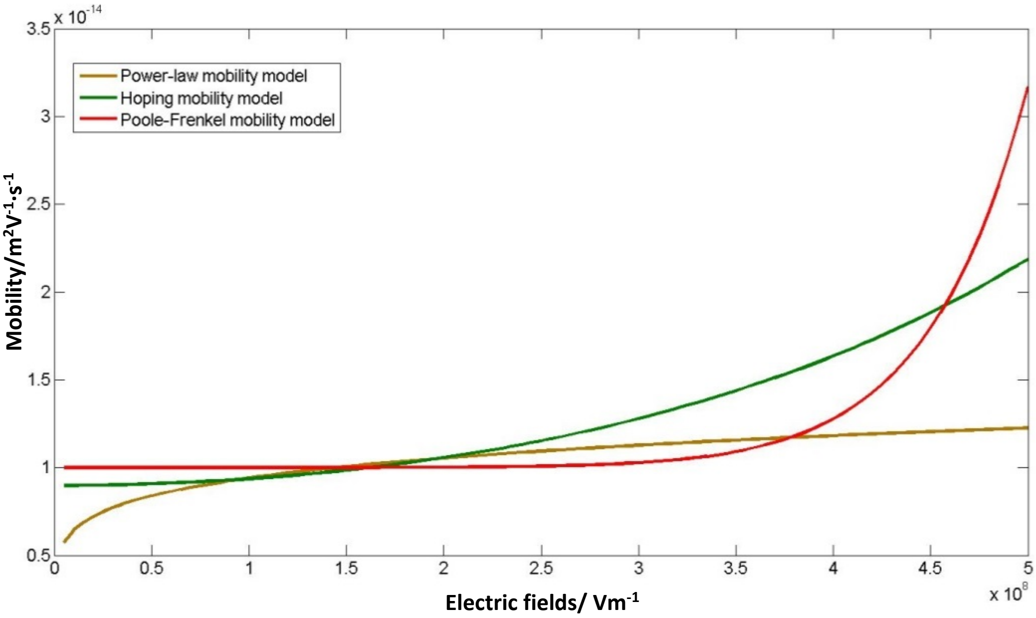

Figure 4-14 Mobility field dependent effects comparison of the three models

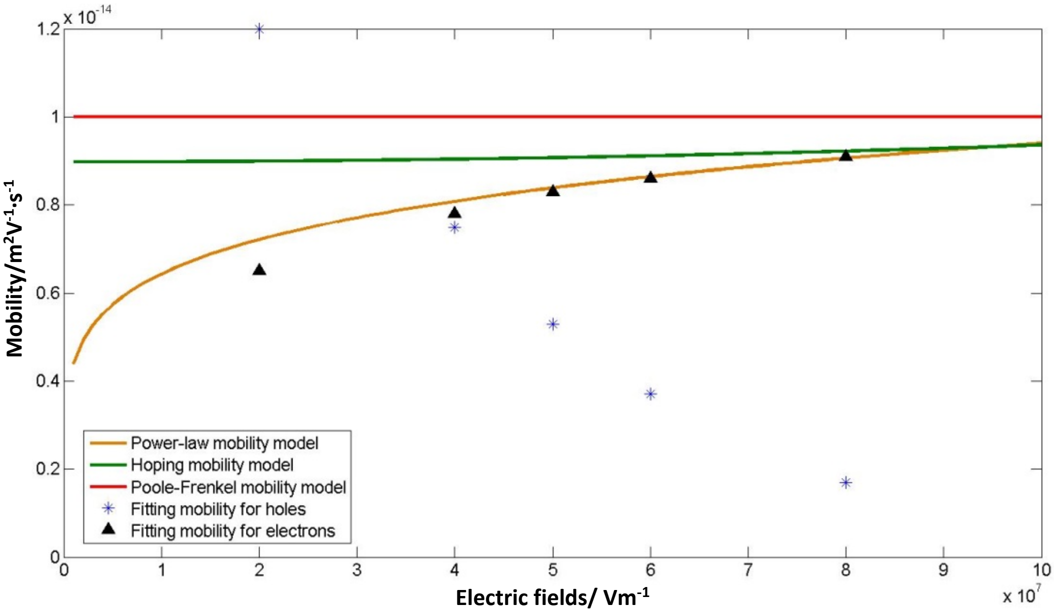

Figure 4-15 Mobility field dependant phenomena comparison among different model

From Figure 4-15, it is clear that the power-law is better at predicting the electron's mobility under various electric stresses, although the Poole-Frenkel mobility demonstrates strong field dependence at high electric fields. However, as for holes, it seems none of these models are suitable for prediction of mobility. This is because the transportation process of positive charge carriers is more complicated than the electrons. Holes' mobility through the amorphous phase (Polyethylene contains numerous amorphous regions) generally exhibit a maximum as a function of the electric field due to super-exchange quantum mechanical tunnelling [112]. Consequently, substituted methods are generally used to deduce the positive charge mobility under various strength fields.

In 2005, Poplavskyy [113] proposed a result of measured velocity of positive charges altering along with the electric field (≤100 kV/mm), and Chen et al. in 2011 [97] completed the high electric field part. The whole picture of positive charge velocity versus the electric field has already shown in Figure 4-4(a), and the measured results are curve fitted to obtain a function predicting the positive charge mobility as a function of the electric fields.

4.3.4 Evaluation of final adopted model

The final adopted parameters for simulation model under DC, AC and superposed AC and DC fields are presented in Table 4-1 and Table 4-2. To evaluate the model for various conditions, the maximum numerical differences under various cases are recorded below in Table 4-3. Simulated charge distributions after 1 hour of field stressing are used in comparison with the measured results to reduce the depreciation effects caused by the intensive AC fields in measurements. From Table 4-3, it is clear that the current model can relatively accurate predict the charge distributions under DC fields. However, for cases under AC and superposed AC and DC fields, remarkable numerical differences still exists. This may due to ignorance of charge injection threshold phenomenon. The current mobility calculation model also can contribute to the errors, as it is relatively inaccurate in deducing charge mobility under electric fields lower than 20kV/mm. After all, the proposed model can still quantitative-accurately illustrate the charge dynamics under AC and superposed AC and DC fields, as the simulated charge dynamics trends are identical to that observed in the experiment. Therefore, the numerical model is further adopted in Chapter 5 and 6 to investigate the physics behind the experimental observations.

Table 4-4 Comparison of simulation and experimental results

Maximum differences	**20kV/mm**	**40kV/mm**	**60kV/mm]**
DC	9.9%	9.6%	4.3%
AC	35.5%	37%	46.7%
	DC ratio: 0.2	**DC ratio: 0.4**	**DC ratio: 0.5**
Superposed AC and DC fields (50kV/mm)	21.7%	16.7%	13.8%

4.4 Conclusions

In conclusion, a bipolar charge transport simulation model, which can be applied to analyse charge dynamics within solid dielectrics under common operating electric fields, is proposed in this Chapter. The specific settings for this model under various categories of periodical electric fields

(DC, AC and combined AC and DC) are described and explained. A mechanism adapting the simulated results directly comparable to the measured results is proposed, A group of optimised parameters for simulation according to the measured results under HVDC is obtained. The charge carriers' different dynamics and the fields' dependent effects of those dynamics are illustrated and discussed.

From the presented results, it is clear that the numerical model for charge profiles within LDPE under HVDC is quite mature, demonstrating remarkable affinity when compared with the measured results.

The model can also correctly predict the trends of charge dynamics under HVAC and superimposed AC and DC fields. The formation of space charge under ac fields is complicated by the frequent reversal of the applied field, which leads to small quantities of charge accumulation compared to the dc case. However, it seems the current simulation underestimated the accumulated charge amounts under AC fields. The computed specific values still present notable quantity differences when comparing with measured results in Chapter 3. However, the differences will not affect qualitatively predicting and analysing the charge dynamics and local field trends within LDPE. In this way, this model is still adopted in the following Chapters, investigating the charge dynamics under specific operating conditions.

Chapter 5: Space charge dynamics under complex stresses

According to the discussion of previous Chapters, it is noticeable that the charge dynamics under complex stresses are complicated and could be influenced by many factors. In this chapter, the influences of the external fields' on charge dynamics within LDPE are investigated using both proposed measuring procedures (Chapter 3) and bipolar simulation model (Chapter 4). The influences of magnitude, the composition of fields and frequency are the three major factors, representing the influences of characteristics of the applied fields on the space charge dynamics.

For the sake of clarity, the results are divided into three sections in this Chapter. Section 5.1 contains the results of 50Hz pure AC stresses with different applied field magnitudes, aiming to demonstrate the field magnitudes' effects on charge dynamics. Section 5.2 describes the results under applied fields with different DC component's percentages, targeting the effects of the DC offsets ratio. Section 5.3 presents charge profiles under applied fields with different frequencies, for the sake of showing the frequency's impacts on charge dynamics within LDPE.

5.1 Dynamics of space charge under different magnitudes of AC stresses

In this section, the influences of field strengths of the applied HVAC have been investigated both experimentally and numerically based on the improved PEA measuring system and the revised simulation model proposed in Chapters 3 and 4. The fast pulse and signal averager within the improved PEA system have enabled the detection and signal processing of charge profiles within insulation under power frequency periodical fields. Additionally, the proposed analysis procedure for the measured data can better demonstrate the mobile and shallow trapped charges. Therefore, charge dynamics under fast alternating applied fields can be better illustrated. As for simulation, the proposed numerical model can successfully analyse charge dynamics under various applied field conditions. Comparing with experiments, simulations can offer more information, such as specific amounts of mobile and trapped charges, and the cases investigated can be more general and widely ranged. Consequently, the numerical model proposed in Chapter 4 is adopted in this chapter to analyse the underlying reasons for the corresponding various charge dynamics caused by different magnitudes of the applied stress.

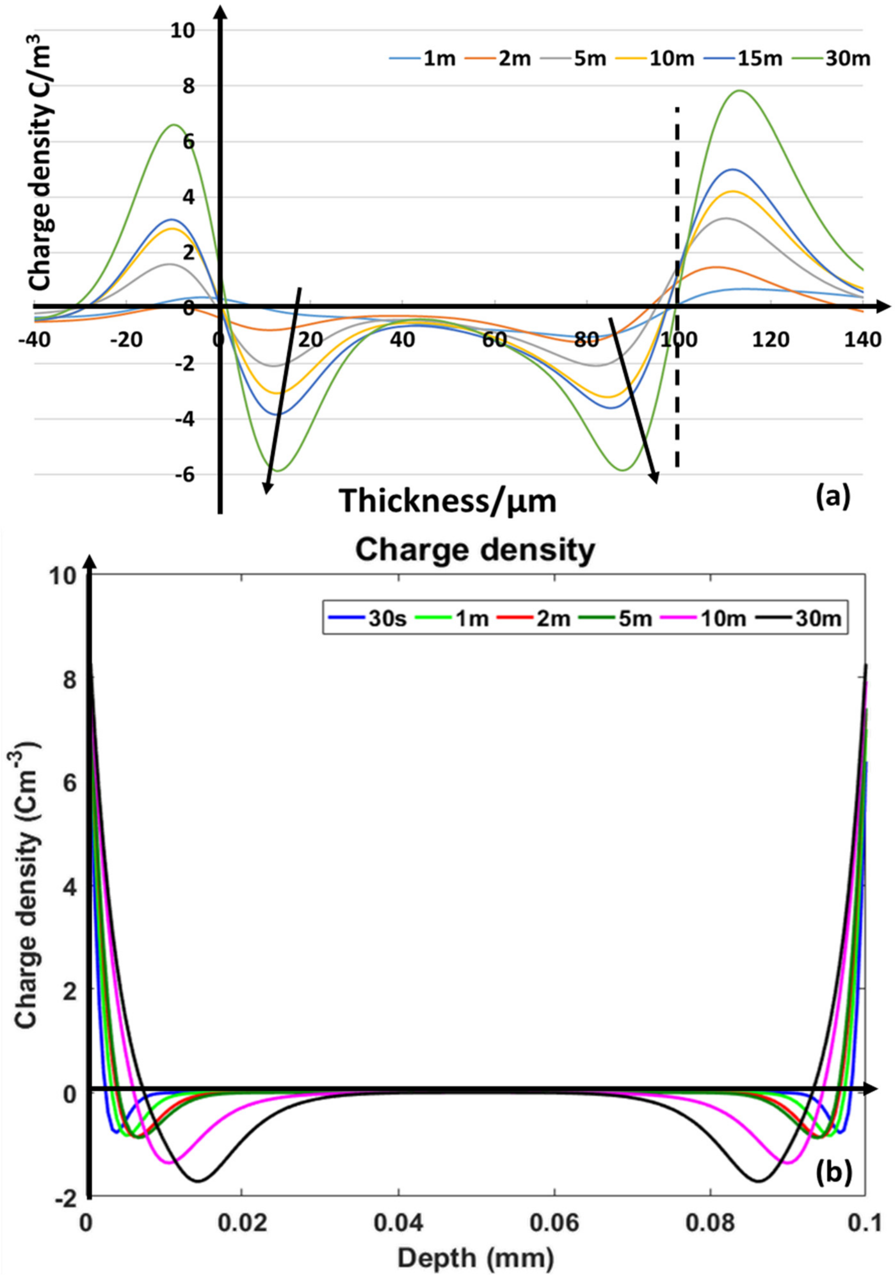

Figure 5-1 Measured Charge evolution after removing the capacitive charge (Applied field phase 90°,graph (a)) and simulated charge profiles (Applied field phase 0°,graph (b)) within initial 30 minutes of ac field stressing (60kV/mm, 50Hz)

Figure 5.1 and Figure 5.2 demonstrate the space charge and local field distribution within the initial 30 minutes of ac field stressing. In order to reduce the influences caused by errors of recovery phases of applied voltage on the charge distribution, charge profiles under the applied voltage around phase 90° at different field stressing times are mainly discussed for the measured results. This is because the magnitude of the applied field changes slightly and slowly around phase 90°, based on the shape of sinusoidal applied fields. However, all simulation results are chosen of profiles at applied phase 0°, to purely demonstrate the space charge influences. 30 minutes is chosen to minimise the ageing effects caused by the high strengths AC fields (The ageing features is discussed explicitly in Section3.3.1).

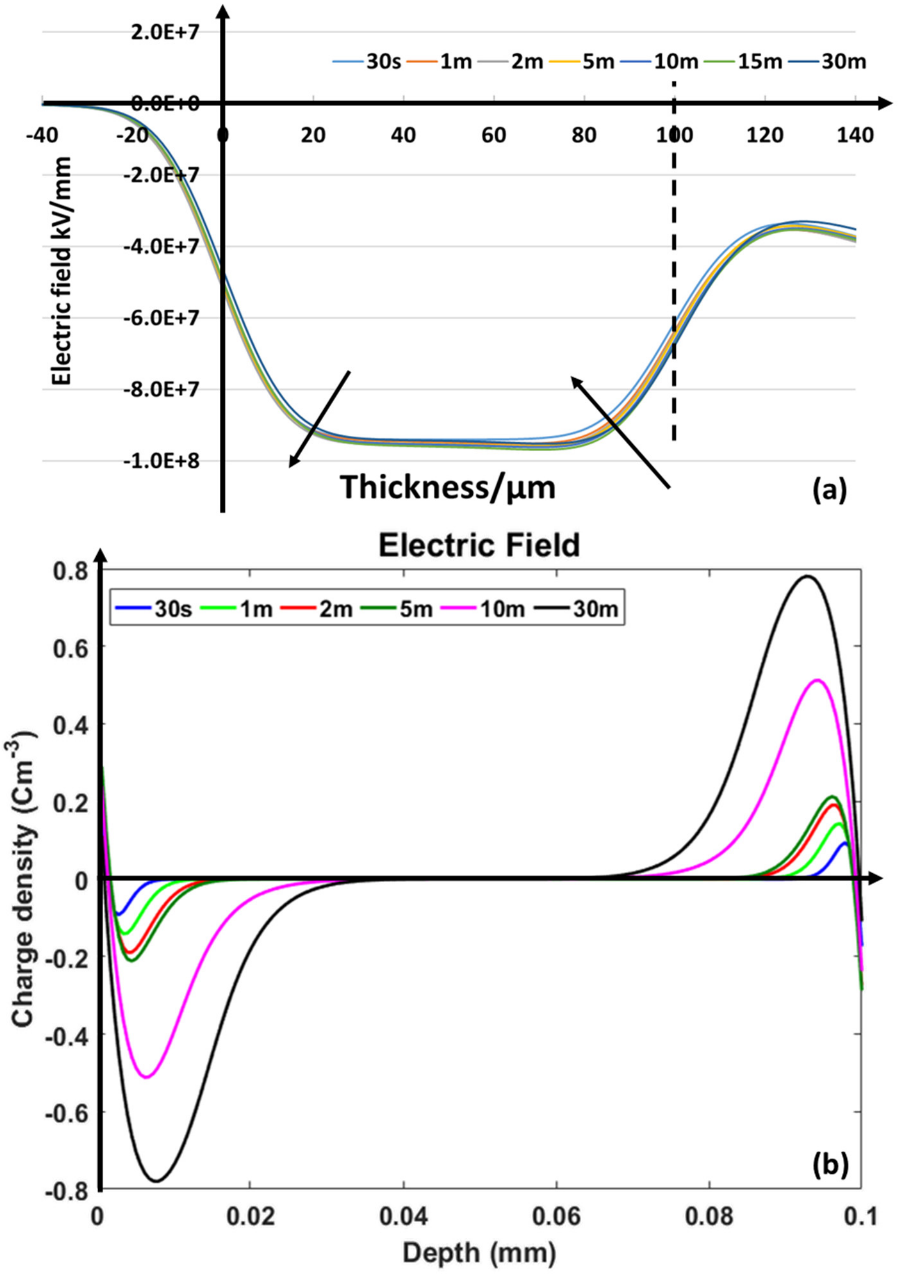

Figure 5-2 Measured (Applied field phase 90°,graph (a)) and simulated (Applied field phase 0°,graph (b)) local field distribution within initial 30 minutes of ac field stressing (60kV/mm, 50Hz)

Both the measurements and simulations demonstrate that the accumulated charge amounts increase along with the stressing time. Negative charges can further transport into the bulk of the sample due to their larger mobility. However, the positive charge adjacent the electrodes, as predicted in simulated profiles can hardly be distinguished from the measured results. This may cause by either the errors of estimating charge carriers' mobility in computing process or the limited resolution of equipment used in measurements. The local field distributions present great similarity in the comparison between the measured and simulated results (The simulated field distributions are only caused by the localised charges.). Maximum changing happens adjacent the electrodes where the charge density is severely changing. From the results, it is clear that the space charge phenomenon is the principal reason of significant local field distortion under HVAC fields.

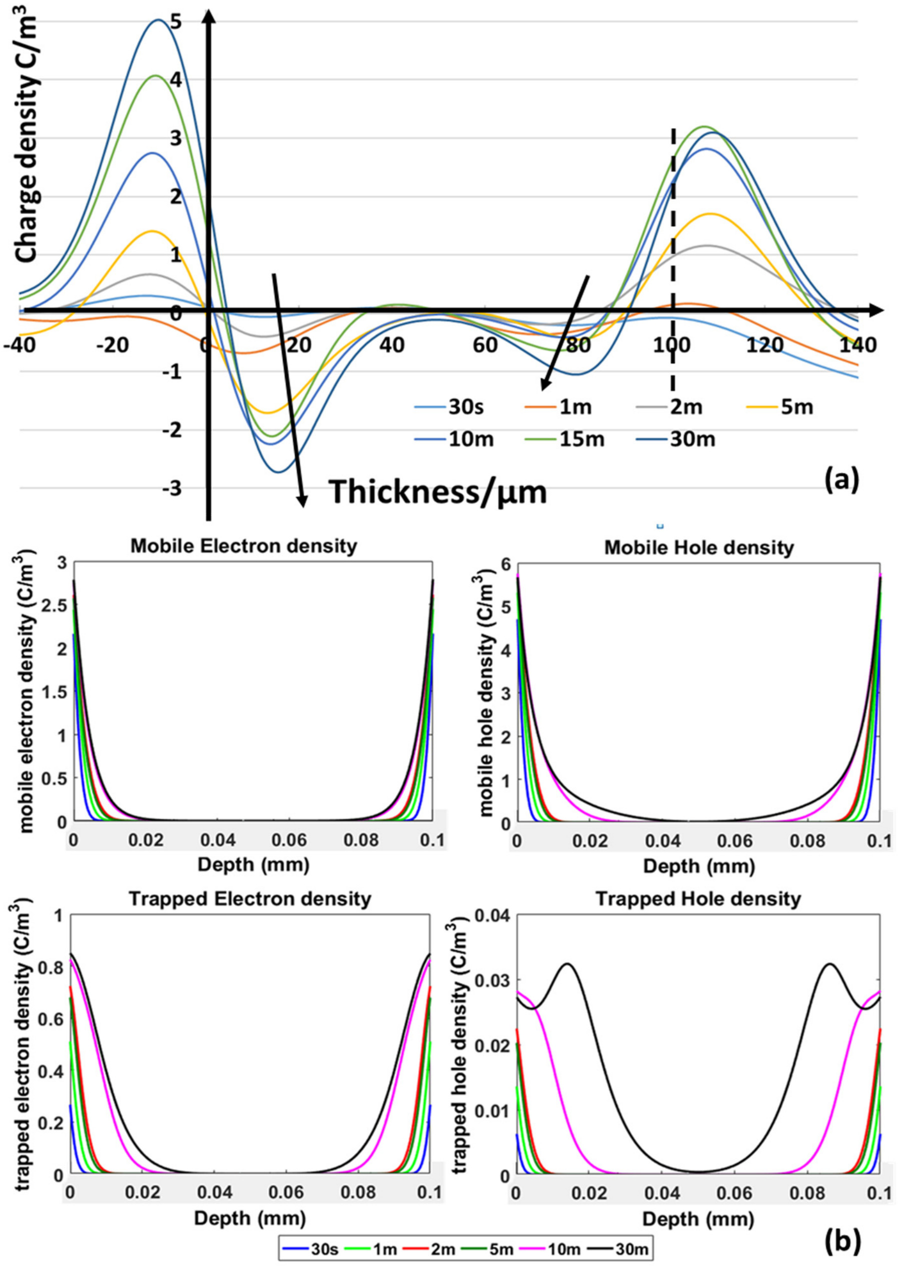

Figure 5-3 Measured charge evolution after removing capacitive charges (Applied field phase 90°,graph (a)) and simulated charge profiles (Applied field phase 0°,graph (b)) within initial 30 minutes of ac field stressing (40kV/mm, 50Hz)

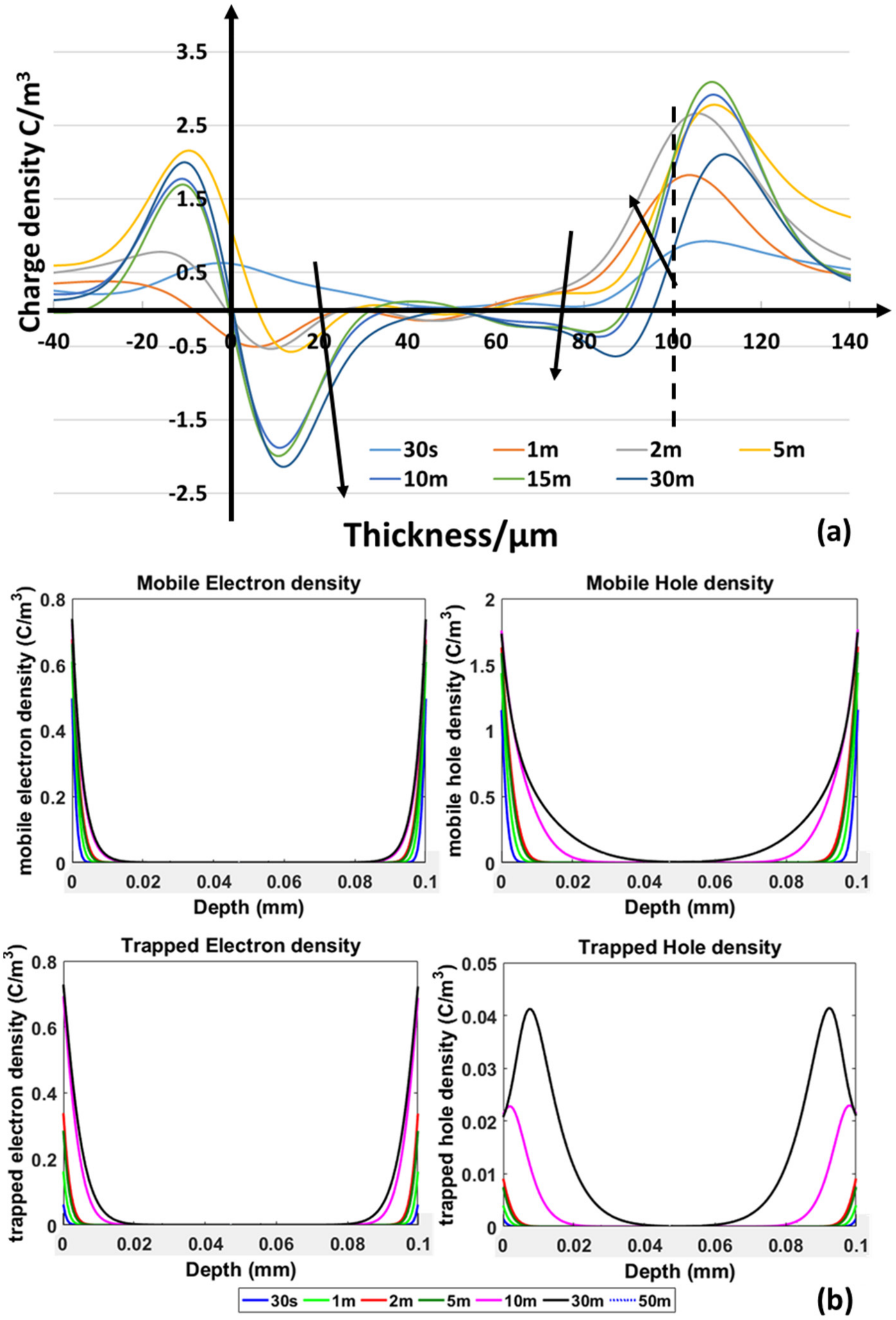

Figure 5-4 Measured charge evolution after removing capacitive charges (Applied field phase 90°,graph (a)) and simulated charge profiles (Applied field phase 0°,graph (b)) within initial 30 minutes of ac field stressing (30kV/mm, 50Hz)

Figure 5-3 and 5-4 present the measured and simulated charge profiles under 40kV/mm and 30kV/mm HVAC fields. Mobile and trapped charges are demonstrated separately in the simulated results. From them, it is clear that the mobile charge amounts are significantly larger than the trapped charges under all applied field cases. Besides, unlike under 60kV/mm fields, specific amounts of positive charges can transport further into the bulking areas of insulation under relatively low field strengths. This existence of positive charges in bulk is further certificated in the decay results after a long-term of field stressing, Figure 5-5, where certain amounts of deep trapped positive charge can be observed in the middle of the testing samples under HVAC fields of 40kV/mm and 30kV/mm fields.

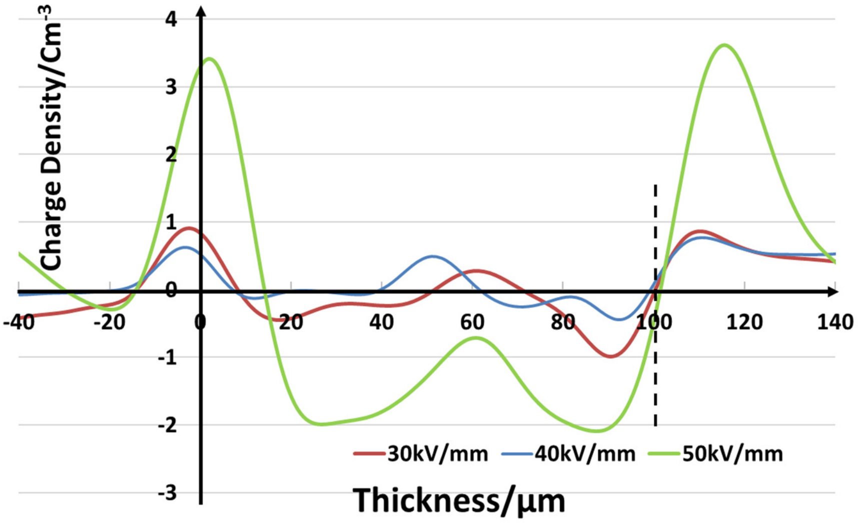

Figure 5-5 Deep trapped charges comparison after 7 hours 50Hz AC fields ageing (from 30kV/mm to 50kV/mm)

Figure 5-1 to 5-4 demonstrate the charge evolution under different magnitudes of the applied voltage strengths within initial 30 minutes. A similar trend of charge dynamics can be observed. However, the maximum amount of charges are apparently different. The higher the applied electric fields, the more accumulated charges adjacent to the electrodes. Severe reduction of charge amounts takes place when the field is reduced from 60kV/mm to 40kV/mm. Based on this trend, it is predictable that, the amount of charges adjacent to the electrodes will become more significant when the applied field is higher than 60kV/mm. Consequently, their effect on the local electric field distortion will be further enhanced, which may cause critical ageing to the insulating material and even trigger the breakdown of the overall insulator. In fact, several breakdown occurred during charge measurements when 60kV/mm was applied to the samples longer than 4 hours. The measured deeply trapped charges within the samples, as compared in Figure 5.5, present a similar reduction trend along with decreasing applied fields. Charge amount also dramatically decrease when the electric field decreases from 50kV/mm to 40kV/mm, although the deeply trapped charge amounts are relatively small compared with the shallow trapped charge adjacent to the electrodes shown in the subtracted results.

A significant amount of charge within LDPE can be observed under 50Hz HVAC stresses based on the improved PEA system and proposed data analysis method (Chapter 3). On the other hand, numerical modelling provides an alternative approach to investigate charge dynamics under applied field within wider ranges of magnitudes. As the results presented in Figure 5-1 to 5-4 and previous Chapters, the proposed model can quantitative analyse charge dynamics well under various applied fields. In this section, the model has also been used to investigate the dynamics of positive (Figure 5-6) and negative charge amounts (Figure 5-7) under various magnitudes of HVAC fields.

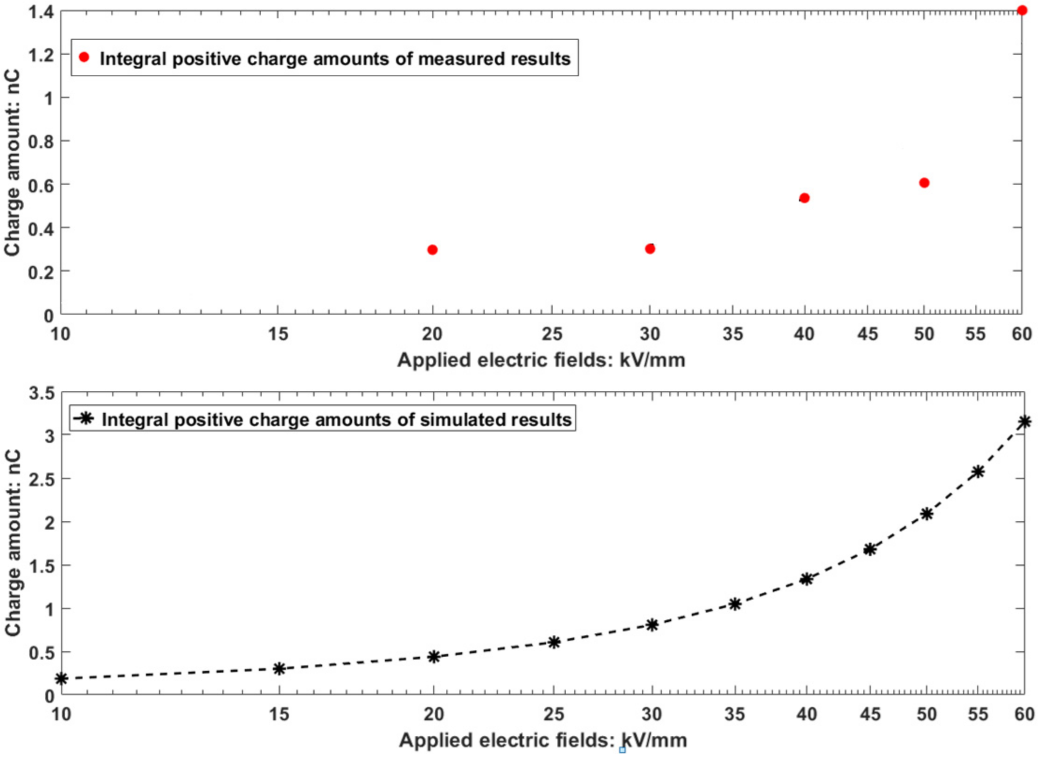

Figure 5-6 Integrated positive charge amounts of both simulated and measured results under various applied fields

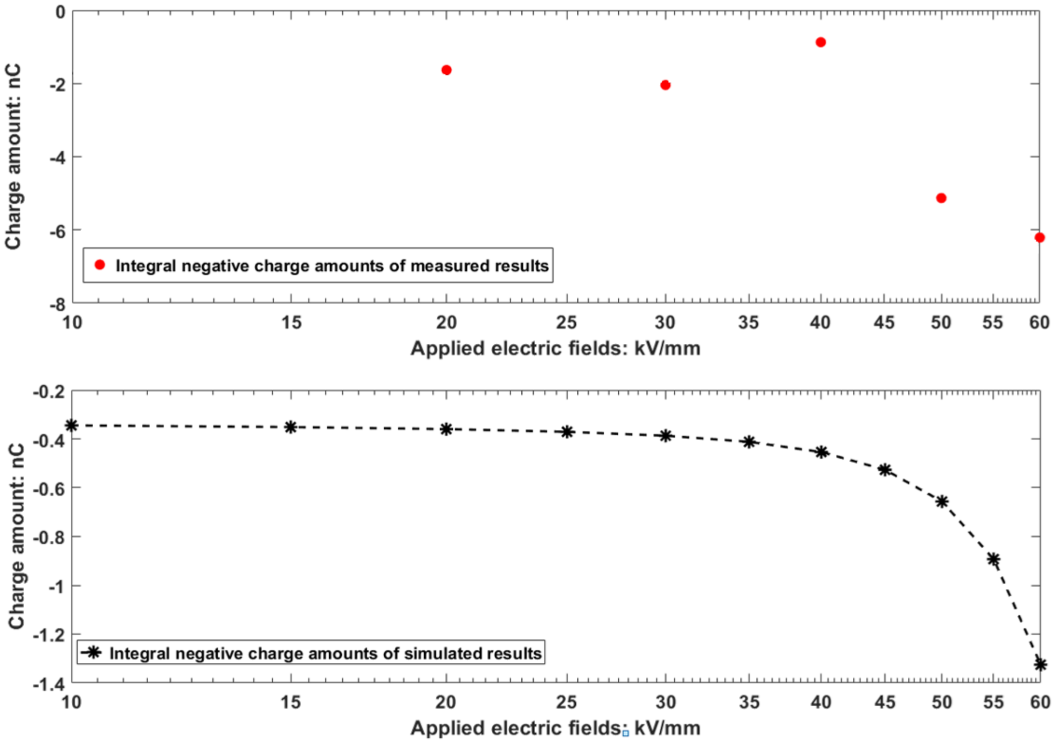

Figure 5-7 Integrated negative charge amounts of both simulated and measured results under various applied fields

Additionally, the maximum field distortion under various cases is presented in Figure 5-8. In these three graphs, the asterisk line indicates the fitting trends using polynomial functions, while the dots illustrate the actual results obtained from measurement and simulation. To eliminate the effects of ageing of testing materials caused by the long-term stressing fields, the measured results after one hour are shown here for comparison.

From Figure 5-6 and 5-7, it is obvious that the trend of simulated charge amounts presents remarkable similarity comparing with the fitted trends of measured results, although the exact numbers still show some differences. The accumulated charge amounts are increasing with applied field magnitude rising, and the increase rate of negative charges become more significant under more intensive fields. This indicates the difference of electrical performances, mobility and electrical injection, between positive and negative charges are intensified by the increased HVAC field. When the electric field is further measured above 40kV/mm, the field distortion is dramatically increased due to the exponential relationship.

The differences between the maximum field distortions of simulated and measured results are limited as illustrated in Figure 5-8, which is validate the simulation model can be applied to predict the electric field distortion. The maximum field distortion increases with the applied field. The local field distortion is mainly caused by the localised charges within the insulation. The localised charge amount rises when applied field magnitude increases due to the enhanced injection rate and transport mobility. This eventually causes the enlarging local field distortion along with the applied field. Therefore, based on all above, the various electrical performances (Mobility and injection rate) of positive and negative charges are the essential factor causing the space charge accumulation under HVAC stresses.

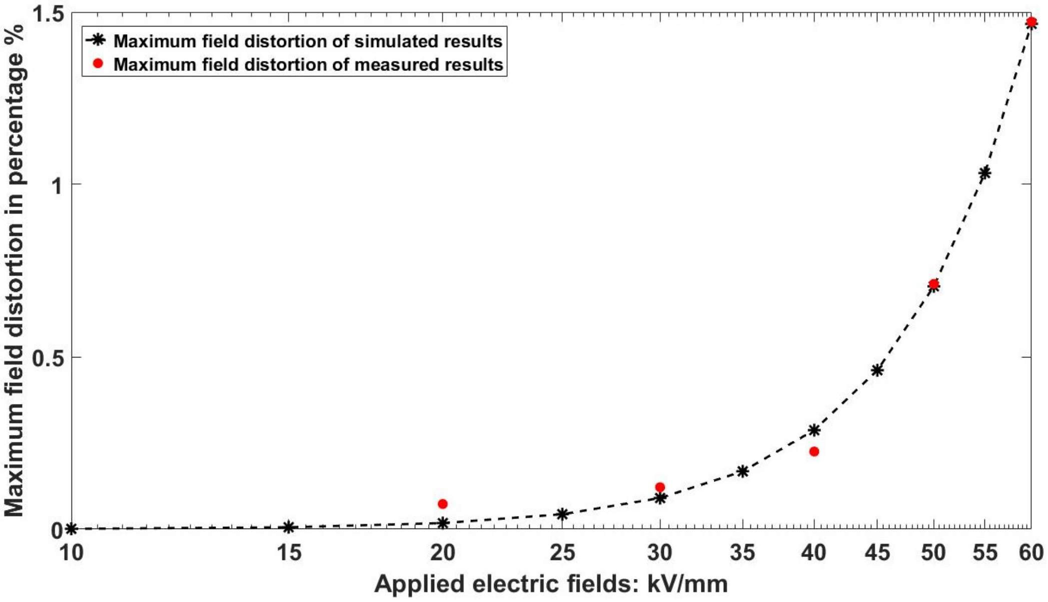

Figure 5-8 Deduced maximum field distortion of both simulated and measured results under various applied fields

In summary, the applied fields' magnitude mainly influences the charge dynamics under HVAC based on their effects on charge amounts and carriers' mobility. This trend is consistent with characteristics under HVDC. Increased the localised charge amounts and enhanced charge transport mobility can be observed with the increasing HVDC magnitudes. The enhanced charge dynamics can intensify the local field distortion. Besides, charges mainly accumulate adjacent the electrodes under HVAC fields, which results in the maximum field distortion occurring in the surface region of the insulation. Furthermore, precise charge injection mechanism and mobility's fields-dependent model is essential for interpreting charge dynamics under AC conditions, as a broader range of local electric fields is changing. By applying the mobility fields dependent mechanism in the current simulation model, only the mobility of holes is certified by the measurements, and the measures began with a relatively high field. This model is precise enough for simulating charge dynamics under HVDC. Under HVDC, the local fields are not altering in a large scale, and the movements of holes dominate the overall charge transport process (Section 3-2). However, that's not the same for charge dynamics under HVAC, which causes the noticeable specific amounts differences when comparing the simulated results under ac (mobility and injection mechanism unchanged) with the measured ones. Therefore, for HVAC conditions, more accurate mobility measurements are required for both holes and electrons, to quantity-accurate modelling the space charge phenomenon.

5.2 Dynamics of space charge under different DC offset's ratios

To better illustrate the charge dynamics under superposed fields with the same power strength, the applied fields in this section are all chosen to have the same RMS magnitude (50kV/mm). The waveform of them is shown in Figure 5.9. The fields' frequency is 50Hz, which is utilised to reflect the common situations in high voltage power systems. The selected ratios for investigation are zero, 0.17, 0.2 0.33, 0.4, 0.5, and one, aiming to present a complete evolution of the DC offset's ratio influences within the combined stresses on the charge dynamic within insulations.

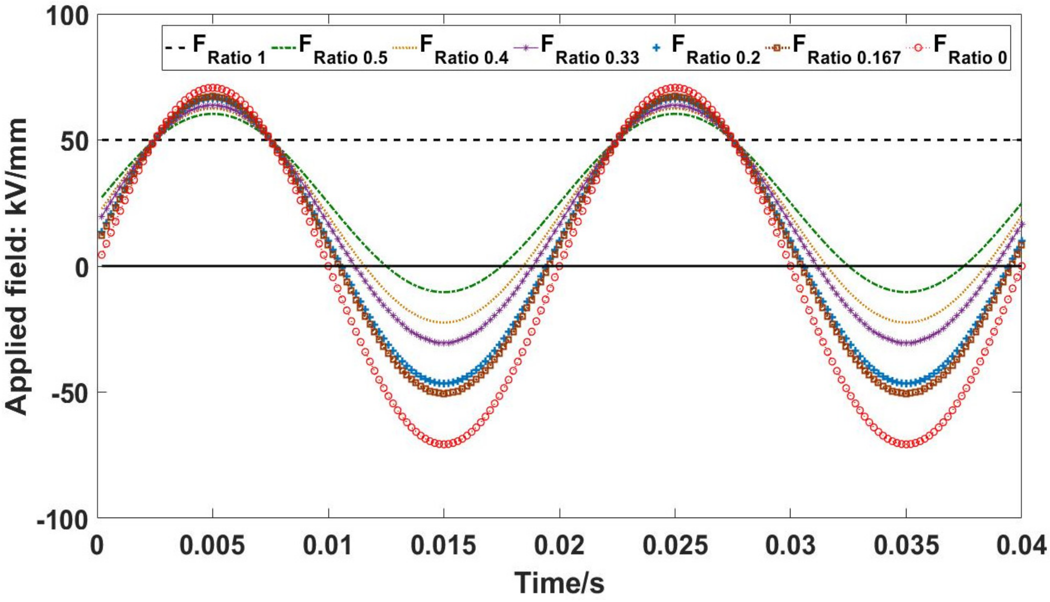

Figure 5-9 First two cycles of applied combined stress with different DC offsets

Based on charge profiles discussed in sections 3.3.2 and 4.2.2, it is clear that the DC component within the applied fields has a significant impact on the charge formation and local field distortion within the insulation. Figure 5-10 presents a comparison of measured and simulated charge profiles under combined stresses with DC offset ratio 0.5. It is clear that the adding of DC offset significantly enhanced the accumulated positive charge amounts comparing Figure 5-10 with Figure 3-18. Charge distributions in Figure 5-10 are more like under pure DC fields after 1 hour of field stressing (Figures 3-9 and 3-11): i.e., positive and negative charges mainly accumulated at one side. The effects of AC components within the applied fields on the charge distribution can only be observed within the very initial stressing time (<2minutes in measurements and <10 minutes in simulations).

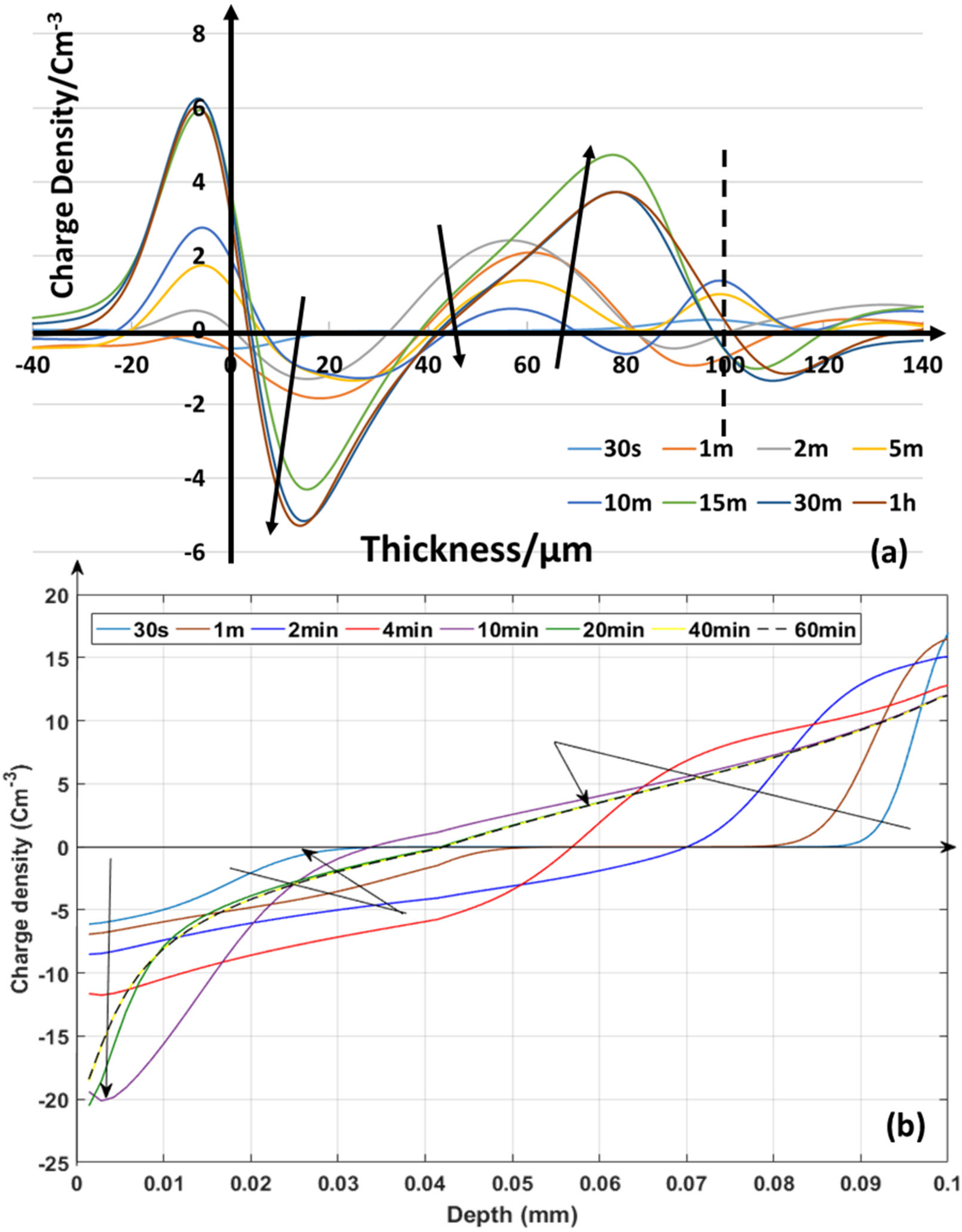

Figure 5-10 Measured Charge evolution after removing the capacitive charge (Applied field phase 90°,graph (a)) and simulated charge profiles (Applied field phase 0°,graph (b)) within 1 hour of combined stress (50Hz, 50kV/mm, DC offset ratio 0.5)

In order to more clearly present the effects of DC offsets' ratio on the charge formation and local electric field distribution within the insulation, the integrated charge amounts and the maximum field distortion of both simulated and measured results are also presented and discussed under various circumstances.

5.2.1 Total charge amounts

In this section, the integration of both simulated and measured results under 50Hz combined AC and DC stresses with various DC offset's ratio are presented, aiming to demonstrate the offset's ratio effects on the charge dynamic within the insulation. The amount of the integral net charge, positive charge, and negative charge are illustrated from Figure 5-10 to Figure 5-12

Figure 5.11 presents the net charges within the sample under combined stresses within different DC offsets. The overall trend for the curves shows a fluctuant period followed by a saturation period. For the majority cases, the charge amount curves reach steady states at around 2 hours. There is an exception for the case under combined AC and DC fields with DC ratio 0.4, where the dynamic ends after approximately five hours. Both continuous polarity reversal and DC offset can affect charge distribution within the materials. It seems these two effects are neutralising each other under high fields, as a massive amount of positive charges observed under HVDC, while mainly negative charges observed under pure HVAC fields. The situation of this two features' effects alters along with the changing of the composition of the superposed fields. Their confliction seems most intensified under superposed fields with ratio 0.4, which also causes the extended dynamic periods.

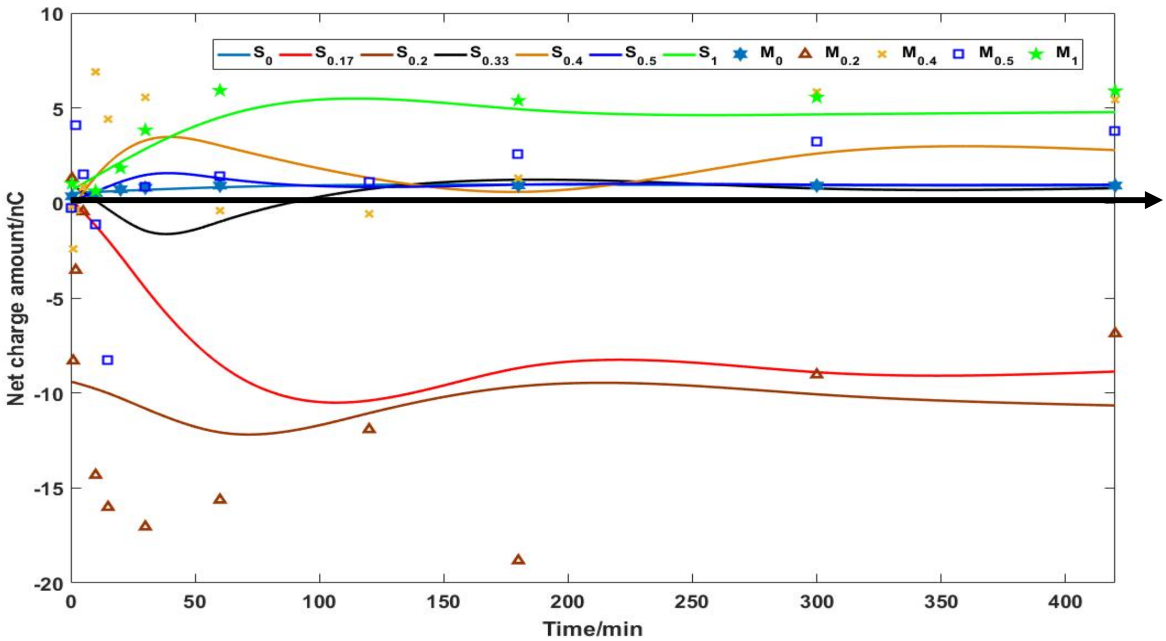

Figure 5-11 Integral net charge's trend over time under various DC offset ratios. S_0, $S_{0.17}$, $S_{0.2}$, $S_{0.33}$, $S_{0.4}$, $S_{0.5}$, and S_1 indicate the simulated results under pure AC fields, under superposed AC and DC fields with DC offset ratio 0.17, 0.2, 0.33, 0.5, and under pure DC fields. M_0, $M_{0.2}$, $M_{0.5}$, and M_1 represents the measured results under pure AC fields, superposed AC and DC fields with DC offset ratio 0.2 and 0.5, as well as pure DC fields

From Figure 5-11, it is clear that simulated and measured results present a great similarity in the charge saturation amounts. The saturated net charge amounts for the seven conditions are different. The maximum saturation amount occurs under DC fields, while the minimum happens at DC offset's ratio 0.2. When the DC offset's ratio is higher than 0.33, the steady state net charge amount is positive, which indicates the point above which the effect of DC offsets on the space charge formation is stronger. This is because under DC voltages positive charge generally dominate the overall charge transportation and accumulation, as discussed in Section 3.2, while mainly negative charges are observed in charge profiles obtained under AC fields. Furthermore, for all the combined field cases, the saturated net charge amounts (absolute values) are larger than that under pure AC, which indicates the additional DC offset can significantly increase the accumulated charge amount of insulation. The total positive charge amount and negative charge amount and their variation with time are presented respectively in Figure 5-12 and Figure 5-13.

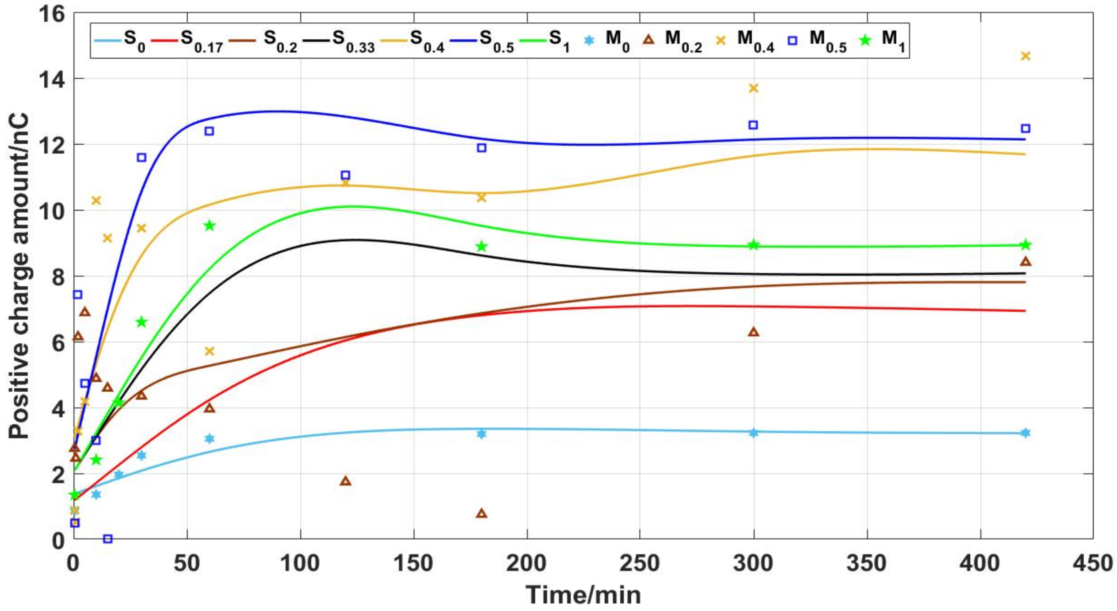

Figure 5-12 Integral positive charge's trend over time under various DC offset ratios. S_0, $S_{0.17}$, $S_{0.2}$, $S_{0.33}$, $S_{0.4}$, $S_{0.5}$, and S_1 indicate the simulated results under pure AC fields, under superposed AC and DC fields with DC offset ratio 0.17, 0.2, 0.33, 0.5, and under pure DC fields. M_0, $M_{0.2}$, $M_{0.5}$, and M_1 represent the measured results under pure AC fields, superposed AC and DC fields with DC offset ratio 0.2 and 0.5, as well as pure DC fields

Figure 5-12 and Figure 5-13 present the specific information of the integrated positive and negative charge of simulated and measured results. The saturated amounts obtained from simulations are similar to those measured results under the same condition, although the results within the initial dynamics period (<300 minutes) present some differences, especially for the ratio 0.2 case.

It can be observed from Figures 5-12, 5-13 that, the magnitude of both positive and negative is similar for pure AC and combined fields conditions, causing smaller net charge amounts presented in Figure 5.11. For positive charges, the charge amount for pure DC is higher than the amount for pure AC while lower than those combined conditions with DC offsets >0.33. Besides, the positive charge amount obtained for the combined conditions increases along with the DC offset's ratio, which indicates the charge formation is more close to the conditions under pure DC fields when the DC component percentage within the combined stress increases. (Remarkable amounts of positive charges are generally observed in polyethylene under DC stresses, while mainly negative charges are observed under AC stresses. Specific results have been illustrated in Chapter 3)

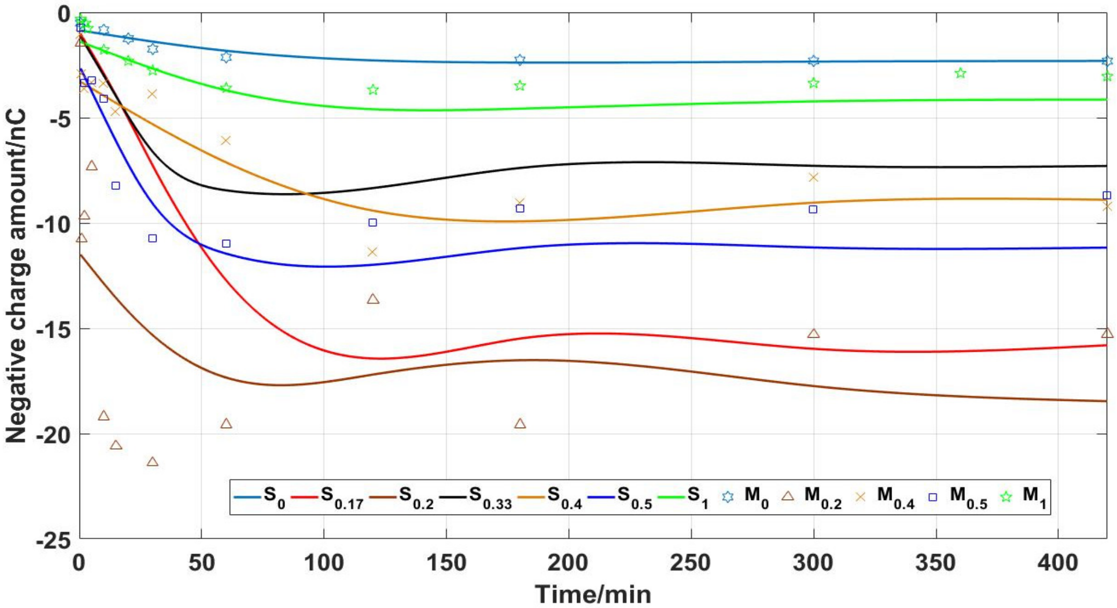

Figure 5-13 Integral negative charge's trend over time under various DC offset ratios. S_0, $S_{0.17}$, $S_{0.2}$, $S_{0.33}$, $S_{0.4}$, $S_{0.5}$, and S_1 indicate the simulated results under pure AC fields, under superposed AC and DC fields with DC offset ratio 0.17, 0.2, 0.33, 0.5, and under pure DC fields. M_0, $M_{0.2}$, $M_{0.5}$, and M_1 represent the measured results under pure AC fields, superposed AC and DC fields with DC offset ratio 0.2 and 0.5, as well as pure DC fields

Nevertheless, the case for the negative charge is much more complicated. The integrated charge amount with a lower DC offset's ratio is larger than the amount under pure AC and DC. However, negative charge amounts will reduce sharply when the offset ratio is higher than 0.33. It is expected as the trapped positive charges are excessive compared to the negative charges when enough DC offset added. Consequently, under fields with relatively high DC offsets, where the injection and transportation of electrons are not strong enough to compensate the influence of positive charges, the amount of electrons will show a complicated relationship with DC offsets, unlike holes, always a positive correlation.

5.2.2 Maximum field distortion

Space charge phenomenon cannot only promote charge transport within insulation but also can cause field distortion. This field distortion can induce the maximum strengths of local field significant exceeding the operating field at certain phases, which can accelerate the ageing of insulating materials or even cause breakdown of the insulation. The exceeding effects get remarkable when the sinusoidal applied field phase is around 90 or 270 degree. Therefore, in this section, the field distortion at 90 degrees, regarded as the maximum field distortion, is investigated under various conditions to illustrate the contribution of space charge phenomenon towards the electrical performances of insulating materials. The maximum field distortion obtained from both measured and simulated results are illustrated in Figure 5-14.

From the graph, it is clear that the maximum field distortion obtained from measured and simulated results both present a non-monotonic trend and maximum values happen when DC offset ratio is around 0.2, where the influences of DC components within applied fields is relatively small. This indicates the field distortion caused by the DC and AC components are neutralising each other, which is consistent with results of integrated charge amounts and observation in local field distributions (Figure 3-12, Figure 3-26).

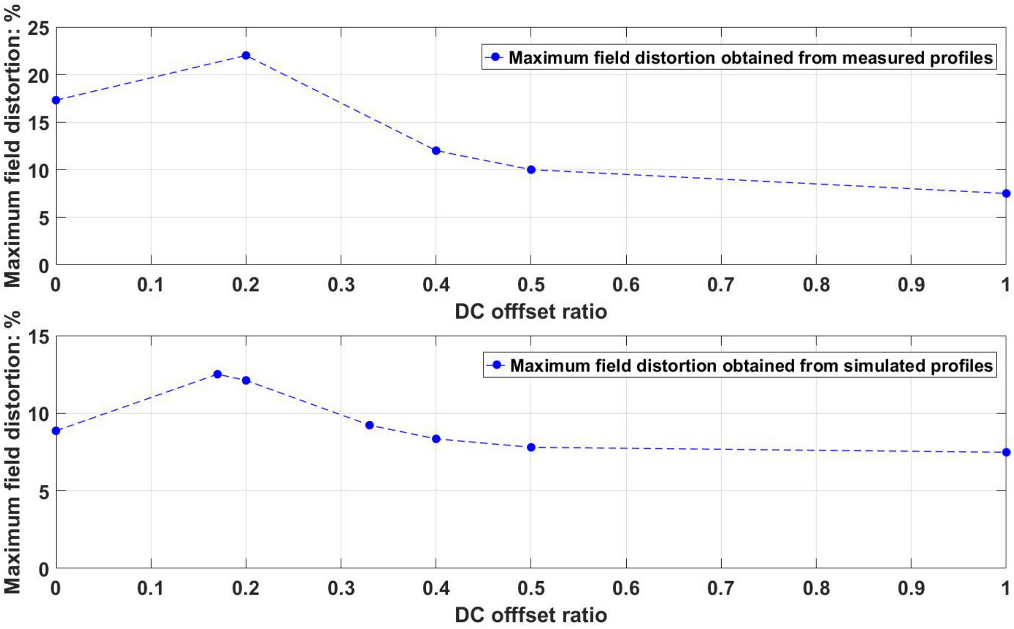

Figure 5-14 Maximum field distortion vs DC offset ratio: Measured results (a), and simulated results (b) The blue points are the maximum field distortion in all cases after 1 hour of fields stressing.

5.2.3 Conclusions

Overall, from both the charge profiles and local electric field distributions, it is clear that the DC component has a significant effect on the space charge phenomenon within insulations. The obtained charge amounts are significantly more massive under combined stresses compared with under pure AC fields, while the corresponding local field distortion under specific offset ratio combined stresses can be more significant than both pure AC and DC conditions. Therefore, to estimate the electrical performance of dielectrics under combined stresses accurately, the composition of the applied field should be exhaustively considered. Currently, in standards [114], equivalent pure AC and DC fields are generally adopted for the dielectrics tests. Evaluation of standard dielectric experiments on the space charge formation and local field distortion within insulation has been discussed in the following section 5.3.

5.3 Comparison of charge dynamics under standard dielectric testing fields and real operating combined AC and DC fields

According to the international standard (IEC 61378-2:2001), equation 5-1 and equation 5-2 (5-1 for DC testing level and 5-2 for AC) are generally used to calculate dielectric withstand tests voltages [114]. In this section, experimental approach has been adopted to evaluate the standard testing procedure. This is because the current simulation model, as discussed in previous chapters, still presents significant numerical differences compared with measured results when analysing charge dynamics under AC and superposed AC and DC fields.

Testing for the six-pulse bridges transformer is used as an example. The number of bridges, N, considered is 4. (For four-pulse bridges transformer. N could be 1 to 4. Choosing 4 is considering the highest testing voltage.) The specific process of deducing the testing voltage for the chosen condition is presented in Appendix D. According to the standard. The testing procedure lasts 1 hour for AC conditions and 2 hours for DC in the standard. During the testing voltage stressing if no partial discharge detected, the insulation is considered passing the qualification test. Partial discharge is believed to be strongly related to the local electric field magnitude and space charge formation [115]. Therefore, in this section, charge amounts and the maximum field distortion obtained from PEA measurements are adopted to evaluate the standard dielectric tests. Results are presented in Figure 5-14 and Figure 5-15.

$$\boldsymbol{U_{dc} = 1.5\big((N - 0.5)U_{dm} + 0.7U_{vm}\big)} \tag{5-1}$$

$$\boldsymbol{U_{ac} = \frac{1.5\left((N-0.5)U_{dm}+\frac{\sqrt{2}U_{vm}}{\sqrt{3}}13\right)}{\sqrt{2}}(rms\ value)} \tag{5-2}$$

where U_{dc} is the dc test voltage; U_{ac} is the AC test voltage (rms value); N is number of four pulse bridges in series from neutral of the DC line to the rectifier bridge connected to the transformer; U_{dm} is the highest dc voltage per value bridge; U_{vm} is the maximum phase to phase ac operating voltage of the valve winding convertor transformer.

From Figure 5-15, it is clear that in the standard test conditions, a strong influence of negative charges can be observed under all DC offset ratio cases. The accumulated negative charge amounts under standard testing conditions are generally larger than the amounts obtained under corresponding real superposed stress conditions. However, when considering the amount of positive charges, it seems that the standard testing environments cannot cover all the cases, especially for cases with higher DC offset ratio (0.5). The obtained positive charge amounts from both AC and DC standard tests are significantly smaller than the amounts obtained in superposed stresses.

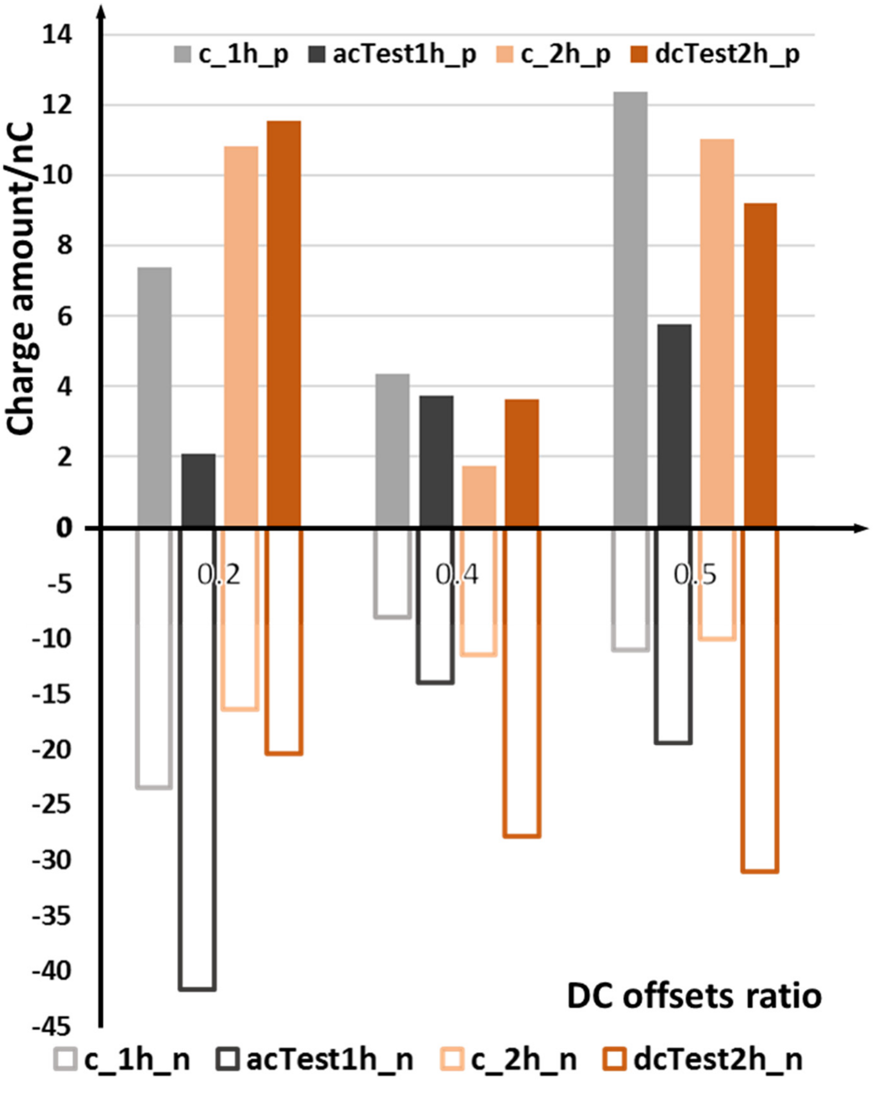

Figure 5-15 Integral charge amounts within LDPE under real combined stresses conditions and pure ac and dc testing conditions.

The Y-axis demonstrates the charge amounts in nC, and. The x-axis shows the DC offset ratio of the issued applied field conditions. The solid squares indicate positive charge amounts (_p), and the hollow bars (_n) represent the negative charge amounts. C_1h and C_2h indicate the measured results after 1 hour and 2 hours of the combined fields stressing respectively. "acTest1h" and "dcTest2h" present the measured results obtained from the standard testing environments. The duration of the test is chosen according to the standard (1 hour AC test and 2 hours DC test). Two durations of the corresponding referred results measured under combined stresses are selected for comparison

When considering the influences caused by charge distributions, the differences between under standard tests and the real superposed stresses become larger. As for the maximum field distortion (The percentage of the maximum field strength enhancements), Figure 5-16, it seems all the standard testing conditions has underestimated the local field distortions. However, it is worth to point out that the difference between the results of real and tested is relatively limited when the DC offset ratio is 0.5.

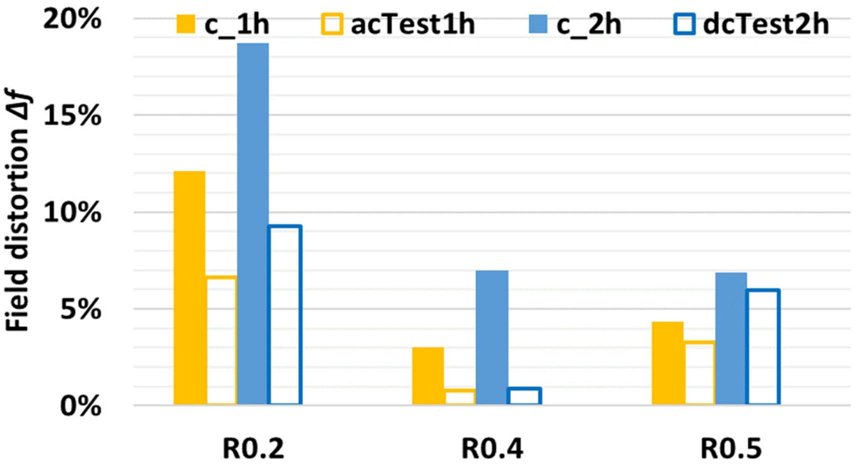

Figure 5-16 Maximum field distortion within LDPE under real combined stresses conditions and under pure ac and dc testing conditions

In industry, when considering the electrical performances of high voltage insulation the conductivity and breakdown strengths of the materials are mainly discussed. Under HVDC fields, conductivity and breakdown strengths of the insulation are strongly influenced by the trapped charge amounts within the insulation. The trapped charges can distort the local field distribution. The intensified local field could further enhance the local conductivity (field dependent), which eventually accelerates the breakdown process within the insulation. Whereas for HVAC and superimposed HVAC and HVDC fields, the breakdown strengths of the materials will be affected by not only the charge amounts but also the distribution of charges. This is because the consistent reversal of the applied field polarity will cause the localised charges within insulation distributing unbalanced: Excessive density of charges accumulate close the electrodes interfaces while almost nothing in bulk. From results in Figures 5-15 and 5-16, it is clear that current standard has underestimated the influences of space charge within insulation under superimposed HVAC and HVDC fields. Although it can be applied to estimate the accumulated charge amounts under combined stresses with relatively low offset ratio, it underestimated the field enhancement caused by local charges in most cases. Furthermore, unlike under DC fields, the charge and the local field dynamics reach equilibrium within an hour, the localised charge amounts and the maximum field distortion are still increasing after severe hours (>2 hours) of AC or superposed AC and DC fields stressing (Discussion in sections 3.3 and 5.2). The 2 hours duration of AC field stressing adopted in the standard tests may not be long enough to evaluate the charges and local field dynamics within the insulation. Based on all above, it is clear that the current testing standard cannot accurately evaluate electrical performances of insulation under combined electric fields, and further revise and improvements are desperately needed in consideration of testing voltage magnitudes and testing durations.

5.4 Dynamics of space charge under different applied field frequency

Another characteristic of the periodical electric fields is the alternative frequency. The impact of applied field frequency on the charge dynamics are investigated in this section. This section contains the results under 0.05Hz, 0.5Hz, 5Hz and 50Hz (power frequency) AC fields and combined stresses with DC offset ratio 0.5. The selection of the analysed frequencies is settled consulting to the paper of Tanaka et al. [116] about the frequency dependence of charge density under AC stress. However, higher applied voltage magnitude (50kV/mm) is adopted in this part, as discussed in 5.1, charge dynamics will be more significant under intensive fields. The frequency's influences under both AC and superposed AC and DC fields are also investigated in this work to demonstrate an overall picture of the effects. In this section, the lowest investigated frequency is 0.05Hz, and therefore the impacts of frequencies on the charge dynamics can clearly demonstrate in a broad range. Choosing the pure AC and combined stress with DC offset ratio 0.5 for discussion is aiming to demonstrate the frequency influence on charge dynamic under two typical cases. From the analysis in Chapters 3 and 4, it is clear that both the proposed experimental and numerical method can fairly detect and evaluate charge dynamics under periodical high voltage stresses. Experimental approaches can directly present the charge profiles within insulation under periodical complex fields, and the results are more close to reality compared with simulation. However, the simulation can more clearly illustrate the differences caused by small alteration of environments. The effects of applied field frequency on the charge dynamics weaken with the increasing DC offset ratio due to the reducing AC component percentage. Therefore, experimental results have been used to analyse influences of frequency on charge dynamics under pure HVAC electric fields, while simulation approach has been chosen to investigate the frequency effects on charge dynamics under combined stresses with DC offset 0.5.

5.4.1 Influences of frequency on charge dynamics under AC electric fields

In this section, charge evolution (Subtracted volt on profiles) under various frequency applied fields are shown from Figure 5-17 to Figure 5-20 and a comparison of remaining charges after 7 hours of different frequencies field stressing are illustrated in Figure 5-21. The application of 7 hours field stressing is because the phenomenon of surface flashover and discharge occasionally happen during the AC measurements, if the stressing time is too long. Besides, long duration of fields stressing the trend of charge dynamics can be more noticeable observed.

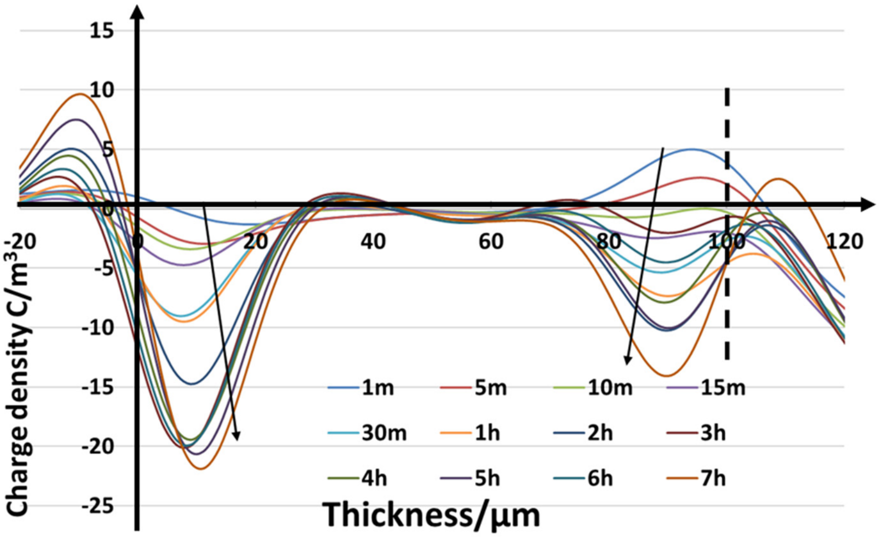

Figure 5-17 Charge evolution around applied fields phase 90° after removing the capacitive charge within 7 hours of ac field stressing (50kV/mm, 50Hz)

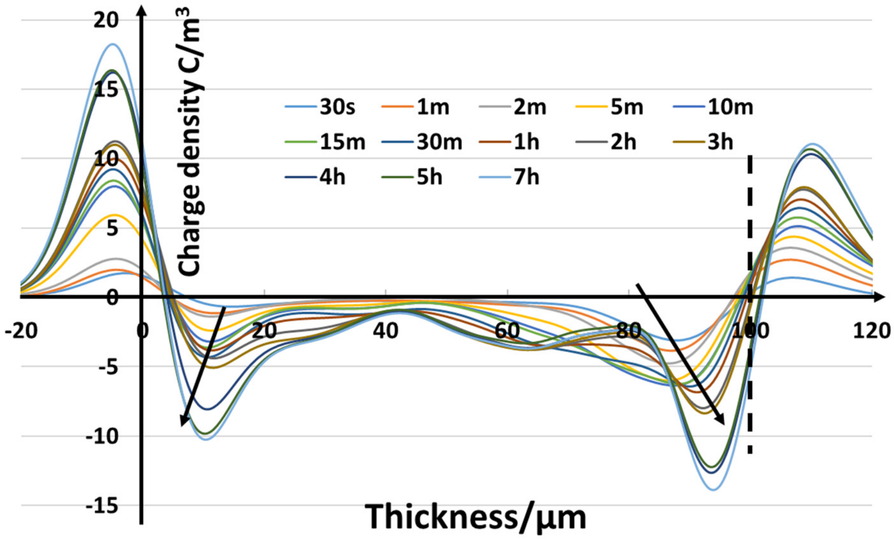

Figure 5-18 Charge evolution around applied fields phase 90° after removing the capacitive charge within 7 hours of ac field stressing (50kV/mm, 5Hz)

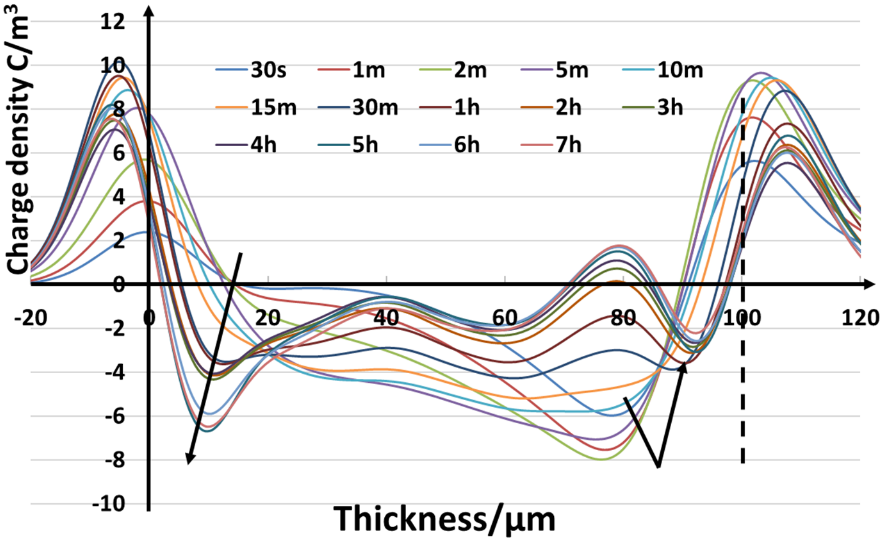

Figure 5-19 Charge evolution around applied fields phase 90° after removing the capacitive charge within 7 hours of ac field stressing (50kV/mm, 0.5Hz)

Figure 5-17 demonstrates the charge profiles within the sample with stressing time under 50Hz 50kV/mm AC stress. In order to demonstrate the influence of duration of voltage on charge formation, charge profiles under applied voltage around phase 90° at different stressing times are focused. From the graphs, it can be observed that the accumulated charge peaks adjacent to the electrodes increase with the stressing time. Besides, the domination of negative charges, especially for a long duration of the voltage application within the insulation, can be observed. Figure 5-18 and Figure 5-19 show charge profiles along with stressing time under 5 and 0.5 Hz applied fields frequency. Together with the results in Figure 5-17, it is noticeable that charges can transport further into the bulk of the insulation under relatively low frequency (<5Hz). The accumulated charges in the bulk decrease along with frequency, while the accumulated charge amounts adjacent to the electrodes increases with the frequency. This indicates charges are more difficult to transport into the bulk area of the insulation if the frequency of the applied field polarity reversal increases. Because the trapped charges under higher frequency applied fields are more close to the electrode, the local electric fields near the electrodes will be further distorted. This may explain the severer ageing for the same material under power frequency HVAC fields, compared with under same strength HVDC stresses [96, 99], as dc case can be regarded as an extreme case of ac, with a frequency equal to zero.

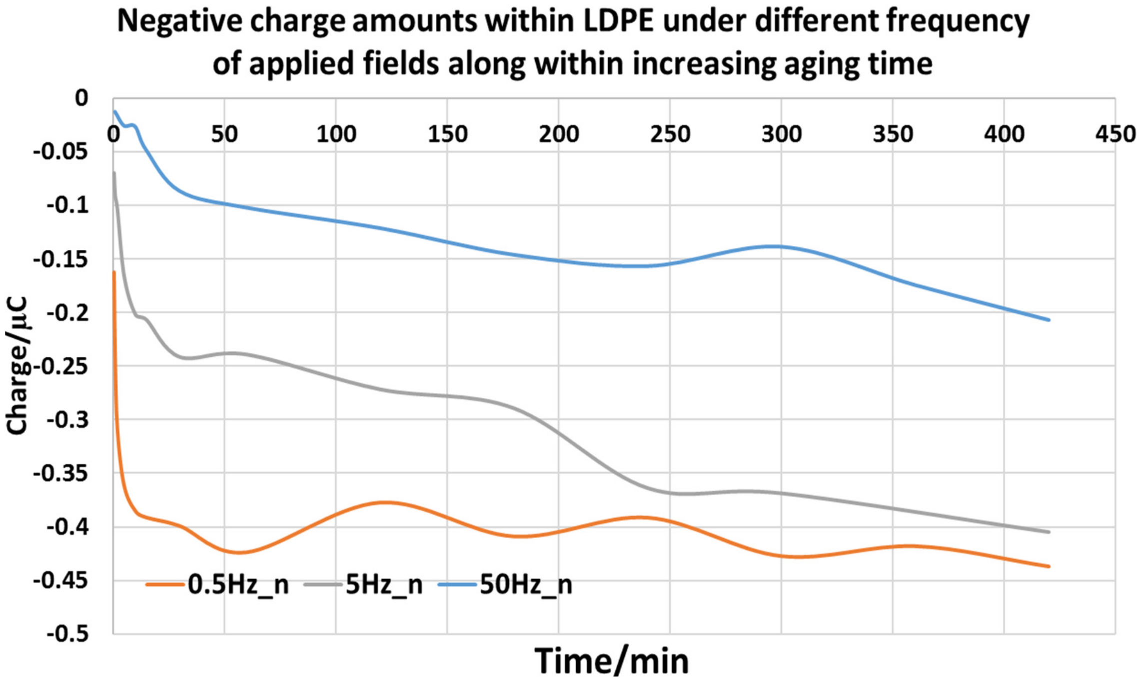

Figure 5-20 Negative charge amounts within insulation evolution with time under different frequency of applied fields

For all frequency cases, negative charges are dominant the charge dynamics within the insulating materials. Therefore, negative charge amounts under various circumstances, are calculated and plotted verse time of the voltage application, as shown in Figure 5-20. It is apparent that the negative charge amount decreases along with frequency. It seems under relatively low frequency (0.5Hz) the negative charge amount can reach a quasi-steady stage after a few minutes applying fields. This may because charges are able to transport across the insulation and reach the opposite electrode, neutralising as well as keeping a balanced charge amount under relatively low frequency applied fields, as similar as the situation under HVDC fields. Figure 5-20 also shows that the lower the applied frequency, the more the charge accumulated inside the insulation. Significant charge amount reduction can be observed when the applied field frequency increase from 5Hz to 50Hz. Charge amount decreases more than 50% when comparing the results under 50Hz and that under 5Hz electric fields.

The deeply trapped charges within the samples, as compared in Figure 5-21, also present a reduction trend along with increasing frequency of the applied fields. Charge amount decreases around 70% when comparing the results under 5Hz and 50Hz electric fields, although the deeply trapped charge amounts for all cases are relatively small comparing with the shallow trapped charge results presented previously in Figures 5-17 to 5-20.

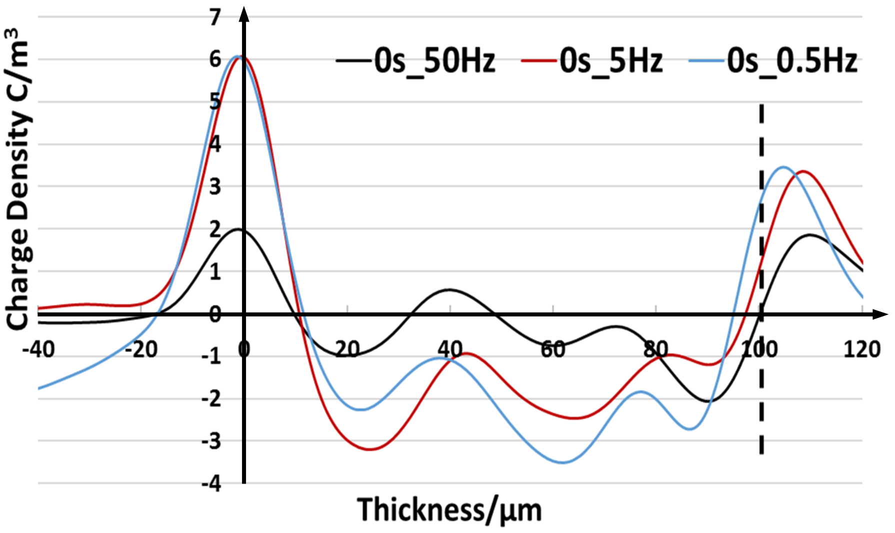

Figure 5-21 Comparison of remaining charges within insulation under different applied fields after instantly removing voltage

In summary, it is clear that the space charge amount within the insulation decreases along with the frequency of the applied field. Based on the present results, it is noticeable that the increasing frequency of the applied fields can significantly change the distribution of the accumulated charges inside the insulation, apart from reducing the overall trapped charge amount (Figure5-16 to Figure 5-18). The presence of charge adjacent to the electrodes under high frequency stresses, even in small amount, can cause severe local fields distortion when the polarity of the applied fields reversed. This constant intensive field distortion can severely degrade the surface region of the insulating materials and even trigger the overall sample breakdown. This may give an explanation why the ac breakdown strength of the material is normally significantly lower than its dc breakdown strength. A specific discussion of space charge's role in the electrical breakdown of solid insulation is illustrated in Chapter 6.

5.4.2 Influences of frequency on charge dynamics under combined stresses with DC offset ratio of 0.5

Figure 5-22 presents the simulated charge distributions under 5Hz combined stress with 50% DC offset. Figure 5-23demonstrates charge distribution under 0.5Hz combined stress with the same ratio, and Figure 5-24 presents results under 0.05Hz combined stress.

It can be clearly observed from the three graphs that the accumulated positive charges move like a packet towards the opposite electrode with time. Similar to the positive charge movements under the DC condition due to the influence of 50% DC component within the applied field. However, the peak values of both accumulated holes and electrons under the combined condition are larger than those under DC condition.

This is because the maximum magnitude of the applied combined field is larger than that of DC field with the same RMS values, causing a larger amount of charge injections. The differences between Figure 5-23 and Figure 5-24 are obvious: under 0.05Hz, the fluctuation can be observed on the accumulated charge profiles due to the long applied field changing cycle. However, the differences between Figure 5-22 and Figure 5-23 can hardly be distinguished. This confirms the limited influences of frequency on the charge formation when the applied field frequency is higher than 0.5Hz. Besides, this also demonstrates the effects of frequency on charge formation under combined AC and DC stresses are relatively limited compared with under pure AC conditions. An integration is applied to the charge density profiles to get the charge amount along with time to better distinguish the influences of applied field frequency on the charge dynamic under combined stresses. Figure 5-25 to Figure 5-26 are the integrated charge of net charge, positive charge, and negative charge. Because the differences among the results under high frequencies are too small to distinguish, the high frequency part is zoomed in on a small graph nearby.

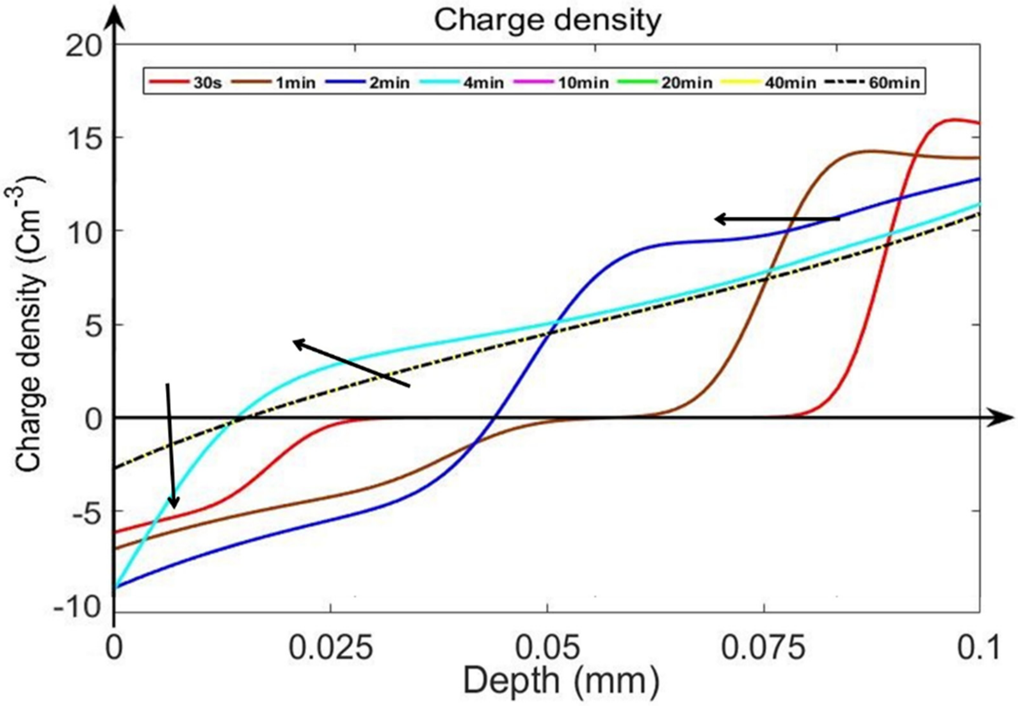

Figure 5-22 Charge distributions under 50kV/mm superposed HVAC and HVDC field with DC offset ratio 0.5 (5Hz)

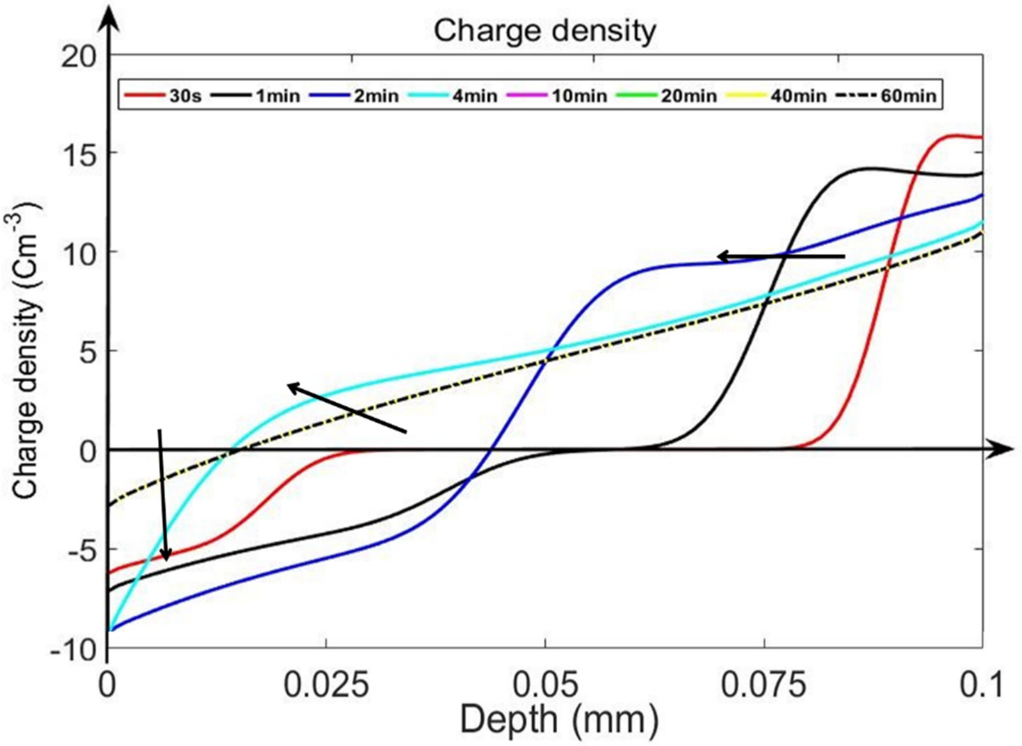

Figure 5-23 Charge distributions under 50kV/mm superposed HVAC and HVDC field with DC offset ratio 0.5 (0.5Hz)

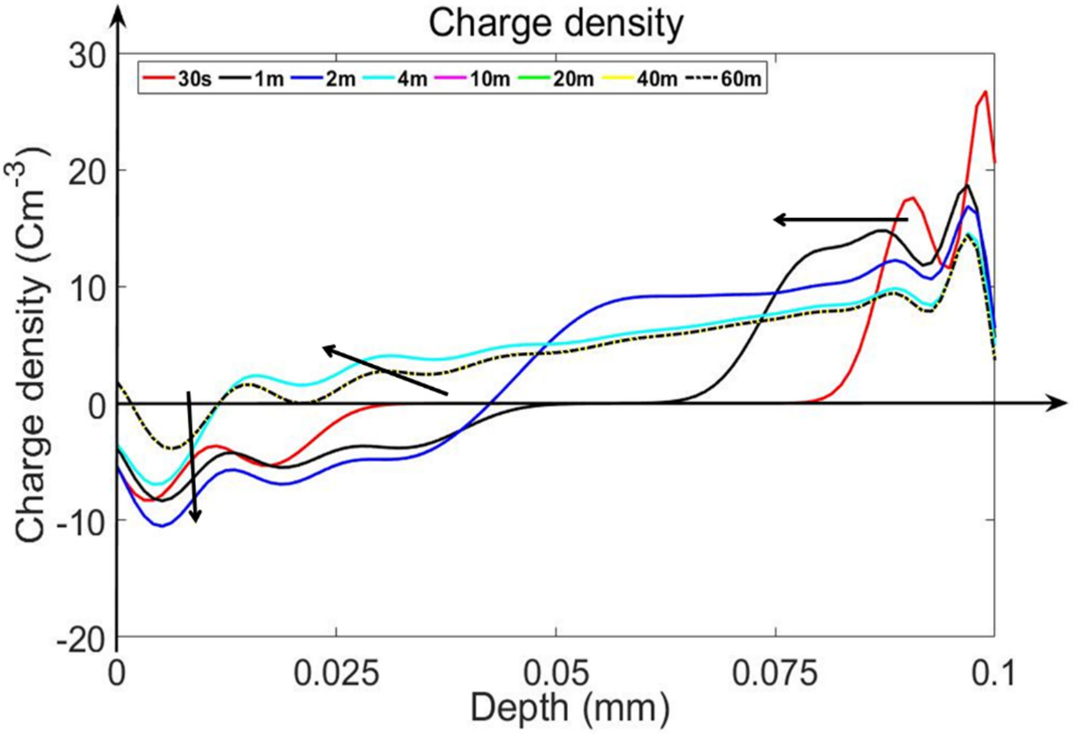

Figure 5-24 Charge distributions under 50kV/mm superposed HVAC and HVDC field with DC offset ratio 0.5 (0.05Hz)

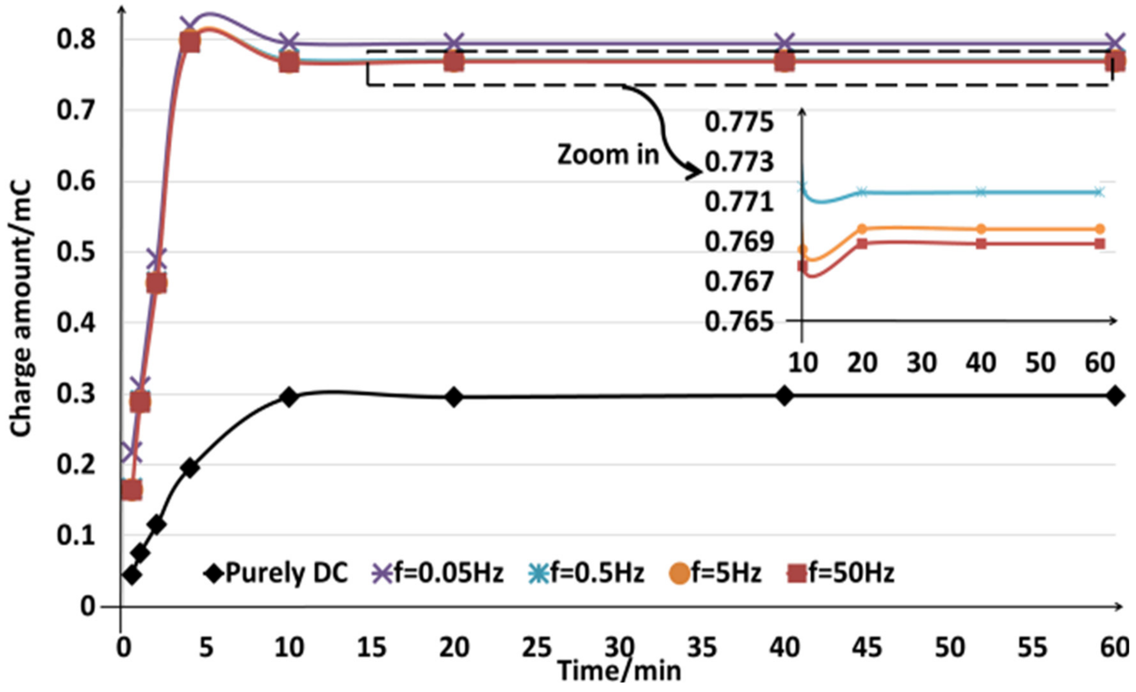

Figure 5-25 Integral net charge's trend over time under 50kV/mm fields with various frequencies

Figure 5-25 demonstrates the integrated net charge amount within the insulation under 50kV/mm DC stress, under 50kV/mm combined AC and DC stresses with frequencies ranging from 0.05 to 50Hz (Ratio 0.5). It can be clearly observed from the graph that the amounts of net charge under the combined AC and DC stresses are significantly larger than that under the DC conditions. The net charge amount decreases with frequency increasing, and this phenomenon becomes insignificant when the applied fields' frequency is higher than 0.5Hz. This inhibition of charge accumulation of applied field's frequency under combined AC and DC conditions is consistent with the experimental results under AC conditions. The accumulated charge amount within insulation decreases sharply when the applied fields' frequency is changing from 10^{-3} to 10^{-2}.

Besides, it can also be observed that the amount of net charges within the insulation under combined stress is positive. This is because under DC fields that holes are easier to inject into the insulation (lower injection barrier) compared to electrons. Therefore, holes are dominant in the charge accumulation dynamics when the DC offset within the superimposed fields is large enough.

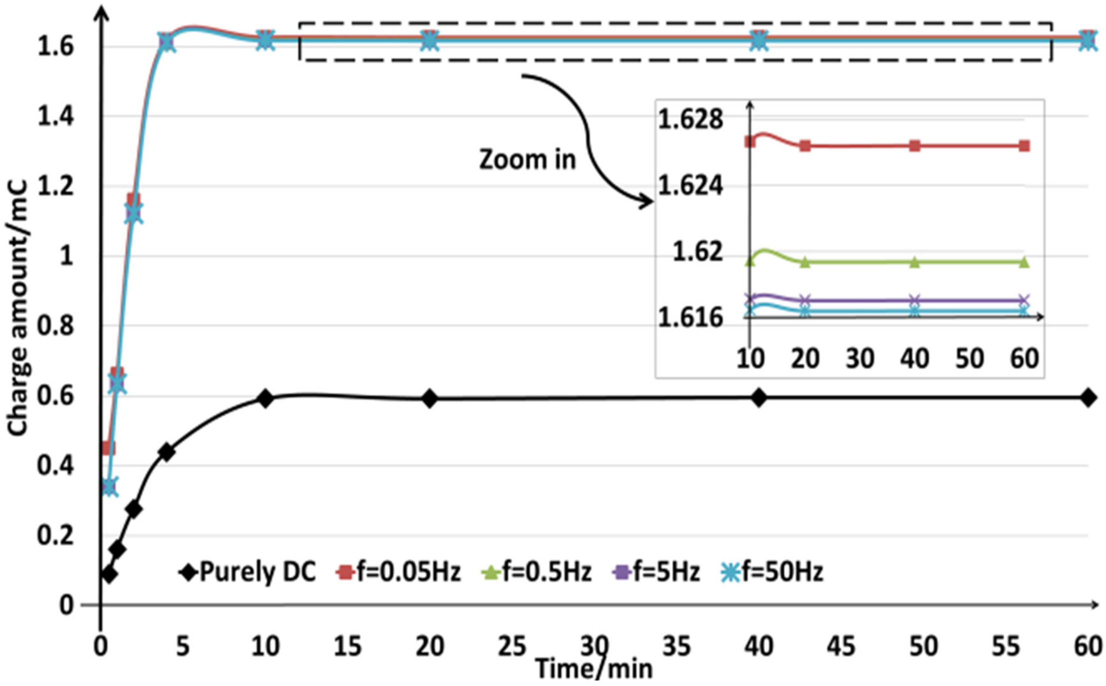

Figure 5-26 Integral total positive charge's trend over time under 50kV/mm fields with various frequencies

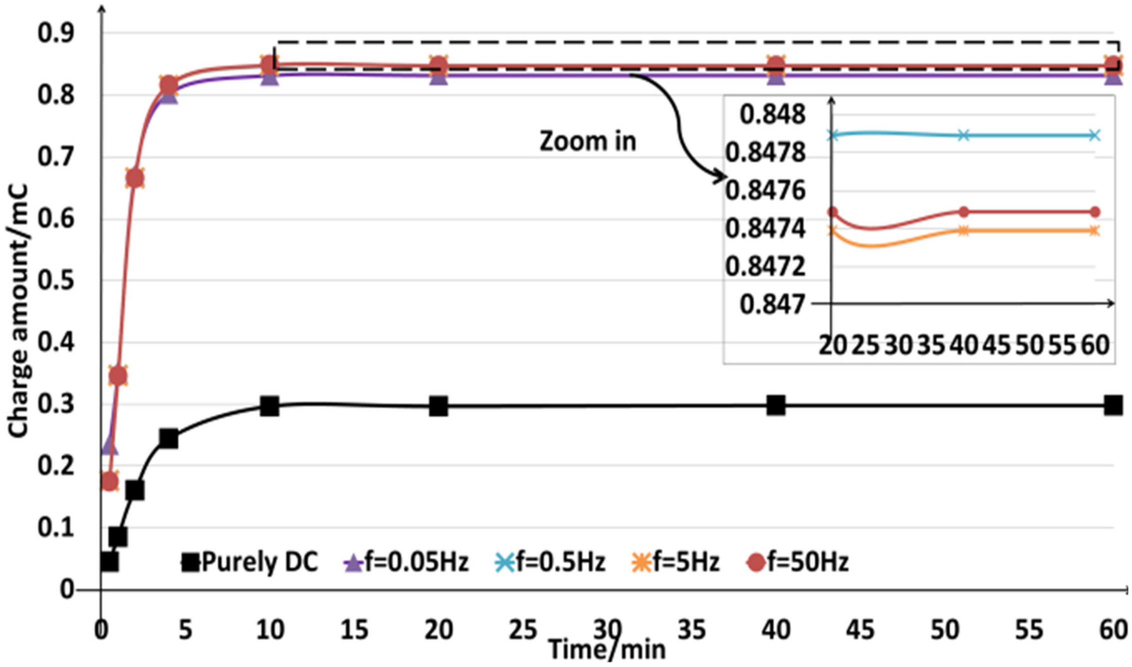

Figure 5-27 Integral total negative charge's trend over time under 50kV/mm fields with various frequencies

Figure 5-26 and Figure 5-27 demonstrate the integrated results of positive charge and negative charge amounts. The total positive charge amount and total negative charge amount under combined with large dc offset (>0.33) are larger than those under purely DC conditions, and the overall accumulated positive charge amounts of them are larger than the negative amounts.

Besides with the frequency increasing, the saturated amount of holes decreases. In contrast, this is not the case for electrons. The minimum amount of the saturated electrons occurs at the frequency of 0.05 Hz instead of 50 Hz. These two graphs also demonstrate the increase in frequency can weaken the charge accumulation within the insulation under the combined conditions.

In conclusion, the results show that the amount of the accumulated charges reduces with the increasing frequency, and the reduction becomes insignificant when the frequency is higher than 0.5 Hz. It is consistent qualitatively with experimental results found under AC conditions. Besides the frequency of the AC component within the applied electric fields can increase the time to reach the steady state. This effect is also relatively weak when the frequency is high.

5.5 Conclusions

In this chapter, the characteristics of applied superposed fields' influences on the charge dynamics within the insulation are analysed using both experimental and simulation approaches. Charge amounts and local field distortion enhance with applied field magnitude. Increased the localised charge amounts and enhanced charge transport mobility can be observed under larger magnitude applied fields, which eventually more severely distort the local fields. Localised charge amounts are significantly larger under combined stresses compared with under pure AC fields. The local field distortion under the superposed stresses can be more significant than under corresponding pure AC and DC conditions. Pure AC and DC tests designed in international standard, IEC 61378-2:2001, cannot reasonably evaluate the electrical performances of insulation under combined electric fields. Further, revise and improvements regarding testing voltage magnitudes, and testing durations are necessary. The amount of charges within the insulation decreases significantly with the applied field frequency. The increasing frequency of the applied fields can also change the shape of the accumulated charges inside the insulation. The fluctuation can be observed on the accumulated profiles under applied fields with low frequency. Overall, the applied fields' magnitudes and composition have more remarkable effects on the charge dynamics. The frequency of the applied fields demonstrates limited impacts on the charge dynamics when the frequency is higher than 0.5Hz, especially for the case where the DC offset percentage is high.

Chapter 6: Space charge and its role in the electrical breakdown of solid insulation

In this chapter, the influences of space charge phenomenon during the electrical breakdown process of solid insulation are investigated based on the proposed bipolar charge simulation model. The hypothesis of the simulation model is discussed in section 6.1. Specific setting of the numerical model is presented in 6.2. Charge dynamics under DC and AC ramping voltages and their roles in DC and AC electrical breakdown are analysed and discussed in section 6.3. The effects of sample thickness, voltage frequency and ramping rate on the charge dynamics and the obtained breakdown strength have also been discussed in sections 6.4 and 6.5 respectively based on the simulation results. Pure empirical observations obtained from numerous experiments are explained based on the analysis of space charge phenomenon within the insulation. Space charge's significant role in electrical breakdown process is clearly demonstrated.

6.1 Hypothesis of electric breakdown theory

Solid insulation plays a unique role in high voltage structures, which can provide the mechanical support for the conducting components while at the same time insulating them from each other. Therefore, it is of great practical importance to have an exhaustive knowledge of ageing and failure mechanisms of solid insulation. If a solid material is pure and homogeneous, the maximum applied voltage it can stand for a short time is defined as the intrinsic breakdown strength of the property. The temperature and environmental conditions of the tests are carefully controlled, and the testing sample is assumed to be without external discharges. The intrinsic breakdown happens in a very short period (about 10^{-8}s). Therefore, it has been postulated to be electronic and regarded as a property of the material and temperature only. The intrinsic strength is generally assumed to be reached when large amounts charge carriers in the insulator have absorbed sufficient energy from the applied fields to cross the forbidden energy gap between the valence and conduction band. In pure homogeneous dielectrics, the conduction and valence bands are separated by a large energy gap, and at room temperature, the electrons cannot acquire sufficient thermal energy to make transitions from the valence to conduction band. In practice, however, all crystals contain some imperfections in their structures, which act as traps for charge carriers laying within the energy band gap. At room temperature, these localised trap levels can assist the charge transport within the insulation, due to the small energy differences between the trapping levels and the bottom of conducting the band. When a field is applied to the insulation, the charge transportation and accumulation will reduce a local charge distribution (space charge distribution) within the insulation. Unbalanced regional charge distribution can severely distort the local electric field within the materials when the applied field is intensive or changing polarity [86, 93, 118]. Charges can acquire more energy from the distorted high electric field, which gives them a higher probability to cross the forbidden gap and trigger breakdown of the whole material. This indicates a breakdown phenomenon is a local event, which is strongly related to the charge dynamics in the insulation.

Several mechanisms (electronic, avalanche, electromechanical, thermal breakdowns, and partial discharges) have been proposed to explain the breakdown process. [85] However, few of them investigated the specific region where breakdown happens. From the charge dynamics presented in the previous Chapters, it is clear that charge accumulates in different areas within the insulation under HVAC and HVDC stresses. Those charges can severely distort the local electric fields within the insulation. Based on the proposed electrical breakdown theory, the place where the breakdown occurs should be affected by those charges. These locations could be differently located under AC and DC fields. The relationship between these breakdown locations and the different AC and DC breakdown strengths of same materials will be investigated in this Chapter.

Currently, few works have considered the space charge phenomenon during AC breakdown process. This is because localised charge amounts under AC stresses can be significantly smaller than same DC stresses due to the continuous polarity changing of the applied field [82, 99, 100]. On the other hand, the measured AC breakdown strength is generally much lower than DC strength for the same material [119, 120]. These two facts seem to conflict with each other. In general, the local field distortion caused by space charge phenomenon is affected by both charge amounts and charge positions. Although the accumulated charge amounts under AC stresses are relatively small compared with the same applied DC stresses, the charges are mainly accumulated adjacent to the electrodes. This can cause severe field distortion at certain applied field phases, and therefore, it is hard to conclude that the local field distortion will be more severe under DC fields then AC.

For electrical breakdown tests, impulse, ramping and long term voltage application is usually used to acquire the material breakdown strengths [122]. The short-term tests, impulse and ramping voltage method, are commonly used for dielectrics breakdown evaluation [122]. As for the longer-term tests, the lower measured strengths are generally obtained, due to the ageing of testing materials. The acquired breakdown strength of short-time tests is more close to ideal intrinsic breakdown strength of testing materials. Besides, regarding the constructing and maintaining costs, ramping voltage tests are more convenient than impulse tests and therefore are more generally applied to evaluate material breakdown strength. Based on all above, charge dynamics under ramping breakdown tests conditions are mainly studied in this section.

In this chapter, the electrical breakdown theory is mainly used to explain the breakdown process within dielectrics, to address the influence of the distorted local electric fields caused by space charge on breakdown position and breakdown strengths of the testing samples. The electrical breakdown theory assumes that breakdown process happens whenever the internal field reaches a critical level, dielectric breakdown strength. The proposed charge transport model is applied to analyse charge dynamics under both AC and DC ramping voltage until breakdown, offering a comprehensive view of space charge’s contribution in electrical breakdown process.

6.2 Numerical model for breakdown

The simulation of the breakdown process is based on the bipolar charge transport theory to analyse charge dynamics inside the insulation. In Chapter 4, a numerical model designed for charge dynamic analysis under both AC and DC fields has been introduced. The obtained numerical results present a significant similarity when comparing with the measured results in Chapter 3. In the model, negative differential mobility has been used to calculate the movements of positive charges. This can facilitate the packet-like charge observation in measurements under pure DC and superposed AC and DC fields. However, for space charge measurements under ramping voltage up to breakdown, the positive charge packets are hardly observed [110], which indicates the negative differential mobility model (Charge mobility model proposed in [97]) is not accurate in predicting charge profiles under extremely high applied fields close to breakdown. Therefore, in this chapter, power’s law is adopted to describe the relationship between the mobility of charge carriers and electric fields under ramping voltage till breakdown. The obtained DC breakdown strength is generally agreed with measured dc breakdown results [55, 110]. The proposed charge simulation model is capable of analysing charge profiles under both AC and DC fields, and are further modified according to the measured charge profiles under extremely high electric fields close to breakdown [86, 109, 110].

Figure 6-1 presents the measured space charge distribution under DC ramping voltage with ramping rate 300V/s and decay results after 7 hours AC field stressing. Figure 6-1 (a) shows the contour plots of charge density distribution within LDPE. The charge density lines are at 10 C/m^3 intervals, and the numerical values denote the charge density Q (C/m^3). Figure 6-1 (b) presents charge density position plot. Figure 6-1 (c) demonstrates the decay charge profiles of LDPE after 7 hours of 50Hz 50kV/mm AC field stressing.

According to measurements, under ramping voltage test, the distribution of positive and negative charge is relatively balanced. The accumulation of negative charge is slightly significant comparing with positive charges. However, under AC case, it is obvious that negative charges dominate the overall dynamics. Therefore, lower Schottky injection barrier and high mobility are designed for electrons in the numerical model. Besides, the mobile charge amount is much higher trapped charge one under both ramping DC voltage and constant strength AC field (Comparing with results in Chapter 3). Thus lower trapping coefficients (<1×10^{-2}) are used for both carriers. After many iterations, trial and adjustments, the final adopted parameters are listed in Table 6-1. An example of computed charge dynamics under ramping DC voltage (ramping rate: 300V/s) and under constant strength AC field are presented below in Figure 6-2(a) and Figure 6-2(b) respectively. The simulated results are very close to the measured ones (Figure 6-1(a), (b)) regarding both distribution shape and accumulated amounts. All these suggest that the proposed model with modified parameter setting can simulate the primary charge dynamics within insulation under both HVAC and HVDC conditions, and it is reasonable to use it to analyse charge dynamics under ramping voltage mode and to investigate the breakdown process.

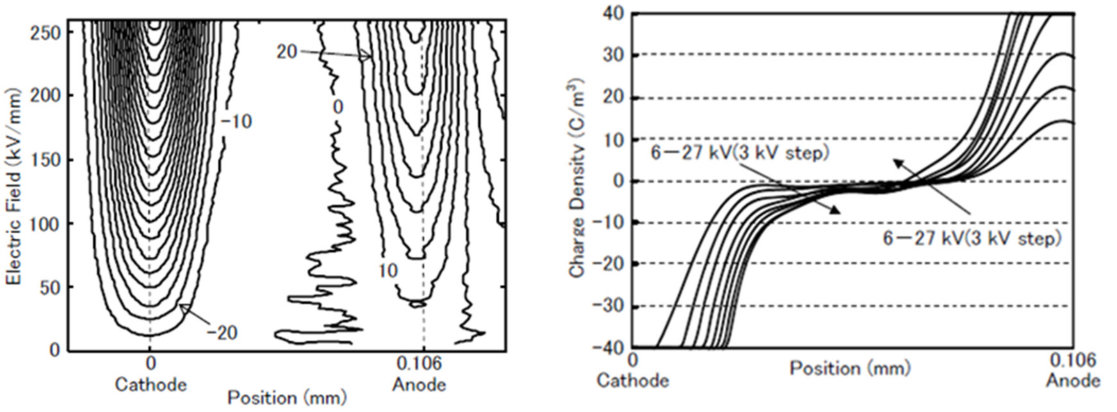

(a) Contour plot of space charge within 0.1mm LDPE sample

(b) Charge density-position plot of the sample within thickness of about 0.1mm

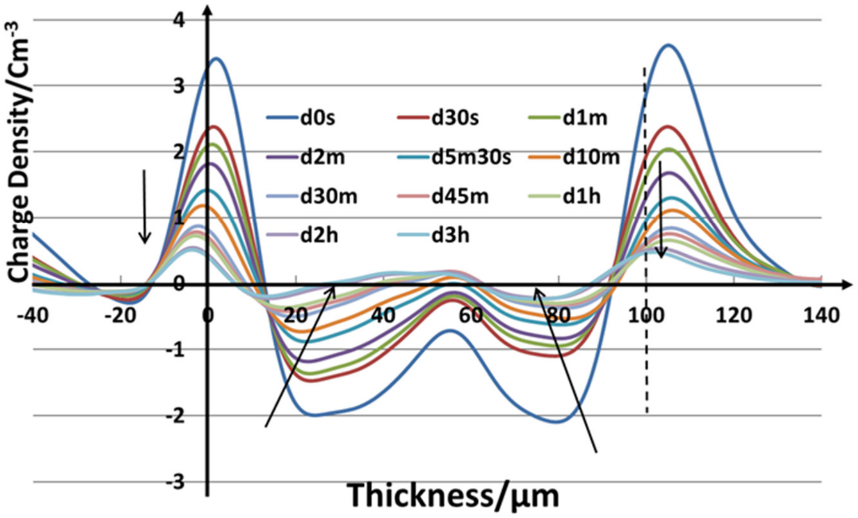

(c) Charge decay results of virgin LDPE after 7 hours of 50Hz 50kV/mm HVAC stress

Figure 6-1 Measured charge profiles under 300V/s DC ramping voltage up to breakdown (a), (b) [110], and charge profiles after 7 hour 50Hz 50kV/mm HVAC field stressing (c)

During the breakdown test, the voltage is applied from the two electrodes to the sample with a fixed ramping rate until the breakdown occurs. The ramping breakdown measurement system typically can test samples up to 0.1 mm thick, and the range of ramp rates can vary from 10 to 300 V/s. The typical ramp rate for samples under DC voltage is 100 V/s, while 50V/s for sinusoidal AC voltage [119, 120, 122]. Therefore, in the numerical modelling, the externally applied voltage is defined as follows:

$$\boldsymbol{V = R \cdot t \cdot sin(2\pi \cdot f \cdot t)} \tag{6-1}$$

where *R* is the ramping rate, and *f* is the external voltage frequency. In the simulation process, *R* and *f* can be changed according to the analysis requirements.

Table 6-1 Parameters for charge dynamics simulation of breakdown strength [91, 109]

Parameter	**Value**	**Unit**
Barrier height for injection		
W_{ei} (electrons)	1.1	eV
W_{hi} (holes)	1.12	eV
Low field Mobility μ_{E0}	9×10^{-16}	$m^2V^{-1}s^{-1}$
Low field Mobility μ_{h0}	3×10^{-16}	
Power law's index of mobility n	1.165	$m^2V^{-1}s^{-1}$
Trap density		
N_{0et} (electrons)	100	Cm^{-3}
N_{0ht} (holes)	100	Cm^{-3}
Trapping coefficients		
Be (electrons)	7×10^{-3}	s^{-1}
Bh (holes)	7×10^{-5}	s^{-1}
Recombination coefficients		
S_0 trapped electron-trapped hole	4×10^{-3}	$m^3C^{-1}s^{-1}$
S_1 mobile electron-trapped hole	4×10^{-3}	$m^3C^{-1}s^{-1}$
S_2 trapped electron-mobile hole	4×10^{-3}	$m^3C^{-1}s^{-1}$
S_3 mobile electron-mobile hole	0	$m^3C^{-1}s^{-1}$
Temperature T	300	K
Breakdown strength level	500	$kVmm^{-1}$

The simulated material is a low-density polyethylene film with the thickness ranging from 50 to 200 µm. From the existing experimental results in [86], it has been observed that the breakdown occurs when the local electric field strength in polyethylene is around 500 kV/mm. Thus in our simulation, the breakdown strength level is settled to be 500kV/mm.

Whenever the maximum local field reaches that value, the breakdown is considered to have occurred. After that, the current applied voltage is divided by the sample thickness to get the apparent breakdown strength, which represents the obtained breakdown strengths in ramping voltage tests. The apparent breakdown strength is deduced as equation 6-2.

$$\boldsymbol{S = \frac{V_B}{D_T} = \frac{R \cdot T_0}{D_T}} \tag{6-2}$$

where S is the apparent breakdown strength; V_B is the measured maximum voltage during the breakdown tests; D_T is the testing sample thickness, and T_0 is the testing time.

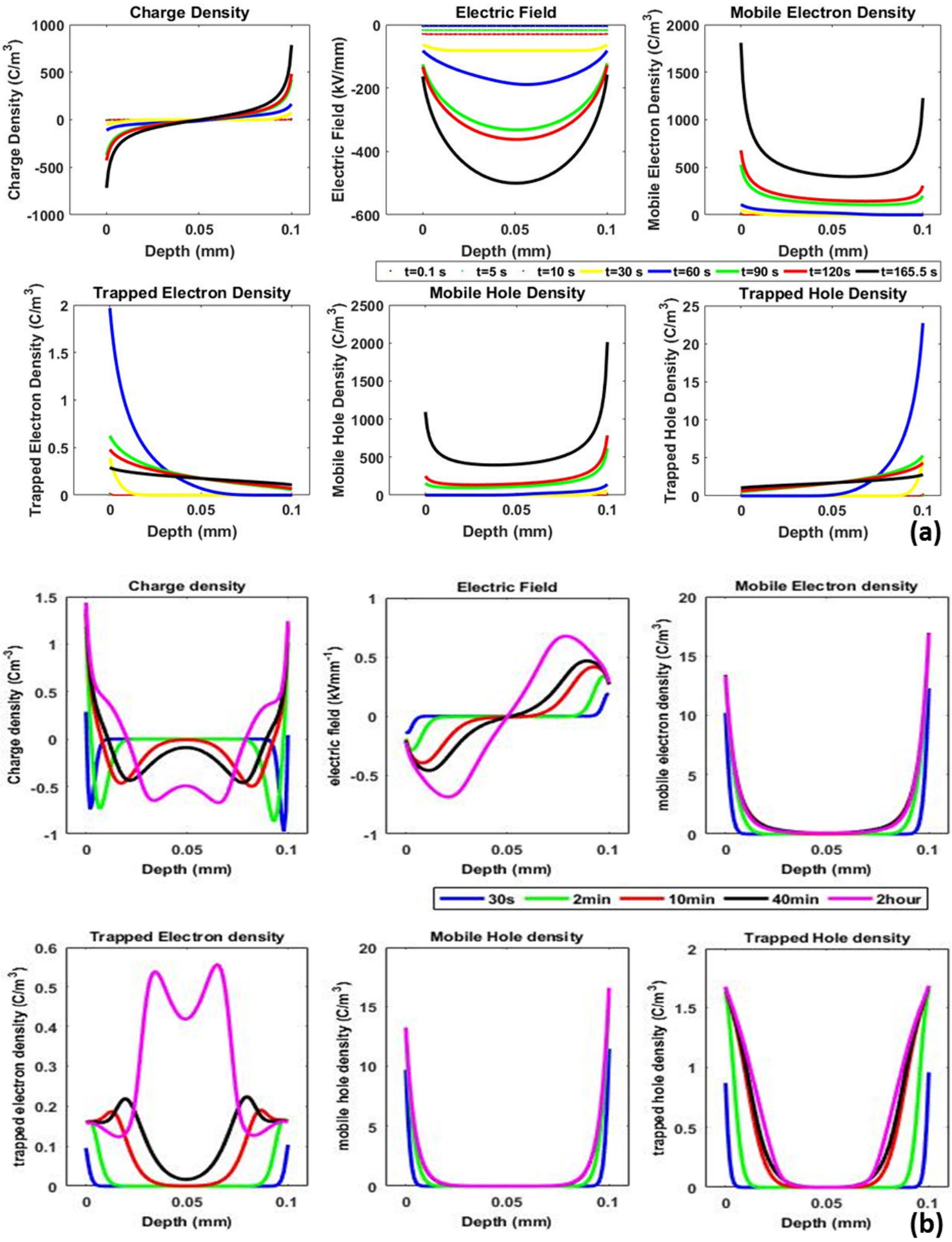

Figure 6-2 Simulated profiles under 300V/s DC ramping voltage (a) (Breakdown happens at 165.5s), and profiles under 50Hz 50kV/mm HVAC stress at phase 0 (b)

6.3 Charge dynamics and their role in breakdown region of the insulating material

Numerous experimental studies on various insulating materials have demonstrated that normally the measured DC breakdown strength of a material (Around 500KV/mm for polyethylene) is much higher than its AC breakdown strength (Around 150kV/mm) [119, 120]. The acquired breakdown strength of the same material increases with decreasing testing sample thickness, and the rising of testing voltage ramping rate (For ramping voltage tests). For AC conditions, the breakdown strength of materials decreases with the increasing frequency of applied voltage. These phenomena are purely empirical, and many hypotheses (defect, percolation and threshold theories) have been tried to explain the phenomena [85]. However, the majority of them are lack of creditable experimental results and not able to describe dynamics under HVDC and HVAC [63].

6.3.1 Charge dynamics under DC ramping voltage tests

Under high HVDC electric fields, the positive charges transporting like a packet is generally observed in measurements of space charge within the insulation. This can strongly distort the local electric field inside and accelerate the breakdown process under HVDC. Therefore, to simulate and analyse breakdown process under HVDC, the charge packet phenomenon should be intensively investigated and considered. A computed example within 50μm LDPE under 50V/s DC ramping voltage until breakdown is discussed here to illustrate the charge dynamics during DC breakdown process. The obtained apparent breakdown strength for this case is 421.8kV/mm, which is very close to the measured DC breakdown strengths of LDPE. [55, 86, 110]

Figure 6-3 presents the charge and field profiles at the breakdown time under a ramping field. Comparing it with profiles obtained under constant strength high voltage fields (Results in Chapters 3 and 4), it is noticeable that charge density under breakdown is significantly larger than those under constant strength fields. Figure 6-4 illustrates the charge composition changing along with field stressing time. It is clear that after 200s (applied field strength >200kV/mm), the majority of the accumulated charges within insulation are mobile charges. These charges can rapidly respond to the rising applied voltage and increase to an enormous amount when the breakdown happens. The recorded field increment and the maximum field distortion in Figure 6-5 further confirm the trend. The non-linear relationship can only be found in the initial 100s in the field increments when the trapped charge percentage counts around 1/4. After that, the field increment is mainly caused by the mobile charges and increases linearly with the applied voltage. Besides, due to mobile charge can quickly transport within insulation, the obtained charge and electric field profiles are relatively balanced. Breakdown happens in the central of the testing sample, as demonstrated in Figure 6-3.

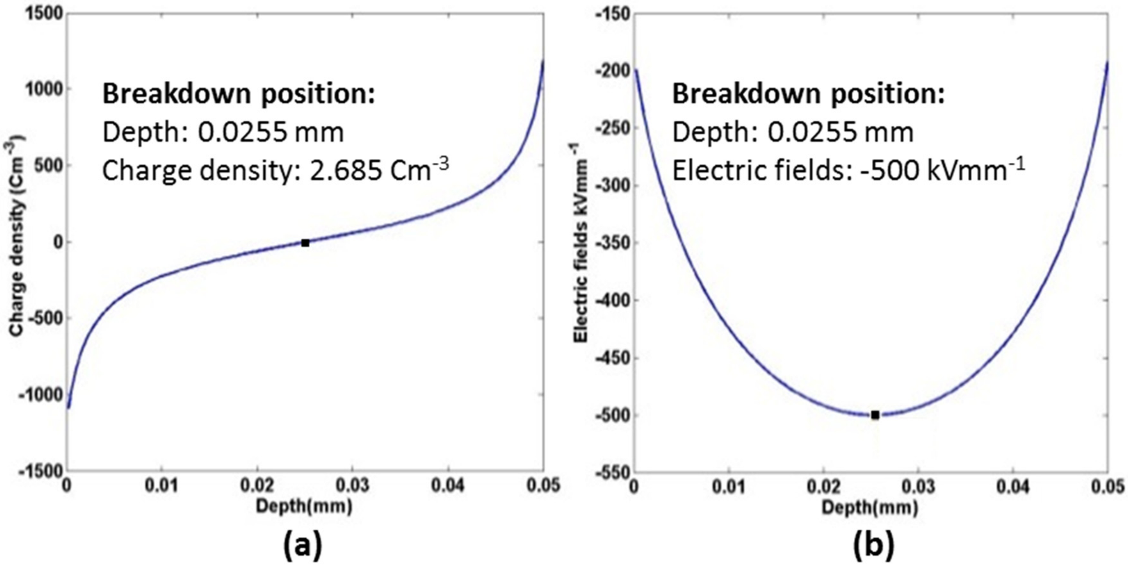

Figure 6-3 Charge (a) and electric fields (b) profiles at the breakdown for 50um LDPE under HVDC with a ramping rate of 50V/s. Apparent breakdown strength for this case: 421.8kV/mm. The marked points in graphs indicate the position where breakdown happens.

The computed breakdown strengths for this case is close to the measured DC breakdown strength of LDPE under ramping voltage tests. [11, 55, 110] The simulated charge and electric fields profiles are also identical to the experimental results under ramping DC voltage till breakdown in [110]. Figure 6-4 presents the field increment, and maximum field distortion deduced from simulated profiles for 50um LDPE under HVDC with a ramping rate of 50V/s. The deduced field increment is a little larger compared with the measured results obtained by Murakami [110]. This may due to the smaller ramping rate used in the simulation, which causes the longer time for charges to distort the local field further. From Figure 6-4, it is obvious that the field increment is insignificant during the initial 50 seconds of testing. This is because ,during the initial 50s, the localised charges are relatively close to the electrodes due to limited charge transportation under relatively low strengths of fields, and the homecharge accumulation adjacent the electrodes suppress the further charge injections. However, after 100s, the applied electric field is sufficient intensive, which significantly enhance the charge transportation. Therefore the field increment becomes remarkable and in proportion to the applied field strength. The enhanced charge transportation can also relief the local field distortion as charges can be more balanced distributed. The deduced trapped charge percentage in Figure 6-5 confirms the enhanced charge transportation after 100s ramping voltage testing. After 100s, the trapped charge percentage rapidly decrease from more than 20% to less than 5%, which indicates mainly mobile charge existing within the insulation after 100s of ramping DC voltage testing.

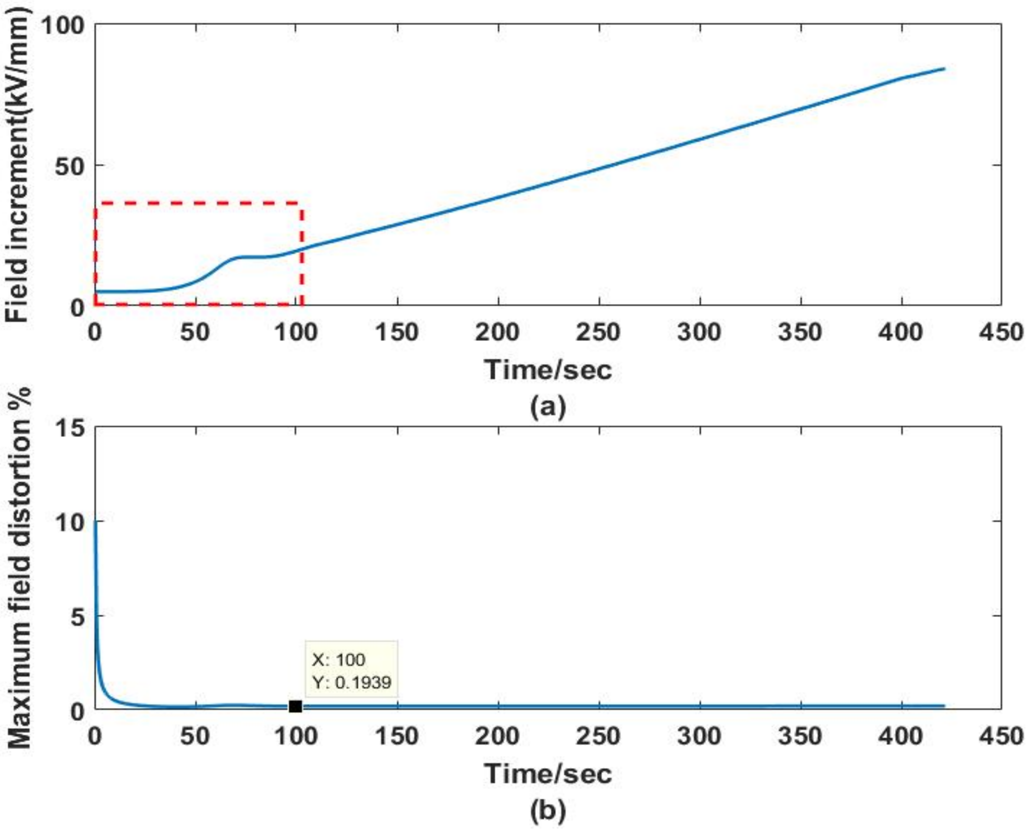

Figure 6-4 Field increment and maximum field distortion within the sample during the breakdown testing process

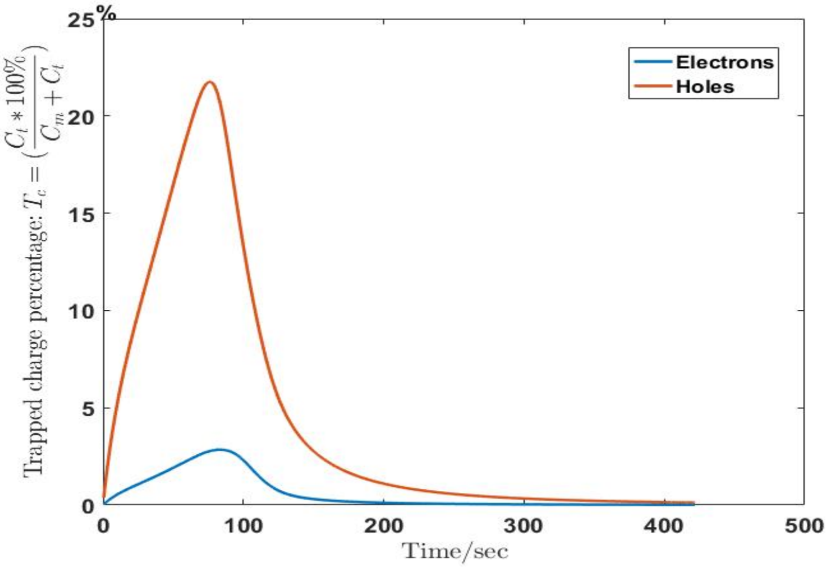

Figure 6-5 Charge composition vs. field stressing time. The graph illustrates the trapped charge percentage within the overall accumulated charge amounts. The blue line indicates the negative charges while the red line represents the positive charges.

6.3.2 AC breakdown simulation

As for AC breakdown process, generally lower breakdown strengths are obtained comparing with under DC voltages for the same material in ramping test measurements. Besides based on results in Chapters 3-5, it is apparent that charge and field profiles within insulation present remarkable differences under AC and DC conditions due to the quick change of the applied field polarity. Therefore, it is of great significance to using the proposed breakdown simulation model analyse charge dynamics within insulation under AC ramping voltage and explain the general observations in breakdown tests.

Figures 6-6 and 6-7 present a simulated example of 50μm LDPE subjected to 50 Hz HV AC voltage, increasing from zero with a ramping rate of 50 V/s until breakdown. The obtained breakdown strength for this condition is 160.8 kV/mm. This computed breakdown strength is close to the measured results obtained by Hussin et al. [119]. In [119], following the analysis using Weibull distribution on the breakdown data of 50um LDPE under the same testing condition, the characteristic breakdown strength of 192.2kV/mm was obtained, with a 90% lower and uppers bounds of 148 kV/mm and 226 kV/mm respectively. Charge profiles at the breakdown cycle are illustrated in Figure 6-6, and the corresponding electric fields are shown in Figure 6-7.

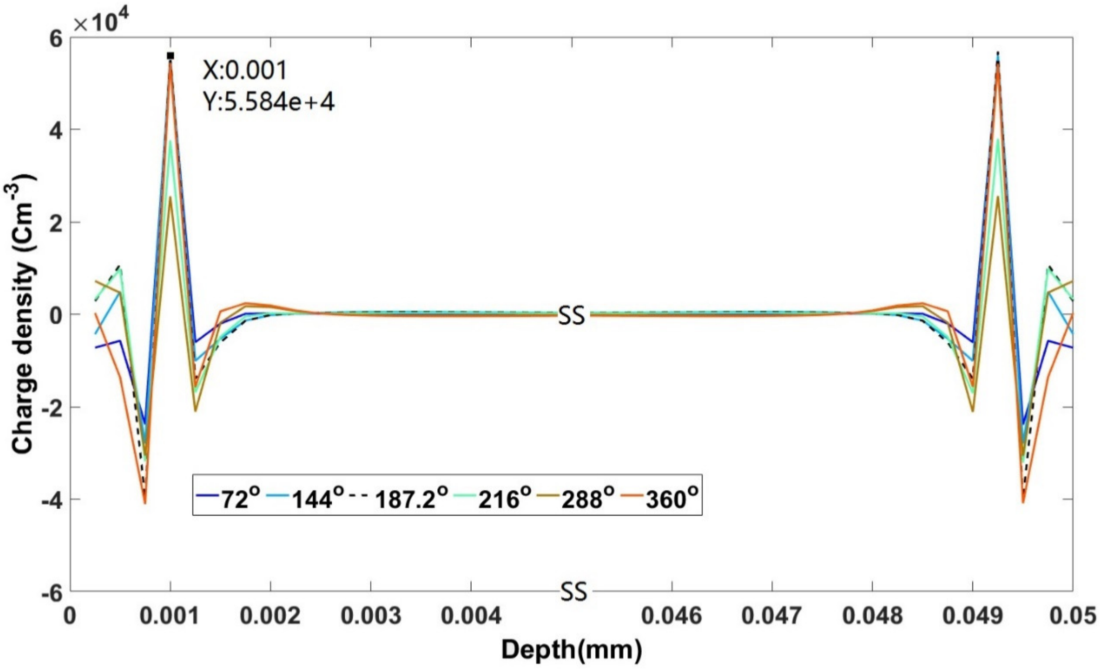

Figure 6-6 Charge profiles corresponding to breakdown cycle for 50um LDPE under 50Hz HVAC with a ramping rate of 50V/ s. Apparent breakdown strength for this case: 160.8 kV/mm. The marked points in graphs indicate the position where breakdown happens.

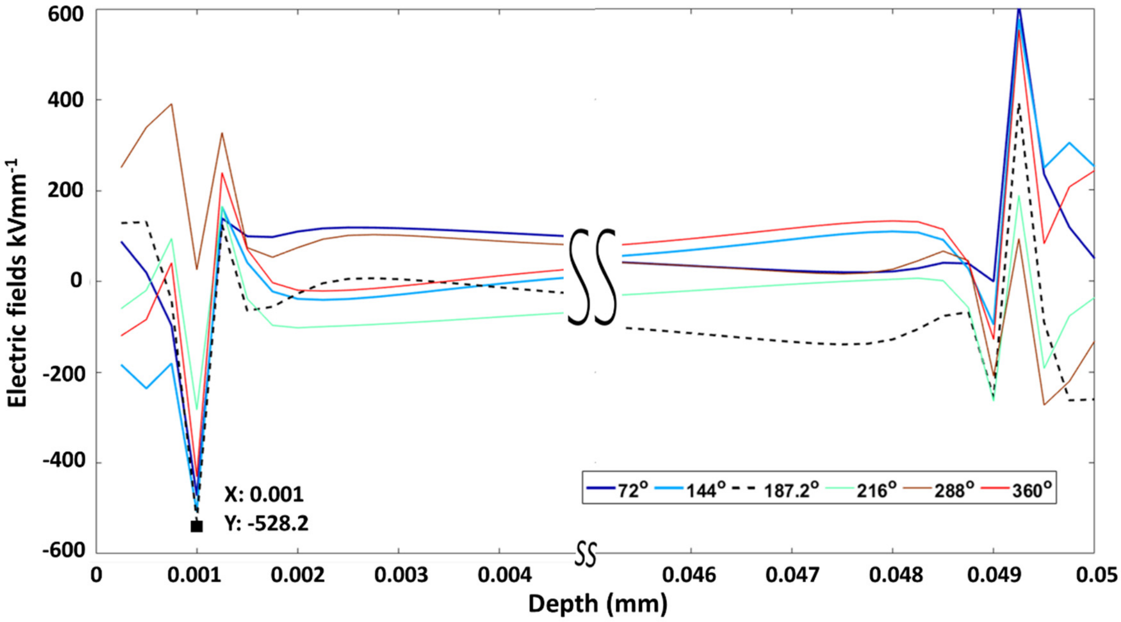

Figure 6-7 Electric fields profiles corresponding to breakdown cycle for 50um LDPE under 50Hz HVAC with a ramping rate of 50V/s. Apparent breakdown strength for this case: 160.8 kV/mm. The marked points in graphs indicate the position where breakdown happens.

For the computed DC results show a much higher breakdown strength of 421.8 kV/mm, and it is likely that the breakdown initiates from the middle of the sample where the maximum electric field occurs. On the other hand, under AC conditions, the highest fields' distortion happens typically near the electrodes. Although the integral area charge density at breakdown time is smaller under AC stress (6.93x 10^{-3} C/m^2) than DC stress (1.24x10^{-2} C/m^2), the maximum peak value of the charge density is significantly larger under AC stress (5.58 x 10^4 C/m^3) than DC stress (1.19 x 10^3 C/m^3). This adjacent electrode charge peaks obtained under AC condition distorts the local electric field severely (twice larger than the applied fields). Therefore, the local field reaches the breakdown strength more quickly under the ramping AC stress as all these injected space charges accumulate within a narrow region near the electrodes and significantly distort the local electric fields near the surface. On the other hand, the injected charges under DC conditions can move further into the bulk of the sample, and the maximum electric fields distortion happens in the middle of the sample, where the holes and electrons encounter each other. Therefore, the local field under ramping DC voltage will take a longer time to reach the breakdown level, compared with the AC voltage, which corresponding the lower DC apparent breakdown strength of materials. Section 6.2.3 presents a more specific analysis of the breakdown regions under various applied fields.

6.3.3 Breakdown region

From both measured and simulated results in this work, it is clear that charges accumulate in different regions under DC and AC stresses. Those trapped charges can severely distort the local electric fields within the insulation. Local electric field enhancements will accelerate ageing and eventually lead to the breakdown. All these above indicate breakdown may take place in different regions under DC and AC fields.

Figures 6-3, 6-4 and 6-6 and 6-7 present computed examples demonstrating the charge distributions and electric fields within polyethylene under DC and AC stresses respectively when the breakdown happens. The simulated conditions for these two are the same, except for the applied fields. From graphs, it is obvious that the charge dynamics under DC and AC ramping stresses are different: Under DC stress, charges can transfer further into the bulk of the material, while under AC, they mainly accumulate adjacent to the electrode. These different charge distributions can cause different local field distortions, which eventually will make the value and the location of the maximum electric fields (where breakdown happens) different. The field distortion adjacent to the electrodes for AC cases usually is more intensive, as less amount of charge and smaller charge transport distance needed to cause the distortion, compared with the distortion in the middle region under same strength DC fields. Thus, the local electric field under AC condition is more easily and rapidly to reach the breakdown level comparing with under DC stress, which makes the apparent breakdown strength obtained in ramping breakdown tests much lower. (The supplied electric fields of 160.8kV/mm for 50Hz AC and 421.8kV/mm for DC are required respectively.)

To figure out the relationship among charge dynamics, apparent breakdown strengths, and the applied field frequency, Figure 6-8 presents the distance of the breakdown region (left ordinate) and apparent breakdown strength (right ordinate) evolving along with frequency increasing. It is clear that breakdown happens within the area more close to the electrodes under higher frequency applied field, as it is harder for charges under higher frequency fields to transport into the bulk of insulation. Because the majority of them accumulate more closely to the electrodes with the increasing frequency, the field within the region close to the electrodes of the material is more severely and rapidly distorted. Therefore, breakdown can be triggered under lower applied electric field when the frequency is higher.

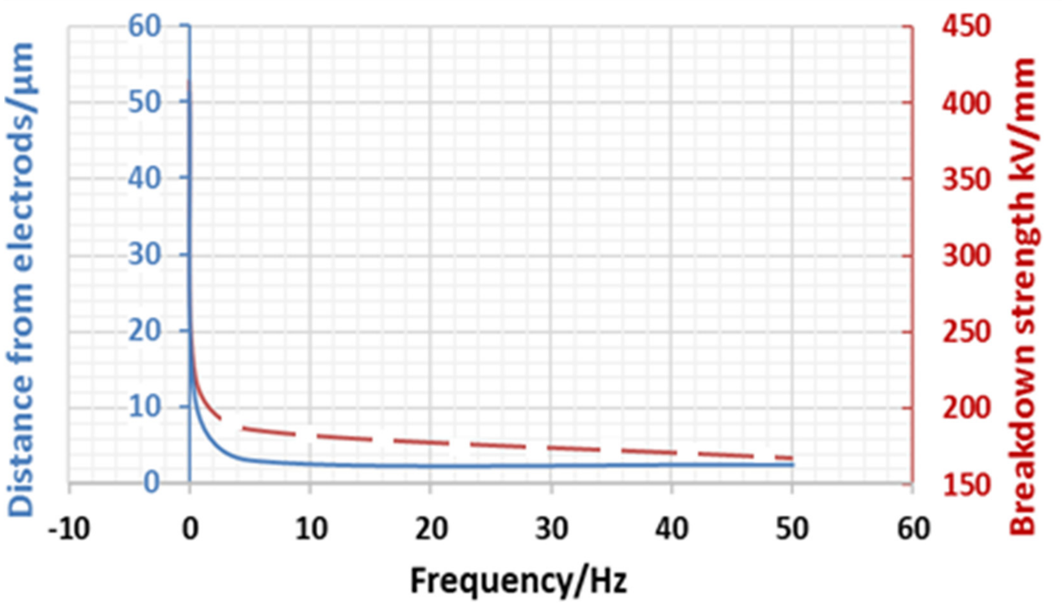

Figure 6-8 Computed results of the distance of breakdown region towards electrodes and the breakdown strength of 100 μm samples under various frequency applied fields with ramping rate 100V/s.

The blue curve is matching with the blue Y coordinate (left), indicating the distance of breakdown place from the electrodes changing with applied field frequency. The red dash line matches with the red Y coordinate (right), presenting the breakdown strength changing with applied field frequency.

Breakdown region corresponds to the place where the local electric field is most severely distorted. Besides, breakdown region can also represent where the most intensive charge dynamics happen in the insulation. From Figure 6-8, it is also distinct that the distance of breakdown region to the electrode demonstrates a similar trend as the apparent breakdown strength when the ramping rate (R) and the thickness (D_T) are fixed. Therefore, the distance, D, is proportional to the stressing time to achieve breakdown, T_0, based on 6-2, when R and D_T are fixed. This means the breakdown region can, as a factor, indicate how rapidly the breakdown process conducts. ($T_0 \propto D$)

All these above confirm the assumption that the apparent breakdown strengths of insulation are strongly related to the region where the breakdown takes place. Breakdown happens more rapidly and more closely to the surface of dielectrics when the frequency of the applied fields is higher. The more severely unbalanced and distorted electric fields, caused by charge dynamics, is a significant reason leading to the lower apparent breakdown strengths of the same material under HVAC comparing with under HVDC. Besides, the investigation of breakdown region can link the charge dynamics in micro view with the overall material characteristics. Therefore, breakdown region should be much more concerned in the study of breakdown process.

6.4 Relationship between breakdown strength and testing sample thickness

Based on numerous experimental results [89, 110, 123], the apparent breakdown strength of insulating material demonstrates a decreasing trend along with adding testing sample thickness. An inverse power's law, shown in 6-3, is generally used to analyse the trend [123], and the principle can apply to various kinds of dielectrics under different conditions. However, this principle is purely empirical, and many attempts (defect, percolation and threshold theories) have been tried to explain the phenomenon. Most of them are lack of creditable experimental results and not able to describe dynamics in the material under higher electric fields. [63]

$$E(d) = k \cdot d^{-n} \qquad \textbf{6-3}$$

where *E* is the applied electric field at the breakdown, in this Chapter it is equal to *S*, and *k* and *n* are two constants that are associated with the testing materials.

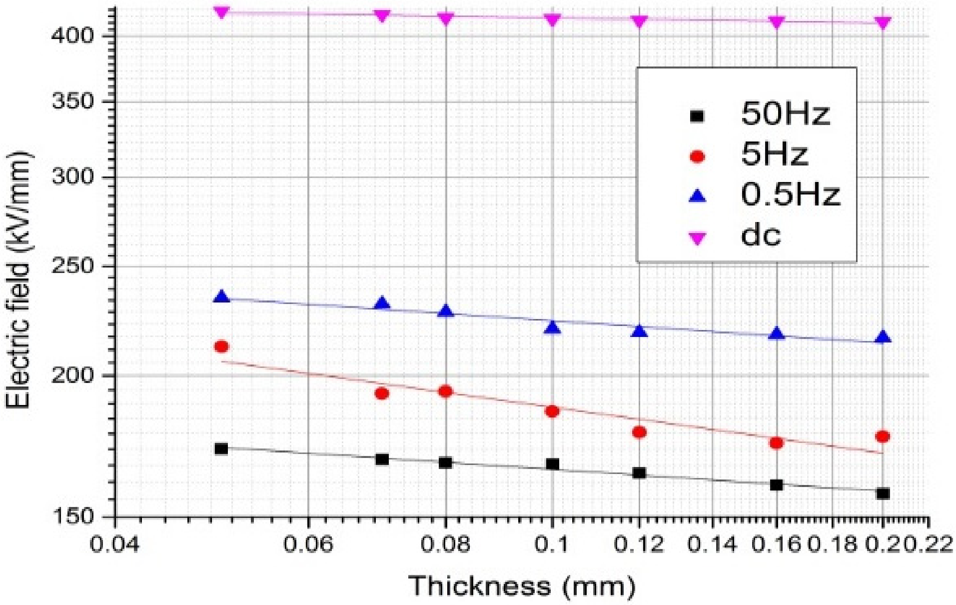

Figure 6-9 Breakdown strengths versus sample thickness under different frequencies fields (Fitted index of power law: -0.0645—50Hz, -0.1351—5Hz, -0.0653—0.5Hz, -0.0151—DC)

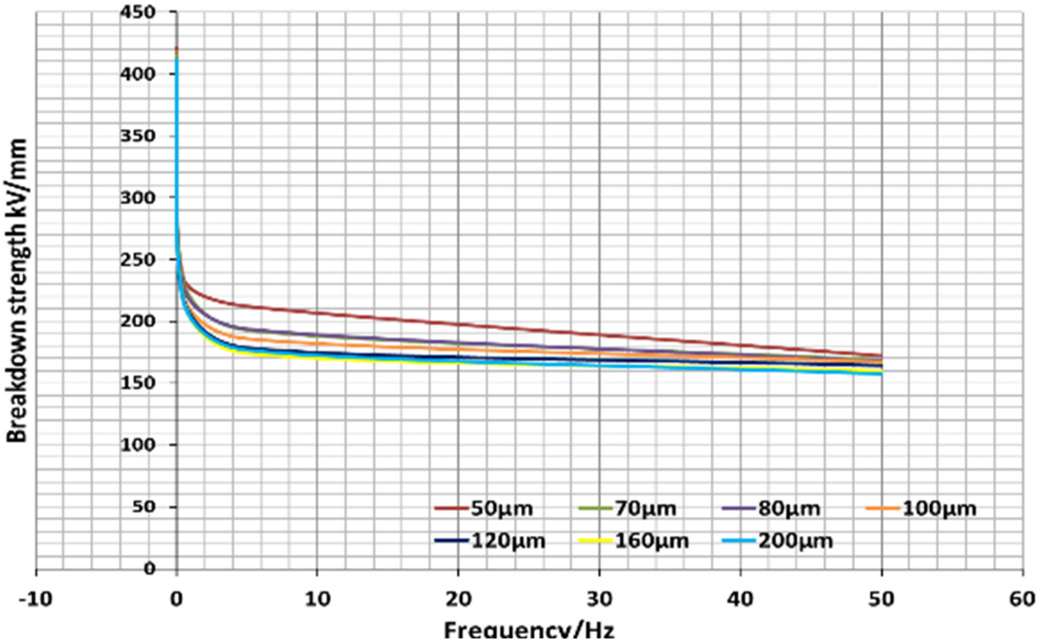

Figure 6-10 Breakdown strengths versus frequencies within different thickness sample

In this section, the relationship of the sample thickness and breakdown strengths is analysed and discussed using the simulated results with a range of thickness from 50µm to 200µm under different frequency stresses with a fixed voltage ramping rate of 100V/s. The calculated results are presented in Figure 6-9 and Figure 6-10. Figure 6-9 demonstrates the calculated apparent breakdown strengths of materials decreasing along with the increasing of testing sample thickness. The reduction trend follows the inverse power's law, consistent with the phenomena observed in experiments [89, 110, 123]. From the fitted indexes of the power's law under various applied fields frequencies, it is clear that the breakdown strength changes more severely with the alteration of the thickness under AC stress. However, all the fitted power indexes are smaller than its typical value, 0.5, observed in measurements [123]. This may indicate the apparent breakdown thickness dependent phenomenon is an integral characteristic caused by multiple factors. Charge dynamics under high voltage stress are only part of the reason. Defects, percolation, and some other procedure may have also contributed to the trend. Figure 6-10 presents the results in Figure 6-9 in another view. In Figure 6-10, the trend of apparent breakdown strength decreasing within increasing of the applied frequency under all cases is more directly illustrated. In addition, it is easy to distinguish that the apparent breakdown strength presents a significant difference among thickness when the applied fields' frequency is changing from 0.5Hz to 20Hz. Moreover, for all frequency cases, the apparent breakdown strength decreases sharply when the thickness is enhancing from 50µm to 100µm. The differences of the strengths are relatively small when the testing sample thickness is larger than 100µm.

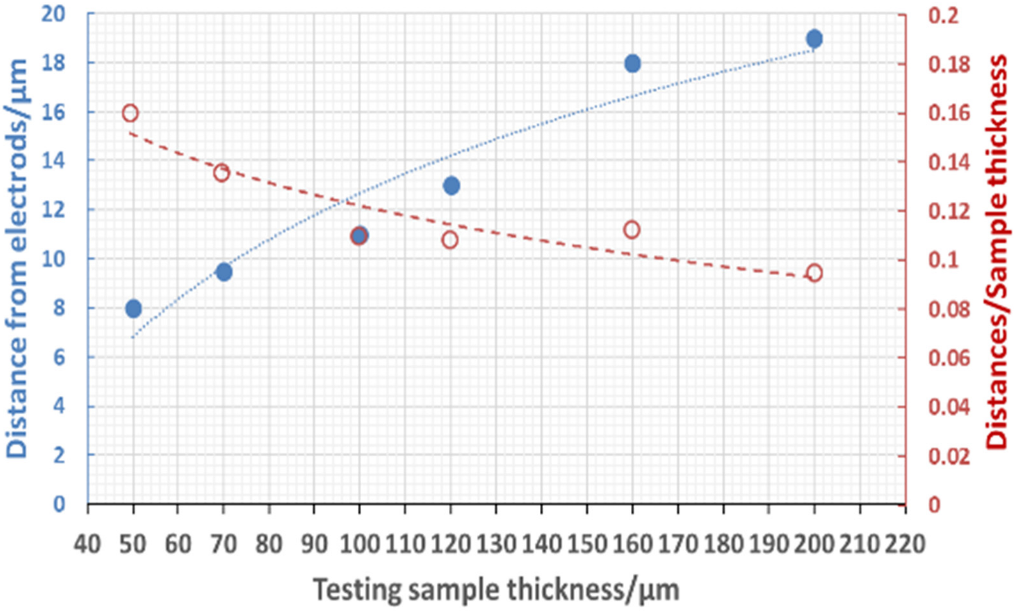

Figure 6-11 The distance of breakdown region towards electrodes of various thickness samples under 0.5Hz HVAC fields with ramping rate 100V/s.

The blue dot curve is matching with the blue Y coordinate (left), indicating the distance of breakdown place from the electrodes changing with testing sample thickness. The red dash line matches with the red Y coordinate (right), presenting the breakdown strength changing with testing sample thickness.

The distance of breakdown region towards electrodes of various thickness testing sample is recorded in Figure 6-11, to directly illustrate how inter charge dynamics cause the apparent breakdown strength changing with thickness. Results under 0.5Hz fields are chosen to discuss, as the charge can evolve within a relatively large region under this lower frequency AC stresses. From Figure 6-11, it is clear that the distance *D* increases, while the distance to thickness ratio, $(\frac{D}{D_T})$, decreases along with thickness adding. The trends in Figure 6-11 indicates the electric fields distortion, caused by severe charge dynamics in the surface region under HVAC, is alleviated along with the testing sample thickness increasing. However, this relief is quite limited, as in thicker samples, the localised charges will become more difficult to transport to the other side. Breakdown still happens adjacent to the electrodes (from $(\frac{D}{D_T})$, it is actually closer) within thicker samples under HVAC stresses with relatively high frequency (>0.5Hz).

Besides, the fitted trend line of $(\frac{D}{D_T})$ vs. D_T (thickness) seems to have a decreasing changing rate, which indicates the extent of $(\frac{D}{D_T})$ changing reducing with thickness adding. That leads to limited changes of breakdown strength can be found for all frequency cases when the testing sample thickness is larger than 100 µm. Furthermore, when applied fields frequency increases, *D* reduces, but the extent of the changing rate is also decreasing (Figure 6-9). That explains the significant differences observed among results under applied voltage with frequency lower than 20Hz in Figure 6-11.

In summary, the computed apparent breakdown strength shows a similar relationship with the testing sample thickness comparing with observation in practice. This confirms the charge dynamics within the insulation is a significant reason causing the apparent breakdown strength affected by thickness. The apparent breakdown strength can have an enormous gap between the intrinsic breakdown strength, especially for the thicker sample under higher frequency applied fields. Breakdown region can be recorded as a factor containing information of charge dynamics and electric fields distortion, to explain the relationship between apparent breakdown strength and testing sample thickness. The simulation model and explanation in this Chapter are quite preliminary, and based on many assumptions aiming to simplify the situation. In reality, the trend of apparent breakdown strength decreasing with the increase of testing sample thickness may be caused by numerous reasons, including the effects of charge dynamics with the insulation. Nevertheless, based on the results shown in this session, bipolar charge theory demonstrates a promising possibility to simulate and investigate the charge dynamics during breakdown process.

6.5 Relationship between breakdown strength and voltage ramping rate

In addition to the thickness dependent trend of the measured breakdown strengths, it has been reported that the ramping rate of the applied voltage can influence the measured apparent breakdown strength of the material. Different ramping rates have been used to measure the breakdown strength in various publications [89, 110, 119, 120]. To compare the apparent breakdown strength obtained by the measurements with different ramping rates, the effect of the ramping rate on breakdown strength is analysed and discussed using the proposed model.

Figure 6-12 presents the computed apparent breakdown strength under both HVAC and HVDC conditions. For both conditions, the material breakdown strength increases along with the ramping rate rising. A similar trend for the apparent breakdown strength has been observed experimentally. [124] Rapid increase of the apparent breakdown strength happens from the ramping rate adding from 50V/s to 250V/s. However, it seems the ramping rate has severer influences on apparent strengths under AC conditions. From 50V/s to 500V/s, a change of more than 100kV/mm has been observed. This may be account for the differences in testing breakdown strength for materials under AC conditions presented in literature. Even for the same testing system and testing environment, the influence caused by the various ramping rates should also be taken into consideration for comparing breakdown strengths of material under HVAC electric fields.

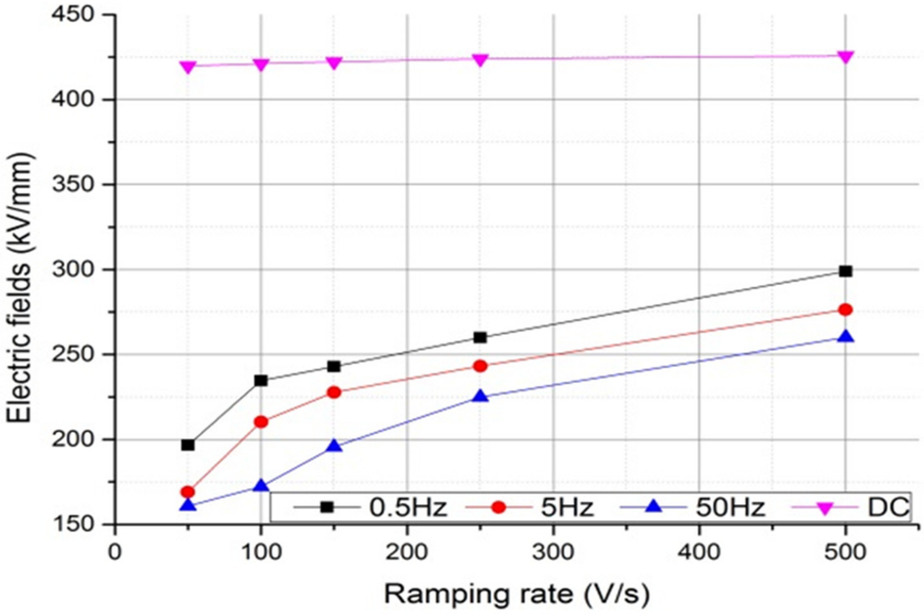

Figure 6-12 Breakdown strengths under different ramping rate of applied fields.

The distance of breakdown region towards electrodes (D) under different ramping rates (R) is recorded and analysed in Figure 6-13. An initial approach is proceeded here to explain how charge dynamics can cause the apparent breakdown strength increasing along with ramping rate rising. From Figure 6-13, it is clear that the distance D decreases, while the product of the distance and ramping rate, ($D \cdot R$), increasing along with thickness adding. This indicates severe charge dynamics within insulation happens more closely towards electrodes, under higher ramping rate stresses. However, the influences of these dynamics on the local field distribution are weakened along with ramping rate increasing. This is because under higher ramping rate fields, it takes a shorter time to achieve the same applied field strength and the charge formation and transport require specific time to cause severe fields distortion.

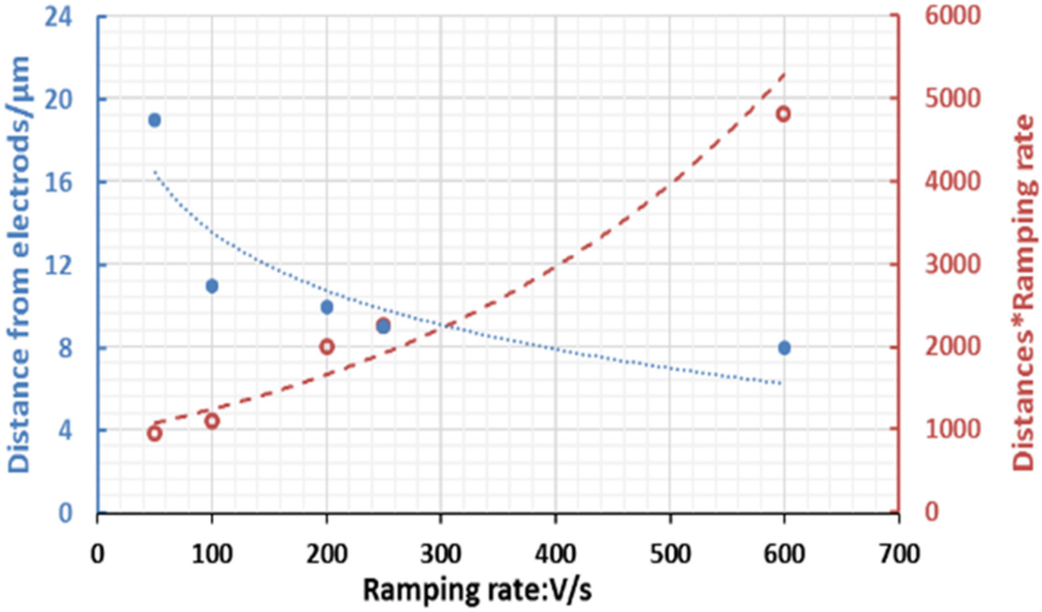

Figure 6-13 The distance of breakdown region towards electrodes of 100 μm samples under 0.5Hz HVAC fields with different ramping rates.

The blue dot curve is matching with the blue Y coordinate (left), indicating the distance of breakdown place from the electrodes changing with testing voltage ramping rate. The red dash line matches with the red Y coordinate (right), presenting the breakdown strength changing with testing voltage ramping rate.

In conclusion, the apparent breakdown strength increases along with applied field's ramping rate rising. In the evaluation of materials' breakdown strength, the ramping rate's effects should be taken into account. Currently, there is no general agreed trend illustrating how apparent breakdown strength increases with the ramping rate raising. The work here presents a possibility to use simulation and analysis of charge dynamics within insulation during the breakdown process deducing and explaining the relationship. However, large amounts of experimental work are still needed to convince the trend and explanation.

6.6 Conclusions

In this chapter, a simulation model suitable for analysis for both AC and DC breakdown process has been proposed, based on bipolar charge transport theory. The influences of common factors, applied field's frequency, testing sample thickness and applied field's ramping rate, have been investigated and explained based on the model. The obtained charging trends of apparent breakdown strength are consistent with general observations in breakdown strength measurements. This confirmed the feasibility to use charge dynamics to explain and investigate materials' integral characteristics, like apparent breakdown strengths. It has also been found that the apparent breakdown strength is strongly related to the place where breakdown happens. The different breakdown happening regions caused by divergent charge dynamics is a significant reason leading the apparent breakdown strength of the same material different, under AC and DC conditions. Different testing sample thickness as well as applied field ramping rate can also change the breakdown happening region and the obtained apparent breakdown strengths.

Chapter 7: Conclusions and future work

7.1 Conclusions

This work concentrates on analysing charge dynamics in polyethylene under various periodical high voltage. A PEA system along with the promoted data analysis procedure has been proposed and used to investigate charge dynamics under various electric stresses. A numerical simulation model based on bipolar charge transport theory is proposed and specified for different applied fields' conditions. A procedure of comparing measured results and simulated results are illustrated, and for the simulation under HVDC, the parameter setting has been optimised to ensure the simulation quantitatively accurate compared with measurements. Based on the research, it has been found that the various local field distortion caused by the different charge dynamics is the fundamental reason accounting for the different electric performances of dielectrics under various applied field conditions. The features of applied fields such as magnitude, frequency and composition on the charge dynamics within insulation have also been analysed taking advantage of experimental results and the proposed numerical model. The influences of ageing within the insulation caused by various stressing fields are discussed using Raman and FTIR spectra. Furthermore, space charge's contribution in electrical breakdown of solid insulation is also investigated, adopting the proposed numerical model.

For the experimental part, PEA techniques have been used to measure charge profiles within LDPE under HVDC, HVAC and superimposed AC and DC electric fields. A phase recovery process accompanying with subtraction methods has been developed to straightforwardly illustrate the accumulated charge profiles under periodic stresses in the different phase angles within a cycle and the charge evolution along with stressing time at the same applied field phase. The measured results clearly demonstrate that charge dynamics present various characteristics under HVDC and HVAC stresses. Charges transfer from electrodes into the bulk of insulation continually under HVDC, while mainly accumulated adjacent electrodes under HVAC stress. Remarkable amounts of positive charges can be observed within LDPE under HVDC, especially for the field strength higher than 40kV/mm. On the other hand, mainly negative charges can be found under HVAC fields. These cause the different field distortion under DC and AC fields, which eventually results in different ageing and electrical breakdown mechanism under the two cases. Raman spectra and ATR- FTIR tests have been done to check the ageing status of the various stressed samples, which confirmed the different ageing effects caused by the applied fields' magnitudes and frequency of polarity reversals. When small percentages of DC offset added in, charge accumulation and transportation become more complicated. The overall accumulated charge amount is significantly enhanced under superimposed electric fields, compared with under pure AC cases. Nevertheless, the situations for the specific charge distributions and local field distortion is more complicated. Under superimposed electric fields with relatively low DC offset ratio (<0.33), charge and local field distributions are more close to profiles under pure AC fields with increased amounts, and as for fields with higher DC offset ratio, the distributions are similar to those under pure DC fields. The influences of applied field polarity reversals can only be observed very initially.

To understand the underlying physics behind the measured results, a numerical model based on charge transport theory is proposed to analyse the charge profiles within LDPE under various applied fields in this work. The proposed model can predict the charge dynamics under HVDC fields quantitatively accurate. The differences between the measured and simulated results can be controlled within 5%. The model has also been used to analyse charge dynamics and local field trends under AC and superposed AC and DC fields, although at current stage its results cannot match the measured values well as under DC cases. The model can successfully predict the trends of charge dynamics and local field distortion caused by space charge phenomenon under AC and superposed fields. The main reason lead to the quantitative differences between measured and simulated results under AC, and superposed fields are the lack of accurate charge transport mechanism under relatively low applied fields strengths (<20kV/mm). Under AC and superposed AC and DC fields, the electric field within insulation alters within a significantly broader range comparing with under pure DC cases, and there is a remarkable amount of time when the field strength is lower than 20kV/mm.

The features of the applied fields are analysed using both measured and simulated results. Within the examined range, the magnitude and composition of the applied fields seem to have more significant effects on the charge dynamics within insulation, compared to the frequency of the applied fields. With the enhancement of applied field magnitude, the accumulated charge amounts under HVAC fields can be significantly increased. Due to charges mainly localise adjacent the electrodes, severe local field distortion along with accelerated ageing happen within the surface region of insulation. This severely unbalanced charge distribution can further accelerate and even trigger the breakdown of the materials. When additional DC offset is added to the applied AC fields, the accumulated net charge amount increased dramatically compared with results under pure AC fields. Charges can further transport into the bulk area of insulation with the help of the DC offset and localised positive charges can be observed along with the DC offset ratio increase. However, the maximum field distortion within the insulation presents a complicated relationship along with the adding DC offset ratio. The influences of consist changing of applied field polarity and DC offset on the charge formation and transportation seem to neutralise each other, which eventually results in the maximum field distortion happens under superposed fields with relatively low DC offset ratio (around 0.2 in the issuing condition: 50Hz 50kV/mm fields). As for influences of applied field frequency, it is clear that the overall net charge amount decrease along with the increasing frequency, and sharp deductions mainly happen within the range of 10^{-3} Hz to 10^{-1}Hz. The trend applies to the superposed fields with both higher or lower AC fields percentage, although the effects of frequency are relatively insufficient under superposed fields with a small portion of AC elements. The observations under various kinds of superposed AC and DC fields also indicate the relationships of charge profiles and the features (magnitude, compositions, and frequency) of applied fields are non-linear. Using pure HVAC and HVDC voltage to test the insulating materials separately, cannot entirely replace the working environments of insulation under superimposed AC and DC stresses.

The analysis of breakdown strengths of LDPE under various kinds of applied stresses can be regarded as an application of the proposed numerical model. The influences of common factors: apply field's frequency, testing sample thickness and apply ramping voltage rate, have been investigated based on the proposed model. It has been noticed that the regions where breakdown initiated are different for DC and AC conditions, which eventually results in the lower AC breakdown strength compared with the DC strength of the same material. The obtained trends for the apparent breakdown strength are consistent with general observations in breakdown strength measurements. The acquired breakdown strength of insulation demonstrates a decreasing trend along with adding testing sample thickness. The breakdown strength increases along with applied field's ramping rate. The proposed numerical model also offers an initial approach of explaining the empirical rules within AC and DC ramping breakdown tests, based on space charge dynamics. Based on the discussion, space charge phenomenon's significant contribution to the electrical breakdown of solid insulation is clearly illustrated.

7.2 Future work

Bipolar charge transport theory has been employed to implement the simulation work in the thesis. The simulation results can present the necessary behaviours of space charge and its evolution trend in polyethylene subjected to various kinds of electric fields. For DC fields quantitative analysis with high accuracy compared with measured results is possible based on optimised parameters. However, for AC and superposed conditions, the current developed model is still remote from numerical accuracy, and the model is reasonable for qualitative analysis only. This is because the current model ignored the effects of injection thresholds and charge carriers' mobility calculation model contains notable errors when the field strength is lower than 20kV/mm. In future, with the help of involving injection thresholds and more accurate measured mobility results, the proposed numerical model will perform better in quantitative analysis of charge dynamics under AC and superposed AC and DC fields.

Besides, based on the measured charge profiles in this thesis, it is clear that the structure of the surface region of the testing sample can be altered after several hours of HVAC field stressing. The current simulation model does not consider these effects. In future, the depreciation of the insulating materials will be studied in the numerical model to better illustrate and explain the charge dynamics inside the insulation, especially under intensive AC and superposed AC and DC fields.

As for breakdown process simulation, the influences of defects and percolation will be taken into account to define when the breakdown happens in future. It will not ideally like the current situation, assuming breakdown occurs wherever the local electric fields reach a specific value, and the testing sample has uniform electric characteristics. The extent of the ageing and damaging will also be investigated in different regions of the tested samples to experimentally confirm that the place where breakdown happens will be different under divergent categories of the applied field.

The bipolar charge transport model may also be capable of being applied to other solid additive-free dielectrics based on sufficient experimental and numerical investigations. However, if the model is applied to the multilayer structure, interfaces should be settled between each layer. The mechanism of charge passing through the interface can consult the experimental observations as well as the existing set of metal and dielectrics interfaces. Cable geometry and temperature gradient can also be realised by revising the initialisation of voltage and temperature setting of the simulation. Also, in the proposed simulation model, concerns have mainly been focused on the charge generation, transport, and neutralisation under various electric fields. The specific trapping and detrapping characteristics are not exhaustively considered. The trapping features of real charges depend on the distribution of trapping energy levels within the insulating materials, and detrapping mechanism are significantly affected by the physical or chemical defects existing in the insulation. The correlation between the trapping characteristics and the charge accumulation is essential for the understanding of trap charge origins and their influences on the performance of insulating materials under high voltage. These trapping and detrapping characteristics of charges are not analysed explicitly in this work. Consequently, a new description of the trapping and detrapping process based on trapping energy levels can be proposed in future, with the help of more specific inspection of trapped charges generation and relaxation. Furthermore, the current numerical model regards all localised charges within insulation are generated from electrical injections. This is not appropriate for hybrid or mixed insulating materials, where ionisation and polarisation are the primary sources of space charge. Therefore additional mechanism of simulating ionisation and polarisation can be introduced to the model to study the charge dynamics within the hybrid or mixed insulating materials. With all these aspects, the simulation model can be more sophisticated, and the computed charge and fields' dynamics will be more close to reality.

In this work, single layer low-density polyethylene has been chosen as investigated materials for both simulation and experimental work. In reality, oil press boards and crossing linked polyethylene are the widely used as high voltage insulating materials, and multilayer structures are more generally involved. Therefore, in future, research can be applied to the widely used insulating materials with multilayer structures based on the contribution of this work. Cable geometry and temperature gradient can also be considered to make the measurements and simulations more close to the operating reality.

In future, the PEA system used for this work can be modified capable of detecting thick and multilayer samples by reselection of sensor thickness and revision of equipment structure. Data analysis processes may also need to be revised and developed to fit the new situations. For example, the reflection and refraction of acoustic waves at interfaces of multilayer structure should be exhaustively investigated in the calibration process, when consider testing multilayer structure samples using PEA techniques. The structure of PEA system should also be modified to minimise the overlapping of real charge peaks and inauthentic peaks caused by the reflection in detecting process. The applied voltage distribution within the multilayer sample caused by the different permittivity and conductivity of materials at each layer should also be considered and discussed. The PEA system can be further developed into a cable PEA system to detect charge dynamics within cable geometry. The temperature gradient can also be achieved if an additional heating circulatory system is associated.

Appendices

Appendix A: PEA measurement results

PEA measured charge profiles in LDPE under HVDC

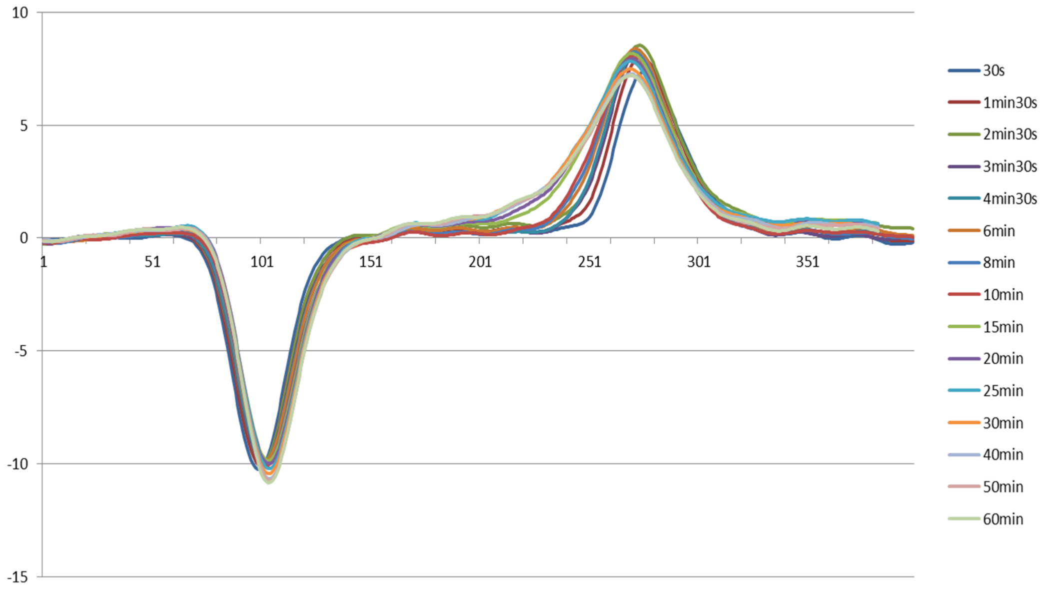

PEA measured charge profile in 180µm LDPE under 3.6kV HVDC

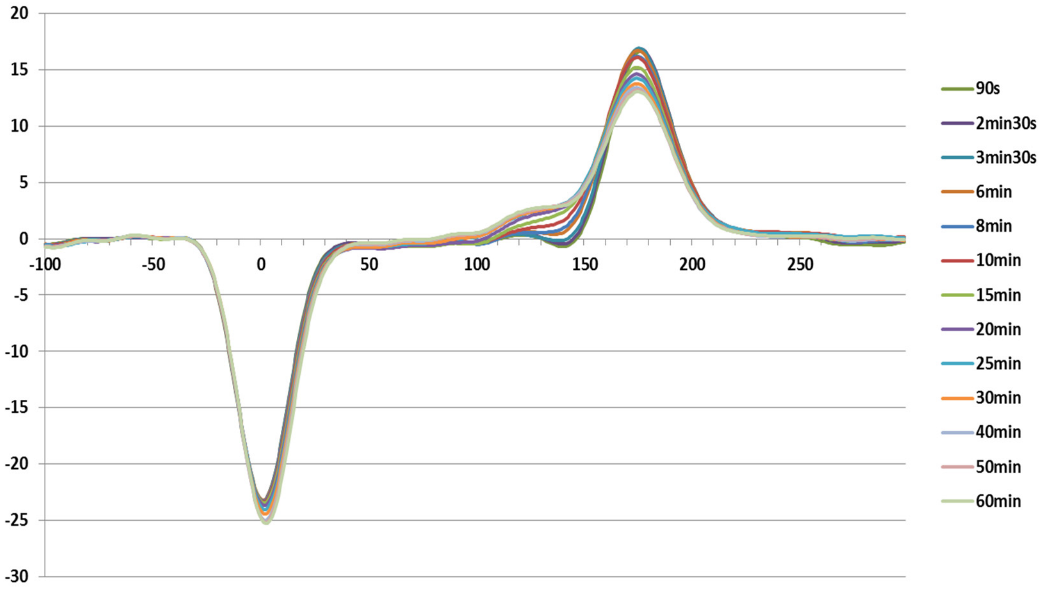

PEA measured charge profile in 180µm LDPE under 4.5kV HVDC

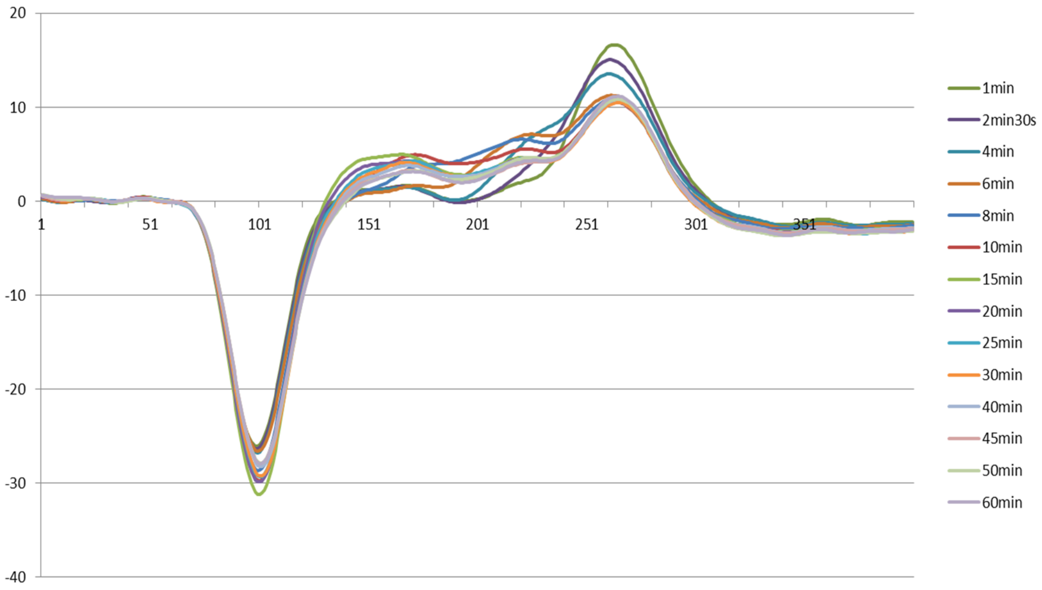

PEA measured charge profile in 180µm LDPE under 7.2kV HVDC

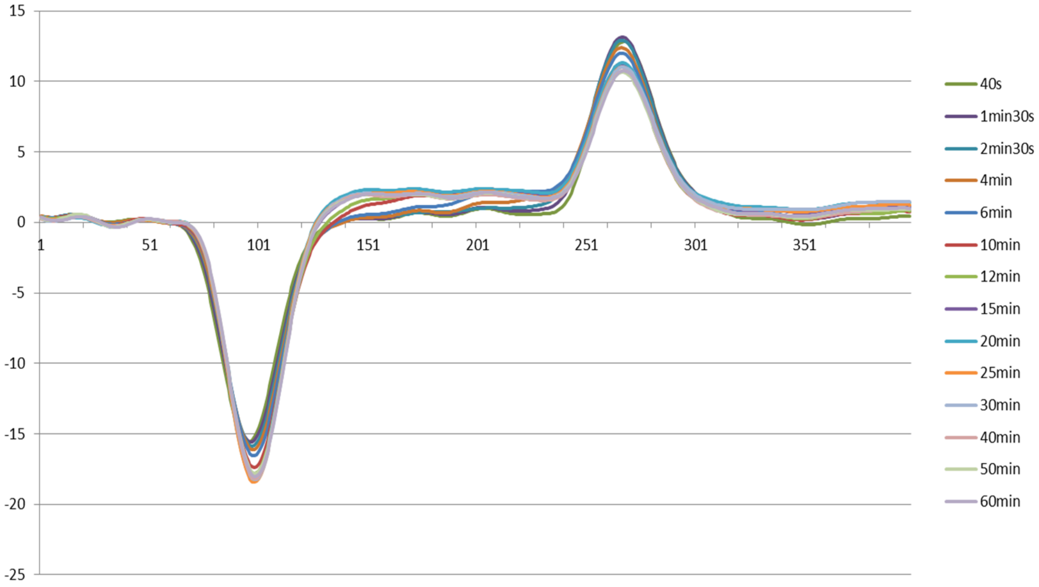

PEA measured charge profile in 180µm LDPE under 9kV HVDC

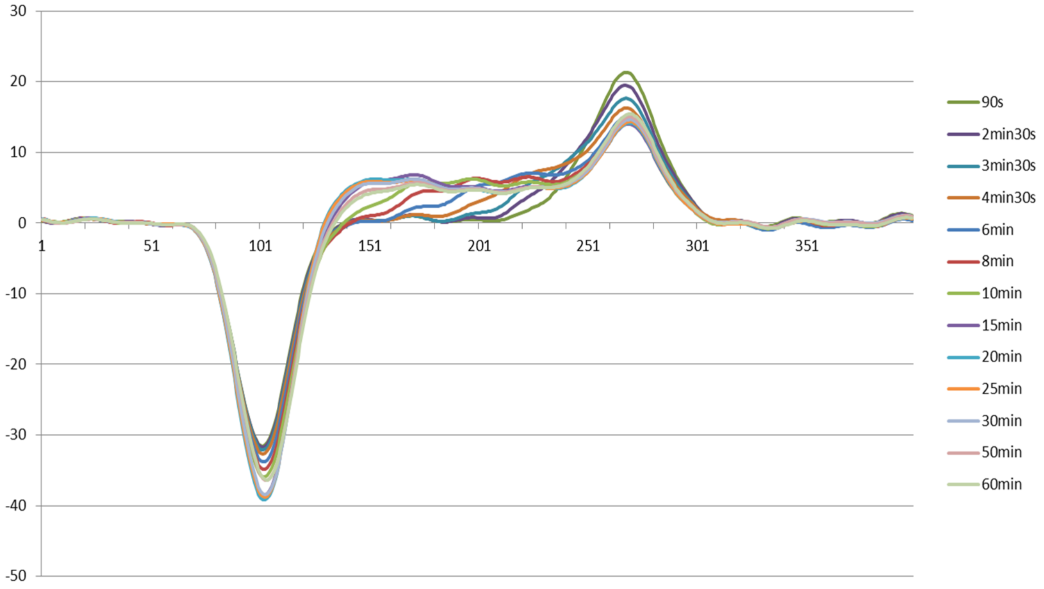

PEA measured charge profile in 180µm LDPE under 10.8kV HVDC

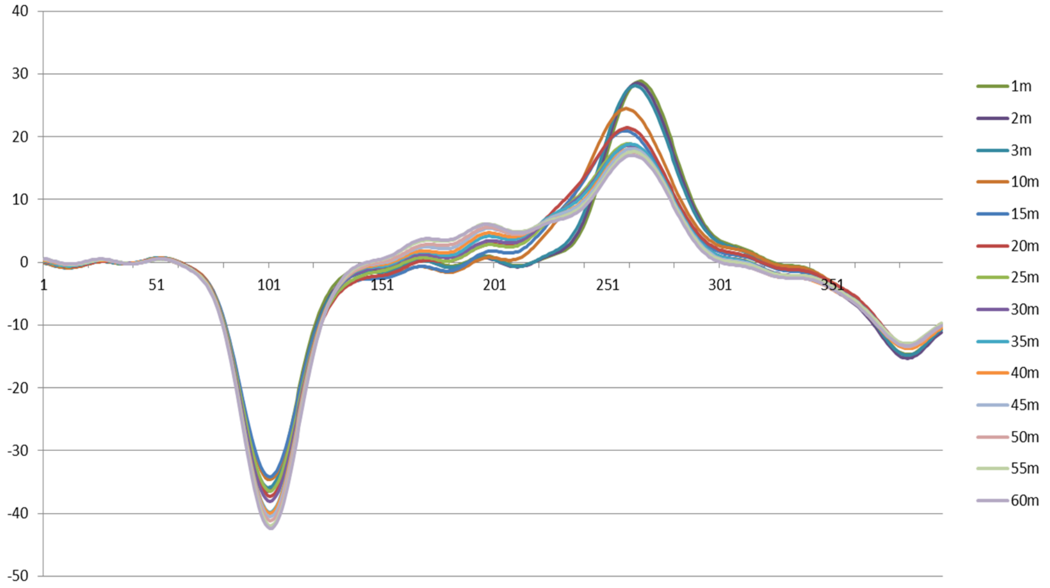

PEA measured charge profile in 180µm LDPE under 13.5kV HVDC

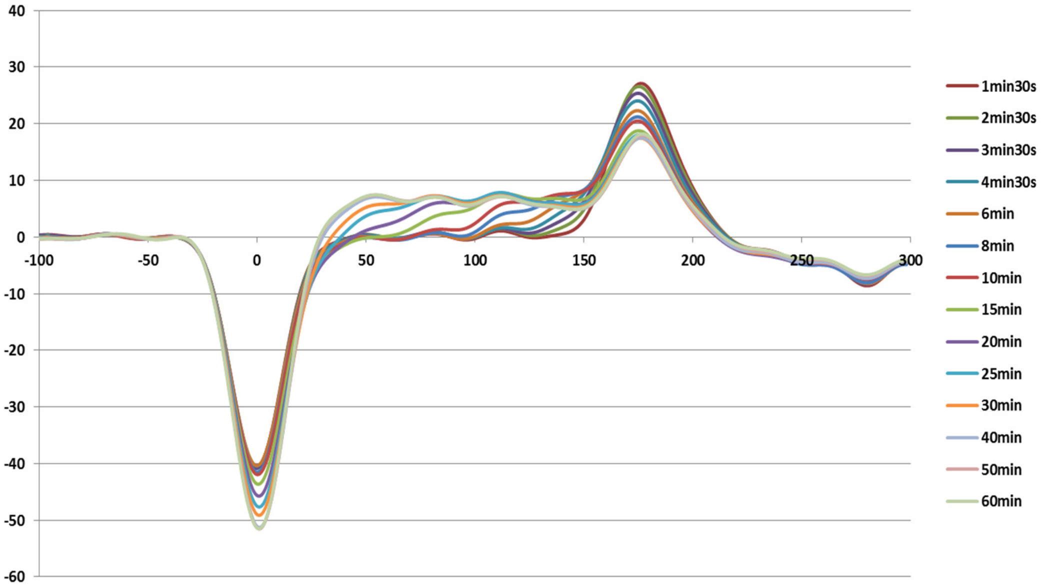

PEA measured charge profile in 180μm LDPE under 14.4kV HVDC

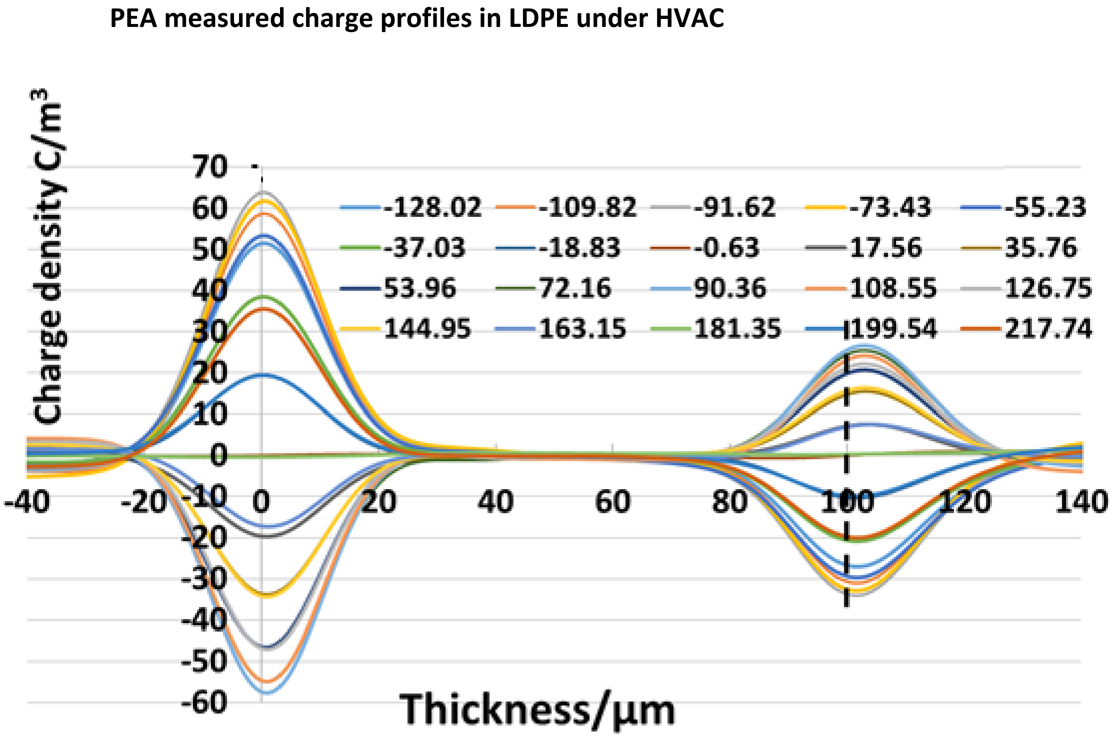

PEA measured charge profile in 100μm LDPE under 50Hz 5kV HVAC

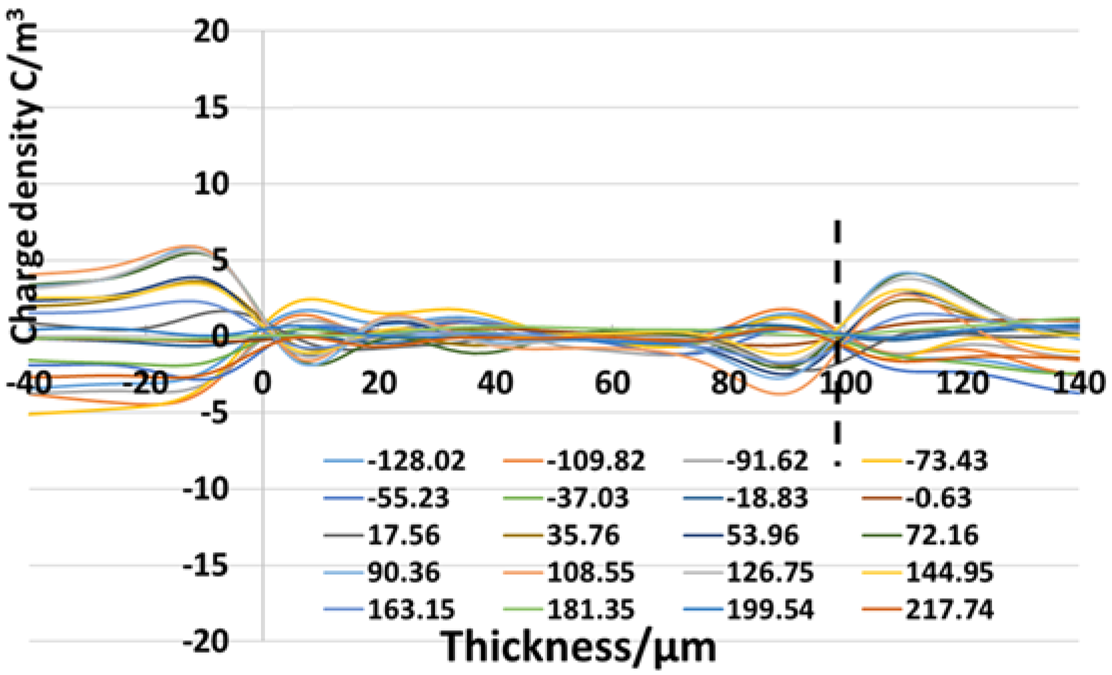

PEA measured charge profile in 100µm LDPE under 50Hz 5kV HVAC

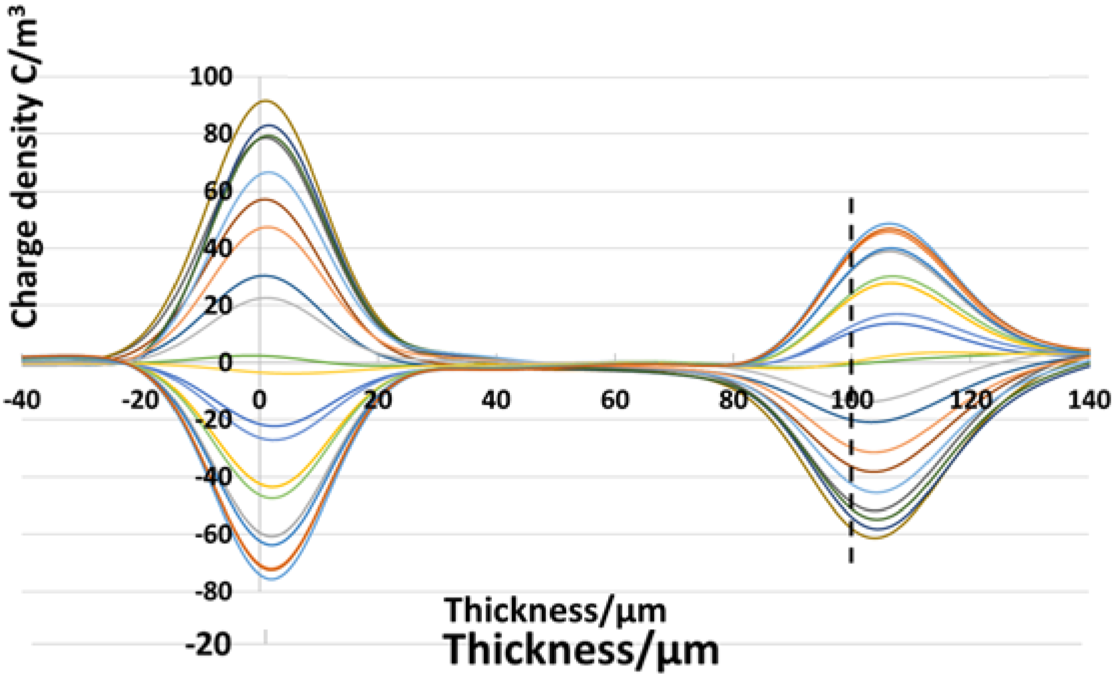

PEA measured charge profile in 100µm LDPE under 50Hz 5kV HVAC

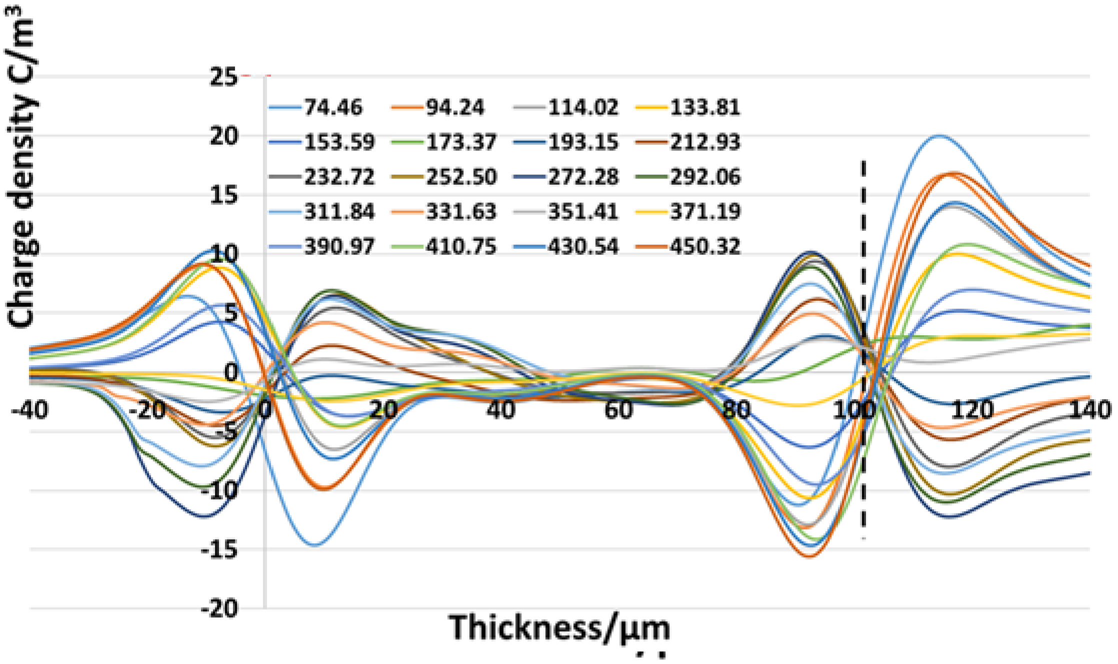

PEA measured charge profile in 100µm LDPE under 50Hz 5kV HVAC

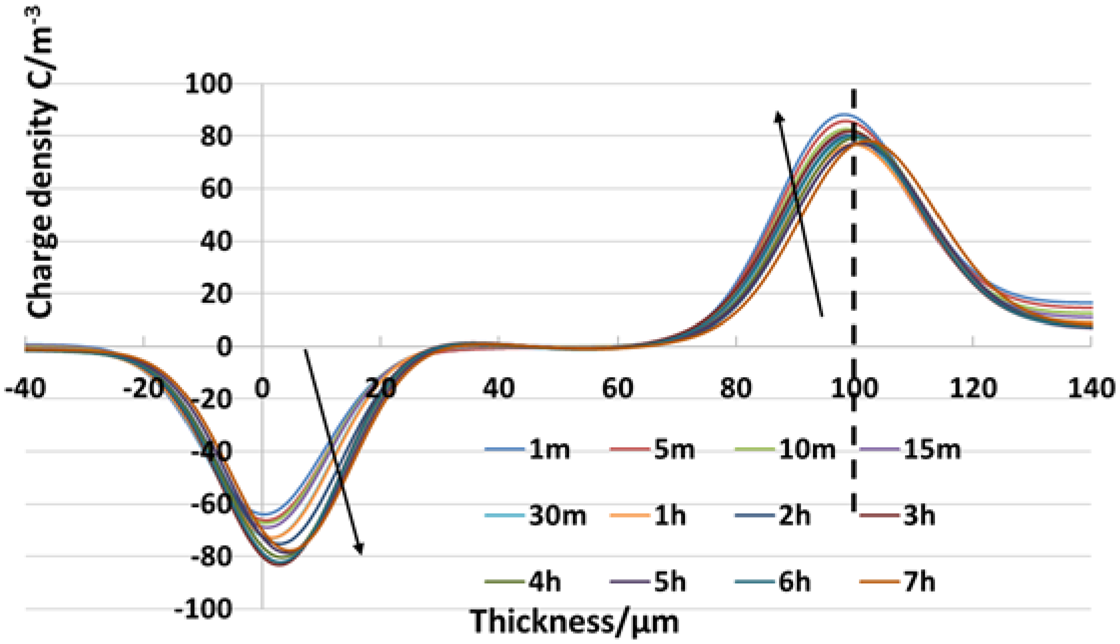

PEA measured charge profile in 100µm LDPE under 50Hz 5kV HVAC

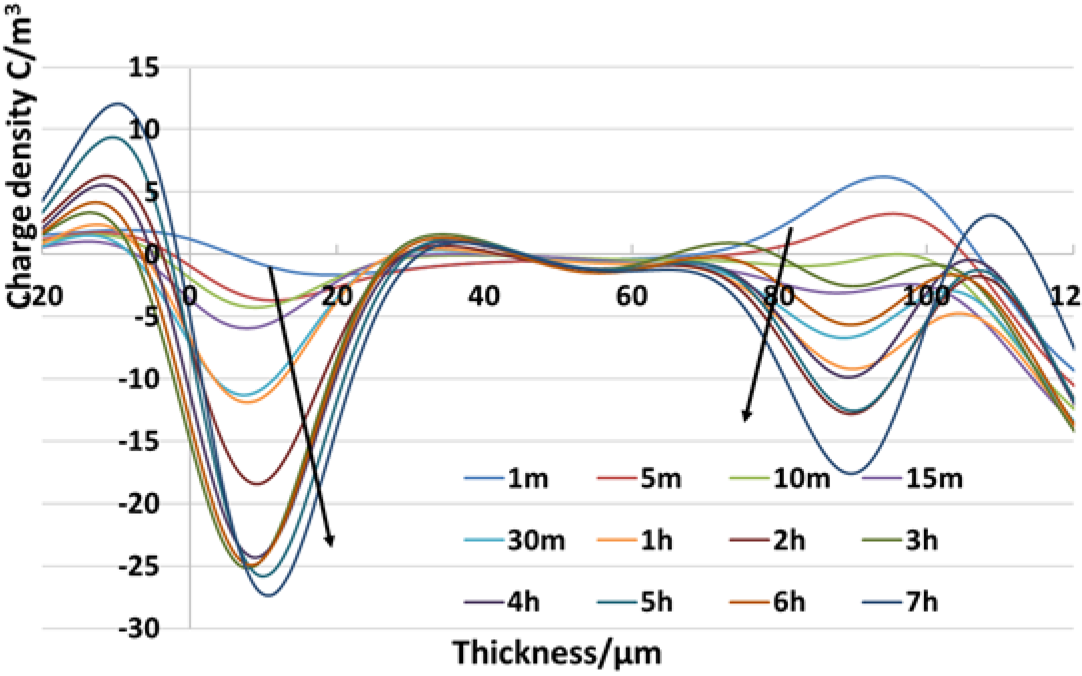

PEA measured charge profile in 100µm LDPE under 50Hz 5kV HVAC

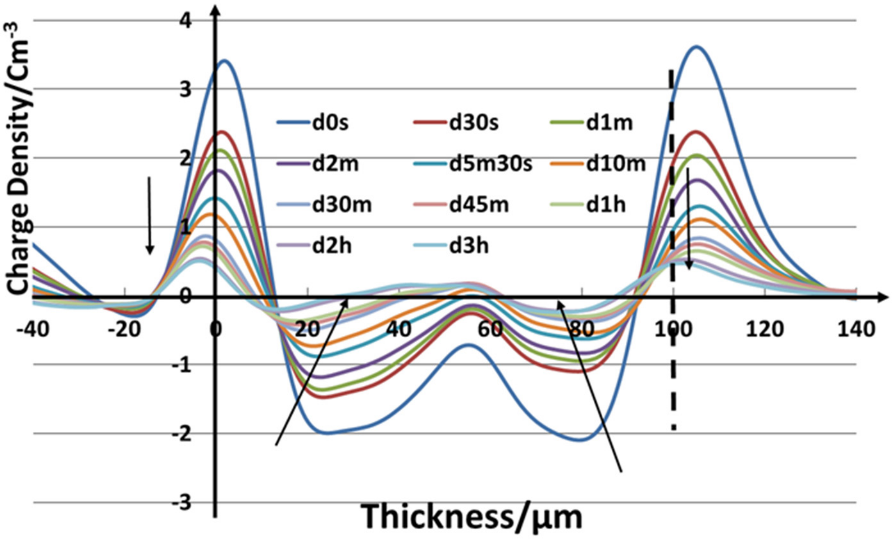

PEA measured charge profile in 100µm LDPE under 50Hz 5kV HVAC

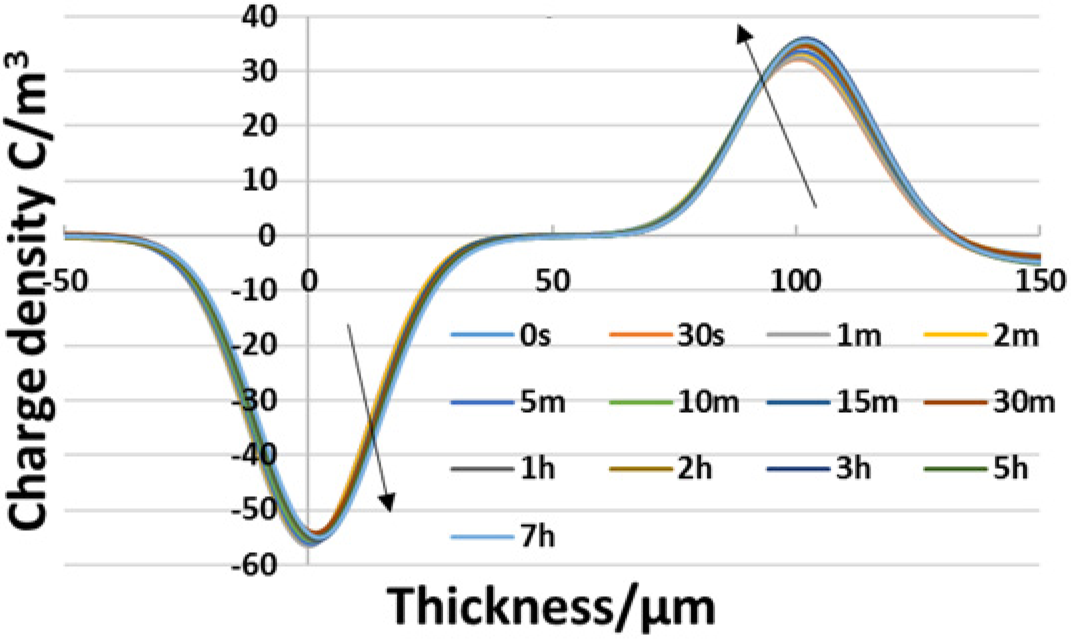

PEA measured charge profile in 100μm LDPE under 50Hz 4kV HVAC

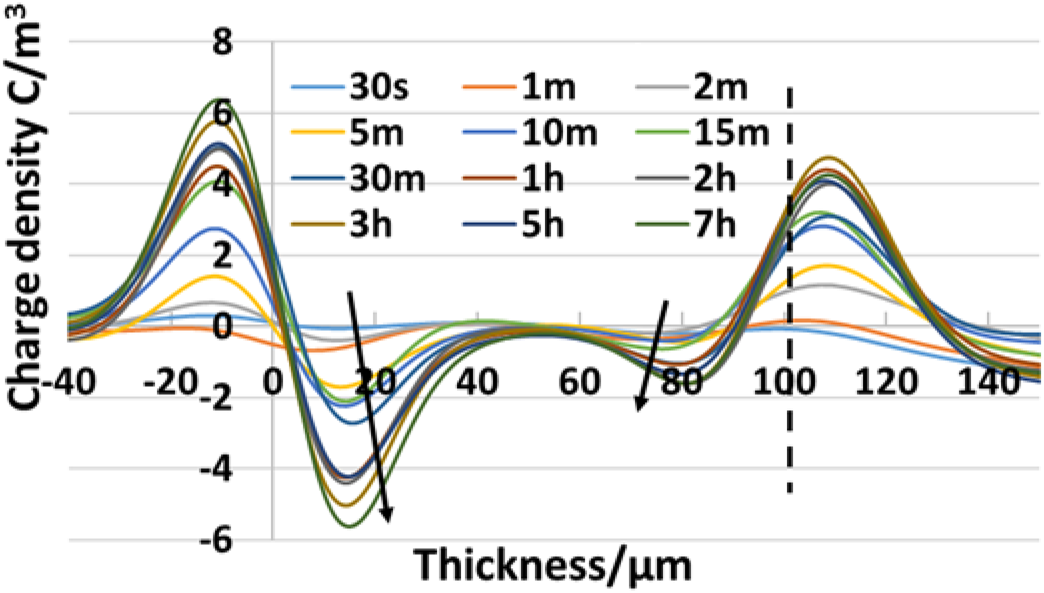

PEA measured charge profile in 100μm LDPE under 50Hz 4kV HVAC

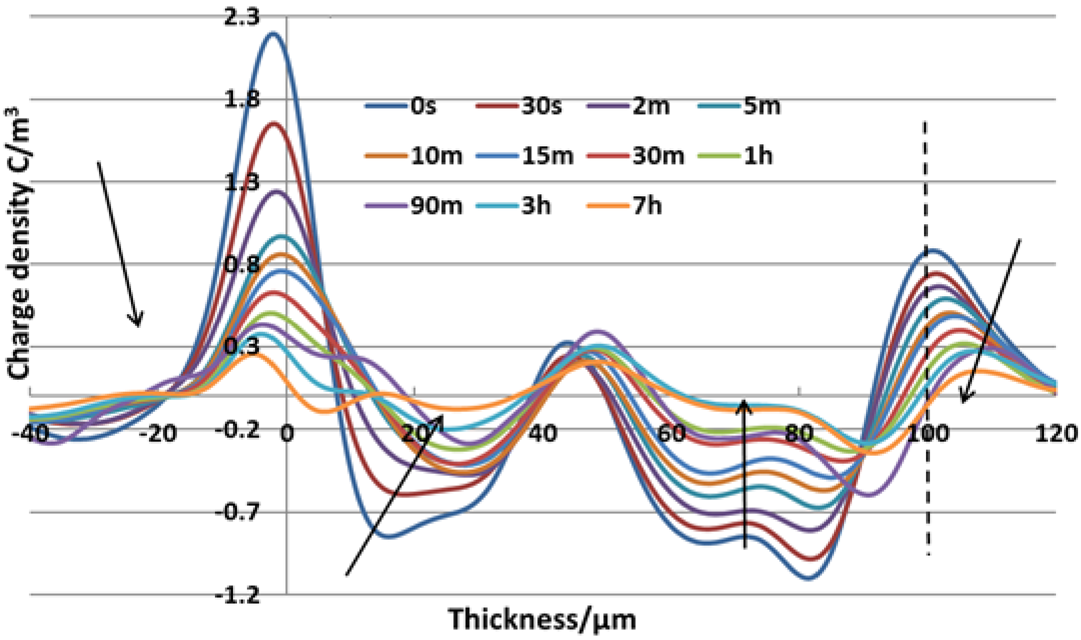

PEA measured charge profile in 100µm LDPE under 50Hz 4kV HVAC

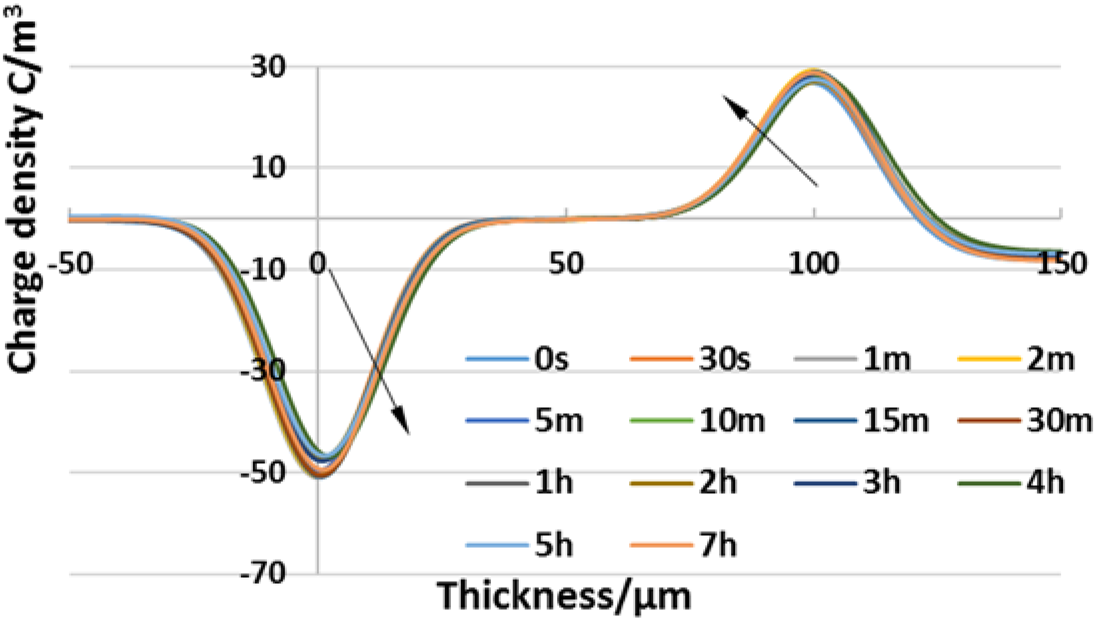

PEA measured charge profile in 100µm LDPE under 50Hz 3kV HVAC

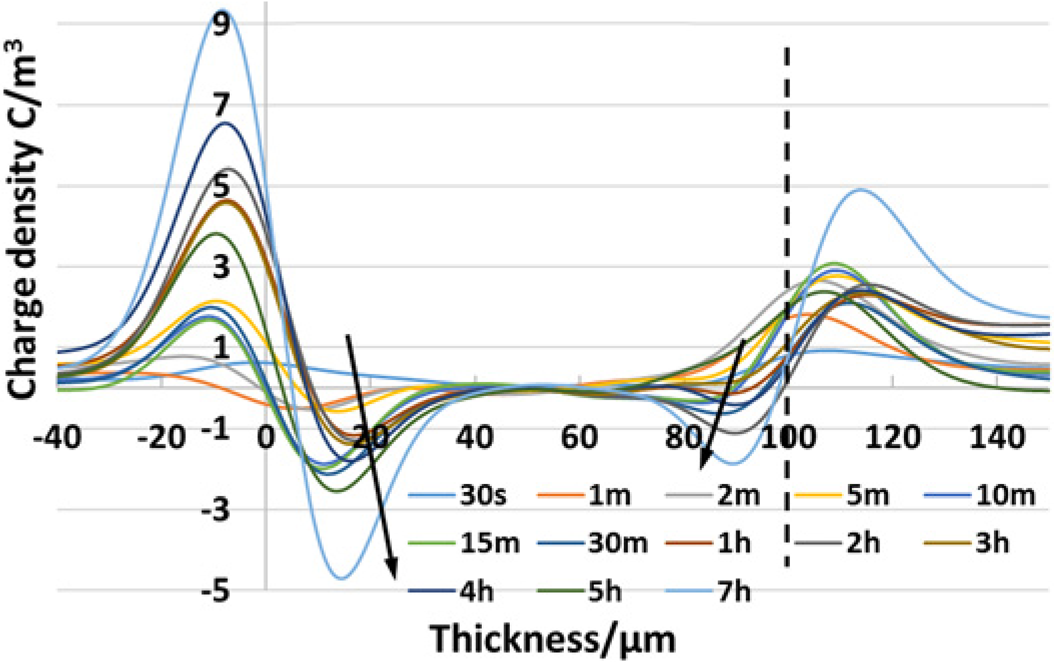

PEA measured charge profile in 100µm LDPE under 50Hz 3kV HVAC

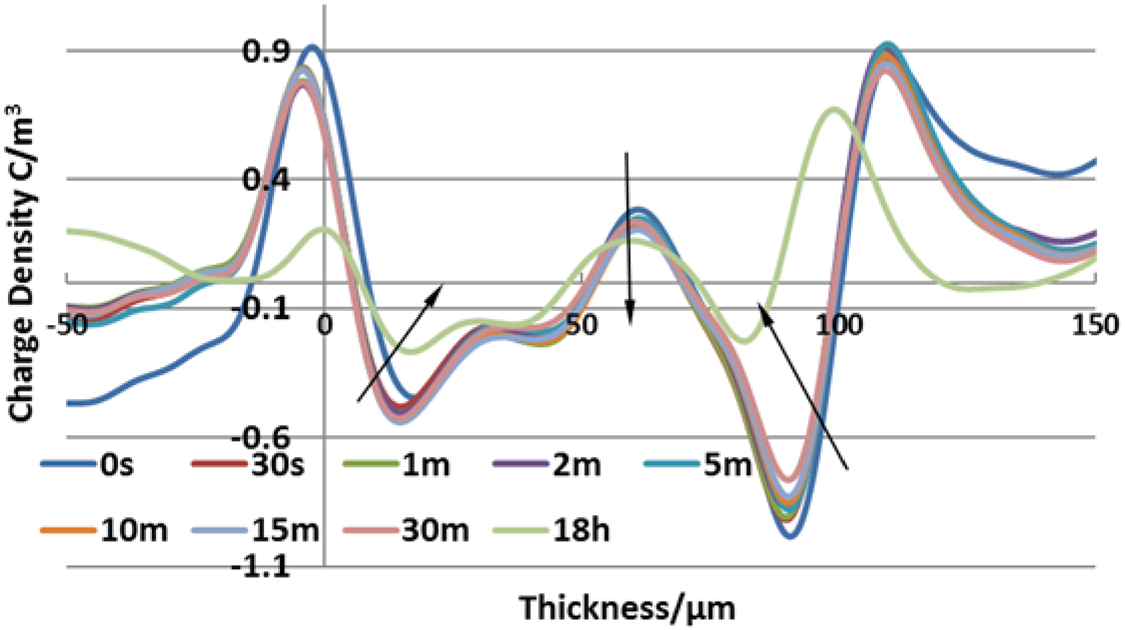

PEA measured charge profile in 100µm LDPE under 50Hz 3kV HVAC

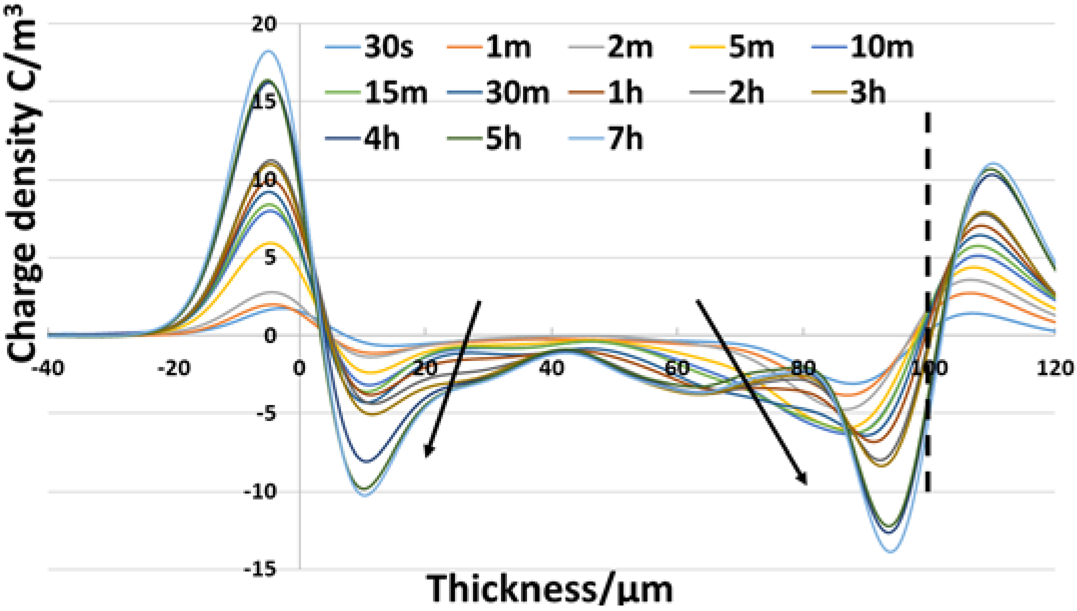

PEA measured charge profile in 100µm LDPE under 5Hz 5kV HVAC

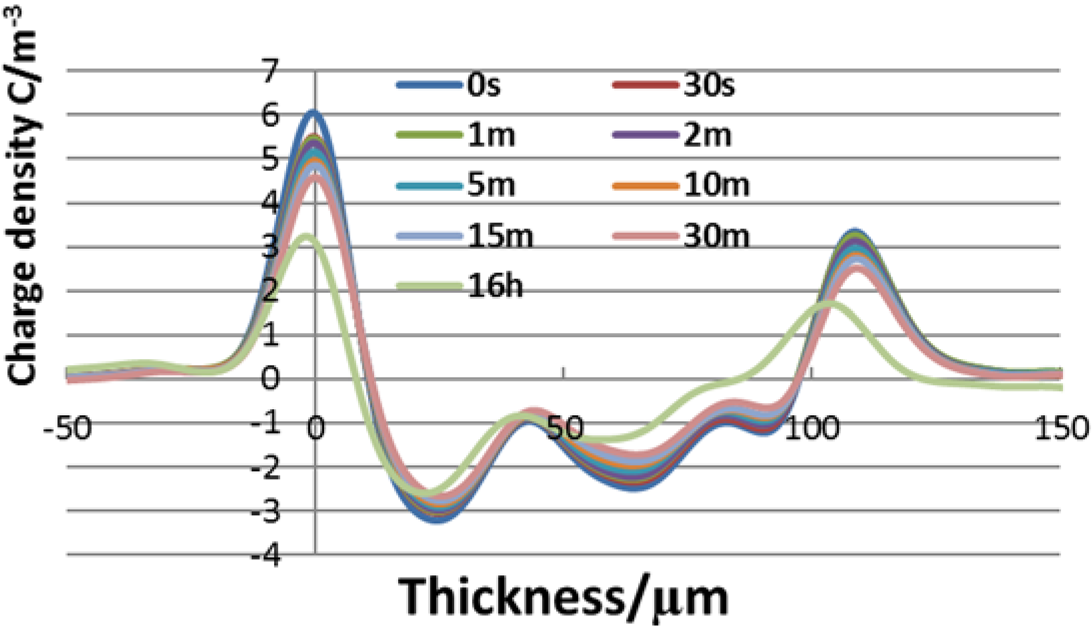

PEA measured charge profile in 100µm LDPE under 5Hz 5kV HVAC

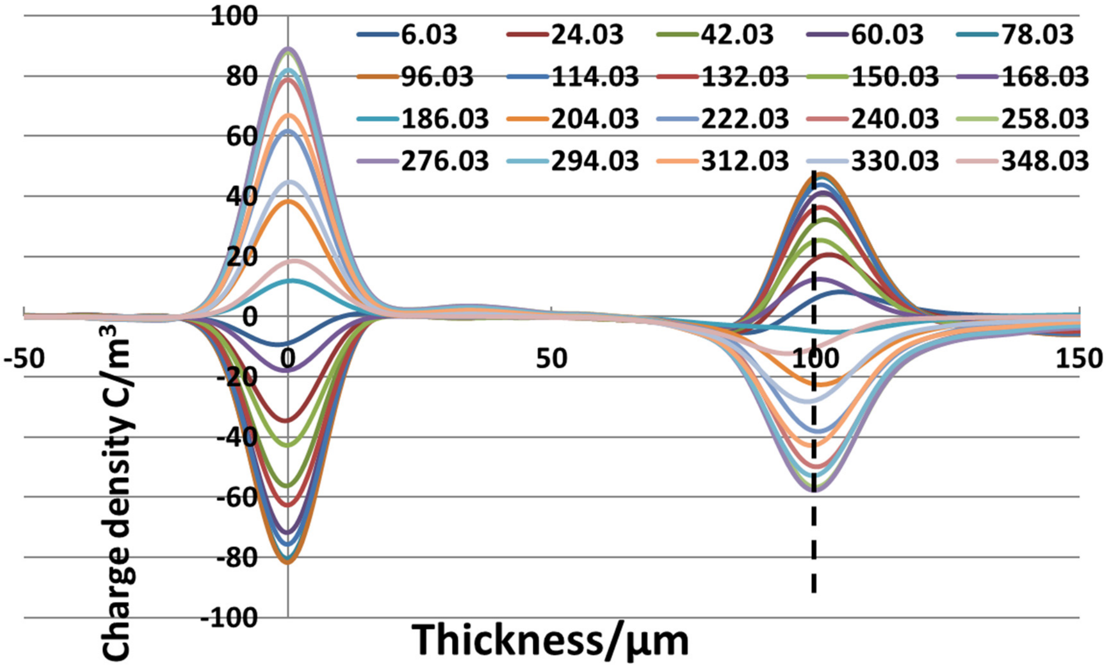

PEA measured charge profile in 100µm LDPE under 0.5Hz 5kV HVAC

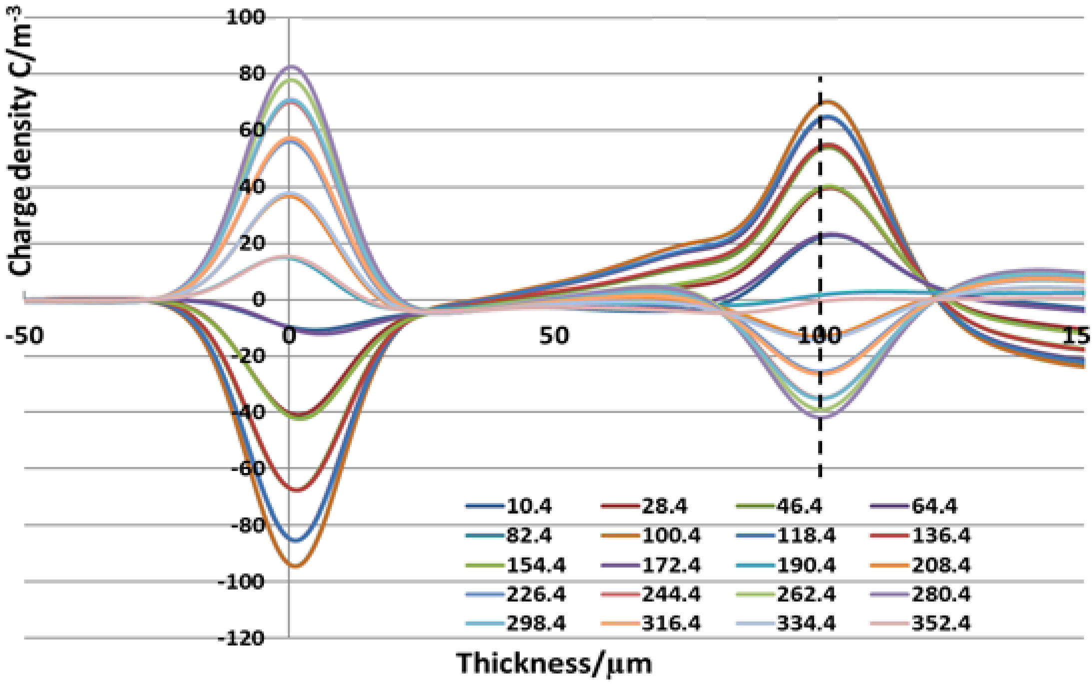

PEA measured charge profile in 100µm LDPE under 0.5Hz 5kV HVAC

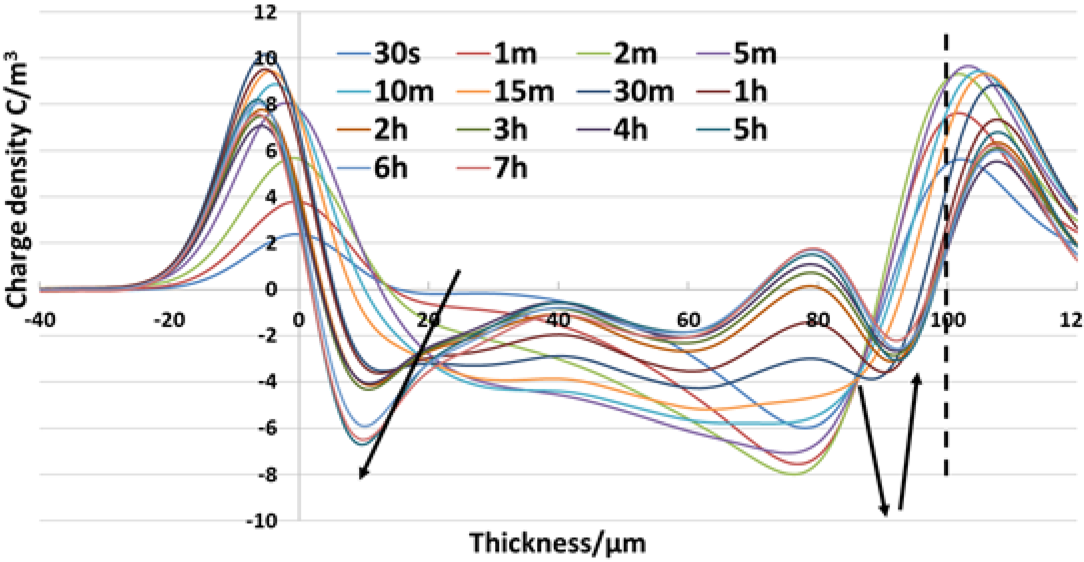

PEA measured charge profile in 100µm LDPE under 0.5Hz 5kV HVAC

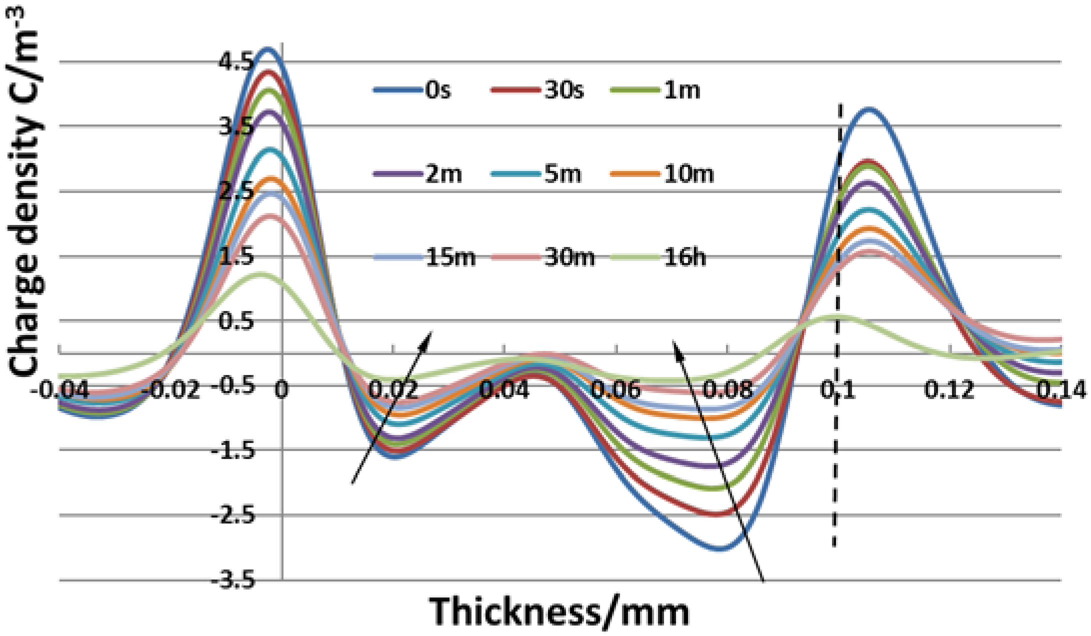

PEA measured charge profile in 100µm LDPE under 0.5Hz 5kV HVAC

PEA measured charge profiles in LDPE under superimposed HVAC and HVDC

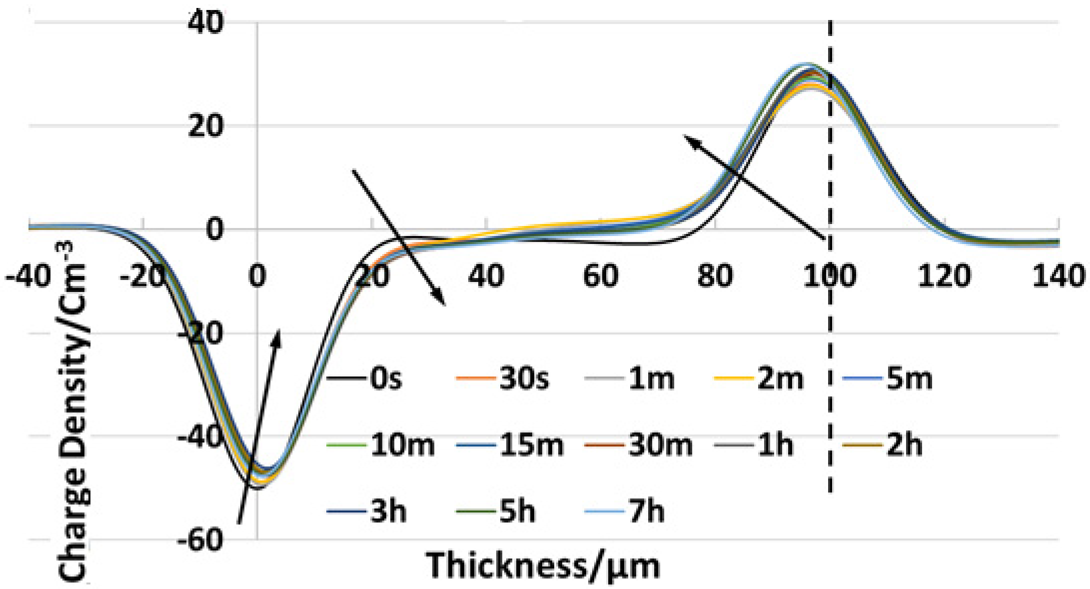

PEA measured charge profile in 100µm LDPE under 50Hz 5kV combined HVAC and HVDC fields with offset ratio 0.5

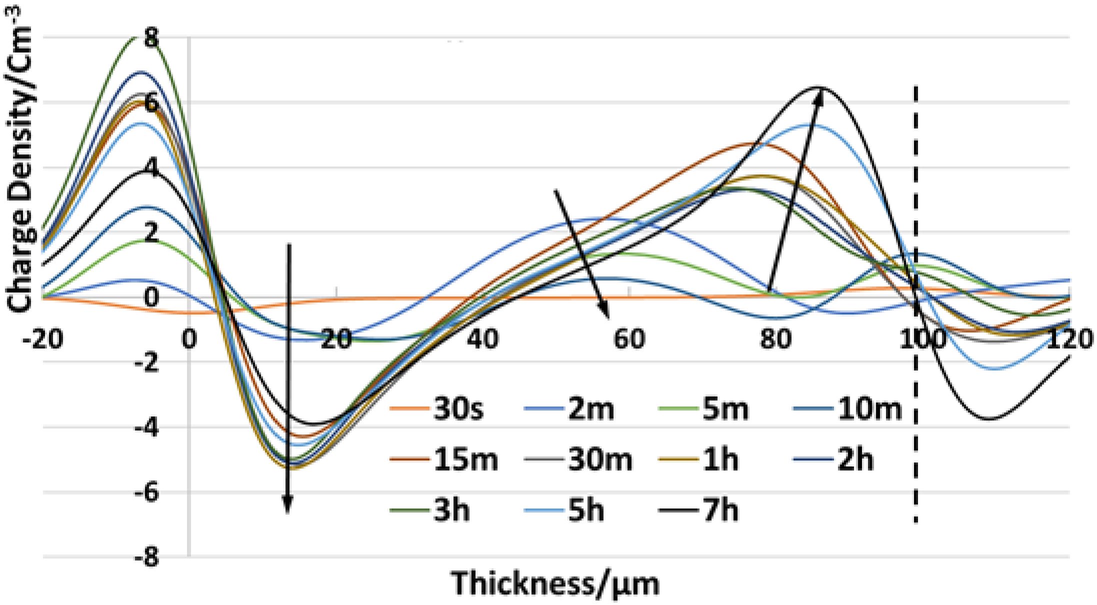

PEA measured charge profile in 100µm LDPE under 50Hz 5kV combined HVAC and HVDC fields with offset ratio 0.5

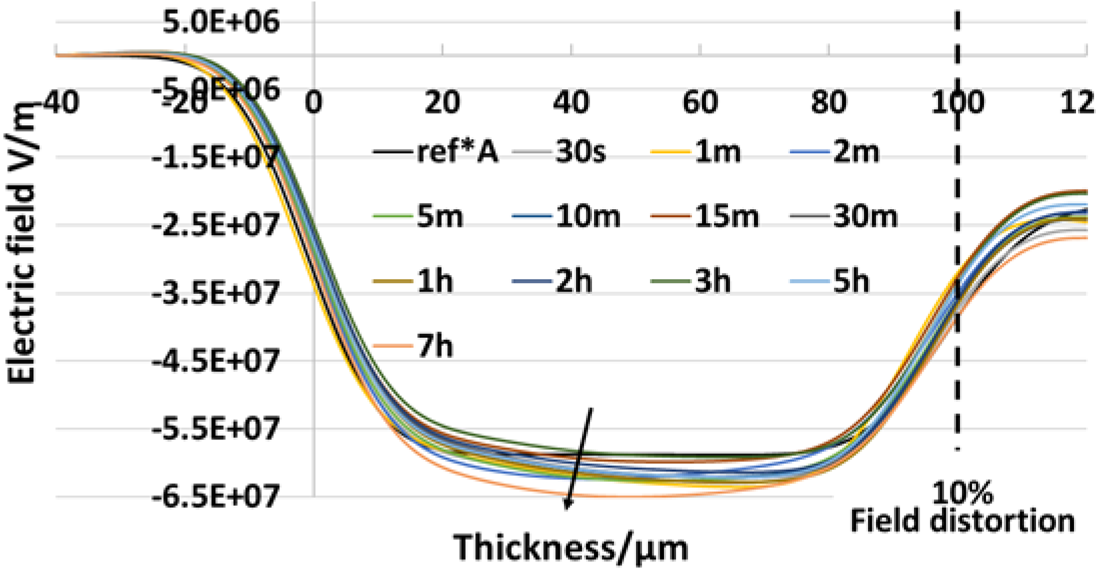

PEA measured electric fields in 100µm LDPE under 50Hz 5kV combined HVAC and HVDC fields with offset ratio 0.5

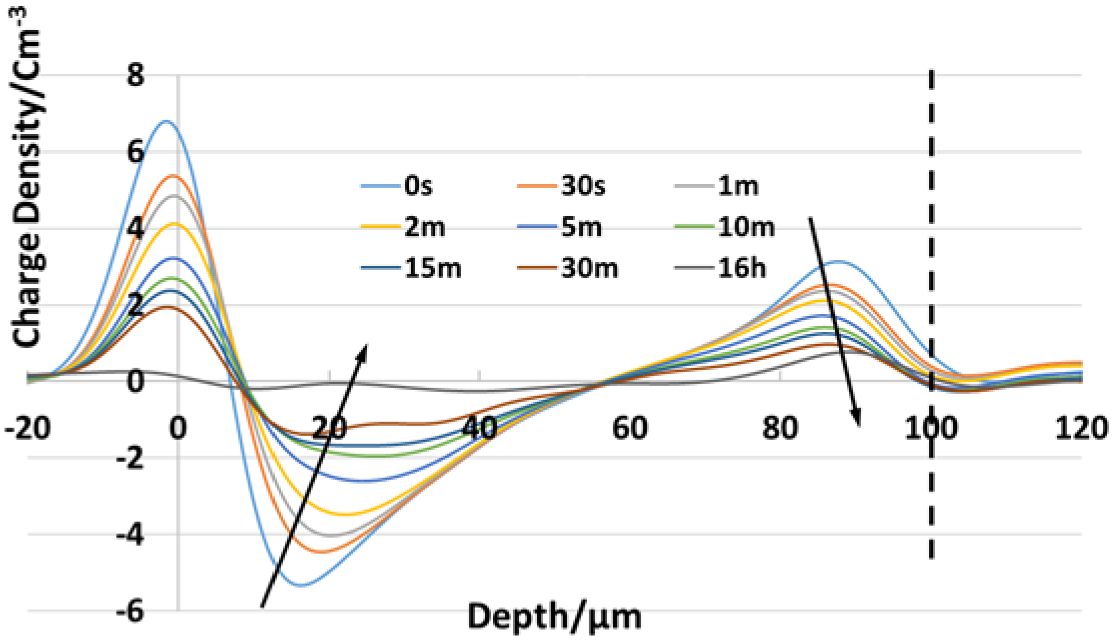

PEA measured charge profile in 100µm LDPE under 50Hz 5kV combined HVAC and HVDC fields with offset ratio 0.5

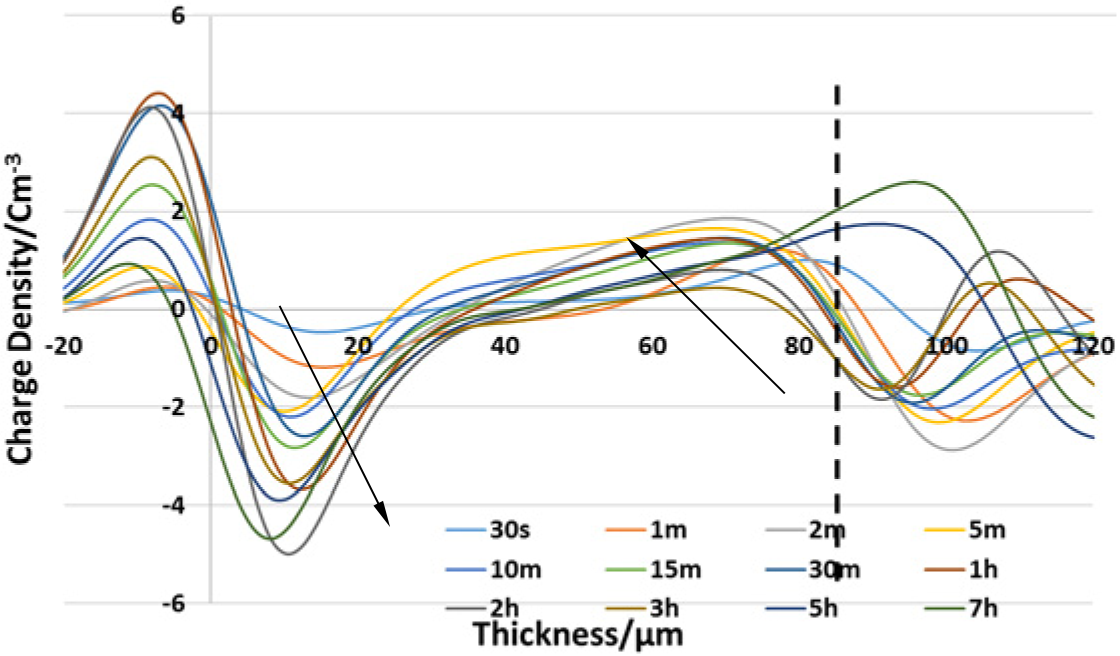

PEA measured charge profile in 100µm LDPE under 50Hz 5kV combined HVAC and HVDC fields with offset ratio 0.4

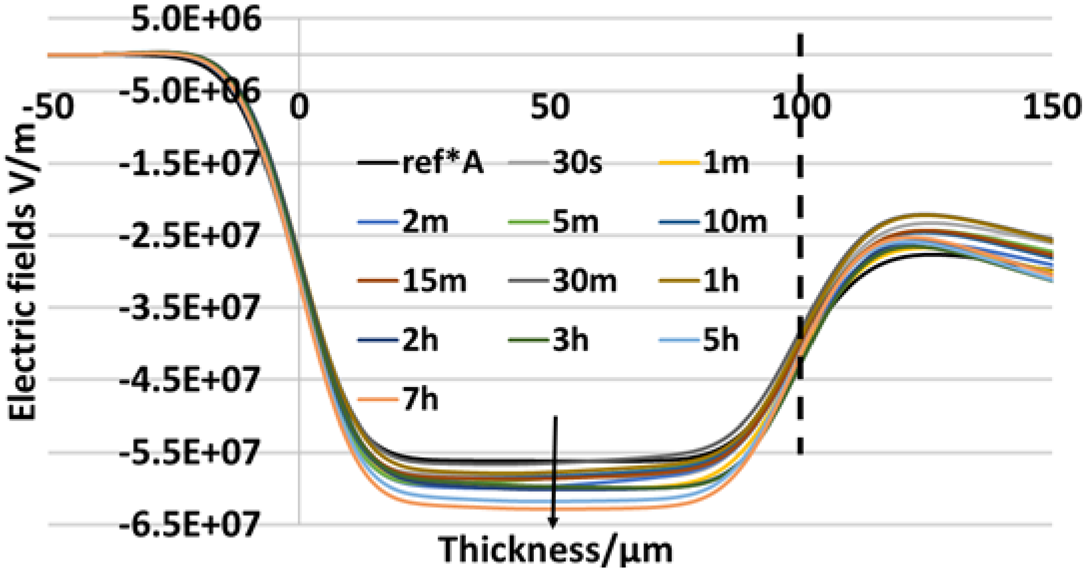

PEA measured electric fields in 100µm LDPE under 50Hz 5kV combined HVAC and HVDC fields with offset ratio 0.4

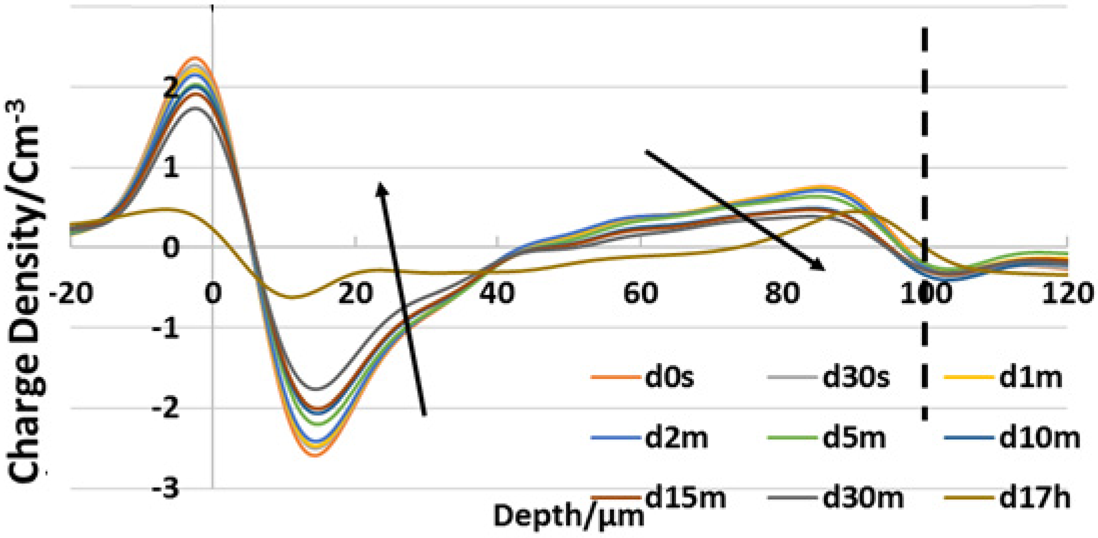

PEA measured charge profile in 100µm LDPE under 50Hz 5kV combined HVAC and HVDC fields with offset ratio 0.4

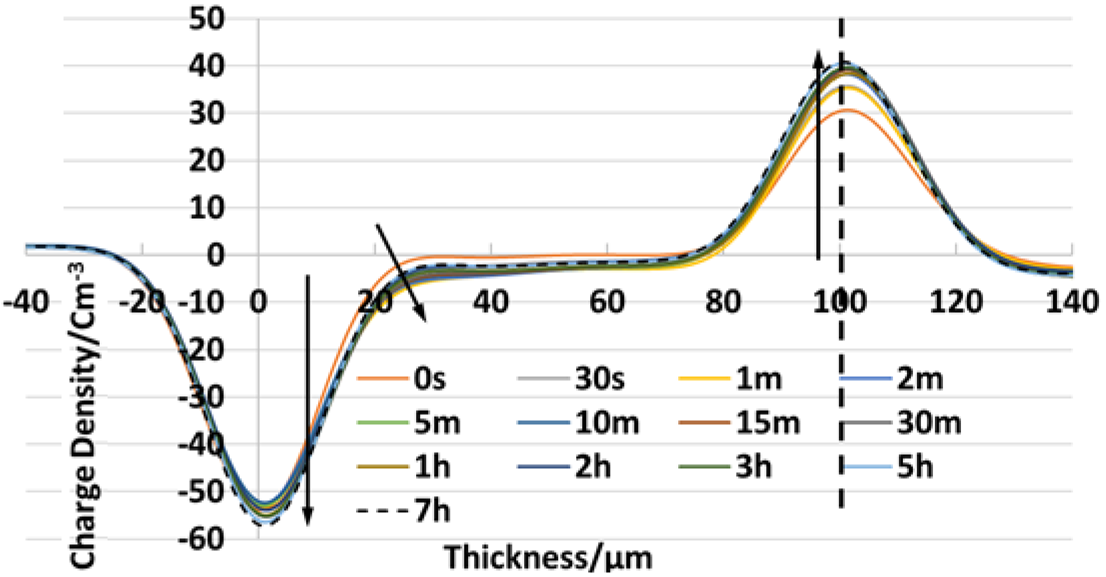

PEA measured charge profile in 100µm LDPE under 50Hz 5kV combined HVAC and HVDC fields with offset ratio 0.2

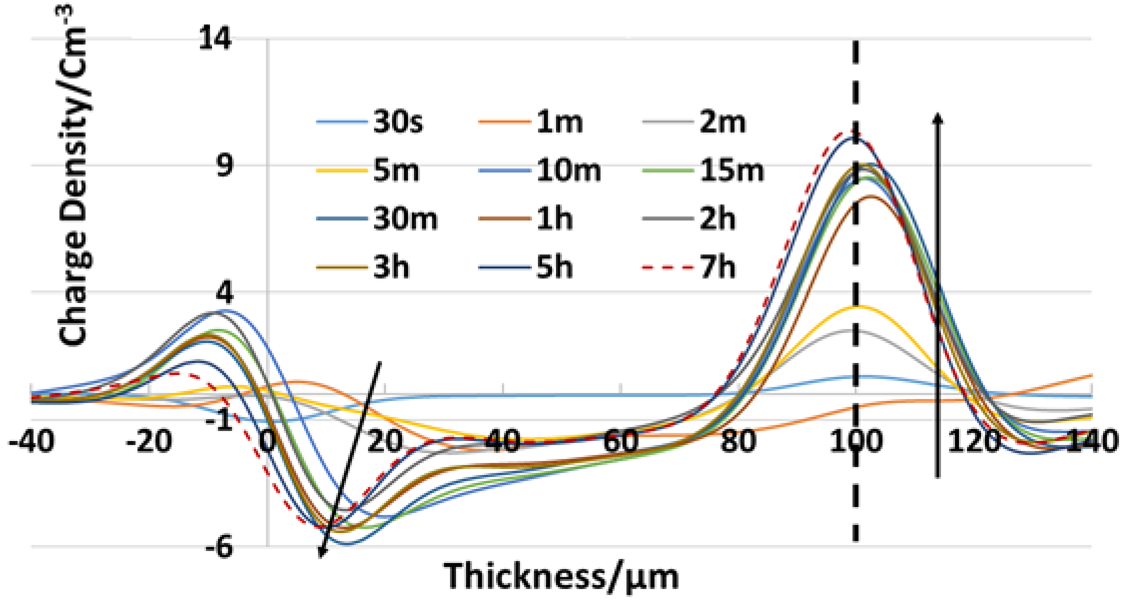

PEA measured charge profile in 100µm LDPE under 50Hz 5kV combined HVAC and HVDC fields with offset ratio 0.2

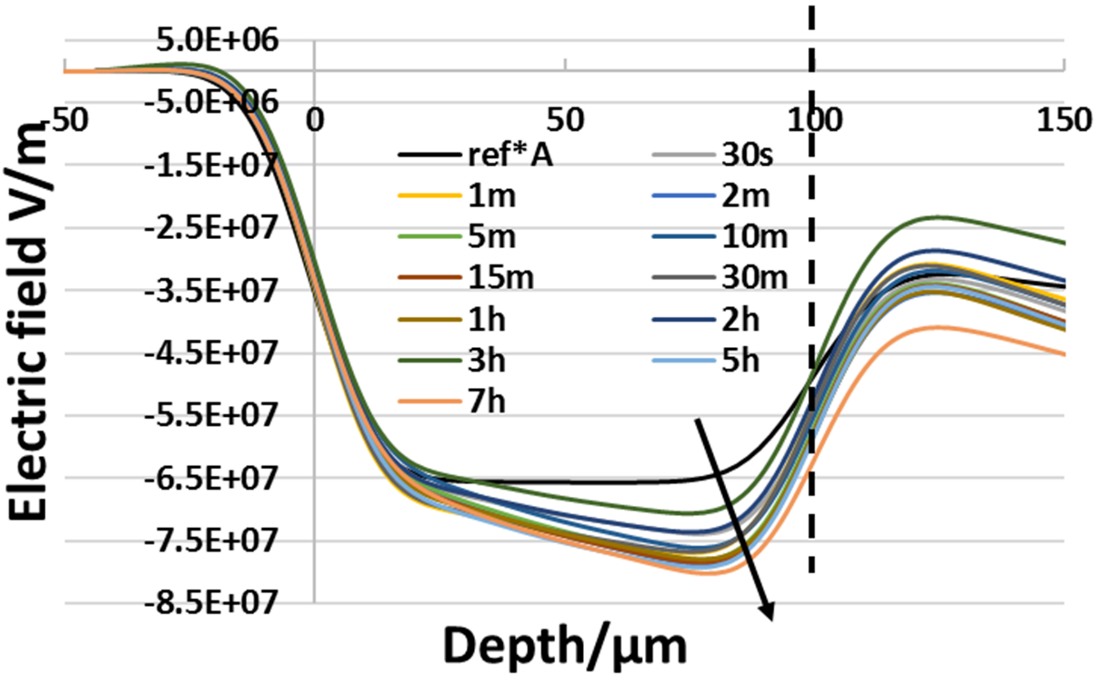

PEA measured electric fields in 100µm LDPE under 50Hz 5kV combined HVAC and HVDC fields with offset ratio 0.2

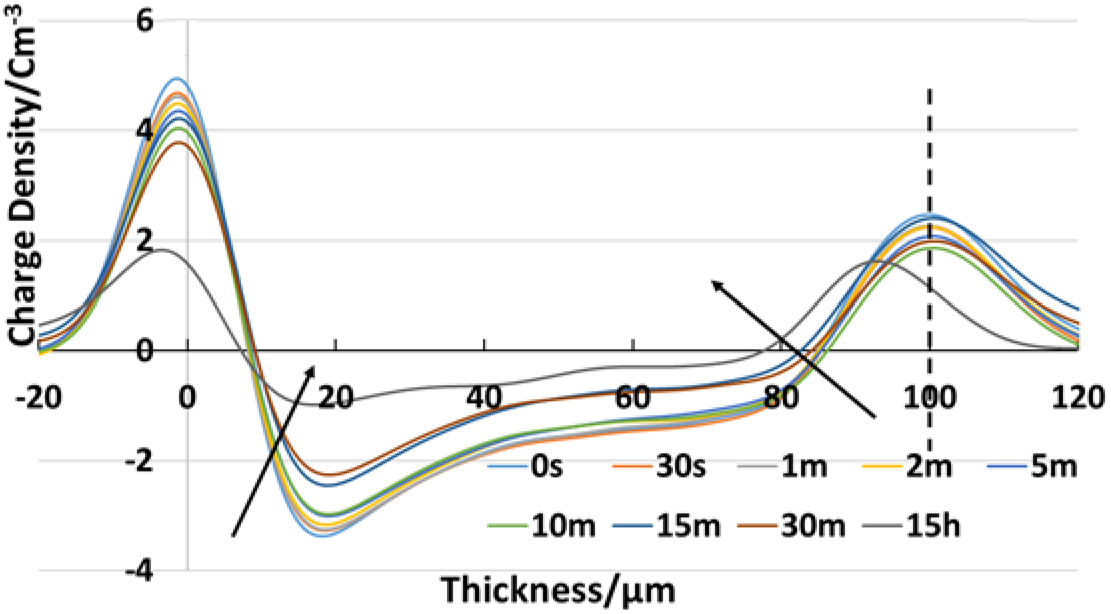

PEA measured charge profile in 100µm LDPE under 50Hz 5kV combined HVAC and HVDC fields with offset ratio 0.2

Appendix B: Raman and ATR-FTIR results

The Raman spectroscopy of the samples was performed using a Renishaw Raman RM1000 system with a 780 nm diode laser; a laser power of 25 mW was used throughout. The spectrometer was set up in line with Renishaw's recommendations for the confocal operation of the instrument. Microscope objectives of 50× and 5× magnification (NA 0.75 and 0.12, respectively) were used to acquire Raman spectra from various locations to give depth profiles for each sample. To proceed the obtained data, firstly spikes and noises (single events and random positions) are removed using multiple accumulations (>1000 times) and polynomial filters. Then the data is normalisation with the baseline correction using the following procedure (The normalisation reference peak chosen for this work is 1294cm^{-1} based on results in [101, 102].):

1. **Calculate the average intensity values for all wavenumbers:** $$\boldsymbol{a_m = \frac{\sum_k a(k)}{k}}$$
2. **Centre the intensities:** $$a'(k) = a(k) - a_m$$
3. **Divide the centred intensities by the length of the spectrum** $$a''(k) = \frac{a'(k)}{\sqrt{\sum_k (a''(k))^2}}$$

After the normalisation, the new spectrum will have a length of 1. An example illustrates the differences between the original spectrum, and the normalised one is illustrated in the following graph:

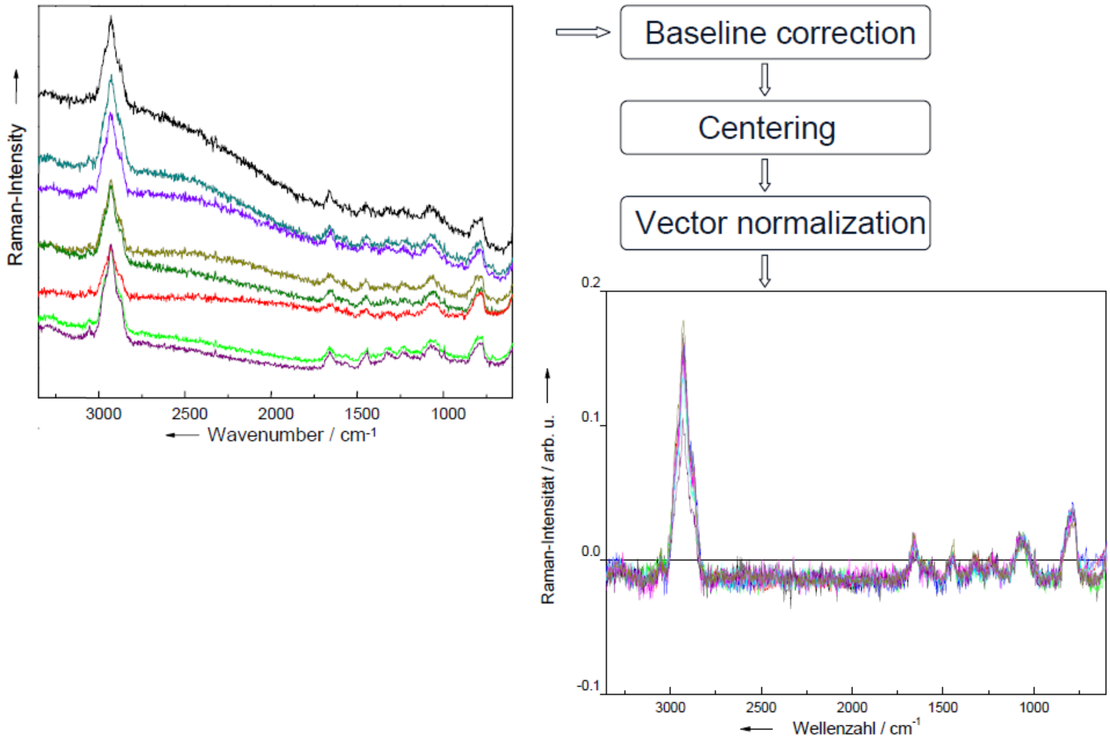

The normalised Raman spectra used in section 3.3.2 are presented below:

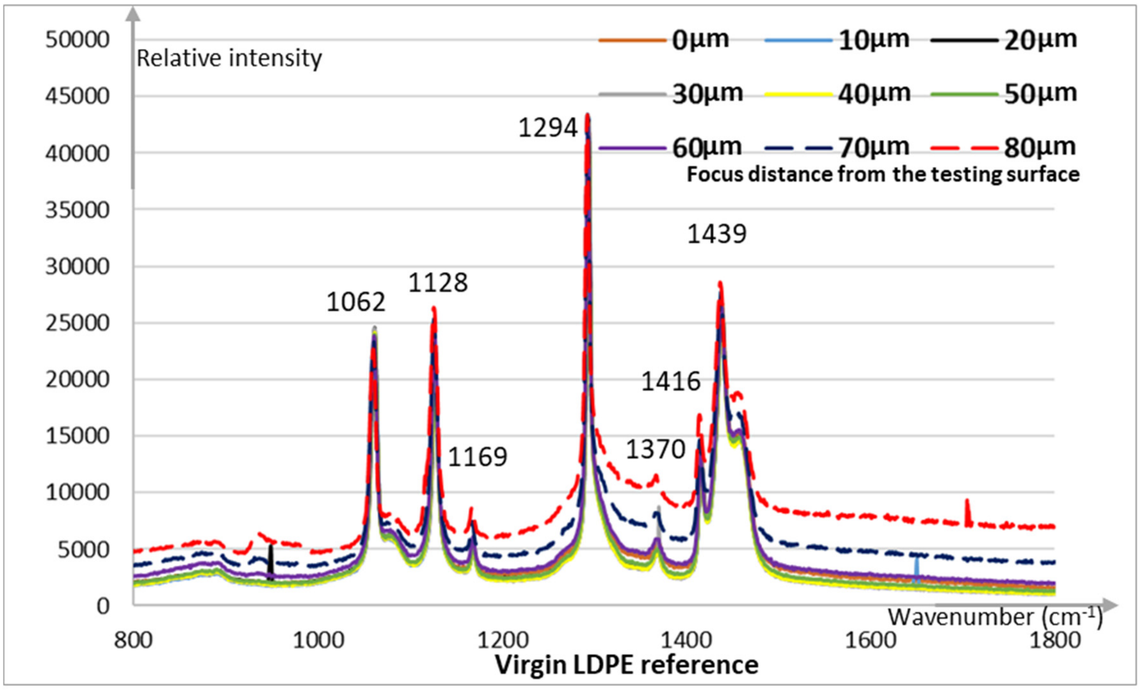

Raman spectra of virgin LDPE film at different focus thickness points (0 µm-80 µm)

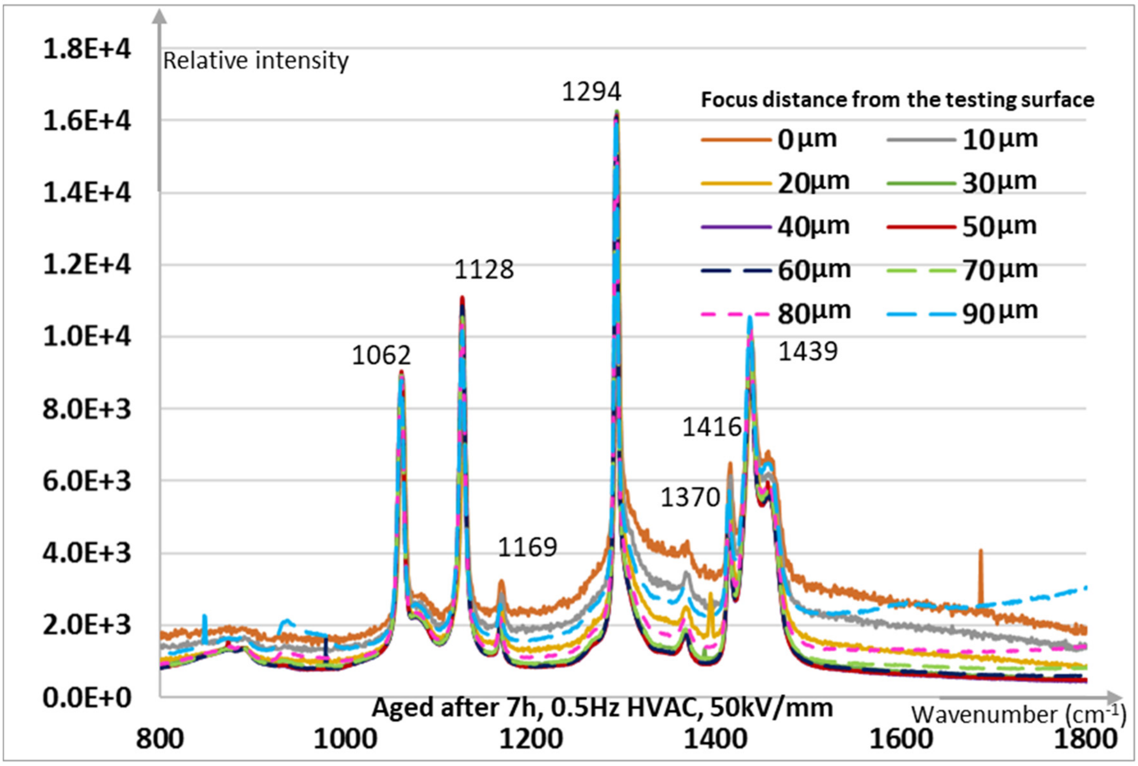

Raman spectra of aged LDPE film after 7hour of 0.5Hz 50kV/mm HVAC at different focus thickness points (0 µm-90 µm)

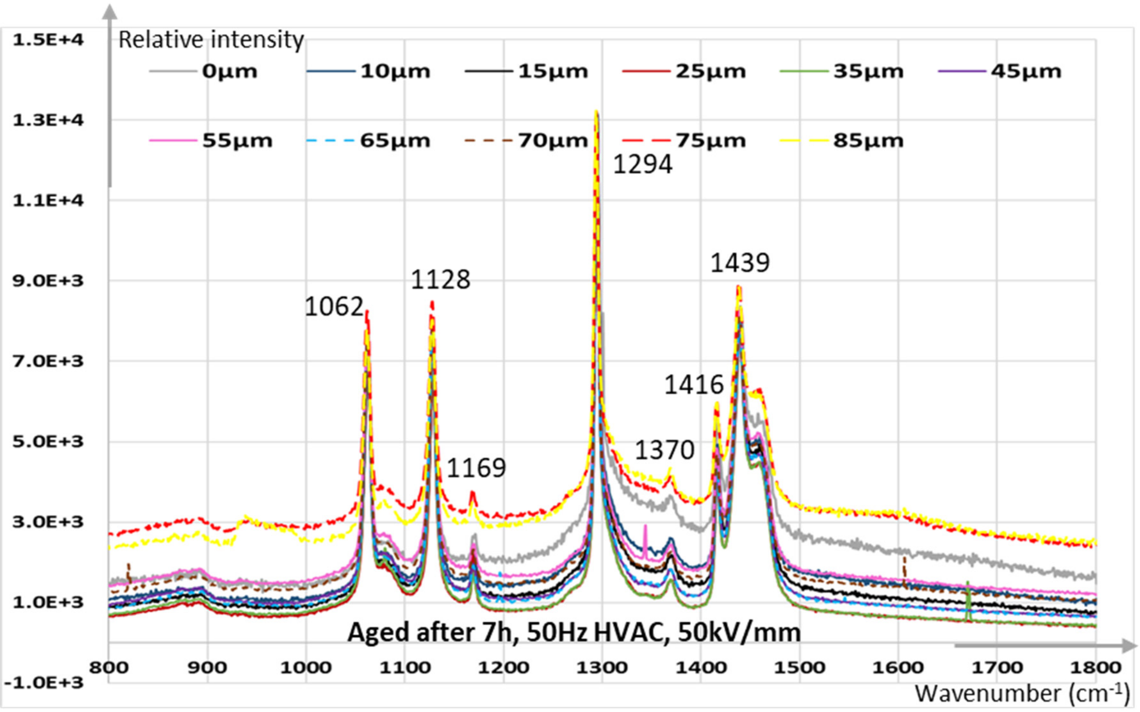

Raman spectra of aged LDPE film after 7hour of 0.5Hz 50kV/mm HVAC at different focus thickness points (0 μm-85 μm)

Similar denoise and normalisation procedure has been used for ATR-FTIR results presented in section 3.3.2. The only difference is the results are demonstrating Transmittance v.s. Wavenumbers rather than Relative intensity v.s. Wavenumbers.

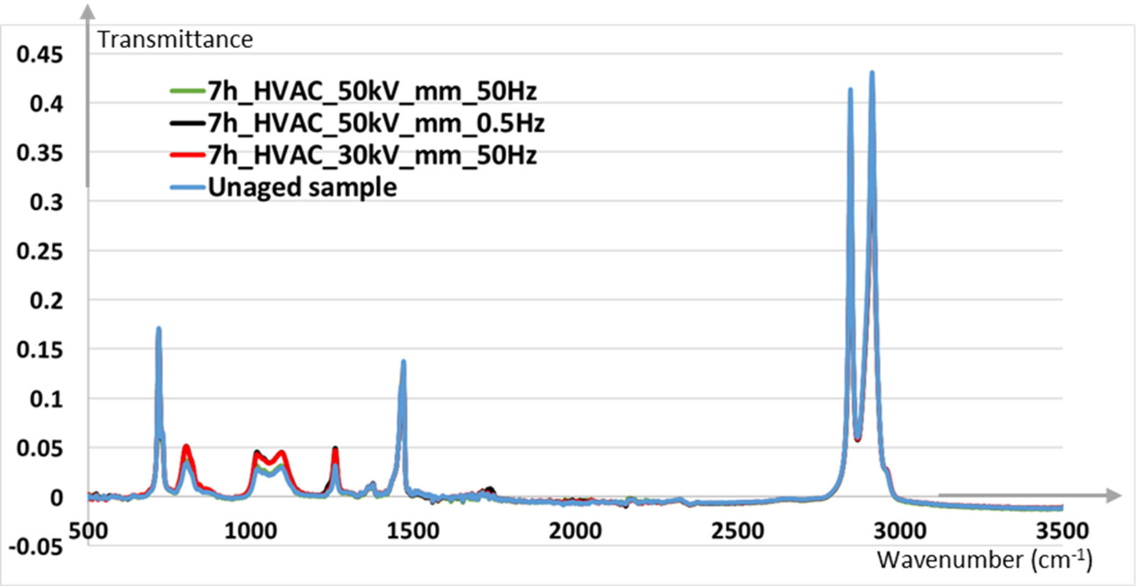

Reflectance Fourier transform infrared (ATR-FTIR) spectroscopy of LDPE sample after 7 hour of various AC field stressing (wavenumber 500-3500 cm^{-1})

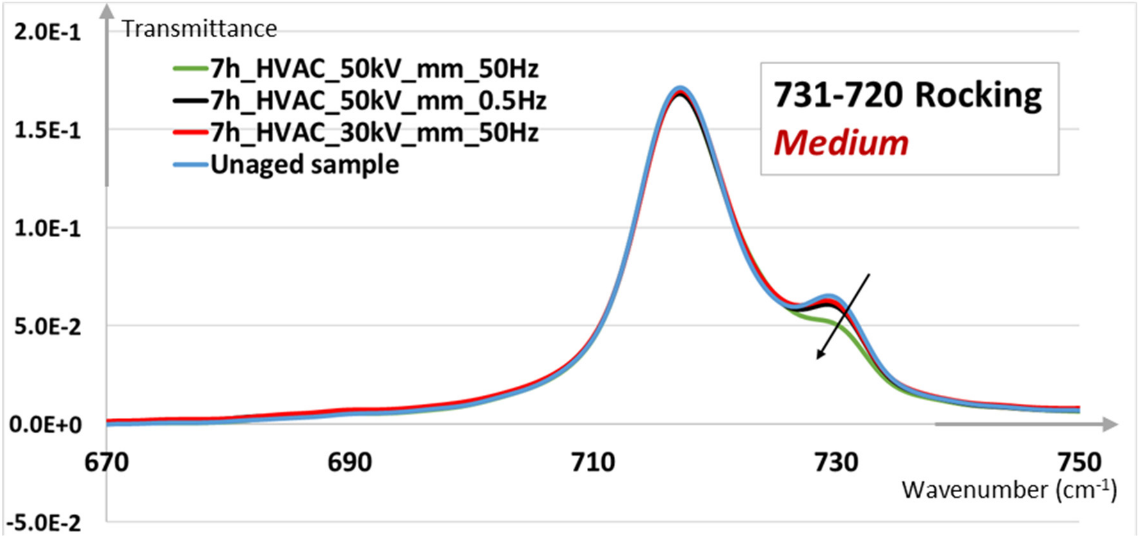

Reflectance Fourier transform infrared (ATR-FTIR) spectroscopy of LDPE sample after 7 hour of various AC field stressing (wavenumber 670-750 cm^{-1})

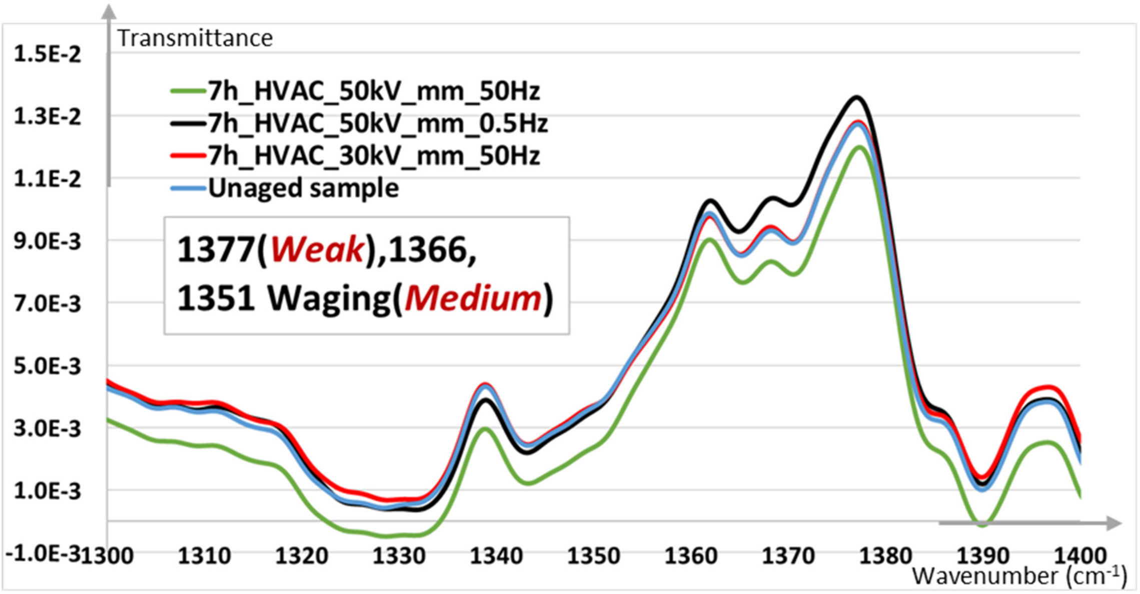

Reflectance Fourier transform infrared (ATR-FTIR) spectroscopy of LDPE sample after 7 hour of various AC field stressing (wavenumber 1300-1400 cm^{-1})

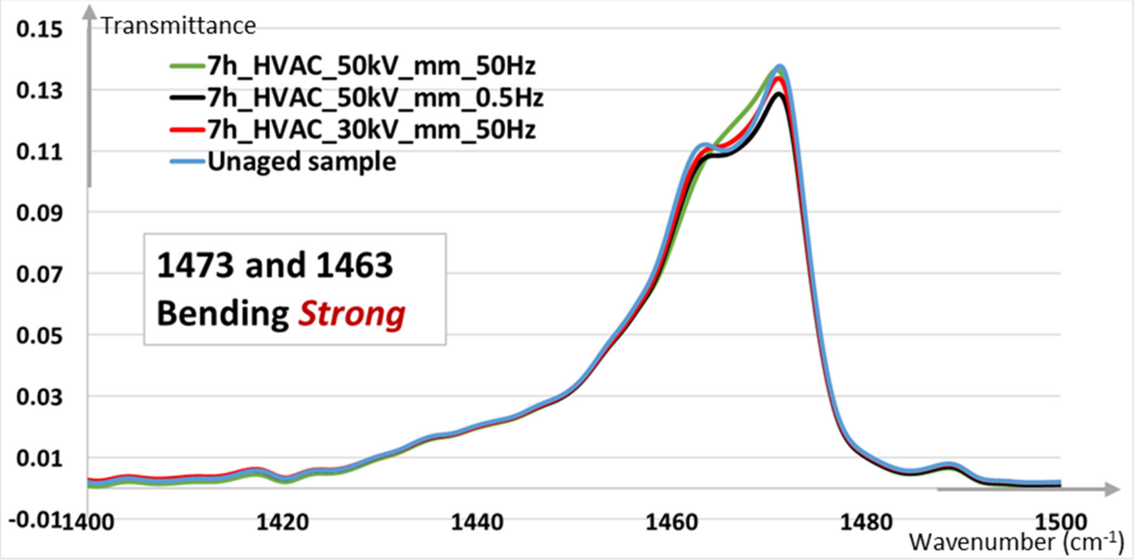

Reflectance Fourier transform infrared (ATR-FTIR) spectroscopy of LDPE sample after 7 hour of various AC field stressing (wavenumber 1400-1500 cm^{-1})

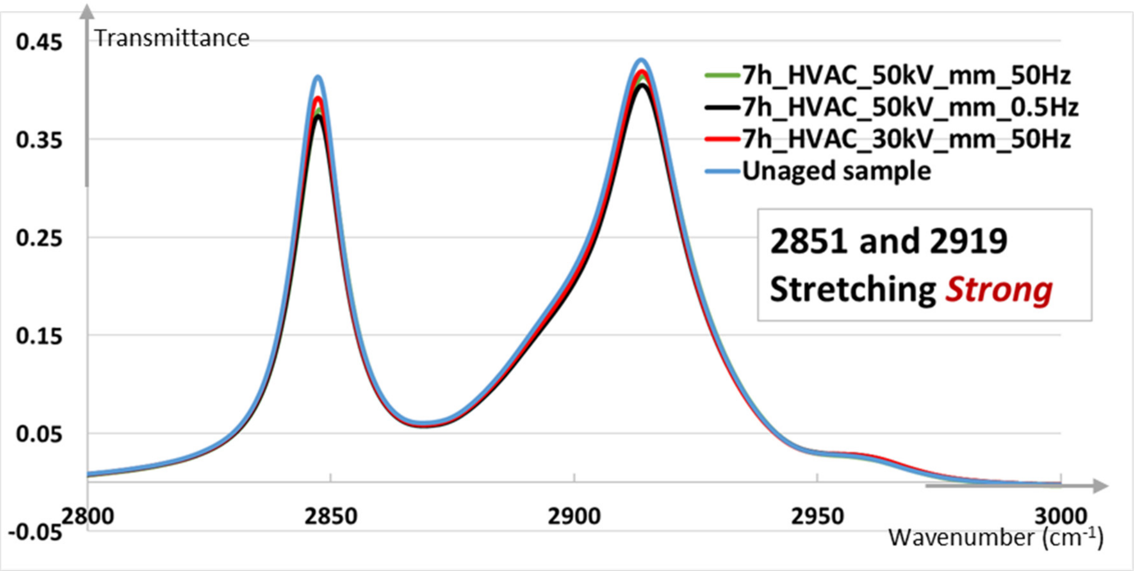

Reflectance Fourier transform infrared (ATR-FTIR) spectroscopy of LDPE sample after 7 hour of various AC field stressing (wavenumber 2800-3000 cm^{-1})

Appendix C: Fitting results of simulation and experiments under HVDC

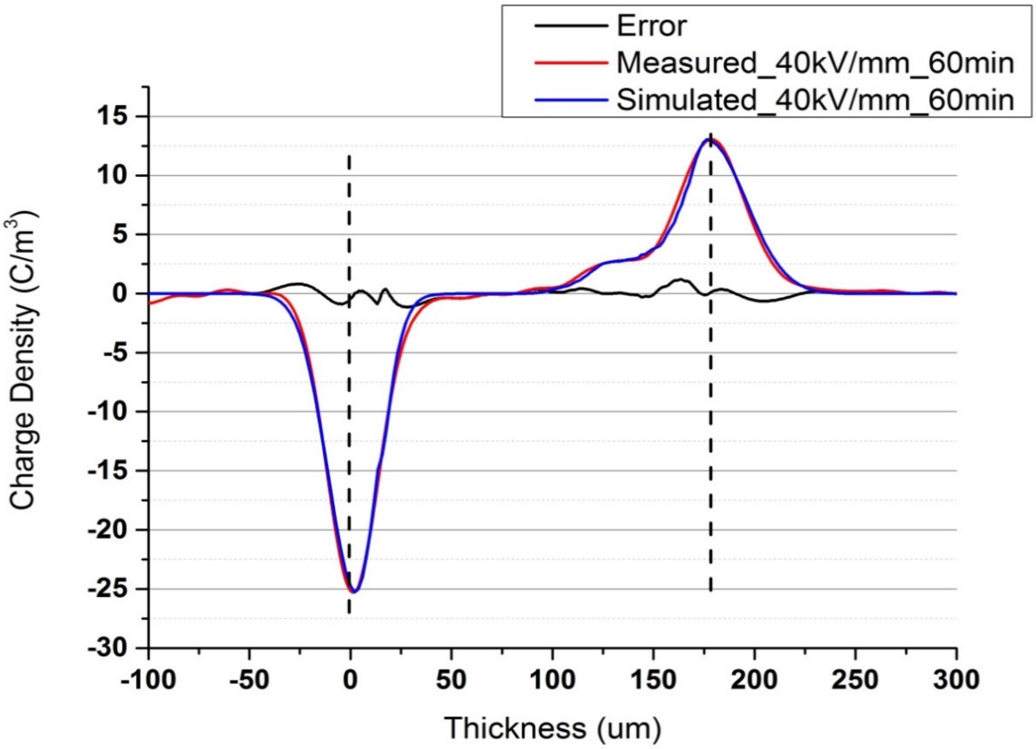

The fitting results of simulation and experiments under 40kV/mm HVDC at 60mins

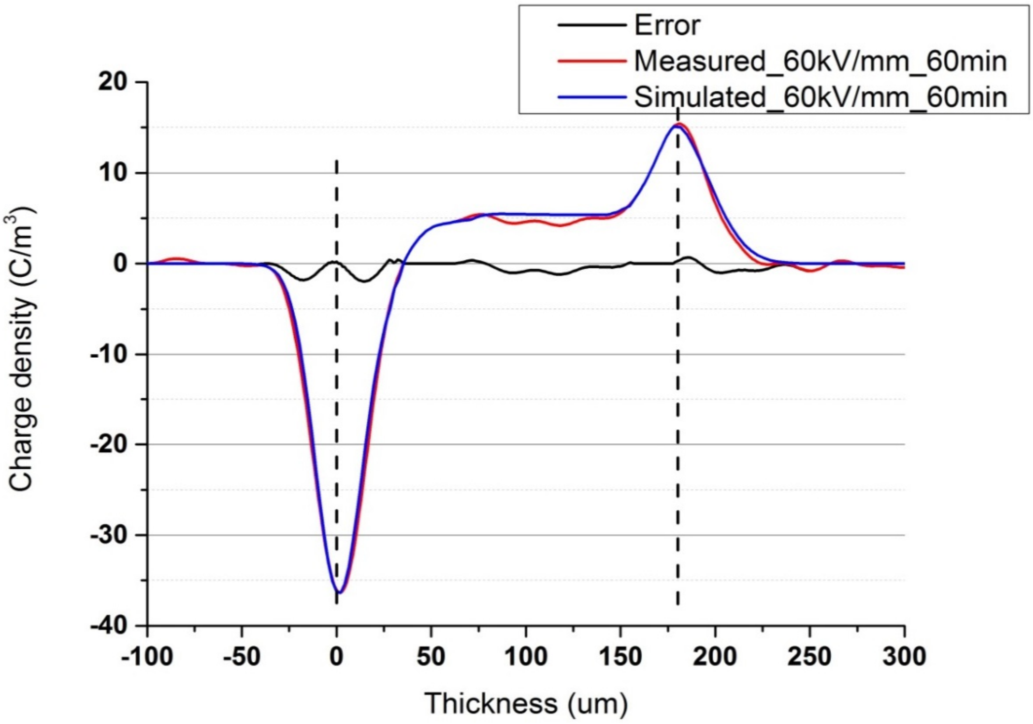

The fitting results of simulation and experiments under 40kV/mm HVDC at 60mins

Appendix D: Standard dielectric tests for Line-commutated converter transformers

The converter transformer is an integral part of an HVDC system. In an HVDC system the converter transformer serves several functions:

- Supply of AC voltages in two separate circuits with a relative phase shift of 30 degrees for reduction of low order harmonics (5Th and 7th harmonics).
- Act as a galvanic barrier between the AC and DC systems to prevent the DC potential to enter the AC system.
- Reactive impedance in the AC supply to reduce short circuit currents and to control the rate of rising in valve current during communication.
- Voltage transformation between the AC and the DC system.
- Reasonably broad ranges with small steps to give necessary adjustments in supply voltage.

The HVDD systems typically have their converters arranged several pulse bridges connected in series, where the bottom end of the lower bridge is tied to the ground. In a Line-commutated converter (LCC) transformers, thyristors are used to change the direction of power transmission. Polarity reversal caused by the AC fields is essential to the operation of thyristors. Therefore filter cannot be added between the transformers and converters to separate the AC and DC operating range. The DC potentials on the two converter valves side winding will then affect the stresses applied to the transformer when they are operating. A Figure demonstrates an example of an LCC link structure is presented below:

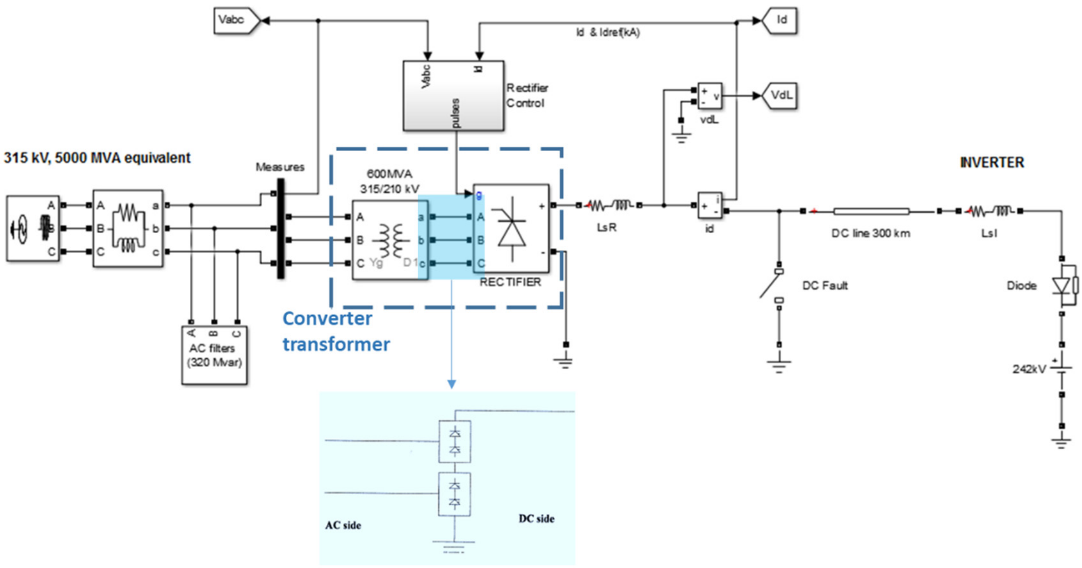

Simple 6-Pulse HVDC Transmission System 500 MW (250kV- 2kA)

Appendix

According to the standard (IEC 61378-2:2001), for DC and AC separate source withstand tests shall be applied to all terminals of converter transformer windings, and the testing level should be deduced using the following equations:

$$U_{dc} = 1.5\left((N-0.5)U_{dm} + 0.7U_{vm}\right)$$

$$U_{ac} = \frac{1.5\left((N-0.5)U_{dm} + \frac{\sqrt{2}U_{vm}}{\sqrt{3}}\right)}{\sqrt{2}}(rms\ value)$$

In this section 5.2.3, the case issued is six-pulse bridges transformer, and the number of bridges, N, considered is 4. U_{dm} indicates the highest DC voltage per valve bridge, and U_{vm} represents the maximum phase to phase AC operating voltage of the valve windings of the transformer.

For 100μm LDPE issuing 50kV/mm superimposed stresses with DC offset ratio 0.2, 0.4 and 0.5, the AC and DC component magnitudes and testing levels are deduced and presented in the following table:

	AC component magnitudes	DC component magnitudes	AC testing voltage RMS values	DC testing voltage
0.2	4 kV	1 kV	4.39 kV	3.675 kV
0.4	3 kV	2 kV	4.45 kV	5.775 kV
0.5	2.5 kV	2.5 kV	4.49 kV	5.9 kV

Table: Standard testing voltages for various DC offset conditions

The profiles used in section 5.3 calculating charge amounts and field distortion are presented below:

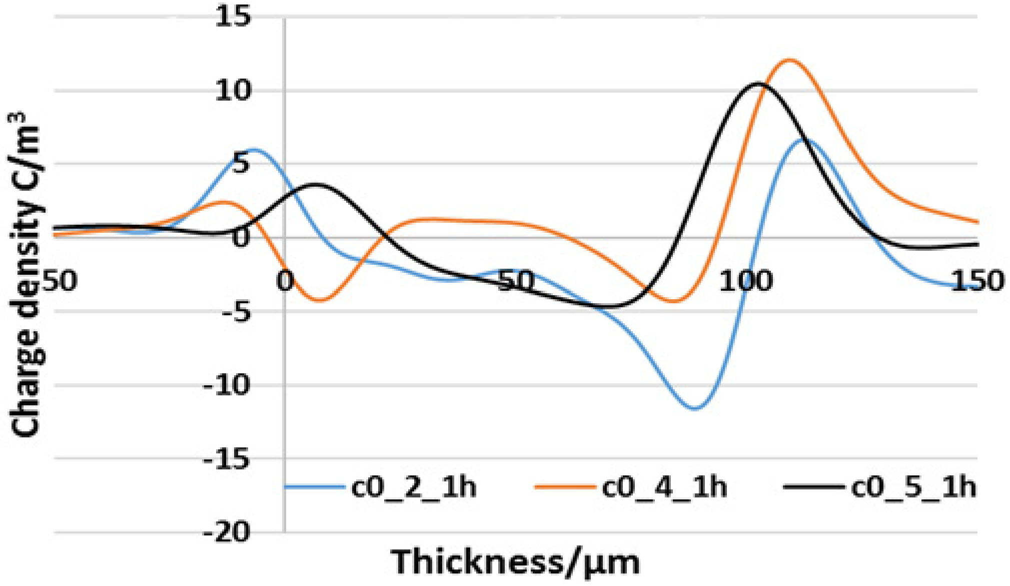

Charge profiles instantly after 1 hour of AC tests

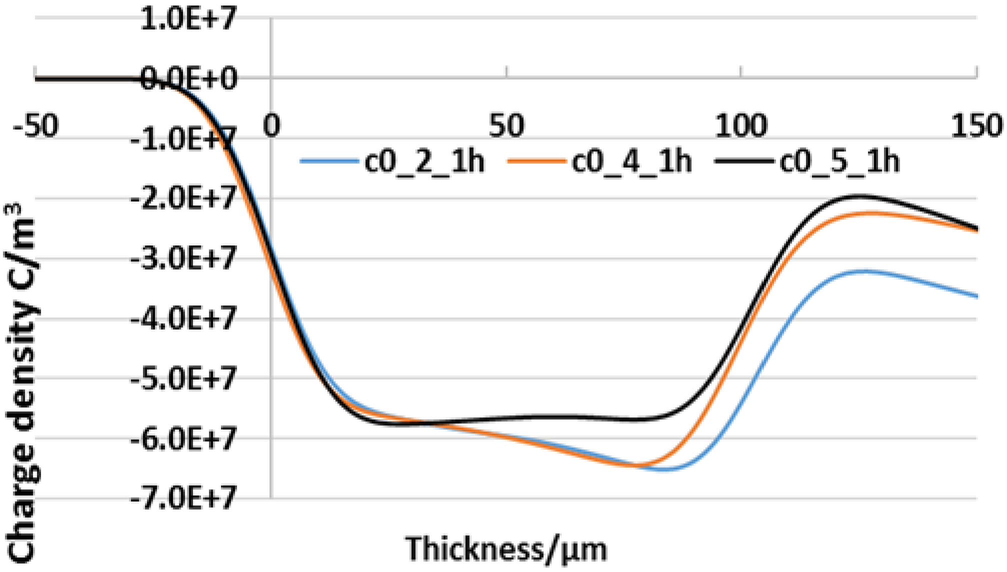

Electric fields instantly after 1 hour of AC tests

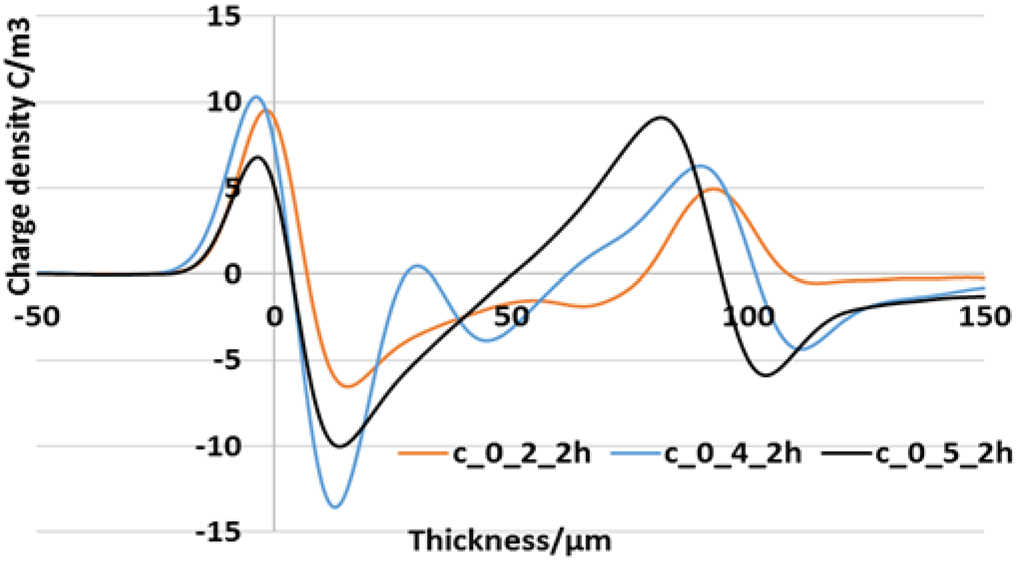

Charge profiles instantly after 2 hour of DC tests

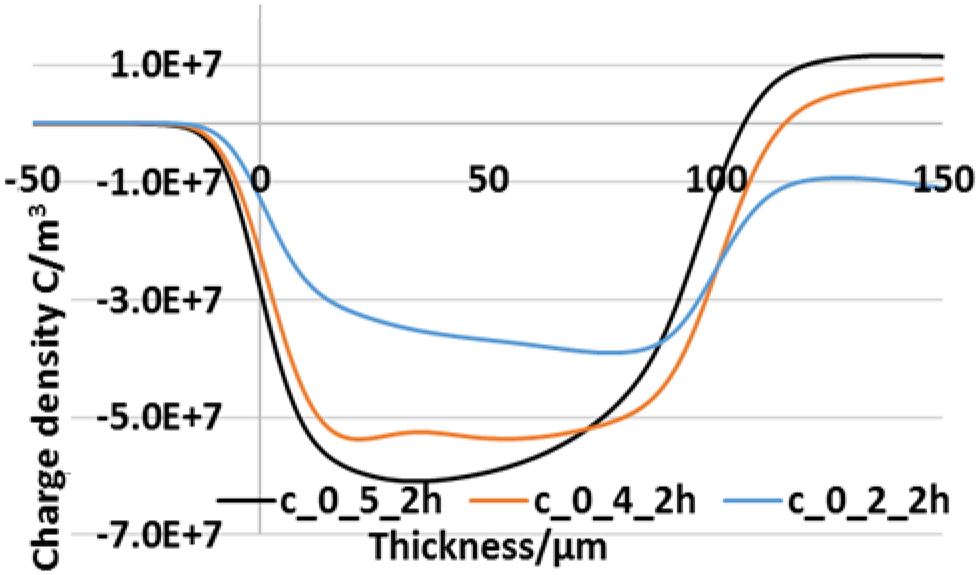

Electric fields instantly after 2 hour of DC tests

List of References

[1] Z. Yewen, J. Lewiner, C. Alquie, and N. Hampton, "Evidence of strong correlation between space charge build up and breakdown in cable insulation," Dielectrics and Electrical Insulation, IEEE Transactions on, vol. 3, pp. 778-783, 1996.

[2] J. Lewiner, "Evolution of experimental techniques for the study of the electrical properties of insulating materials," Electrical Insulation, IEEE Transactions on, vol. EI-21, pp. 351-360, 1986.

[3] R. Fleming, "Space charge in polymers, particularly polyethylene," Brazilian Journal of Physics, vol. 29, pp. 280-294, Jun 1999.

[4] Y. Li and T. Takada, "Progress in space charge measurement of solid insulating materials in japan," IEEE Electrical Insulation Magazine, vol. 10, pp. 16-28, Sep-Oct 1994.

[5] M. Fu and G. Chen, "Space charge measurement in polymer insulated power cables using flat ground electrode PEA system," Science, Measurement and Technology, IEE Proceedings, vol. 150, pp. 89-96, 2003.

[6] E. Belgaroui, I. Boukhris, A. Kallel, G. Teyssedre, and C. Laurent, "A new numerical model applied to bipolar charge transport, trapping and recombination under low and high dc voltages," Journal of Physics D: Applied Physics, vol. 40, p. 6760, 2007.

[7] J. Alison and R. M. Hill, "A model for bipolar charge transport, trapping and recombination in degassed cross-linked polyethylene" vol. 27. Bristol, ROYAUME-UNI: Institute of Physics, 1994.

[8] S. Roy, P. Segur, G. Teyssedre, and C. Laurent, "Description of bipolar charge transport in polyethylene using a fluid model with a constant mobility: model prediction," Journal of Physics D: Applied Physics, vol. 37, pp. 298-305, 2004.

[9] J. Tian, J. Zou, Y. Wang, J. Liu, J. Yuan, and Y. Zhou, "Simulation of bipolar charge transport with trapping and recombination in polymeric insulators using Runge–Kutta discontinuous Galerkin method," Journal of Physics D: Applied Physics, vol. 41, p. 195416, 2008.

[10] J. Peacock, Handbook of polyethylene: structures, properties, and applications. New York: Marcel Dekker, 2000.

[11] L. Dissado and J. C. Fothergill, Electrical degradation and breakdown in polymers. London: P. Peregrinus, 1992.

[12] L. Bowen, An introduction to polymer physics. Cambridge; New York: Cambridge University Press, 2002.

[13] J. Hall, "History and bibliography of polymeric insulators for outdoor applications," IEEE Transactions on Power Delivery, vol. 8, pp. 376-385, 1993.

[14] J. Mark, Polymer data handbook: Oxford University Press, 1999.

[15] Shin-Etsu Silicone Ltd, "Characteristics properties of silicone rubber compounds,"., pp. 1-16, 2005.

[16] T. Lewis, "Polyethylene under electrical stress," IEEE Transactions on Dielectrics and Electrical Insulation, vol. 9, pp. 717-729, 2002.

[17] D. Malpass and I. Wiley, Introduction to industrial polyethylene: properties, catalysts, processes. Salem, Mass.: Hoboken, 2010.

[18] P. Argaut, H. Auclair, and E. Favrie, "Development of 500 kV low density polyethylene insulated cable," in 3rd International Conference on Power Cables and Accessories 10kV - 500kV, 1993, pp. 77-81.

[19] W. J. Plate, T. H. Ling, and J. F. Nuccio, "Reassessment of polyethylene power cable," IEEE Transactions on Power Apparatus and Systems, vol. 82, pp. 990-1002, 1963.

[20] G. Moore, Electric Cables Handbook. Oxford: Wiley-Blackwell, 1997.

[21] B. A. B. P. Ltd, "XLPE compounds for extra high voltage cables," 2010.

[22] R. Vogelsang, O. Sekula, H. Nyffenegger, and W. Weissenberg, "Long-term experiences with XLPE cable systems up to 550 kV," in KONFERENCA SLOVENSKIH ELEKTROENERGETIKOV CIGRE SC B1 Kranjska Gora, 2009.

[23] M. Salah Khalil, "International research and development trends and problems of HVDC cables with polymeric insulation," IEEE Electrical Insulation Magazine, vol. 13, pp. 35-47, 1997.

[24] R. Eichhorn, "Treeing in solid extruded electrical insulation," IEEE Transactions on Electrical Insulation vol. EI-12, pp. 2-18, 1977.

[25] G. Chen and C. Tham, "Electrical treeing characteristics in XLPE power cable insulation in frequency range between 20 and 500 Hz," IEEE Transactions on Dielectrics and Electrical Insulation, vol. 16, pp. 179-188, 2009.

[26] N. Shimizu, N. Nagura, T. Suzuki, and A. Tanida, "Electroluminescence and degradation in PE caused by electron impact," in 2003 Annual Report of Conference on Electrical Insulation and Dielectric Phenomena 2003, pp. 361-364

[27] Z. Fan, T. Takahashi, J. Suzuki, H. Miyata, S. Iemura, T. Itoh, T. Nakiri, and N. Shimizu, "Relation between electroluminescence and degradation in XLPE," IEEE Transactions on Dielectrics and Electrical Insulation, vol. 8, pp. 91-96,2001

[28] Blythe, Electrical properties of polymers. Cambridge, Eng.; New York: Cambridge University Press, 1979.

[29] G. Montanari, G. Mazzanti, F. Palmieri, A. Motori, G. Perego, and S. Serra, "Space-charge trapping and conduction in LDPE, HDPE and XLPE," Journal of Physics D-Applied Physics, vol. 34, pp. 2902-2911, Sep 21 2001

[30] K. Kao, Dielectric phenomena in solids: with emphasis on physical concepts of electronic processes. Amsterdam ; Boston: Academic Press, 2004

[31] Y. Li, M. Yasuda, and T. Takada, "Pulsed electroacoustic method for measurement of charge accumulation in solid dielectrics," Dielectrics and Electrical Insulation, IEEE Transactions on, vol. 1, pp. 188-195, 1994

[32] J. G. Simmons and G. W. Taylor, "Nonequilibrium steady-state statistics and associated effects for insulators and semiconductors containing an arbitrary distribution of traps," Physical Review B-Solid State, vol. 4, pp. 502-&, 1971.

[33] J. G. Simmons, "Poole-frenkel effect and Schottky effect in metal-insulator-metal systems," physical review, vol. 155, pp. 657-660, 03/15/ 1967.

[34] G. G. Raju, Dielectrics in electric fields. New York: Marcel Dekker, 2003

[35] P. A. Leighton, "Electronic processes in ionic crystals," Journal of Chemical Education, vol. 18, p. 249, 1941/05/01 1941

[36] N. Ando and F. Numajiri, "Experimental investigation of space-charge in XLPE cable using dust figure," IEEE Transactions on Electrical Insulation, vol. 14, pp. 36-42, 1979.

[37] M. Khalil and B. Hansen, "Investigation of Space-Charge in Low-Density Polyethylene Using a Field Probe Technique," IEEE Transactions on Electrical Insulation, vol. 23, pp. 441-445, Jun 1988.

[38] Z. Xu, "Space charge measurement and analysis in low density polyethylene films," Doctoral, School of Electronics and Computer Science, University of Southampton, 2009.

[39] G. Mazzanti, G. Mazzanti, and M. Marzinotto, Extruded cables for high-voltage direct-current transmission: advances in research and development, First edition. Ed. Hoboken, New Jersey: Piscataway, NJ: John Wiley & Sons, 2013.

[40] R. E. Collins, "Analysis of spatial-distribution of charges and dipoles in electrets by a transient heating technique," Journal of Applied Physics, vol. 47, pp. 4804-4808, 1976.

[41] H. Vonseggern, "Thermal-pulse technique for determining charge-distributions - effect of measurement accuracy," Applied Physics Letters, vol. 33, pp. 134-137, 1978.

[42] S. B. Lang and D. Das-Gupta, "A technique for determining the polarization distribution in thin polymer electrets using periodic heating," Ferroelectrics, vol. 39, pp. 1249-1252, 1981.

[43] P. Notingher, S. Agnel, A. Toureille, B. Rousset, and J. L. Sanche, "Characterization of electric charge in non-irradiated and irradiated MOS structures by thermal step and capacitance-voltage measurements," 2002 Annual Report Conference on Electrical Insulation and Dielectric Phenomena, pp. 95-100, 2002

[44] G. M. Sessler, J. E. West, and G. Gerhard, "High-resolution laser-pulse method for measuring charge distributions in dielectrics," Physical Review Letters, vol. 48, pp. 563-566, 1982.

[45] Alquie, G. Charpak, and J. Lewiner, "Pulsed Laser Determination of Surface Electric Charge-Distributions," Journal De Physique Lettres, vol. 43, pp. L687-L693, 1982.

[46] S. Kurtz and R. Anderson, "Properties of the meta-polymer interface observed with space charge mapping techniques," Journal of applied physics, vol. 60, pp. 681-687, 1986.

[47] Tanaka, M. Maeda, and T. Takada, "Observation of charge behaviour in organic photoconductor using pressure-wave propagation method," IEEE Transactions on Electrical Insulation, vol. 27, pp. 440-444, 1992.

[48] T. Takada and T. Sakai, "Measurement of electric-fields at a dielectric electrode interface using an acoustic transducer technique," IEEE Transactions on Electrical Insulation, vol. 18, pp. 619-628, 1983.

[49] A. Vazquez, G. Chen, A. E. Davies, and R. Bosch, "Space charge measurement using pulsed electroacoustic technique and signal recovery," Journal of the European Ceramic Society, vol. 19, pp. 1219-1222, 1999.

[50] D. Davies, "The examination of the electrical properties of insulators by surface charge measurement," Journal of Scientific Instruments, vol. 44, p. 521, 1967.

[51] J. Yarmchuk and G. E. Keefe, "High-resolution surface-charge measurements on an organic photoconductor," Journal of Applied Physics, vol. 66, pp. 5435-5439, Dec 1 1989.

[52] M. A. Noras. 2003, Charge detection methods for dielectrics – overview.

[53] J. Zhao, "Dynamics of space charge and electroluminescence modelling in polyethylene," doctoral, electronics and computer science, University of Southampton, 2012.

[54] K. Fukunaga, "Progress and prospects in pea space charge measurement techniques," electrical insulation magazine, IEEE, vol. 24, pp. 26-37, 2008.

[55] Y. Murakami, M. Nemoto, S. Okuzumi, S. Masuda, M. Nagao, N. Hozumi, et al., "DC conduction and electrical breakdown of MgO/LDPE nanocomposite," Dielectrics and Electrical Insulation, IEEE Transactions on, vol. 15, pp. 33-39, 2008.

[56] T. Chao, G. Chen, M. Fu, and L. Rui-jin, "Space charge behaviour in multi-layer oil-paper insulation under different DC voltages and temperatures," Dielectrics and Electrical Insulation, IEEE Transactions on, vol. 17, pp. 775-784, 2010.

[57] W. Xia, Z. Mingbo, C. Xi, P. Zongren, W. Kai, L. Song, et al., "The effect of temperature gradient on space charge accumulation at SR/XLPE interface under DC stress," in Solid Dielectrics (ICSD), 2010 10th IEEE International Conference on, 2010, pp. 1-4.

[58] T. Mizutani, "Space charge measurement techniques and space charge in polyethylene," Dielectrics and Electrical Insulation, IEEE Transactions on, vol. 1, pp. 923-933, 1994.

[59] M. Fukuma, M. Nagao, and M. Kosaki, "Computer analysis on transient space charge distribution in polymer," in Properties and Applications of Dielectric Materials, 1994., Proceedings of the 4th International Conference on, 1994, pp. 24-27 vol.1.

[60] K. Kaneko, T. Mizutani, and Y. Suzuoki, "Computer simulation on formation of space charge packets in XLPE films," Dielectrics and Electrical Insulation, IEEE Transactions on, vol. 6, pp. 152-158, 1999.

[61] G. Chen and S. Loi, "Space charge modelling in solid dielectrics under high electric field based on double charge injection model," presented at the MRS Fall Meeting, 2005.

[62] J. Zhao, Z. Xu, G. Chen, and P. L. Lewin, "Numeric description of space charge in polyethylene under ac electric fields," Journal of Applied Physics, vol. 108, 2010.

[63] G. Chen, J. Zhao, S. Li, and L. Zhong, "Origin of thickness dependent dc electrical breakdown in dielectrics," Applied Physics Letters, vol. 100, p. 222904, 2012.

[64] K. Fukunaga, "Industrial applications of space charge measurement in Japan," IEEE Electrical Insulation Magazine, vol. 15, pp. 6-18, 1999.

[65] T. Takada, T. Maeno, and H. Kushibe, "An electric stress-pulse technique for the measurement of charges in a plastic plate irradiated by an electron beam," Electrical Insulation, IEEE Transactions on, vol. EI-22, pp. 497-501, 1987.

[66] T. Maeno, T. Futami, H. Kushibe, T. Takada, and C. M. Cooke, "Measurement of spatial charge-distribution in thick dielectrics using the pulsed electroacoustic method," IEEE Transactions on Electrical Insulation, vol. 23, pp. 433-439, 1988.

[67] M. Yasuda, M. Ito, and T. Takada, "Measurement of charge-distributions in coaxial-cable using the pulsed electroacoustic method," Japanese Journal of Applied Physics Part 1-Regular Papers Short Notes & Review Papers, vol. 30, pp. 71-73, 1991.

[68] N. Hozumi, T. Okamoto, and T. Imajo, "Space charge distribution measurement in a long size XLPE cable using the pulsed electroacoustic method," in Electrical Insulation, Conference Record of the 1992 IEEE International Symposium on, 1992, pp. 294-297.

[69] R. Liu, T. Takada, and N. Takasu, "Pulsed electro-acoustic method for measurement of space charge distribution in power cables under both DC and AC electric fields," Journal of Physics D: Applied Physics, vol. 26, p. 986, 1993.

[70] Y. Liu and M. M. A. Salama, "Investigating space charge dynamics in polymers by the improved pulsed electro-acoustic method," in Electrical Insulation and Dielectric Phenomena, 1996., IEEE 1996 Annual Report of the Conference on, 1996, pp. 169-173 vol.1.

[71] S. Imai, Y. Tanaka, T. Fukao, T. Takada, and T. Maeno, "Development of new PEA system using open upper electrode (pulsed electro-acoustic method)," in Electrical Insulation and Dielectric Phenomena, 2004. CEIDP '04. 2004 Annual Report Conference on, 2004, pp. 61-64.

[72] G. Chen, Y. Chong, and M. Fu, "Calibration of the pulsed electroacoustic technique in the presence of trapped charge," Measurement Science and Technology, vol. 17, pp. 1974-1980, 2006.

[73] X. Wang, D. Tu, Y. Tanaka, T. Muronaka, T. Takada, C. Shinoda, et al., "Space charge in XLPE power cable under DC electrical stress and heat treatment," Dielectrics and Electrical Insulation, IEEE Transactions on, vol. 2, pp. 467-474, 1995.

[74] S. Hole, C. Alquie, and J. Lewiner, "Measurement of space-charge distributions in insulators under very rapidly varying voltage," Dielectrics and Electrical Insulation, IEEE Transactions on, vol. 4, pp. 719-724, 1997.

[75] Y. Tanaka, H. Kitajima, M. Kodaka, and T. Takada, "Analysis and discussion on conduction current based on simultaneous measurement of TSC and space charge distribution," Dielectrics and Electrical Insulation, IEEE Transactions on, vol. 5, pp. 952-956, 1998.

[76] M. Fu, G. Chen, L. A. Dissado, and J. C. Fothergill, "Influence of thermal treatment and residues on space charge accumulation in XLPE for DC power cable application," Dielectrics and Electrical Insulation, IEEE Transactions on, vol. 14, pp. 53-64, 2007.

[77] F. Rogti, A. Mekhaldi, and C. Laurent, "Space charge behaviour at physical interfaces in cross-linked polyethylene under DC field," Dielectrics and Electrical Insulation, IEEE Transactions on, vol. 15, pp. 1478-1485, 2008.

[78] C. Montanari, G. Mazzanti, E. Boni, and G. De Robertis, "Investigating ac space charge accumulation in polymers by PEA measurements," 2000 Annual Report Conference on Electrical Insulation and Dielectric Phenomena, Vols. II, pp. 113-116, 2000.

[79] Y. Ching, H. Miyake, Y. Tanaka, T. Takada, H. Nakama, and G. Chen, "Space charge in polyethylene under AC electric stress using the pulsed electroacoustic method," in Electrical Insulation and Dielectric Phenomena, 2004. CEIDP '04. 2004 Annual Report Conference on, 2004, pp. 77-80.

[80] C. Thomas, G. Teyssedre, and C. Laurent, "Space charge measurements in low-density polyethylene under ac stress by the pulsed electro-acoustic method," in Electrical Insulation and Dielectric Phenomena(CEIDP), 2008. Annual Report Conference on, 2008, pp. 325-328.

[81] C. Thomas, G. Teyssedre, and C. Laurent, "A new method for space charge measurements under periodic stress of arbitrary waveform by the pulsed electro-acoustic method," Dielectrics and Electrical Insulation, IEEE Transactions on, vol. 15, pp. 554-559, 2008.

[82] J. Zhao, G. Chen, and L. S. Zhong, "Space charge in polyethylene under combined ac and dc voltages," IEEE Transactions on Dielectrics and Electrical Insulation, vol. 21, pp. 1757-1763, Aug 2014.

[83] G. Teyssedre and C. Laurent, "Charge transport modeling in insulating polymers: From molecular to macroscopic scale," Ieee Transactions on Dielectrics and Electrical Insulation, vol. 12, pp. 857-875, Oct 2005.

[84] N. Liu, C. Zhou, G. Chen, and L. Zhong, "Determination of threshold electric field for charge injection in polymeric materials," Applied Physics Letters, vol. 106, p. 192901, 2015.

[85] V. Zakrevskii, N. Sudar, A. Zaopo, and Y. A. Dubitsky, "Mechanism of electrical degradation and breakdown of insulating polymers," Journal of applied physics, vol. 93, pp. 2135-2139, 2003.

[86] K. Matsui, Y. Tanaka, T. Takada, T. Fukao, K. Fukunaga, T. Maeno, et al., "Space charge behaviour in low density polyethylene at pre-breakdown," Dielectrics and Electrical Insulation, IEEE Transactions on, vol. 12, pp. 406-415, 2005.

[87] A. Bradwell, R. Cooper, B. Varlow "Conduction in polyethylene with strong electric field and the effect of pre-stressing on the electric strength," Proceedings of the Institution of Electrical Engineers, vol. 118, pp. 247-254, 1971.

[88] F. Forlani and N. Minnaja, "Electrical breakdown in thin dielectric films," Journal of Vacuum Science and Technology, vol. 6, pp. 518-526, 1969.

[89] H. Zhou, F. Shi, and B. Zhao, "Thickness dependent dielectric breakdown of PECVD low-k carbon doped silicon dioxide dielectric thin films: modeling and experiments," Microelectronics journal, vol. 34, pp. 259-264, 2003.

[90] K. Matsui, Y. Tanaka, T. Takada, T. Fukao, and T. Maeno, "Short-duration space charge observation in LDPE at the electrical breakdown," IEEE Transactions on Fundamentals and Materials, vol. 123, pp. 669-675, 2003.

[91] J. Zhao, G. Chen, and P. L. Lewin, "Investigation into the formation of charge packets in polyethylene: Experiment and simulation," Journal of Applied Physics, vol. 112, pp. 034116-034116-6, 2012.

[92] J. Auge, C. Laurent, D. Fabiani, and G. Montanari, “Investigating DC polyethylene threshold by space charge, current and electroluminescence measurements,” IEEE Trans. Dielectric Electrical Insulation. 7, 797–803 (2000).

[93] C. Zhou and G. Chen, "Influences of frequency on space charge formation in polyethylene under high voltage AC electric fields," in Electrical Insulation and Dielectric Phenomena (CEIDP), 2016 IEEE Conference on, 2016, pp. 117-120.

[94] N. Hozumi, H. Suzuki, T. Okamoto, K. Watanabe, and A. Watanabe, "Direct observation of time-dependent space charge profiles in XLPE cable under high electric fields," Dielectrics and Electrical Insulation, IEEE Transactions on, vol. 1, pp. 1068-1076, 1994.

[95] H. Kon, Y. Suzuoki, T. Mizutani, M. Ieda, and N. Yoshifuji, "Packet-like space charges and conduction current in polyethylene cable insulation," IEEE transactions on dielectrics and electrical insulation, vol. 3, pp. 380-385, 1996.

[96] J. Jones, J. Llewellyn, and T. Lewis, "The contribution of field-induced morphological change to the electrical ageing and breakdown of polyethylene," IEEE Transactions on Dielectrics and Electrical Insulation, vol. 12, pp. 951-966, 2005

[97] G. Chen and J. W. Zhao, "Observation of negative differential mobility and charge packet in polyethylene," Journal of Physics D-Applied Physics, vol. 44, Jun 1 2011.

[98] G. Chen, S. T. Li, and L. S. Zhong, "Space charge in polymeric insulation under ac electric fields-- A schematic model," in Electrical Insulation and Dielectric Phenomena (CEIDP), 2013 IEEE Conference 2013, pp. 663-666.

[99] G. Chen, M. Fu, X. Z. Liu and L. S. Zhong, “AC ageing and space-charge characteristics in low-density polyethylene polymeric insulation”, Journal of Applied Physics, 97, 083713, 2005.

[100] C. Laurent., et al. (2004). "Time-resolved space charge and electroluminescence measurements in polyethylene under ac stress." Dielectrics and Electrical Insulation, IEEE Transactions on 11(4): 554-560.

[101] H. Sato, M. Shimoyama, T. Kamiya, T. Amari, S. Šašic, T. Ninomiya, et al., "Raman spectra of high density, low density, and linear low density polyethylene pellets and prediction of their physical properties by multivariate data analysis," Journal of applied polymer science, vol. 86, pp. 443-448, 2002.

[102] A. MacDonald, A. Vaughan, and P. Wyeth, "On confocal Raman spectroscopy of semi-crystalline polymers: the effect of optical scattering," Applied spectroscopy, vol. 57, pp. 1475-1481, 2003.

[103] J. Gulmine, P. Janissek, H. Heise, and L. Akcelrud, "Polyethylene characterization by FTIR," Polymer Testing, vol. 21, pp. 557-563, 2002.

[104] S. Roy, G. Teyssedre, C. Laurent, G. Montanari, and F. Palmieri, "Description of charge transport in polyethylene using a fluid model with a constant mobility: fitting model and experiments," Journal of Physics D: Applied Physics, vol. 39, pp. 1427-1436, 2006.

[105] M. Alison and R. M. Hill, "A model for bipolar charge transport in insulators," in Conduction and Breakdown in Solid Dielectrics, 1995. ICSD’95, Proceedings of the 1995 IEEE 5th International Conference on, 1995, pp. 319-323.

[106] S. Roy, G. Teyssèdre, and C. Laurent, "Modelling space charge in a cable geometry," IEEE Transactions on Dielectrics and Electrical Insulation, vol. 23, pp. 2361-2367, 2016.

[107] N. Bakhvalov, "Courant–Friedrichs–Lewy condition", in Hazewinkel, Michiel, Encyclopedia of Mathematics, Springer, ISBN 978-1-55608-010-4, 2001.

[108] T. Sonnonstine and M. Perlman, "Surface-potential decay in insulators with field-dependent mobility and injection efficiency," Journal of Applied Physics, vol. 46, p. 3975, 1975.

[109] J. Zhao, Z. Xu, G. Chen, and P. L. Lewin, "Numeric description of space charge in polyethylene under ac electric fields," Journal of Applied Physics, vol. 108, Dec 15 2010.

[110] Y. Murakami and G. Chen, "Influence of Film Thickness on Space Charge Formation under dc Ramp Voltage," presented at the IEEE 2013 International Conference on Solid Dielectrics.

[111] P. Blom, M. Jong, and M. Munster, "Electric-field and temperature dependence of the hole mobility in poly (p-phenylene vinylene)," Physical Review B, vol. 55, pp. R656-R659, Jan 1 1997.

[112] J. Jones, J. Llewellyn, and T. Lewis, "The contribution of field-induced morphological change to the electrical ageing and breakdown of polyethylene," IEEE Transactions on Dielectrics and Electrical Insulation, vol. 12, pp. 951-966, 2005.

[113] D. Poplavskyy, W. Su, and F. So, "Bipolar charge transport, injection, and trapping studies in a model green-emitting polyfluorene copolymer," Journal of Applied Physics, vol. 98, pp. 014501-014501-11, 2005.

[114] BS EN 61378-2:2001 Convertor transformers. Transformers for HVDC applications, 2001; IEC 61378-2:2001 Convertor transformers. Transformers for HVDC applications, 2001

[115] H. Illias, G. Chen, and P. Lewin, "Modelling of partial discharge activity in spherical cavities within a dielectric material," IEEE Electrical Insulation Magazine, vol. 27, pp. 38-45, 2011.

[116] T. Tanaka, T. Ito, Y. Tanaka, and T. Takada, "Frequency dependence of interfacial space charge formed in laminated dielectrics under AC voltage application conditions," in Electrical Insulation and Dielectric Phenomena, 2000 Annual Report Conference on, 2000, pp. 796-799 vol.2.

[117] A. See, J. C. Fothergill, L. A. Dissado, and J. M. Alison, "Measurement of space-charge distributions in solid insulators under rapidly varying voltage using the high-voltage, high-speed pulsed electro-acoustic (PEA) apparatus," Measurement Science & Technology, vol. 12, pp. 1227-1234, Aug 2001.

[118] F. Zheng, Y. Zhang, B. Gong, J. Zhu, and C. Wu, "Formation and migration of space charge packet in low density polyethylene," Science in China Ser. E Engineering & Materials Science, vol. 48, pp. 354-360, 2005.

[119] N. Hussin, J. Zhao, and G. Chen, "The AC breakdown and space charge characteristics of LDPE in the presence of crosslinking by-product," in Electrical Insulating Materials (ISEIM), Proceedings of 2011 International Conference on, 2011, pp. 65-68.

[120] M. Nagao, K. Takano, Y. Mizuno, and M. Kosaki, "Intrinsic AC breakdown of low-density polyethylene film above room-temperature," Proceedings of the 3rd International Conference on Properties and Applications of Dielectric Materials, vols 1 and 2, pp. 1165-1168, 1991.

[121] C. Zhou and G. Chen, "Space charge and AC electrical breakdown strength in polyethylene," IEEE Transactions on Dielectrics and Electrical Insulation, vol. 24, pp. 559-566, 2017.

[122] MIL-STD-202G, Method 301, Dielectric Withstanding Voltage

[123] H. Kim and F. Shi, "Thickness dependent dielectric strength of a low-permittivity dielectric film," Dielectrics and Electrical Insulation, IEEE Transactions on, vol. 8, pp. 248-252, 2001.

[124] C. Chauvet and C. Laurent, "Weibull statistics in short-term dielectric breakdown of thin polyethylene films," Electrical Insulation, IEEE Transactions on, vol. 28, pp. 18-29, 1993.